In-Situ/Operando X-Ray Diffraction applied to Advanced Functional Films and Devices

Kien Nguyen

THÈSE

Pour obtenir le grade de

DOCTEUR DE L'UNIVERSITÉ GRENOBLE ALPES

École doctorale : PHYS - Physique
Spécialité : Physique des matériaux
Unité de recherche : Laboratoire d'Electronique et de Technologie de l'Information (LETI)

Diffraction des Rayons X Opérando appliquée aux films fonctionnels et dispositifs

In-Situ/Operando X-Ray Diffraction applied to Advanced Functional Films and Devices

Présentée par :

Kien NGUYEN

Direction de thèse :

Patrice GERGAUD Ingénieur HDR, CEA Centre de Grenoble	Directeur de thèse
Nicolas VAXELAIRE CEA	Co-encadrant de thèse

Rapporteurs :

THOMAS W. CORNELIUS
Chargé de recherche HDR, CNRS DELEGATION PROVENCE ET CORSE
NATHALIE LE CALVEZ LEMEE
Professeur des Universités, UNIVERSITE D'AMIENS - PICARDIE J VERNE

Thèse soutenue publiquement le **6 juillet 2023**, devant le jury composé de :

THOMAS W. CORNELIUS Chargé de recherche HDR, CNRS DELEGATION PROVENCE ET CORSE	Rapporteur
NATHALIE LE CALVEZ LEMEE Professeur des Universités, UNIVERSITE D'AMIENS - PICARDIE J VERNE	Rapporteure
HUBERT RENEVIER Professeur des Universités, GRENOBLE INP	Président
MARYLINE GUILLOUX-VIRY Professeur des Universités, UNIVERSITE DE RENNES	Examinatrice
DENIS REMIENS Professeur des Universités, Université Polytechnique Hauts de France	Examinateur

Acknowledgement

I would first like to thank my reviewers Mr. Thomas Walter Cornelius and Ms. Nathalie Lemée - Le Calvez for evaluating this thesis work as well as the other members of the jury Mr. Hubert Renevier, Ms. Maryline Guilloux-Viry and Mr. Denis Remiens. Thank you for your comments and for the discussions we had on the day of the defense.

I would particularly like to thank my thesis director Patrice Gergaud. It is mainly thanks to him, his scientific expertise in XRD and his support that my thesis went well. A big thank you also to my supervisor Nicolas Vaxelaire for his daily help and encouragement. I would also like to thank Joel Eymery and Gwenaël Le Rhun for attending my CSI and for giving me a lot of useful advice for the realization of this thesis. Thanks again to Gwen for the very interesting discussions which allowed me to enrich my knowledge of PZT materials in particular and ferroelectric materials in general. It was always a pleasure to collaborate with him. Thanks also to Guillaume Freychet for giving me advice on the improvement of my thesis report.

I would like to thank Thanh-Tra Nguyen for his help at the beginning of my thesis. Although the time we worked together was quite short, I was able to learn a lot of the XRD technique thanks to him. I also thank Edoardo Zatterin and Ewen Bellec who helped us at the ESRF. Thanks also to Hugo Kuentz for helping me with the TF2000 and DBLI measurements. I would like to thank my office roommates Hugo. Thank you for your good mood, for the interesting discussions we had together. It was always a pleasure to share the office with you.

I thank my Vietnamese friends at the CEA. Thank you for being there with me during the difficult times as well as during the happy times.

I would like to thank my family with all my heart. Thank you for supporting me all these years.

And finally a big thank you to my girlfriend, Mai, for always supporting me in my life.

List of abbreviations

Abbreviation	Definition
5G	Fifth-generation
AC	Alternative Current
AFG	Arbitrary Functional Generator
BAW	Bulk Acoustic Wave
BNC	Bayonet Neill-Concelman
CEA	Commissariat à l'Energie Atomique et aux Energies Alternatives
CMOS	Complementary metal oxide semiconductor
DBLI	Double Beam Laser Interferometer
DC	Direct Current
DHM	Dynamic Hysteresis Measurement
ESRF	European Synchrotron Radiation Facility
FWHM	Full Width Half Maximum
ICDD	International Centre for Diffraction Data
IDT	Interdigital Transducers
ILL	Institute Laue-Langevin
LETI	Laboratoire d'électronique des technologies de l'information
LTE	Long-Term Evolution
MEMS	Microelectromechanical systems
MOCVD	Metal Organic Chemical Vapor Deposition
MOD	Metal Organic Deposition
MPB	Morphotropic phase boundary
NPLC	Number of Power Line Cycles
PDF	Power Diffraction File
PFM	PiezoResponse Force Microscopy
PFNC	Plateforme de Nanocaractérisation
PUND	Positive Up Negative Down
PVD	Physical Vapor Deposition
RAM	Random Access Memory
RF	Radiofrequency
SAW	Surface Acoustic Wave
SAXS	Small-Angle X-ray Scattering
SEM	Scanning Electron Microscopy
SMU	Source-Measure Unit
SOI	Silicon-on-Insulator
XRD	X-ray Diffraction

Table of Contents

General introduction....1
Objective of the thesis....2
Chapter I: Introduction to piezo/ferroelectric materials 4
1. History of development and a general introduction to piezo/ferroelectric materials 4
1.1. History of development of piezo/ferroelectric materials 4
1.2. General introduction to piezo/ferroelectric materials.... 5
1.3. Clamping effect in ferroelectric thin films.... 9
1.4. Applications of piezo/ferroelectric materials.... 10
2. Generality about Lead Zirconate Titanate (PZT) 14
2.1. Lead Zirconate Titante phase diagram 14
2.2. PZT with Morphotropic Phase Boundary composition 16
3. The relation between electrical properties and microstructural defects in ferroelectric materials.... 19
3.1. Fatigue effect in ferroelectric materials.... 19
3.2. Imprint effect.... 21
References of Chapter I 24
Chapter II: Experimental methods 30
Introduction.... 30
1. X-ray Diffraction method.... 31
1.1. Definition of X-rays.... 31
1.2. Generation of X-rays.... 32
1.3. X-ray scattering and diffraction.... 35
1.4. Information accessible with X-ray Diffraction.... 39
1.5. Some optical configurations of X-ray diffraction.... 41
1.6. X-ray Diffraction data analysis.... 45
2. Electrical characterization 46
2.1. Definition of electrical polarization 46
2.2. Methods of measuring the polarization of ferroelectric materials.... 47
3. Piezoelectric coefficient measurement.... 52
3.1. Double beam laser interferometer 52
3.2. X-ray Diffraction 54
4. In-situ biasing X-ray Diffraction setup 55
References for chapter II.... 59

Chapter III. Macroscopic behavior of PZT thin films under external electric field 66
Introduction 66
1. Sample preparation procedure developed at the CEA-LETI 67
2. Morphological aspect 69
3. PZT and peak profiles 70
3.1. XRD peak simulation 70
3.2. Experimental study 72
4. The impact of thickness on the macroscopic properties of PZT with MPB composition 73
5. The impact of texture on the macroscopic properties of PZT with MPB composition 75
6. The impact of AC field cycling on the macroscopic properties of PZT 79
6.1. Materials and method 79
6.2. The evolution of structural properties of PZT due to AC field cycling 79
6.3. Evolution of effective piezoelectric coefficient $d_{33,eff}$ as a function of cycling 80
6.4. The evolution of the domain behavior of PZT under AC field cycling 83
Conclusions of Chapter III 83
References for chapter III 84
Chapter IV. Grain-scale analysis of the behavior of PZT thin-film under applied electric field 91
Introduction 91
1. State of the art in the grain-scale analysis of ferroelectric materials 92
2. Experimental method 95
3. Results and discussions 97
Conclusions 103
References for chapter IV 104
General conclusions 111
Perspectives 113
Résumé 116
Abstract 116

List of figures

Figure 1.1: The first hysteresis loop obtained on Rochelle salt at 0°C (figure from [1]) 4
Figure 1.2: The illustration of a 2D unit cell (a) without and (b) under external stress 5
Figure 1.3: Different crystal groups based on symmetry and their relations to piezo-, pyro- and ferroelectrity 6
Figure 1.4: A polarization curve of ferroelectric material (figure from [18]) 7
Figure 1.5: Illustration of 180° and non-180° domain walls; PS is the spontaneous polarization vector of a single domain 7
Figure 1.6: (a) the ideal butterfly curve without non-180° domain switching [20] and (b) the butterfly curve obtained in a 1 µm thick PZT sample with non-180° domain switching developed in CEA-LETI . 8
Figure 1.7: Reference axes and the scheme of a thin film clamped by the substrate 9
Figure 1.8: Schematic of (a) an inkjet printing system (figure from [23]), (b) the varifocal lens (figure from [24]) and (c) the loudspeaker (figure from [25]) 10
Figure 1.9: Schematic of a surface acoustic wave filter (figure from [26]) 12
Figure 1.10: Operating principle piezoelectric MEMS switch (figure from [27]) 13
Figure 1.11: Illustration of the structure of a FeRAM cell with the crystal structure of a ferroelectric and an electric polarization – electric field hysteresis curve (figure from [28]) 13
Figure 1.12: The perovskite structure of PZT (a) in cubic symmetry state and (b) tetragonally distorted under Curie temperature [32] 15
Figure 1.13: The phase diagram of PZT (figure from [33]) 15
Figure 1.14: Transverse piezoelectric coefficient e_{31} in PZT materials. Measured data are for textured 1um films while calculated data are for epitaxial monodomain (001) film. In addition, results from relaxor ferroelectric $PbMg_{1/3}Nb_{2/3}O_3$–$PbTiO_3$ of 3 µm thick texture films and of Motorola bulk state-of-the-art PZT ceramics are added (figure from [37]) 17
Figure 1.16: Illustration of a-,c- and r-domain in $Ti(Zr)O_6$ octahedral unit cell 17
Figure 1.17: Variation of PZT P4mm and Cm phases as a function of applied voltage (figure from 47]) 18
Figure 1.18: (a) An illustration of fatigue in PZT thin film characterized by the decrease in positive (P_{r+}) and negative (P_{r-}) remanent and (b) the evolution of hysteresis loop as a function of number of cycling 20
Figure 1.19: shifting of the polarization loop due to imprint effect under cycling 22
Figure 1.20: The mechanism of imprint as proposed by (a), (b) Grossmann et al. and (c) Dimos et al. (figure from [59]) 23

General introduction

Multiferroics materials are materials having more than one ferroics orders and they are composed of three types of material: ferroelectric, piezoelectric and ferromagnetic. Among these, ferro- and piezoelectric materials attract many attentions thanks to their potential for technological applications. Piezoelectric materials generate mechanical response under applied electric field. Ferroelectric materials also have piezoelectric properties. Moreover, below a certain temperature named Curie temperature, a spontaneous electrical polarization exists in Ferroelectric materials and can be switched under an applied electric field. For the rest of the thesis, this electrical polarization will be called polarization. The development of ferroelectric thin films started in the late 1960s and early 1970s with the integration of Si devices and thin film processing techniques leading to the exploitation of ferroelectric thin films for the fabrication of non-volatile memories. However, at that time, the difficulties of ferroelectric materials processing and integration delayed the progress of ferroelectric materials technologies. It was not until the 1980s, when some achievements in the processing of complex ferroelectric oxides were observed and in 1987, that the first ferroelectric memory integration with silicon complementary metal-oxide semiconductor (CMOS) was demonstrated by Krysalis Corporation [1]. Also during this time, the first step towards the integration of microsensors with microelectronics were made. With the emerging field of micro electro mechanical systems (MEMS), the benefits of the use of ferroelectric films to improve the functionality of MEMS (sensing functions) was explored. From the late 1990s, the popularity of portable phone raises a high demand for polar thin films and this leads to a number of commercial and widespread products composed of ferroelectric materials such as memories, microdevices and microwave electronics components.

The applications of thin film ferroelectric materials are strongly related to their structural properties. Piezoelectricity and ferroelectricity only appears in non-centro symmetric structures and their domain configuration has a very important contribution to the functional properties of the material. Under an applied field, the switching behavior of spontaneous polarization consists of 180^{o} and 90^{o} domain switching in perovskite (tetragonal) ferroelectric crystal. Spatial distribution, relative volume fraction and dynamic motion of these domains often determine the physical properties of ferroelectric thin films. In particular, 90^{o}-domain switching gives rise to field-induced change in strain for piezoelectric material but it also leads to the degradation of polarization such as fatigue in ferroelectric random access memory application. As a result, the understanding of 90^{o}-domain motion under applied electric field is critical to design functional ferroelectric devices.

Today, the emergence of telecommunication and 5G technologies as well as the wearable, fingerprint and medical devices are all candidates for using the piezo/ferroelectric materials. Piezoelectricity has developed into numerous usage kinds with a variety of applications since the starting of the 20th century, when quartz was the material of choice for sonar in military applications. The piezoelectric market is expected to approach $48.5B in 2024 with a 12.6% of compound annual growth rate from 2018 – 2024 on sensors, actuators and memory devices [2]. Even though the market share is still dominated by bulk-based devices, the thin-film piezo-based devices drive the growth of the piezoelectric market. Piezoelectric materials, both in bulk and thin film form, are very important for developing the Radiofrequency (RF) filters (bulk and surface acoustic waves filters), an essential component for 5G technologies. In the field of thin-film based RF filters, Broadcom and Qorvo are the major companies. Thanks to the development of 5G technology as well as an increasing range of frequencies used in the devices, the market for thin-film based filter is strongly boosted. The piezoelectric effect also offers high actuation performance, which can be applied in a number of applications, from inkjet printheads to linear motors, allowing achieving high precision movements.

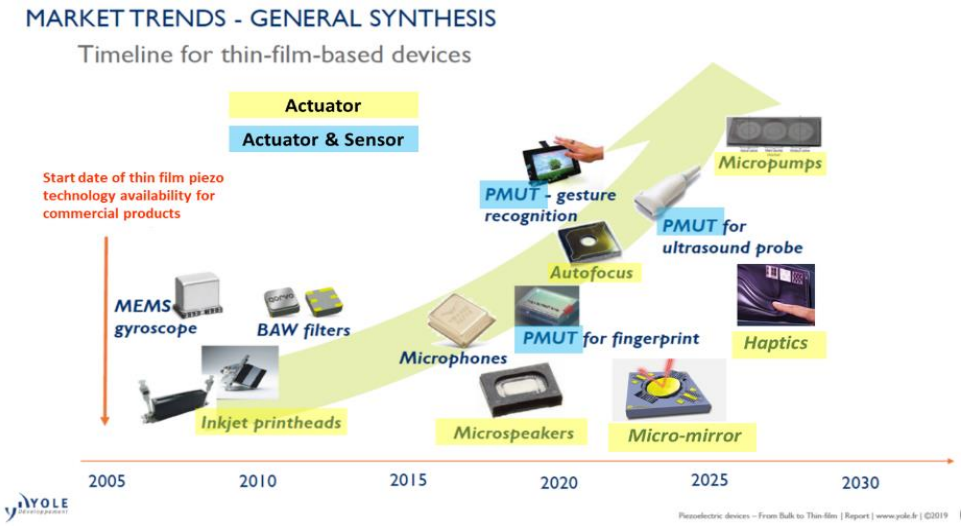

Figure 1: Applications of ferroelectric thin films in commercial products (figure from [3])

Throughout the years, the Laboratory of Electronics and Information technologies, belonging to the Commission of Atomic and Alternative Energy (CEA-LETI) has made some important contributions to the development of ferroelectric materials for microelectronics applications by developing and optimizing the ferroelectric devices (for example by optimizing the interface and electrodes). In 1982, a patent on accelerometer based on capacitive combs was deposited. In the late 2000s, a robust sol-gel method was developed, which allows the deposition of PZT with Morphotropic phase boundary (MPB) composition on Si substrate. This advancement led to the development of the RF switch and then the inkjet print head based on PZT. In the development of ferroelectric-based technologies at CEA-LETI, the Platform of Nano Nanocharacterization (PFNC) plays a vital role. Being well-equipped with advanced materials characterization tools, the PFNC acts as a supporting unit for the technological development through the characterization of advanced materials, thin-film stacks, new architectures and fabrication process. The researchers in PFNC also have some collaborations with external research partners, such as the European Synchrotron Radiation Facility (ESRF) or Institut Laue Langevin (ILL) for complementary characterization techniques. Some of the results in this thesis are obtained in the frame of these collaborations, especially from experiments performed with synchrotron X-ray source.

Objectives of the thesis

For ferro/piezoelectric-based devices, the improvement of the materials is crucial for the improvement of the performance of the devices. This mission consists of not only enhancing the material properties but also alleviating the aging effect as well as improving the time to breakdown. As a result, a better comprehension between the structural parameters and the functional properties is needed. To address this problem, the application of electrical biasing in combination with different techniques – called in-situ biasing - has been used with different structural characterization techniques such as polarization optical microscopy, transmission electron microscopy, and X-ray diffraction (XRD). Among these techniques, XRD has shown to be advantageous for in-situ observation of 90^{o}-domain switching dynamically and quantitatively under applied electric field due to the ability to obtain a wide range of structural information.

From the literature, the in-situ biasing XRD technique has shown to be powerful for the study of microstructural properties of ferroelectric material with MPB composition due to the capability of showing the transformation between different phases around the boundary in the phase diagram under applied field. However, the XRD experiments reported in the literature are often carried out separately with the polarization measurement due to the lack of compatible setup. In our project, the

objective will be to develop an experimental setup which allows the coupling of in-situ biasing XRD with the polarization measurement and the high frequency cycling. As a result, we will obtain the relation between electrical, structural and mechanical behaviors of ferroelectric thin films under both DC and AC applied field in only one single experiment. Furthermore, by doing the fitting on the XRD peaks, the separation of the behaviors of different domain variants existing in the sample could be obtained, allowing us to have a complete understanding of the domain behavior under electric field. Moreover, we will study the behavior at grain-scale on the thin films of PZT, which has parsley been reported previously. This study allows us to have a deeper understanding of the microscopic origin of different macroscopic behaviors and contributes to the development of devices based on piezo/ferroelectric materials.

This thesis was carried out at the PFNC in the CEA-LETI and this manuscript, consisting of five chapters, summarizes all the fundamental knowledge as well as the scientific results obtained during the three years of the thesis. Chapter I aims at providing the background related to the thesis. Firstly, a general introduction to the piezo/ferroelectric material is presented, followed by a description of their behavior under electric field and their applications. Next, we focus on the main material used in this project, Lead Zirconate Titanate material with some brief introduction about its structural and physical properties. As in our project, a special attention is put into the PZT with MPB composition and specially to its structure. To finish the first chapter, we will present a brief summary of the state of the art of the in-situ biasing XRD for studying PZT with MPB composition.

The beginning of Chapter II is dedicated to the introduction of the characterization techniques used and developed during this thesis. We will focus on the XRD technique, with a special emphasis on its principle of operation and its applications for studying the ferro/piezoelectric materials. We will also present the process of data analysis for XRD, including the introduction to the model used for refinement and its usage to extract different parameters of the materials. Then, we will turn our attention to the electrical measurement technique of the ferroelectric materials. In this part, the model of current density in ferroelectric material will be presented, followed by the two polarization techniques used in the project: Positive-Up Negative-Down (PUND) and Dynamic hysteresis measurement (DHM). Next, the measurement of piezoelectric coefficient will be discussed with the introduction of two main techniques used in this thesis: XRD and Double-beam laser interferometer (DBLI). This chapter will be finished with a description of the in-situ biasing XRD setup developed.

Chapter III introduces the results from the behavior of PZT thin film at macroscopic scale under external stimuli. In this part, firstly, the impact of thickness, composition and texture of the sample on the piezo/ferroelectric properties will be presented. Afterwards, the evolution of $d_{33,eff}$ under electrical cycling and temperature will be discussed, followed by the impact of doping on the polarization fatigue properties of PZT. Under electrical cycling, it was found that the $d_{33,eff}$ increases slightly in the wake-up phase before decreasing with a trend similar to the one obtained in remnant polarization. Then, chapter IV will present the multi-scale analysis of domain behavior. In this part, the behavior of different domain variants present in the sample under electric field will be studied at macroscopic and grain-scale.

This manuscript terminates in Chapter V with a general conclusion and some perspectives for future works on piezo/ferroelectric materials using in-situ biasing XRD technique.

Chapter I: Introduction to piezo/ferroelectric materials

1. History of development and a general introduction to piezo/ferroelectric materials

1.1. History of development of piezo/ferroelectric materials

After the exploration of the pyroelectric effect during the mid-18th century, Pierre and Jacques Curie did the first demonstration of direct piezoelectric effect on Rochelle salt in 1880. However, the Curie brothers did not predict the reversed effect. It was first deduced mathematically by Gabriel Lippmann in 1881 and it was immediately experimentally confirmed by the Curies. Piezoelectric material found its first application during the World War I when Paul Langevin and his colleagues applied it in ultrasonic submarine detectors. The device consists of a transducer, made of quartz crystal encapsulated between two steel plates, and a hydrophone to detect the returned echo. As a high-frequency pulse is emitted from the transducer, the reflected sound wave from the object could be obtained. By measuring the time it takes to hear an echo from the reflected sound wave, the distance to the interested object could be calculated [4]. The ferroelectricity was first noticed in Rochelle salt in 1920 by Valasek et al. [5] and the first hysteresis curve measured on ferroelectric material is shown in Figure 1.1. Barium Titanate, one of the most widely used ferroelectric materials, was discovered during World War II in 1941 and the first patent (No. 2 486 560) was applied in 1945 for the transducer based on $BaTiO_3$. In 1952, lead zirconate titanate (PZT) was first reported as a ferroelectric solid-solution system and its phase diagram was established [6] and two years later, the first patent no. 2708244A was applied for the usage of PZT in transducer [7]. The use of PZT helps solving two main problems observed with $BaTiO_3$ transducer. Firstly, $BaTiO_3$ has a low Curie temperature (~ 120^{o}C) and secondly, at -5^{o}C and -90^{o}C, $BaTiO_3$ undergoes polymorphic transitions, thus the dielectric and piezoelectric constants will reach a maximum at these temperatures. As a result, it is unsuitable for the applications in which constant or uniformly varying outputs over a wide range of temperature is needed. [Patent no 2708244, 1952]

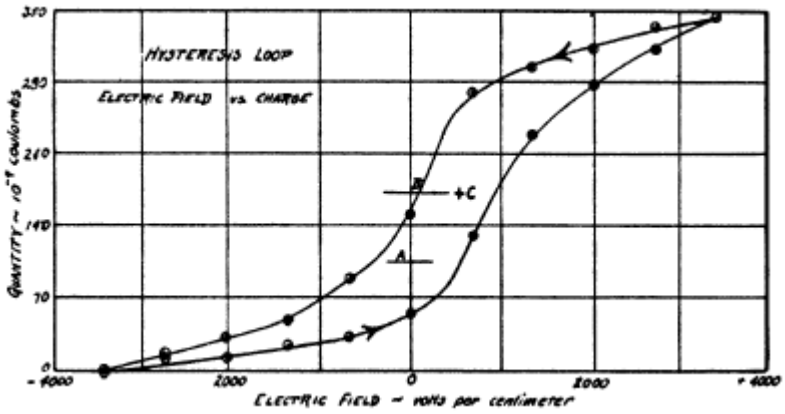

Figure 1.1: The first hysteresis loop obtained on Rochelle salt at 0^{o}C (figure from [1])

From the end of 1970s, the development of ferroelectric materials shifted towards PZT and La-doped PZT thin films. During this period, the majority of works coming from Japanese universities consists of the deposition of PZT using sputtering technique [8]–[10]. From the early to mid-1980s, some industrial labs such as Matsushita [11] [12] and NEC [13] were involved in the development of PZT thin films. In this period, the researchers from Japan helped clarifying the role of substrate temperature in ferroelectric film synthesis as well as the epitaxial growth of PZT-related films while in the US the synthesis by sol-gel [14] and metal-organic decomposition MOD [15] were reported. From the end of 1980s, more techniques were applied for the deposition of ferroelectric thin films including laser deposition [16], Metal-oxide chemical vapor deposition (MOCVD) [17] and activated reactive

evaporation [18]. All those developments have led to the integration of ferroelectric thin films in several applications, such as Surface Acoustic Waves (SAW) devices, electro-optic switches, pyroelectric imagers and non-volatile memories [19].

1.2. General introduction to piezo/ferroelectric materials

Dielectric materials are composed of electrical dipoles which under free state (without any external pressure) organized such that charges cancel out each other to create an equilibrium state. When external pressure is applied, the dipoles are re-organized and align into a dipolar state. However, only piezoelectric materials could develop the surface charge in response to external pressure and to explain this property, it is necessary to take into account the unique atomic structure of piezoelectric materials.

In solids, crystals can be divided into 32 different crystal classes according to their symmetry. There are a subdivision of seven basic crystal systems that are, listed from the most to the least symmetric, cubic, hexagonal, rhombohedral, tetragonal, orthorhombic, monoclinic and triclinic. Among these 32 groups, 21 classes are non-centrosymmetric – a necessary property for being piezoelectric material – and 20 of these are piezoelectric as shown in Figure 1.2. The role of non-centrosymmetric property is illustrated in the Figure 1.3(a) and (b). Without external stress, the centroid of positive and negative charges coincides with each other, denoted by a black dot. When the material is compressed vertically, it expands horizontally. As a result, the centroid of positive and negative charges moves away from each other, thus creating a dipole.

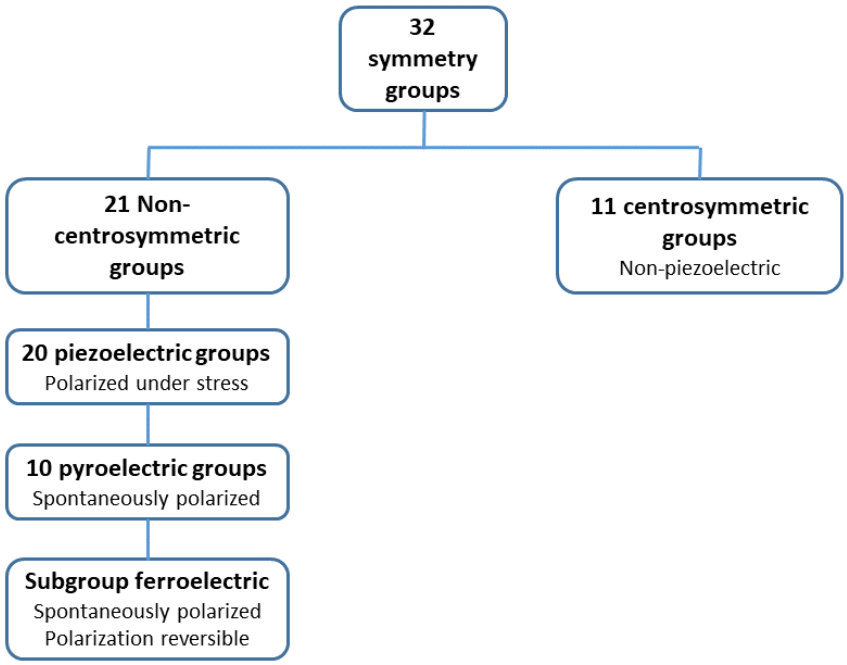

Figure 1.2: Different crystal groups based on symmetry and their relations to piezo-, pyro- and ferroelectricity

From the above arguments, the definition of piezoelectric effect could be expressed as the generation of electrical dipole due to mechanical stress. Being a reversible process, the reversed effect consist in the generation of a mechanical strain by the application of an electric field. The lack of a center of symmetry is necessary for the existence of piezoelectricity because a homogeneous stress is centrosymmetric, thus an unsymmetrical result, such as a vector-quantity-like polarization, cannot be produced. The reversed and direct polarization phenomena could be described by the following equations, respectively:

$$D_i = d_{ik}T_k + \varepsilon_{ij}^{T}E \quad (1.1)$$

$$S_k = s_{kl}^{E}T_l + d_{ik}E_i \quad (1.2)$$

Where *D* is the dielectric displacement, *d* is the piezoelectric constant, *T* the stress, *E* the electric field, *ε* being the dielectric constant, *S* the strain and *s* is the material compliance. The superscript indicates the quantity that is kept constant while the subscript illustrates the orientations along which quantity is determined [7].

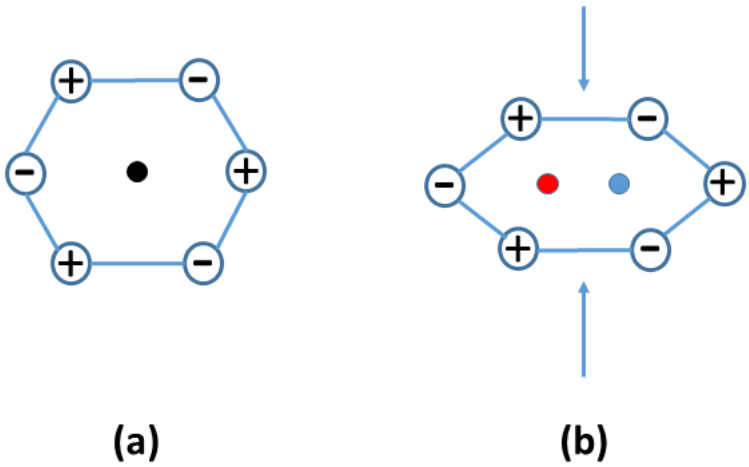

Figure 1.3: the illustration of a 2D unit cell (a) without and (b) under external stress

From Figure 1.3, it can be seen that among the 20 classes of crystal that possesses the piezoelectric properties, ten of them has the **pyroelectric** property. In this type of material, a spontaneous electrical polarization exists which could be changed by the temperature. Under the change in temperature, the position of the atoms within crystal structure is modified slightly, thus changing the polarization. Among the ten crystal classes with pyroelectric property, there is a subgroup which possesses a special property named **ferroelectricity**. Ferroelectric materials also have a spontaneous electrical polarization which can be reversed by the application of an electric field less than the dielectric breakdown of the material itself. Because of this, the polarization state depends not only on the electric field applied, but also on its history. As a result, a difference could be noticed in the shape of the polarization curve of piezoelectric and ferroelectric materials. While in the former case, a linear relation is observed, for ferroelectric material, a hysteresis curve can be achieved as shown in Figure 1.4. In ferroelectric materials, the hysteresis polarization curve only exists under a certain temperature, called **Curie temperature**. Above this point, the materials transfer into **paraelectric** state and the spontaneous polarization vanishes. The hysteresis curve corresponds to the existence of regions that possess an independent polarization, so called **ferroelectric domains.** The ferroelectric domains are formed to minimize the electrostatic energy of the depolarizing field and the elastic energy originate from the mechanical constraint that is generated as the material is cooled through paraelectric-ferroelectric phase transition. Considering the depolarizing field, it has the opposite direction to the spontaneous polarization and is formed whenever there is a nonhomogeneous distribution of charges. The electrostatic energy corresponding to the depolarizing field could be minimized by splitting the ferroelectric samples into domains with oppositely oriented polarization or by compensating the depolarizing charge by electrical conduction through the crystal.

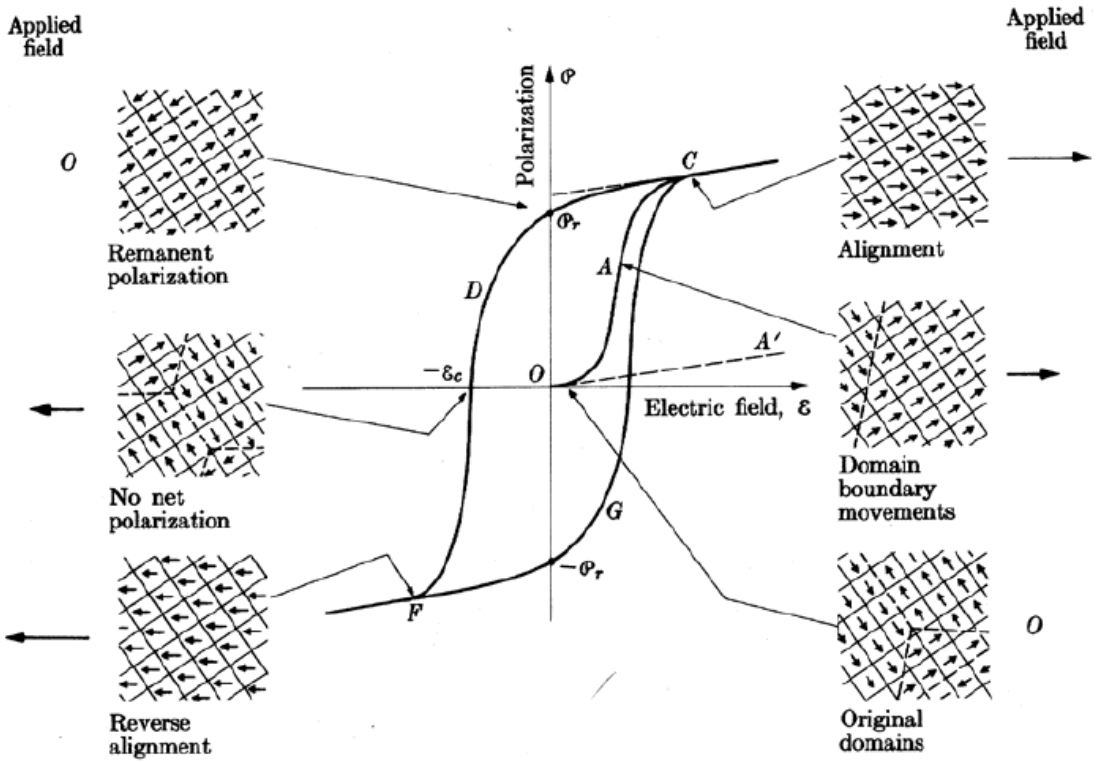

Figure 1.4: A polarization curve of ferroelectric material (figure from [20])

The region that separates two adjacent domains of different polarization direction is known as **domain wall** and they are separated into two types based on the relative polarization direction of the domains with each other: **180° and non-180° domain walls** as demonstrated in Figure 1.5. In the case of the former one, only the difference in the spontaneous polarization vector exists, as a result, it is named the ferroelectric domain walls. For the latter, there is a difference in both the polarization and strain vector and it is called the ferroelastic domain walls. Because the domain walls move under electric field, the macroscopic polarization also depends on their mobility under external stimuli.

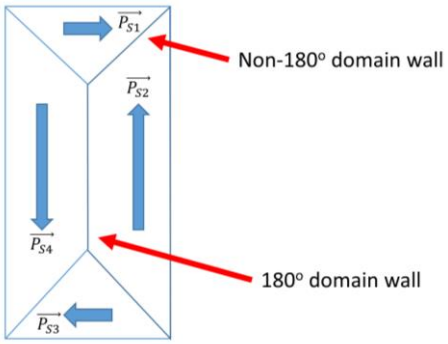

Figure 1.5: Illustration of 180° and non-180° domain walls; $\vec{P}_S$ is the spontaneous polarization vector of a single domain

In case of polydomain crystal, the polarization orientation is considered as a statistical distribution of domains. If an electric field is applied, the domains start to orient in the direction parallel to the applied field, corresponding to an increase in the polarization. This process corresponds to the O-A-C curve in Figure 1.4, which modifies remarkably the arrangement of the domains from the initial random state to the organized one. As the field is decreased to zero, parts of the domains switch back to the initial orientation but most of them still remains in the direction parallel to the field, leading to a non-zero polarization, called remnant polarization P_r. At this state, a microscopic polarization exists, which

originates from the displacement of positive and negative charges in two opposite directions. By increasing the electric field along the opposite direction, the domains will continue to switch until an equal distribution is reached. At this point, the net polarization is zero and the electric field corresponding to this point is called the coercive field E_C. By further increasing the field, a negative saturation polarization is achieved. A complete cycle will result in a typical hysteresis loop.

In addition, domain walls also move under weak and moderate (**subswitching**) fields. This process has a remarkable impact on the dielectric, mechanical and piezoelectric properties of ferroelectric materials. Small displacements of domain walls will have an impact on the ferroelectric polarization and the non-180° domain wall motion also influences the piezoelectric response, so called extrinsic response. It is important to note that, in spite of the irreversible characteristics of this phenomenon, a small part of domain returns to the initial polarization state. This property is called **backswitching** or **relaxation**.

Beside the electrical property, the difference in the mechanical response between piezo- and ferroelectric materials is also remarkable due to the existence of the domain wall motions. As mentioned above, while the non-180° domain wall motion contributes mostly to the piezoelectric response, the 180° domain wall motion contributes dominantly to the ferroelectric property. Because of this, in ferroelectric materials, the mechanical response is the sum of the strain generated by two mechanisms, so-called **intrinsic** and **extrinsic** ones. Considering the first term, it refers to the lattice deformation due to the applied electric field while the second term refers to the domain wall motion. Without this factor, the dielectric and piezoelectric coefficient are mostly independent of the amplitude of the driving force because the intrinsic mechanism dominates, at least at lower field amplitude. As a result, a linear relation between the applied field and the strain is obtained. On the other hand, the domain wall motions give rise to a non-linear relation between the applied electric field and strain [21], leading to a characteristic curve known as “butterfly curve” as shown in Figure 1.6.

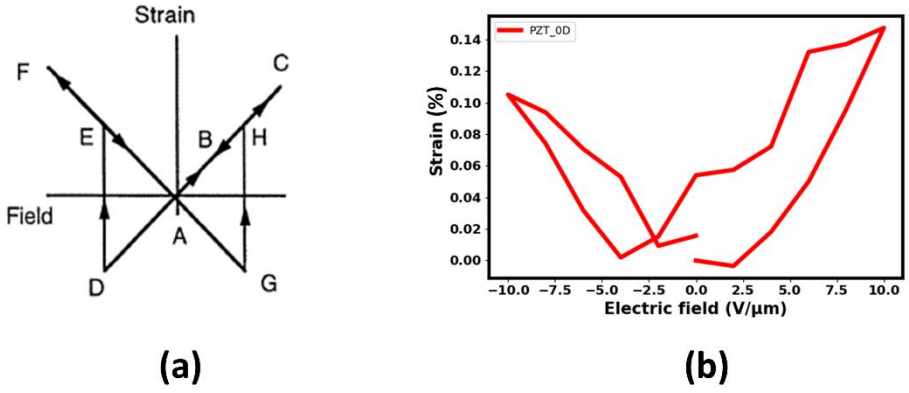

Figure 1.6: (a) the ideal butterfly curve without non-180° domain switching [22] and (b) the butterfly curve obtained in a 1 µm thick PZT sample with non-180° domain switching developed in CEA-LETI

At zero field, the strain in the crystal is considered to be zero (point A). As the field is increased in the direction of spontaneous polarization, the crystal expands through the piezoelectric effect until the maximum field is reached (line A-B-C). After that, the field decreases, leading to the decrease of the strain. When coming back to point A, the strain is again zero. After that, the field reverses its direction. As it is increased in the negative direction, the polarization increases in the negative direction, accompanied by the contraction of the crystal with respect to the point A. At the point D, the field is enough to switch the polarization, leading to the expansion of the crystal (point E). By further increasing the field in the negative direction, the strain keeps on increasing up to point F, and then reversing back to point A as the field is reduced. The polarization reversal of the polarization and the sudden change of the strain happens again at point G. It can be seen that from Figure 1.6(a), most of

the strain behavior is linear, except at point D and G.

In reality, the butterfly curve is more complicated as shown in Figure 1.6(b) due to the impact of non-180° domain switching. This property might lead to remarkable changes in the dimensions of the sample, in addition to the pure piezoelectric response and 180° domain switching in each domain. In fact, from a research by Tsurumi et al. [23], it has been shown that the strain due to non-180° domain wall motion could be comparable to that generated by piezoelectric effect. In real materials, the jump from one polarization state to other is less sudden due to the difference in the coercive field between different domains. In some experiments, the saturated, linear portion of strain-field relationship may not even be observed due to the fact that the single-domain state could only be obtained at very high electric field. In the contrary, the strain-electric field relationship due to domain switching effect is highly non-linear and this part is often observed in real experiments.

1.3. Clamping effect in ferroelectric thin films

In most of the cases, ferroelectric thin films are deposited on a substrate, which is remarkably thicker than the film itself. As a result, the film is clamped by the substrate, leading to the so called **clamping effect** in ferroelectric thin films. Due to this effect, it is necessary to take into account the stress exerted on the film by the substrate. When the substrate is free of motion, the in-plane strain (S_1 and S_2 according to the reference in Figure 1.7) is equal to zero. Moreover, as the surface is free of stress, the stress in the perpendicular direction (T_3) is also zero.

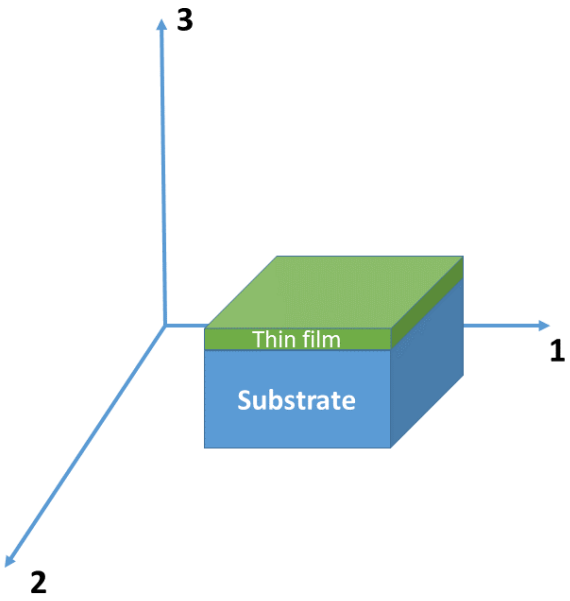

Figure 1.7: Reference axes and the scheme of a thin film clamped by the substrate

By putting these conditions to the piezoelectric equations presented above and considering the symmetry of the strain tensor and equivalence of d_{31} and d_{32}, we obtain the following expressions:

$$S_1 = 0 = s_{11}^E T_1 + s_{12}^E T_2 + d_{31} E_3 \quad (1.3)$$

$$S_2 = 0 = s_{12}^E T_1 + s_{11}^E T_2 + d_{31} E_3 \quad (1.4)$$

$$S_3 = s_{13}^E T_1 + s_{13}^E T_2 + d_{33} E_3 \quad (1.5)$$

By subtracting the equation (1.4) from equation (1.3), an expression proving that $T_1 = T_2$ can be obtained:

$$s_{11}^E T_1 - s_{12}^E T_1 + s_{12}^E T_2 - s_{11}^E T_2 = 0 \quad (1.6)$$

By adding the equation (1.3) to equation (1.4) and with T_1=T_2, we have:

$$(s_{11}^E + s_{12}^E) T_1 = -d_{31} E_3 \quad (1.7)$$

Expressing the term T_1 using the above expression and inserting it to the equation (1.5), taking into consideration the condition $T_1 = T_2$, we have:

$$S_3 = d_{33} E_3 - 2 \frac{s_{13}^E}{s_{11}^E + s_{12}^E} d_{31} E_3 \quad (1.8)$$

Due to the clamping effect, the piezoelectric coefficient d_{33} in thin film is different from that in bulk ceramic sample. As a result, a different quantity is established, so called **effective piezoelectric coefficient** ($d_{33,eff}$):

$$S_3 = (d_{33} - 2 \frac{s_{13}^E}{s_{11}^E + s_{12}^E} d_{31}) E_3 = d_{33,eff} E_3 \quad (1.9)$$

Because in most materials, $d_{31} < 0$, $s_{13} < 0$ and d_{31} is relatively large, the coefficient obtained in thin films is always smaller than in free sample [24].

1.4. Applications of piezo/ferroelectric materials

Thanks to the ability to generate mechanical response under applied electric field, the piezo/ferroelectric materials are used for several applications, which can be summarized into three main families: sensing/actuation, radiofrequency (RF) and memories.

1.4.1. Sensing and actuation application

Thin films of piezoelectric material offer a wide range of advantages in sensing and actuation devices such as large motions, low hysteresis, high available energy densities, high sensitivity for sensors and low power consumption [25]. Among the applications of piezoelectric thin films, inkjet printheads, varifocal lenses and microspeakers are the most matured applications. These applications belong to the category of actuation, where the role of piezoelectric materials consists in moving and controlling a mechanism or a system. The working principles of the three applications are shown in Figure 1.8(a), (b) and (c).

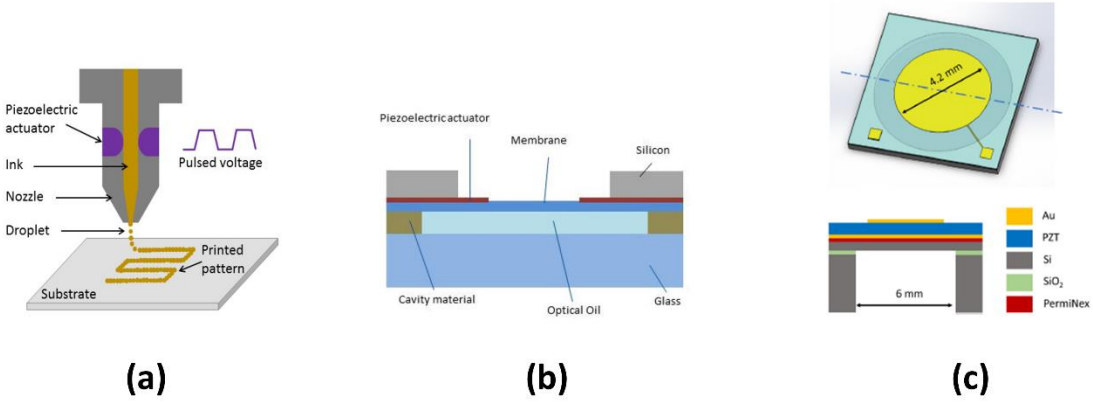

Figure 1.8: Schematic of (a) an inkjet printing system (figure from [26]), (b) the varifocal lens (figure from [27]) and (c) the loudspeaker (figure from [28])

For the inkjet printing system, the viscosity ink is deposited according to the demand by using a digitally controlled actuation mechanism thanks to a piezoelectric element. This electronically driven piezoelectric actuator generates a pressure pulse, which ejects a fluid droplet from the nozzle. By coordinating the electronics and the motion system, the digital patterning of complex layouts on planar surfaces could be done [26]. Concerning the second application, the tuning of the focal length to perform auto-focus or zooming function is obtained by mechanically adjusting the position of the lenses system using motors. However, this solution faces challenges in size, power consumption and speed issues. In order to solve these problems, one of the most promising solution is variable-focus (varifocal) liquid lenses. In this case, the focal length is varied by a change of the lens curvature, which can be done by bending a deformable membrane that encapsulates a liquid. This can be performed by applying a hydraulic pressure in a hermetic chamber that moves the liquid towards the center of the lens and thus modifies the curvature of the membrane. As the PZT film is actuated, the optical oil flows through the membrane centre, leading to the modification of the membrane's curvature and thus varying the focal length [27] as shown in Figure 1.8(b). Figure 1.8(c) illustrates the 3D and cross-sectional schematic of a loudspeaker based on piezoelectric material, consisting of a multi-layer thin diaphragm and an acoustic cavity. The thin ceramic PZT layer is sandwiched between two metal films and suspended on a Silicon-on-insulator (SOI) substrate. A thin layer of polymer is used to bond the PZT to the device layer of the SOI. This speaker structure works based on the d_{31} flexure vibration mode. As an AC voltage is applied to the two metal electrodes, a bending moment in the PZT diaphragm is generated, causing vibration of the diaphragm and generating a sound pressure [28]. Beside the three applications mentioned above, there are also some emerging applications of piezoelectric materials such as micro-mirror [29], haptics [30], micropump [31],…

For MEMS application, the maximization of the piezoelectric coefficient is of considerable importance for reducing the driving voltage or increasing the speed and sensitivity. In order to satisfy this requirement, the materials with ferroelectric properties, which can contribute to the improvement of the mechanical response, are the best candidates. In ferroelectric material, the mechanical response is generated by two mechanisms: intrinsic and extrinsic as mentioned above which lead to better piezoelectric coefficient in comparison with pure piezoelectric material. Among the different ferroelectric materials, the most widely used for MEMS application is based on lead zirconate titanate (PZT), thanks to its greater piezoelectric coefficient in comparison to other materials, such as Aluminum Nitride (AlN) or Zinc Oxide (ZnO). Furthermore, the wide usage of PZT also comes from the developed infrastructure used for its integration on ferroelectric non-volatile access memories, which can be applied for the implementation on MEMS devices [25]. Moreover, the fatigue tests on PZT thin films have shown its strong performance reliability with unipolar field [32]. A more detailed introduction on PZT will be presented later.

1.4.2. RF applications

The unique ability of piezo/ferroelectric materials in generating mechanical response to an applied electric field and vice versa as well as the spontaneous polarization in ferroelectric materials makes them attractive for different technological applications, especially those connected to the development of fifth-generation mobile networks (5G) and Internet of Things (IoT). In this section, we will present the two applications of piezo/ferroelectric materials that are the Surface acoustic wave (SAW) filters and Radiofrequency (RF) switch.

SAW filter is a type of RF filter that can be used in a wide range of applications up to 3 GHz. The filter consists of interdigital transducers (IDTs) which contains interleaved metal electrodes on either end of the device as shown in Figure 1.9. These IDTs are deposited on a piezoelectric substrate. The SAW filter operates by converting electrical energy into acoustic or mechanical energy on the piezoelectric substrate. The input IDT creates acoustic waves from the incident electrical signal and the output

transducer receives the acoustic waves, converting them back into electrical energy.

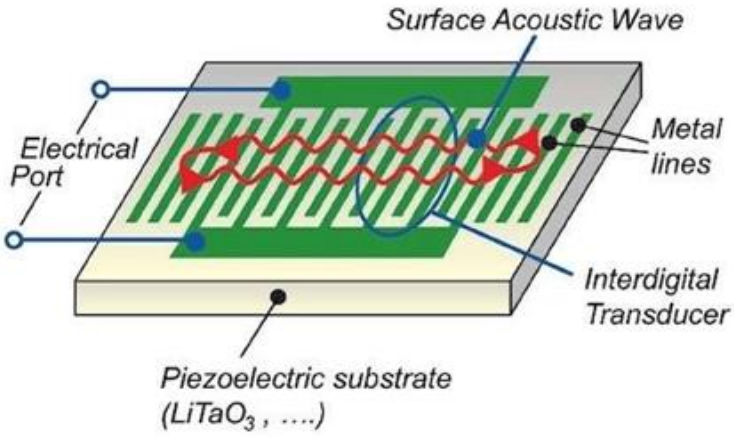

Figure 1.9: Schematic of a surface acoustic wave filter (figure from [33])

Another type of filter which also exploits the piezoelectric material is Bulk Acoustic Wave (BAW) filter. Similar to SAW, BAW filter also operates by converting electrical energy into mechanical energy on a piezoelectric material. However, BAW filter can operate at higher frequency in comparison to SAW (up to 6 GHz), thus it is used for Long-Term Evolution (LTE) communication band higher than 1.9 GHz. BAW filter also has interdigital transducers to convert electrical energy to mechanical energy but unlike SAW filter, the acoustic waves propagate vertically. The structure of the BAW filter is shown in Figure 1.10, in which the piezoelectric film is sandwiched between two electrodes on top and bottom. These electrodes excite the acoustic waves, which propagate vertically between them to form a standing acoustic wave. The resonance frequency is determined by the thickness of the film and the mass of the electrodes.

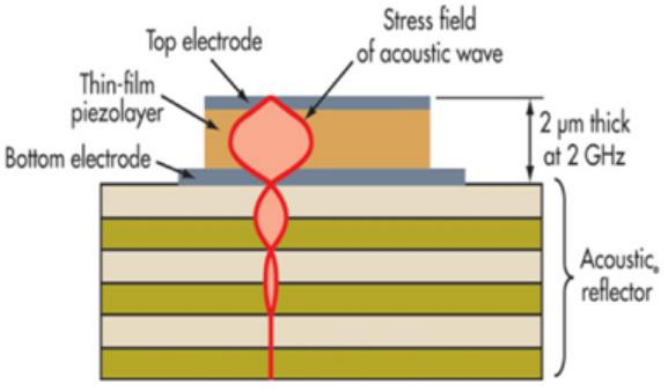

Figure 1.10: Cross-section view of the structure of BAW filter

MEMS switches are devices that use mechanical movement to obtain open or short circuit in RF transmission line and they are designed specifically to operate at RF-to-millimetre wave frequencies (0.1 – 100 GHz). The force required for the mechanical movement is generated by piezoelectric effect and the design as well as working principle of the device is shown in Figure 1.11.

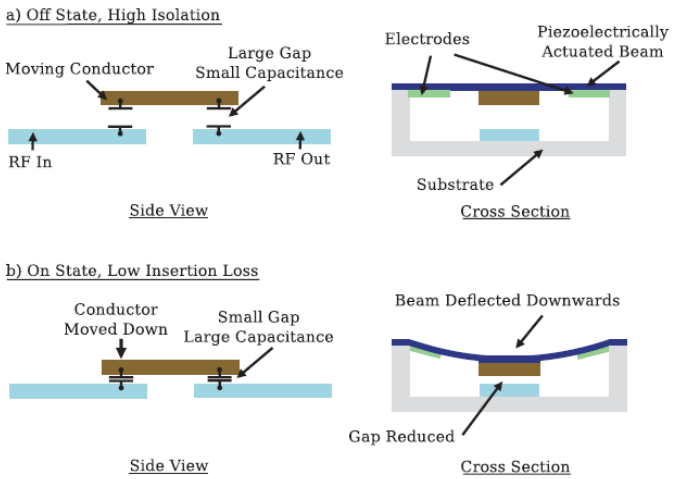

Figure 1.11: Operating principle piezoelectric MEMS switch (figure from [34])

In the RF switch based on piezoelectric materials, the input and output conductors are fixed on the substrate and the moving part is supported by a piezoelectric actuated beam. In the "off" state, the moving part is far from the input and output conductors. In this case, the series capacitance between the input and output of the switch is small, thus blocking the RF signal. When the electric field is applied across the piezoelectric beam, the beam deflects and the mobile conductor is moved closer to the fixed conductor. In this case, the capacitance between the input and output is increased and the signal is passed. The ratio of the insertion loss in the "on" state to the isolation of the switch in the "off" state is determined by the change in the position of the conductor. As a result, in order to optimize the performance of the switch, the movement of the piezoelectric beam should be maximized.

1.4.3. Memory applications

Microelectronics industry now works actively on the development of new memory solutions in which the main objectives are the low volatility of the stocked information, low energy consumption and low read/write time. Among different choices, the Ferroelectric Random Access Memory (FeRAM) is a promising candidate and the structure of a FeRAM cell is shown in Figure 1.12.

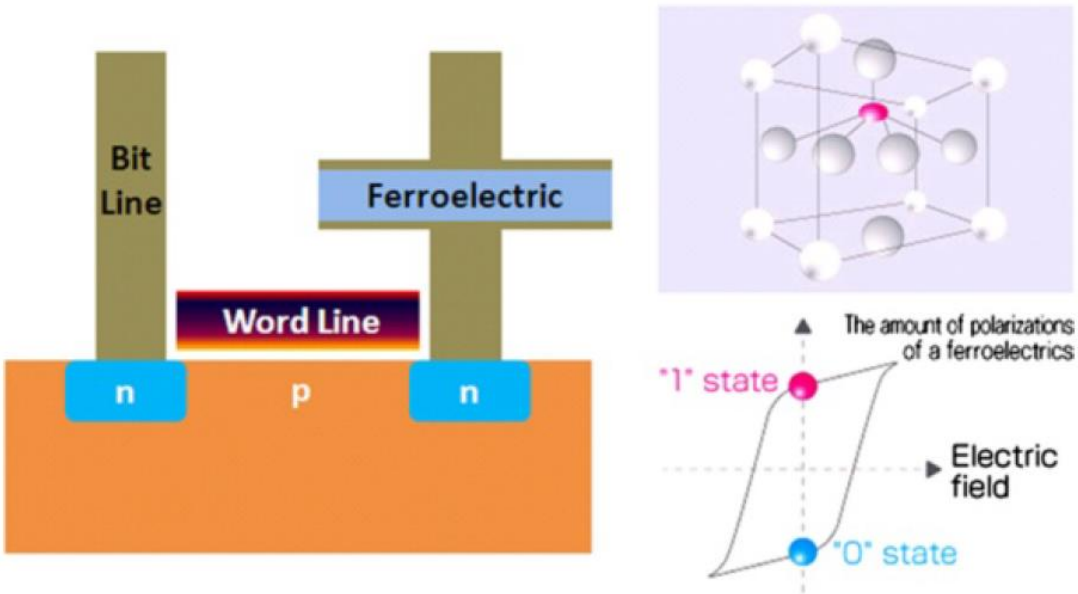

Figure 1.12: Illustration of the structure of a FeRAM cell with the crystal structure of a ferroelectric and an electric polarization – electric field hysteresis curve (figure from [35])

The shown FeRAM cell represents the simplest configuration that consists of a ferroelectric capacitor controlled by a transistor metal oxide semiconductor and this is called the 1T/1C configuration structure. In this case, the binary information (0 or 1) is stored in the ferroelectric capacitor based on its polarization state and the transistor assures the control of the voltage applied on the capacitor. In order to write the bit "0", it is necessary to apply an electric field negative larger than the coercive field E_{C-}. As the field is removed, the material returns spontaneously to the polarization state P_{R+} corresponding to the binary bit "0". Using the same principle, in order to write the bit "1", an electric field larger than the positive coercive field E_{C+} needs to be applied, which will fix the polarization in the positive orientation, corresponding to the bit "1".

Concerning the reading process, if the information is stored in bit "1" (P_{R+} state), the application of a positive field leads to the increase of the polarization. This process is called the polarization of "non-switching" and the current generated is named "j1". In case the information is stored in bit "0" (P_{R-}), the application of an electric field larger than the coercive field will reverse the polarization – so called "switching" and the current response is called "j0" and j0 > j1. After that, by using a comparator, the current j0 and j1 allows the separation of the two polarization states stored in the memory as well as the reading of the information.

Concerning the materials, even though the most matured technology is based on PZT and $Ba_{0.8}Sr_{0.2}TiO_3$ (BST) [36] the difficulties in scaling down (dedicated cleanroom needed) and Pb pollution leads to the need for new materials. Hafnia Oxide (HfO_2) appears to be an emerging replacement thanks to the recent discovery of its ferroelectric properties [37]. In recent years, a strong improvement in the integration process of HfO_2 on non-volatile memories in microelectronic cleanrooms increases its attraction in comparison with PZT or BST. For the moment, different studies have shown that the material works well on the process of 130 nm node with a thickness of 10 nm (in CEA-LETI) [38]. However, the 28 nm node requires decreasing the thickness to 5 nm, which raises questions about its performance at such thickness. Furthermore, questions about reliability, which is crucial for commercialization, as well as the optimization of the electrodes, need to be solved.

2. Generality about Lead Zirconate Titanate (PZT)

2.1. Lead Zirconate Titante phase diagram

In this thesis work the focus is put on Lead Zirconante Titanate (PZT) – one of the most widely used ferro/piezoelectric materials on the market. PZT is a solid solution of $PbTiO_3$ and $PbZrO_3$ and crystallizes in the perovskite structure ABO_3 as shown in Figure 1.13.

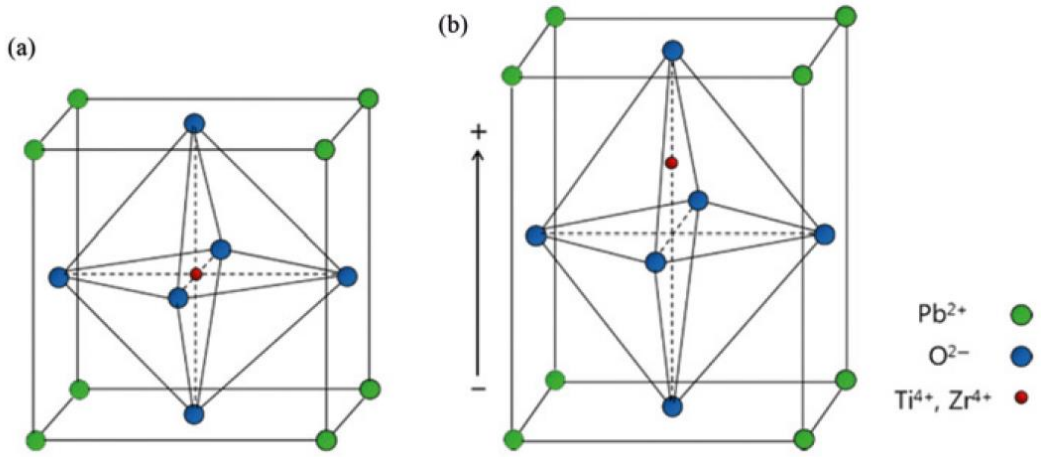

Figure 1.13: The perovskite structure of PZT (a) in cubic symmetry state and (b) tetragonally distorted under Curie temperature [39]

The physical properties of PZT vary remarkably as a function of temperature and Zr/Ti ratio. At temperature higher than Curie temperature, which varies as a function of composition of PZT, the material crystallizes in the cubic phase. Because this phase has the centrosymmetric structure, the barycenter of positive and negative charges coincide with each other, thus the material has paraelectric property. As mentioned above, the ferroelectric property could only be obtained below Curie temperature. For PZT, at Curie temperature, the cubic structure transforms into non-centrosymmetric structures, such as tetragonal, rhombohedral, orthorhombic or monoclinic, depending on the composition. As these structures are non-centrosymmetric, their barycenters of positive and negative charges no longer coincide with each other, giving rise to the existence of a spontaneous polarization.

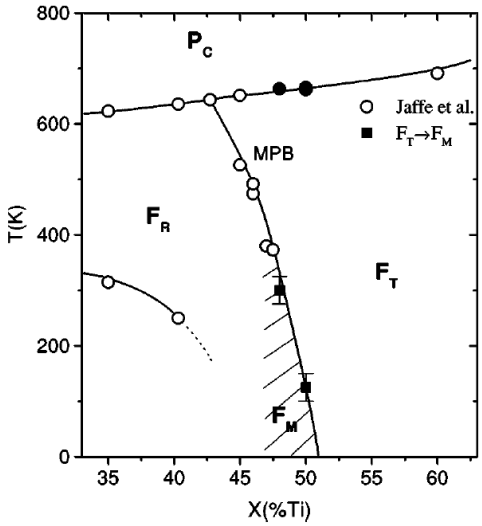

Figure 1.14: The phase diagram of PZT (figure from [40])

The Zr/Ti ratio has an important impact on the crystallographic structure of the sample as shown in Figure 1.14. If the amount of Ti is superior to 48%, the sample possesses a tetragonal structure. In tetragonal phase, spontaneous polarization orients along <100> direction. As the <100> direction has six equivalent orientations, the polarization could be pointed along six different orientations, leading to the possibility of six domain configurations. In case Zr ratio is higher than 52%, the PZT will crystallize in the rhombohedral phase. In the rhombohedral phase, the spontaneous polarization is oriented along <111> orientation, leading to eight possible domain configurations. Near the boundary between tetragonal and rhombohedral phases, at the so called Morphotropic Phase Boundary (MPB) the

monoclinic phase could exist, whose polarization vector lies in <110> crystallographic orientation.

2.2. PZT with Morphotropic Phase Boundary composition

In this research, a special attention is put onto the PZT with morphotropic phase boundary (MPB) composition because it has shown the best piezoelectric performance in comparison with other compositions. MPB refers to the transition between two ferroelectric crystallographic phases of a particular ferroelectric material. For PZT, it is the transition between tetragonal and rhombohedral phases resulting from the variation of composition or pressure. In this section, the nature of MPB, its high piezoelectric performance as well as the way to obtain it will be addressed. In a research by Ahart et al. [41], the origin of MPB has been discussed by studying lead titanate ($PbTiO_3$) samples. By carrying out cryogenic, high-pressure, in-situ Raman spectroscopy and synchrotron X-ray diffraction experiments, the researchers found a phase transition sequence from tetragonal to monoclinic at 10 GPa, monoclinic M_c to monoclinic M_A at 15 GPa and monoclinic to rhombohedral at 20 GPa. The existence of rhombohedral phase at high pressure is due to a zone-boundary instability. This result indicates that the morphotropic phase boundary region could exist under pressure at cryogenic temperatures. First-principles calculations show that as the pressure increases, the lattice strain decreases with a ground state along <111> orientation in rhombohedral phases. The monoclinic phase between rhombohedral and tetragonal phases comes from the higher-order terms in a Taylor expansion of the energy, which corresponds to a rotation of the polarization direction. The ease of polarization rotation is the nature of the high electromechanical coupling in transition region. The obtained results showed that presence of MPB composition that generates large electromechanical response does not require random field, compositional heterogeneity, polar nanoregions, mesostructural heterogeneity or nano domains. However, this research suggests that the MPB composition could be obtained by applying chemical pressure by the substitution of atoms and especially those high coupling materials such as PMN-PT and PZN-PT could compositionally tune the inherent transition achieved in $PbTiO_3$ to ambient pressure.

In the paper by Rossetti et al. [42], the 2-4-6 Landau polynomial has been exploited to explain the nanoscale domain structures near the Morphotropic Boundary (MB) in PZT. It was found that at MB line, the crystallographic anisotropy of the polarization diminishes. As the domain wall energy (γ) is determined by the energy for polarization rotation within the domain boundary region between adjacent domains, the domain wall energy decreases as well. Because the domain size is proportional to the domain energy $\sqrt{\gamma}$, the domain structures near the MB line are reduced to nanoscale dimension. This observation is coherent with the results from transmission electron microscopy that show the reduction of domain structure to nanometer scale at the MB region.

In the study of Wada and Tsurumi [23], the relation between the piezoelectric performance and the domain size was established by investigating Barium Titanate ($BaTiO_3$) samples. It was found that piezoelectric coefficients such as d_{31} and k_{31} increased remarkably with decreasing domain size. Furthermore, it was noticed that for $BaTiO_3$ crystal with a domain size of 6.5 µm, the obtained d_{31} is 180.1 pC/N and k_{31} of 41.4 %. This data is close to that of 'soft' PZT ceramics (d_{31} = 171.1 pC/N and k_{31} = 34.4 %). This indicates that the samples with fine domain sizes are necessary to achieve high electromechanical response. This study was complemented by a simulation work by Ahluwalia et al. [43], in which the simulation using Ginzburg-Landau model confirms the enhancement of piezoelectric coefficient by reducing the domain size in the samples with multidomain states. This indicates the metastability of the multidomain states which could be switched easily as the number of domain walls increases. Finally, the texture of the ferroelectric films has also been shown to impact the macroscopic piezo-response. In the review article by Setter et al. [44], the authors have shown that for PZT, the maximum piezoelectric coefficient $e_{31,eff}$ is obtained in sample of (100) rhombohedral films, whose composition lies closed to the MPB as illustrated in Figure 1.15. This also turned out to be the

orientation where the maximum of the piezoelectric responses is achieved, for monodomain epitaxial thin films with the pseudo-cubic (001).

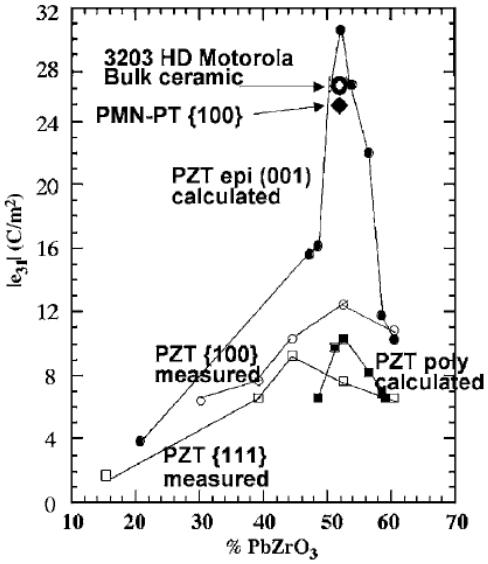

Figure 1.15: Transverse piezoelectric coefficient e_{31} in PZT materials. Measured data are for textured 1um films while calculated data are for epitaxial monodomain (001) film. In addition, results from relaxor ferroelectric $PbMg_{1/3}Nb_{2/3}O_3$–$PbTiO_3$ of 3 µm thick texture films and of Motorola bulk state-of-the-art PZT ceramics are added (figure from [44])

In conclusion, the microstructure of ferroelectric materials with MPB composition is complex. It might be composed of a mixture of small and unstable domains of different crystallographic phases. These domains have low polarization rotation energy, low shear stress and this could be the origin of the high electromechanical response. In the following manuscript, we choose to use the rhombohedral (R3m space group) and tetragonal (P4mm space group) phases for XRD peak indexation (in the article of Hinterstein et al., the Cm space group was used). The reason is that we do believe that we can not discriminate R3m (rhombohedral) and Cm (monoclinic) phases. As a result, three domain variations exist in our samples, which are the a- and c-domains, belonging to the P4mm space group and rhombohedral, or r-domain, which belongs to the R3m space group. The illustration of these domains is shown in Figure 1.16.

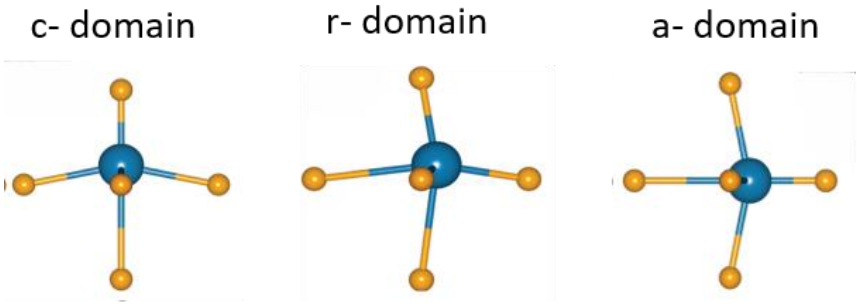

Figure 1.16: Illustration of a-, c- and r-domains in $Ti(Zr)O_6$ octahedral unit cell

2.2.1. Contribution of in-situ biasing XRD to the research of PZT with MPB composition

At the MPB composition, the phase coexistence leads to different unique behaviors of ferroelectric materials under electric field (phase transformation, domain switching, piezoelectric effect). As a result, the in-situ biasing XRD technique is very useful to study this type of material. Indeed, XRD enables the observation of the variation of different parameters such as the domain size, the strain or

the ratio between different domain variants under electric field. These informations are critical to have a better understanding of the behavior of ferroelectrics materials under applied electric field. In the article by Guo et al. [45], the authors tried to explain the origin of high piezoelectric response in PZT by exploiting the in-situ biasing XRD using synchrotron source on the PZT ceramic samples with different Ti contents of 0.42, 0.45 and 0.48. It was found that in PZT with composition close to MPB, the piezoelectric strain orients along the directions associated with monoclinic distortion rather than the direction of the applied field. Based on this observation, it was suggested that the monoclinic is an intermediate phase between the tetragonal and rhombohedral phases located at the MPB of PZT. In combination with the simulation work by Bellaiche et al. [46], the large piezoelectricity is due to the very large value of d_{15} coefficient in single crystal. In the article by Hinterstein et al. [47], the in-situ biasing XRD has been carried out on synchrotron source to study the PZT ceramic with composition near the MPB. The improvement in the piezoelectric and dielectric properties in PZT with MPB composition was believed to stem from (1) the coexistence of rhombohedral and tetragonal phases that can be linked with martensitic phase transition theory or by (2) the existence of monoclinic *Cm* phase. In this study, the researchers have proved the existence of monoclinic phase in the sample through the Rietveld full diffractogram refinement as illustrated in Figure 1.17(b). Furthermore, the phase ratio of monoclinic also illustrates the reversible butterfly behavior as a function of applied field as shown in Figure 1.17(c), which indicates an increase of the monoclinic abundance at high electric field at the expense of tetragonal phase. This illustrates a transformation from tetragonal to monoclinic phase at higher electric field. As a result, Hinterstein and co-workers believe that the polarization mechanism is responsible for the improved electromechanical properties in MPB composition instead of the martensitic transition mechanism. In another article by Kovacova et al. [48], the correlation between electric-field-induced phase transition and piezoelectricity in PZT thin films with MPB composition has been studied. Using the in-situ biasing XRD using lab-source equipment, the authors found a transformation from tetragonal (P4mm space group) to rhombohedral (R3m space group) phase under applied field as shown in Figure 1.17, which is reported to be much more pronounced than domain switching effect. Besides that, the piezoelectric coefficient $d_{33,eff}$ was measured by both a commercial equipment as well as from the XRD peaks displacement under applied field. The results from the two methods are coherent with each other and showed that there is a correlation between the piezoelectric response and the field-induced phase transition in MPB PZT films. As a result, the authors suggest that the $d_{33,eff}$ could be enhanced by promoting the field-induced phase transition especially through the tuning of the PZT composition.

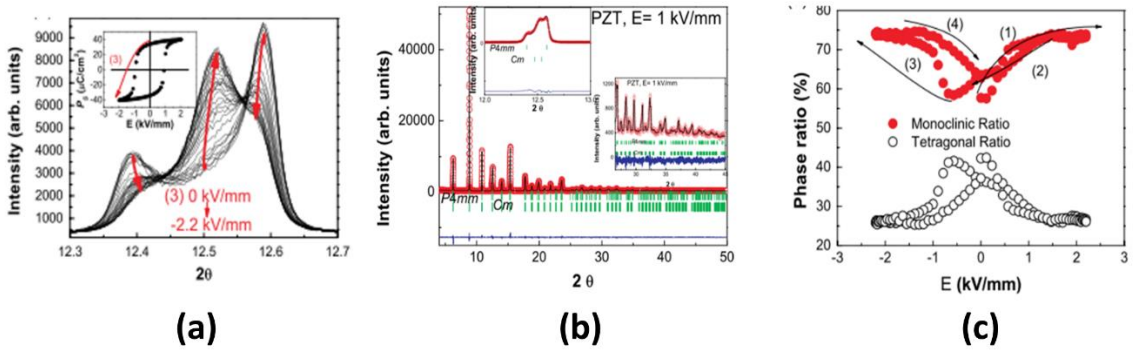

Figure 1.17: (a) the influence of applied field on the (002) peak, (b) Rietveld refinement of PZT at 1 kV/mm and (c) evolution of Monoclinic-tetragonal phase ratio under electric field (figure from 47])

In a study by Cornelius et al. [49], the role of imprint and composition on piezoelectric response and electrical properties of $PbZr_{1-x}Ti_xO_3$ with compositions around MPB (x = 0.47, 0.49 and 0.50) have been studied by in-situ synchrotron XRD. The asymmetrical butterfly loops of the piezoelectric strain obtained from the (100) and (110) crystalline directions of the films with different composition reveals the imprint effect in the film. The asymmetries reveal that the effective coefficient is higher along the

negative field than the positive field and they are more pronounced in the PZT film with x = 0.5. This is following the asymmetry ΔE_c in coercive field of the polarization loop and dielectric curves. These results showed that the imprint effect is more pronounced in the film with x = 0.50 and tends to disappear for the film with x = 0.47. Cornelius et *al.* also published later a research on the piezoelectric response and electrical properties of La-doped PZT (PLZT) with Zr/Ti = 52/48 (MPB composition) using in-situ biasing synchrotron XRD [50]. The researchers found that at low lanthanum concentrations (0 and 3 mol%), a Bragg peak with double-peak profile exists while it disappears for films with 12 mol% La content. This double-peak profile is believed to stem from the inconsistent sum of the conventional peak and the new peak which originates from the coexistence of nanodomains and coarse domains. As the content of La is increased, the tetragonality in PZT decreases, leading to the reduction of the nanodomain and coarse domains coexistence, associated with a decrease in the spontaneous polarization in the unit cell. For all composition of La ranging from 0 – 12% mol, the butterfly curves associated with the piezoelectric are plotted and showed the existence of a dependence of the asymmetry on the proportion of La. These asymmetries are due to the internal electric field in PLZT films and they are reversely proportional to the ratio of La. The mechanical response of PLZT with different La ratios under DC and AC fields has also been studied. Results showed that while the PLZT12 showed a butterfly behavior for DC and AC electric fields, samples with lower La concentration only exhibits the same behavior for AC frequencies around 0.1 Hz and linear behavior for frequencies larger than 1 Hz. The maximum piezoelectrically induced strain was found to be smaller for AC fields than for DC fields, and it decreases with increasing the AC frequency.

3. The relation between electrical properties and microstructural defects in ferroelectric materials

One of the objective of this PhD thesis was to contribute to the improvement of the performance of ferroelectric-based devices through the improvement of materials. This consists of enhancing the material properties and mitigating the fatigue problem as well as improving the breakdown time. In order to achieve those objectives, it is necessary to have a better understanding of the correlation between the electrical and structural properties of the materials. In this thesis, this problem is addressed through the usage of in-situ biasing XRD technique. In particularly, we implement a new protocol to study the domain mobility during an ageing protocol.

3.1. Fatigue effect in ferroelectric materials

In ferroelectric materials, the fatigue effect is defined as the loss of switchable polarization as a function of applied electric field. Figure 1.18(a) and (b) show a typical fatigue behavior of PZT thin films which consists of two main parts: the initial increase in remnant polarization from 1 – 1e4 cycles (so called **wake-up effect**) and the decrease of remnant polarization from 10^4 – 10^8 cycles. For the wake-up effect, due to the thermal treatment during the elaboration process, the electrodes could be partially oxidized, inducing oxygen vacancies near the interfaces of ferroelectric film and electrodes. These defects create built-in bias which might suppress the ferroelectric dipoles polarization near the field and could even reorient the dipoles in opposite directions. As a result, the overall polarization is not maximized. As the cycling is applied, the defects are redistributed, leading to the redistribution of the built-in bias and polarizing the dipoles in the same orientations [51].

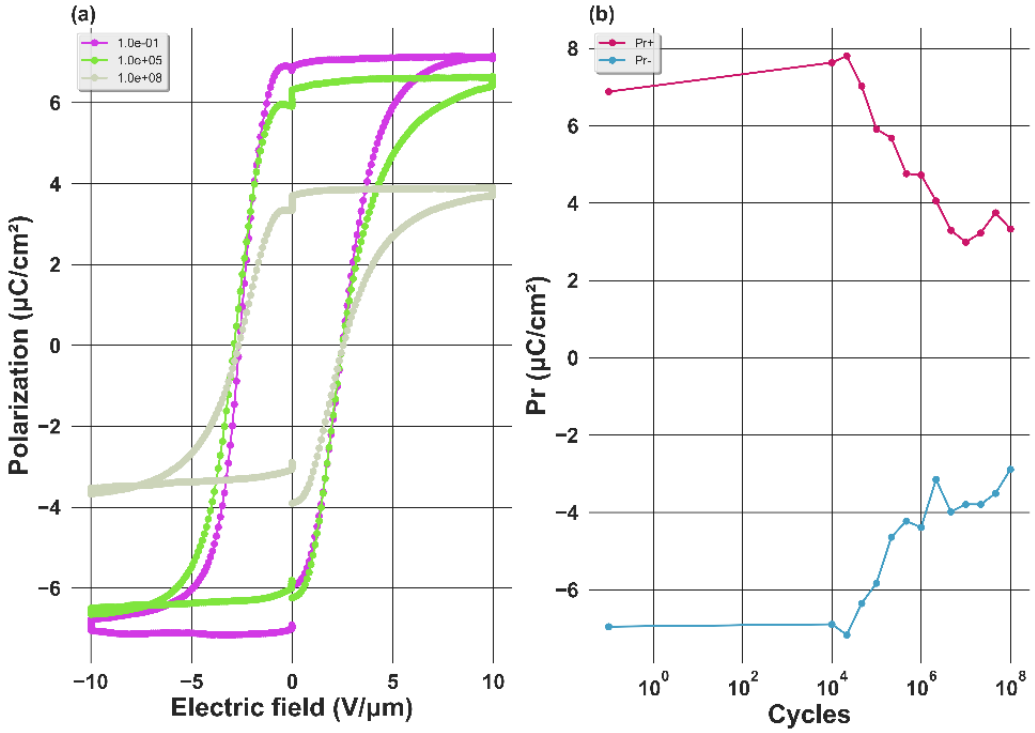

Figure 1.18: (a) An illustration of fatigue in PZT thin film characterized by the decrease in positive (P_{r+}) and negative (P_{r-}) remanent and (b) the evolution of hysteresis loop as a function of number of cycling

Concerning the fatigue effect, the nature as well as the impact of doping on the alleviation of the effect will be discussed. The exact nature of ferroelectric fatigue is not well understood, but a number of mechanisms has been proposed. The first mechanism associated with the fatigue effect is microcracking [52]. It exists in the ferroelectric materials with morphotropic phase boundary composition with large tetragonal lattice distortion. At this composition, the applied electric field lead to two main phenomena: domain switching and phase transformation. As a result, a large grain deformation is observed under electric field and due to the intergranular strain, cracks could be initiated [53]. The second explanation for the fatigue effect is the domain-wall pinning effect. From the article by Al-Shareef et al. [54], under applied electric field cycling, the charge carriers are injected into the ferroelectric films from the electrodes. These free electronic charges may be trapped at the domain-wall region where there is a discontinuity of polarization, thus prohibiting the domain wall motion. The polarization fatigue process is considered a result of the competition between the domain-wall pinning due to electronic charge trapping and unpinning of the domain walls due to electric field. As a result, the weak fatigue in films might not indicate that the domain pinning is absent but it could be that the depinning force is as important as the pinning one. Considering the domain-wall pinning effect, an important contribution to this phenomenon is the oxygen vacancies, as a result it is necessary to mention its role in the fatigue of ferroelectric materials.

In metal oxides, oxygen vacancies are considered point defects, created during the manufacturing process or during the electric field cycling [55]. In a research by Pesic et al. [56], it was found that at fatigued state, O vacancy defects are generated at higher speed at the interface between film/electrode. As a result, this region has a higher density of defects and lower permittivity, resulting in a higher factor of degradation and faster bond breakage. When the electric field is applied, the charge trapping effect occurs, thus increasing the field over the interface while reducing it inside the bulk. Therefore, the ferroelectric film experiences a lower switching field with a reduction of the number of switching domains. Moreover, the charge trapping also creates dipoles that impede the switching of the domains, resulting in the partial or even complete pinning of the domains. Finally, the cycling leads to the creation of vacancy within the grains. These defect sites could create the leakage

current path and leading to the breakdown.

In another research by Warren et al. [57], the researchers have found that annealing the films in an oxygen-deficient atmosphere may lead to polarization reduction and changes in the hysteresis loop. The authors argued that this suppression of polarization is due to the oxygen vacancies, which act as pinning centers for domain walls in films. Moreover, other simulation works have also been carried to study the mechanism of oxygen vacancies in reducing the achievable polarization. Scott et al. [58] [59] proposed that the oxygen-deficient regions might grow into the bulk and screen a part of the sample from the applied field, leading to polarization losses. The formation of regions with high oxygen vacancy density at film/metal electrode interface also initiates the formation of an n-type layer, which increases the electron injection rate during cycling. As these electrons are trapped at domain walls, the domain wall pinning will be increased.

As the fatigue effect is harmful for the device performance, one of the well-known method to alleviate this effect is through the doping of the sample. In an article by Li et al. [60], the effect of Nb doping on fatigue properties of PZT thin films elaborated by sol-gel process has been studied. It was found that a concentration of 2% of Nb improved remarkably the fatigue resistance of the film. The origin of this improvement lies in the fact that in the PZT lattice, the Nb^{5+} ions replace either Zr^{4+} or Ti^{4+} ions due to their similar ionic radii and generate additional positive charge. To maintain the charge neutrality, lead vacancies are created and known to reduce the local stress in the lattice, thus promoting the mobility of domain walls and contributing to a better fatigue resistance [61]. Furthermore, the doping of Nb is also reported to be an efficient way to prevent the separation of oxygen ions from the perovskite structure, thus alleviating the accumulation of space charges that associate with oxygen vacancies at Pt/PZT interface. Finally, the introduction of Nb in PZT films leads to a modification of internal electric field, which impacts the electromigration of charged defects.

3.2. Imprint effect

In ferroelectric materials, the imprint effect is the existence of a preferred polarization state under certain conditions that is characterized by the horizontally shifting of the hysteresis polarization vs electric field curve as shown in Figure 1.19. This property is considered to be detrimental especially for memory devices. As mentioned in the part 4.3, the positive and negative polarization state could be used to store bit “1” or bit ”0”. As a result, the development of a preferential polarization state can make it difficult to switch to the non-preferential one. Because of that, after a long storage period in the same state or many rewrites into the same preferential state, it may be difficult for the device to store different state of data [62].

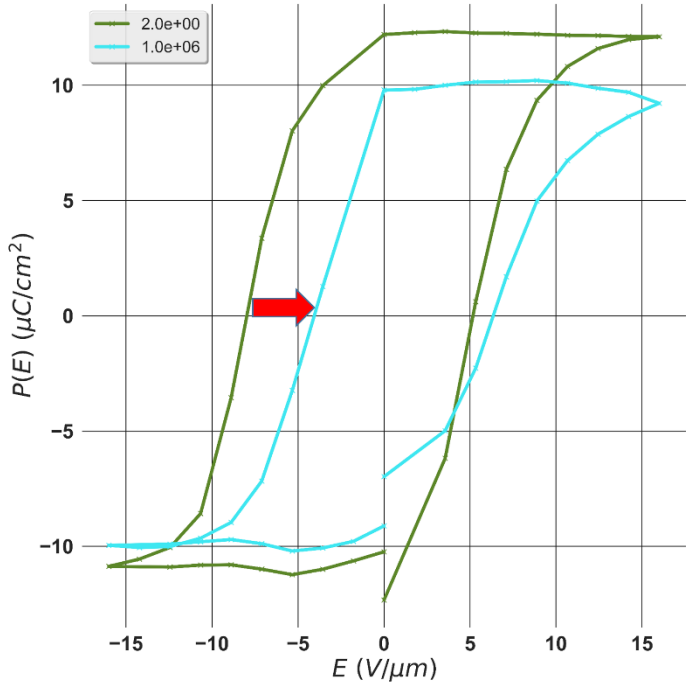

Figure 1.19: shifting of the polarization loop due to imprint effect under cycling

The first mechanism proposed is due to the alignment of defect dipoles. This scenario was proposed to explain the formation of an internal electric field in the acceptor-doped ferroelectric ceramics [63], [64]. The interpretation of this phenomenon is based on the charge neutrality rules in which the doping of acceptors leads to the formation of oxygen vacancies. The created permanent dipoles (acceptor/oxygen vacancy) could be aligned in the direction of spontaneous polarization in ferroelectric material. If the material is polarized, this alignment of defect dipoles stabilizes the macroscopic polarization state by forming an internal electric field, which is characterized by the shifting of the hysteresis cycle. Moreover, the model proposed by Artl et al. allows explaining the acceleration of imprint by the temperature thanks to the thermal activation of the mobility of the oxygen vacancies.

In the article by Dimos et al. [65], the bulk screening model on PZT thin films has been proposed. In ferroelectric materials with conducting electrodes, the depolarization field induced by polarization charges is usually screened by free electronic charges on the electrodes. As a result, the depolarization field is completely screened, leading to a zero electric field in the material if the polarization and screening charges locate at the same position. However, if a thin layer exists at the interface between the electrode and the ferroelectric film in which the spontaneous polarization is absent, the external screening charges and the polarization charges are spatially separated, giving rise to a residual depolarization field E_{RES} as illustrated in Figure 1.20(c). In the ferroelectric layer, E_{RES} is responsible for the charge separation. As the charges are separated, they are trapped at the interface electrode-ferroelectric film and screen the ferroelectric polarization. If the time constant of redistribution of these screening charges exceeds the ferroelectric polarization switching time by several orders of magnitude, these screening charges will cause an internal bias field that shifts the hysteresis loop horizontally.

In the article by Grossmann and co-workers [66], a development of the model from Dimos et al. has been proposed, which suggests that the imprint is caused by a large electric field within a thin surface layer at the interface between the electrode and the ferroelectric film as shown in Figure 1.20(a) and (b). The authors proposed that there is always an imprint in PZT and SBT films even in the case of zero bias. As a result, to fulfill the Maxwell condition, the E_{RES} needs to be compensated by an electric field, which exists at the interface and parallel to the polarization. This electric field, so-called E_{if}, can cause

the injection of electronic charges from the electrodes to the film or charge separation inside the surface layer. If these charges are trapped at the interface, they might lead to an evolution of internal bias upon time. Unlike the hypothesis proposed by Dimos and co-workers, it is this electric field but not the depolarizing field that is responsible for the separation of the charges in the interior of the surface layer and leading to the imprint. The application of an external field in the orientation of the polarization will reinforce the imprint through the increase of the internal field. Furthermore, at the interface between surface layer and the ferroelectric bulk the presence of two electric fields pointing in opposite directions (E_{if} and E_{Res}) results in a good trapping condition for electronic charges at this region.

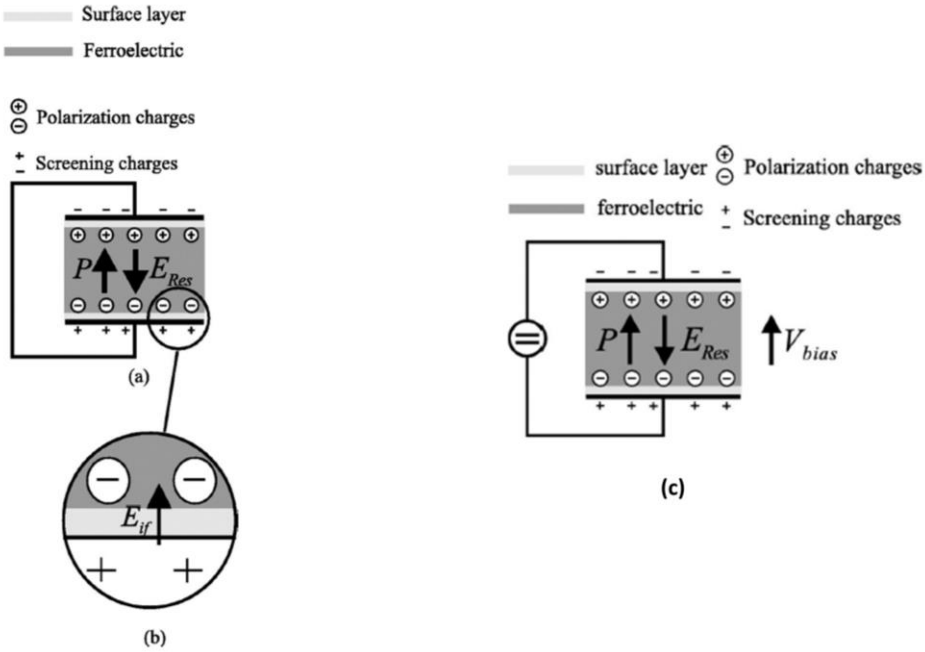

Figure 1.20: The mechanism of imprint as proposed by (a), (b) Grossmann et al. and (c) Dimos et al. (figure from [66])

References of Chapter I

[1] J. Evans *et al.*, "A discrete ferroelectric memory," in *2012 12th Annual Non-Volatile Memory Technology Symposium Proceedings*, Singapore: IEEE, Oct. 2012, pp. 33–36. doi: 10.1109/NVMTS.2013.6632857.

[2] Jérôme Mouly, "PIEZOELECTRIC DEVICES: FROM BULK TO THIN-FILM 2019," Yole development.

[3] Eric Mounier, Dimitrios Damianos, "Status of the MEMS industry 2019," Yole development.

[4] J. Bok and C. Kounelis, "Paul Langevin (1872-1946) - De la butte Montmartre au Panthéon : parcours d'un physicien d'exception," *Reflets Phys.*, no. 1, pp. 14–16, Sep. 2006, doi: 10.1051/refdp/2006007.

[5] J. Valasek, "Piezo-Electric and Allied Phenomena in Rochelle Salt," *Phys. Rev.*, vol. 17, no. 4, pp. 475–481, Apr. 1921, doi: 10.1103/PhysRev.17.475.

[6] A. T. Gen Shirane, "Phase Transitions in Solid Solutions of PbZrO3 and PbTiO3 (I) Small Concentrations of PbTiO3," *J. Phys. Soc. Jpn.*, vol. 7, pp. 5–11, Jan. 1952, doi: https://doi.org/10.1143/JPSJ.7.5.

[7] G. H. Haertling, "Ferroelectric Ceramics: History and Technology," *J. Am. Ceram. Soc.*, vol. 82, no. 4, pp. 797–818, Apr. 1999, doi: 10.1111/j.1151-2916.1999.tb01840.x.

[8] M. Ishida, S. Tsuji, K. Kimura, H. Matsunami, and T. Tanaka, "EPITAXIAL GROWTH OF FERROELECTRIC PLZT [(Pb, La)(Zr,Ti)Oa1 THIN FILMS," p. 6.

[9] M. Oikawa and K. Toda, "Preparation of Pb(Zr,Ti)O_3 thin films by an electron beam evaporation technique," *Appl. Phys. Lett.*, vol. 29, no. 8, pp. 491–492, Oct. 1976, doi: 10.1063/1.89133.

[10] M. Ishida, H. Matsunami, and T. Tanaka, "Preparation and properties of ferroelectric PLZT thin films by rf sputtering," p. 4.

[11] H. Adachi, T. Kawaguchi, K. Setsune, K. Ohji, and K. Wasa, "Electro-optic effects of (Pb, La)(Zr, Ti)O_3 thin films prepared by rf planar magnetron sputtering," *Appl. Phys. Lett.*, vol. 42, no. 10, pp. 867–868, May 1983, doi: 10.1063/1.93795.

[12] K. Iijima, Y. Tomita, R. Takayama, and I. Ueda, "Preparation of *c* -axis oriented $PbTiO_3$ thin films and their crystallographic, dielectric, and pyroelectric properties," *J. Appl. Phys.*, vol. 60, no. 1, pp. 361–367, Jul. 1986, doi: 10.1063/1.337654.

[13] N. Shohata, S. Matsubara, Y. Miyasaka, and M. Yonezawa, "Epitaxial Growth of PbTiO3on MgAl2O4/Si Substrates," in *Sixth IEEE International Symposium on Applications of Ferroelectrics*, Jun. 1986, pp. 580–584. doi: 10.1109/ISAF.1986.201210.

[14] S. K. Dey, K. D. Budd, and D. A. Payne, "Thin-film ferroelectrics of PZT of sol-gel processing," *IEEE Trans. Ultrason. Ferroelectr. Freq. Control*, vol. 35, no. 1, pp. 80–81, Jan. 1988, doi: 10.1109/58.4153.

[15] J. Xu, A. S. Shaikh, and R. W. Vest, "High K BaTiO/sub 3/ films from metalloorganic precursors," *IEEE Trans. Ultrason. Ferroelectr. Freq. Control*, vol. 36, no. 3, pp. 307–312, May 1989, doi: 10.1109/58.19168.

[16] G. M. Davis and M. C. Gower, "Epitaxial growth of thin films of $BaTiO_3$ using excimer laser ablation," *Appl. Phys. Lett.*, vol. 55, no. 2, pp. 112–114, Jul. 1989, doi: 10.1063/1.102393.

[17] M. Okada, S. Takai, M. Amemiya, and K. Tominaga, "Preparation of *c* -Axis-Oriented $PbTiO_3$ Thin Films by MOCVD under Reduced Pressure," *Jpn. J. Appl. Phys.*, vol. 28, no. Part 1, No. 6, pp. 1030–1034, Jun. 1989, doi: 10.1143/JJAP.28.1030.

[18] K. Iijima, T. Terashima, K. Yamamoto, K. Hirata, and Y. Bando, "Preparation of ferroelectric $BaTiO_3$ thin films by activated reactive evaporation," *Appl. Phys. Lett.*, vol. 56, no. 6, pp. 527–529, Feb. 1990, doi: 10.1063/1.103300.

[19] R. A. Roy, K. F. Etzold, and J. J. Cuomo, "Ferroelectric Film Synthesis, Past and Present: A Select Review," *MRS Proc.*, vol. 200, p. 141, 1990, doi: 10.1557/PROC-200-141.

[20] N. Menou, "Technologie FeRAM: fiabilité et mécanismes de défaillance de condensateurs

ferroélectriques élémentaires et intégrés," p. 239.
[21] C. M. Fancher *et al.*, "The contribution of 180° domain wall motion to dielectric properties quantified from in situ X-ray diffraction," *Acta Mater.*, vol. 126, pp. 36–43, Mar. 2017, doi: 10.1016/j.actamat.2016.12.037.
[22] D. Damjanovic, "Ferroelectric, dielectric and piezoelectric properties of ferroelectric thin films and ceramics," *Rep. Prog. Phys.*, vol. 61, no. 9, pp. 1267–1324, Sep. 1998, doi: 10.1088/0034-4885/61/9/002.
[23] S. Wada and T. Tsurumi, "Enhanced piezoelectricity of barium titanate single crystals with engineered domain configuration," *Br. Ceram. Trans.*, vol. 103, no. 2, pp. 93–96, Apr. 2004, doi: 10.1179/096797804225012747.
[24] K. Lefki and G. J. M. Dormans, "Measurement of piezoelectric coefficients of ferroelectric thin films," *J. Appl. Phys.*, vol. 76, no. 3, pp. 1764–1767, Aug. 1994, doi: 10.1063/1.357693.
[25] S. Trolier-Mckinstry and P. Muralt, "Thin Film Piezoelectrics for MEMS," p. 11.
[26] E. Jabari, F. Ahmed, F. Liravi, E. B. Secor, L. Lin, and E. Toyserkani, "2D printing of graphene: a review," *2D Mater.*, vol. 6, no. 4, p. 042004, Aug. 2019, doi: 10.1088/2053-1583/ab29b2.
[27] S. Nicolas *et al.*, "Fabrication and characterization of a new varifocal liquid lens with embedded PZT actuators for high optical performances," in *2015 28th IEEE International Conference on Micro Electro Mechanical Systems (MEMS)*, Jan. 2015, pp. 65–68. doi: 10.1109/MEMSYS.2015.7050887.
[28] H. Wang, Z. Chen, and H. Xie, "A high-SPL piezoelectric MEMS loud speaker based on thin ceramic PZT," *Sens. Actuators Phys.*, vol. 309, p. 112018, Jul. 2020, doi: 10.1016/j.sna.2020.112018.
[29] M. Tani, M. Akamatsu, Y. Yasuda, and H. Toshiyoshi, "A two-axis piezoelectric tilting micromirror with a newly developed PZT-meandering actuator," in *2007 IEEE 20th International Conference on Micro Electro Mechanical Systems (MEMS)*, Jan. 2007, pp. 699–702. doi: 10.1109/MEMSYS.2007.4432994.
[30] P. Laitinen and J. Mawnpaa, "Enabling mobile haptic design: piezoelectric actuator technology properties in hand held devices," in *2006 IEEE International Workshop on Haptic Audio Visual Environments and their Applications (HAVE 2006)*, Nov. 2006, pp. 40–43. doi: 10.1109/HAVE.2006.283787.
[31] H. K. Ma, B. R. Hou, H. Y. Wu, C. Y. Lin, J. J. Gao, and M. C. Kou, "Development and application of a diaphragm micro-pump with piezoelectric device," *Microsyst. Technol.*, vol. 14, no. 7, pp. 1001–1007, Jul. 2008, doi: 10.1007/s00542-007-0462-6.
[32] P. Muralt, "PZT thin films for microsensors and actuators: Where do we stand?," *IEEE Trans. Ultrason. Ferroelectr. Freq. Control*, vol. 47, no. 4, pp. 903–915, Jul. 2000, doi: 10.1109/58.852073.
[33] "What is a SAW Filter ?," *everythingRF*. https://www.everythingrf.com/community/what-is-a-saw-filter
[34] T. Giffney, M. Yu, K. C. Aw, and H. Zhang, "Contactless RF MEMS switch using PZT actuation," in *The 8th Annual IEEE International Conference on Nano/Micro Engineered and Molecular Systems*, Apr. 2013, pp. 861–864. doi: 10.1109/NEMS.2013.6559860.
[35] J. S. Meena, S. M. Sze, U. Chand, and T.-Y. Tseng, "Overview of emerging nonvolatile memory technologies," *Nanoscale Res. Lett.*, vol. 9, no. 1, p. 526, Dec. 2014, doi: 10.1186/1556-276X-9-526.
[36] Volker Rzehak, "Low-Power FRAM Microcontrollers and Their Applications," Texas Instrument, 2019.
[37] J. Müller *et al.*, "Ferroelectricity in yttrium-doped hafnium oxide," *J. Appl. Phys.*, vol. 110, no. 11, p. 114113, Dec. 2011, doi: 10.1063/1.3667205.
[38] T. Francois *et al.*, "Demonstration of BEOL-compatible ferroelectric Hf0.5Zr0.5O2 scaled FeRAM co-integrated with 130nm CMOS for embedded NVM applications," in *2019 IEEE International Electron Devices Meeting (IEDM)*, Dec. 2019, p. 15.7.1-15.7.4. doi: 10.1109/IEDM19573.2019.8993485.

[39] S. Priya *et al.*, "A Review on Piezoelectric Energy Harvesting: Materials, Methods, and Circuits," *Energy Harvest. Syst.*, vol. 4, no. 1, pp. 3–39, Aug. 2019, doi: 10.1515/ehs-2016-0028.

[40] B. Noheda *et al.*, "Tetragonal-to-monoclinic phase transition in a ferroelectric perovskite: The structure of PbZr 0.52 Ti 0.48 O 3," *Phys. Rev. B*, vol. 61, no. 13, pp. 8687–8695, Apr. 2000, doi: 10.1103/PhysRevB.61.8687.

[41] M. Ahart *et al.*, "Origin of morphotropic phase boundaries in ferroelectrics," *Nature*, vol. 451, no. 7178, pp. 545–548, Jan. 2008, doi: 10.1038/nature06459.

[42] G. A. Rossetti and A. G. Khachaturyan, "Inherent nanoscale structural instabilities near morphotropic boundaries in ferroelectric solid solutions," *Appl. Phys. Lett.*, vol. 91, no. 7, p. 072909, Aug. 2007, doi: 10.1063/1.2771095.

[43] R. Ahluwalia, T. Lookman, A. Saxena, and W. Cao, "Domain-size dependence of piezoelectric properties of ferroelectrics," *Phys. Rev. B*, vol. 72, no. 1, p. 014112, Jul. 2005, doi: 10.1103/PhysRevB.72.014112.

[44] N. Setter *et al.*, "Ferroelectric thin films: Review of materials, properties, and applications," *J. Appl. Phys.*, vol. 100, no. 5, p. 051606, Sep. 2006, doi: 10.1063/1.2336999.

[45] R. Guo, L. E. Cross, S.-E. Park, B. Noheda, D. E. Cox, and G. Shirane, "Origin of the High Piezoelectric Response in PbZr 1 − x Ti x O 3," *Phys. Rev. Lett.*, vol. 84, no. 23, pp. 5423–5426, Jun. 2000, doi: 10.1103/PhysRevLett.84.5423.

[46] L. Bellaiche, A. García, and D. Vanderbilt, "Finite-Temperature Properties of Pb (Zr 1 − x Ti x) O 3 Alloys from First Principles," *Phys. Rev. Lett.*, vol. 84, no. 23, pp. 5427–5430, Jun. 2000, doi: 10.1103/PhysRevLett.84.5427.

[47] M. Hinterstein *et al.*, "Structural Description of the Macroscopic Piezo- and Ferroelectric Properties of Lead Zirconate Titanate," *Phys. Rev. Lett.*, vol. 107, no. 7, p. 077602, Aug. 2011, doi: 10.1103/PhysRevLett.107.077602.

[48] V. Kovacova, N. Vaxelaire, G. Le Rhun, P. Gergaud, T. Schmitz-Kempen, and E. Defay, "Correlation between electric-field-induced phase transition and piezoelectricity in lead zirconate titanate films," *Phys. Rev. B*, vol. 90, no. 14, p. 140101, Oct. 2014, doi: 10.1103/PhysRevB.90.140101.

[49] T. W. Cornelius *et al.*, "Piezoelectric response and electrical properties of Pb(Zr 1-x Ti x)O 3 thin films: The role of imprint and composition," *J. Appl. Phys.*, vol. 122, no. 16, pp. 164104–164104, Oct. 2017, doi: 10.1063/1.4994939.

[50] T. W. Cornelius *et al.*, "Piezoelectric Properties of Pb1−xLax(Zr0.52Ti0.48)1−x/4O3 Thin Films Studied by In Situ X-ray Diffraction," *Materials*, vol. 13, no. 15, p. 3338, Jul. 2020, doi: 10.3390/ma13153338.

[51] P. Jiang *et al.*, "Wake-Up Effect in HfO2-Based Ferroelectric Films," *Adv. Electron. Mater.*, vol. 7, no. 1, p. 2000728, 2021, doi: 10.1002/aelm.202000728.

[52] Q. Y. Jiang, E. C. Subbarao, and L. E. Cross, "Effect of composition and temperature on electric fatigue of La-doped lead zirconate titanate ceramics," *J. Appl. Phys.*, vol. 75, no. 11, pp. 7433–7443, Jun. 1994, doi: 10.1063/1.356637.

[53] M. Majkut, J. E. Daniels, J. P. Wright, S. Schmidt, and J. Oddershede, "Electromechanical Response of Polycrystalline Barium Titanate Resolved at the Grain Scale," *J. Am. Ceram. Soc.*, vol. 100, no. 1, pp. 393–402, Jan. 2017, doi: 10.1111/jace.14481.

[54] H. N. Al-Shareef, A. I. Kingon, X. Chen, K. R. Bellur, and O. Auciello, "Contribution of electrodes and microstructures to the electrical properties of Pb($Zr_{0.53}$ $Ti_{0.47}$)O_3 thin film capacitors," *J. Mater. Res.*, vol. 9, no. 11, pp. 2968–2975, Nov. 1994, doi: 10.1557/JMR.1994.2968.

[55] C. Künneth, R. Batra, G. A. Rossetti, R. Ramprasad, and A. Kersch, "Thermodynamics of Phase Stability and Ferroelectricity From First Principles," in *Ferroelectricity in Doped Hafnium Oxide: Materials, Properties and Devices*, Elsevier, 2019, pp. 245–289. doi: 10.1016/B978-0-08-102430-0.00006-1.

[56] M. Pešić *et al.*, "Physical Mechanisms behind the Field-Cycling Behavior of HfO2-Based Ferroelectric Capacitors," *Adv. Funct. Mater.*, vol. 26, no. 25, pp. 4601–4612, 2016, doi:

https://doi.org/10.1002/adfm.201600590.
[57] W. L. Warren *et al.*, "Polarization suppression in Pb(Zr,Ti)O $_3$ thin films," *J. Appl. Phys.*, vol. 77, no. 12, pp. 6695–6702, Jun. 1995, doi: 10.1063/1.359083.
[58] H. M. Duiker *et al.*, "Fatigue and switching in ferroelectric memories: Theory and experiment," *J. Appl. Phys.*, vol. 68, no. 11, pp. 5783–5791, Dec. 1990, doi: 10.1063/1.346948.
[59] J. F. Scott, C. A. Araujo, B. M. Melnick, L. D. McMillan, and R. Zuleeg, "Quantitative measurement of space-charge effects in lead zirconate-titanate memories," *J. Appl. Phys.*, vol. 70, no. 1, pp. 382–388, Jul. 1991, doi: 10.1063/1.350286.
[60] H. Zou, "Effect of Nb Doping on Crystalline Orientation, Electric and Fatigue Properties of PZT Thin Films Prepared by Sol-Gel Process," *J. Ceram. Sci. Technol.*, no. 04, 2017, doi: 10.4416/JCST2017-00031.
[61] H. Sun, Y. Zhang, X. Liu, S. Guo, Y. Liu, and W. Chen, "The effect of Mn/Nb doping on dielectric and ferroelectric properties of PZT thin films prepared by sol–gel process," *J. Sol-Gel Sci. Technol.*, vol. 74, no. 2, pp. 378–386, May 2015, doi: 10.1007/s10971-014-3608-x.
[62] J. M. Benedetto, "Imprint induced failure modes in ferroelectric non-volatile memories," *Integr. Ferroelectr.*, vol. 15, no. 1–4, pp. 29–38, Feb. 1997, doi: 10.1080/10584589708015694.
[63] G. Arlt and H. Neumann, "Internal bias in ferroelectric ceramics: Origin and time dependence," *Ferroelectrics*, vol. 87, no. 1, pp. 109–120, Nov. 1988, doi: 10.1080/00150198808201374.
[64] R. Lohkämper, H. Neumann, and G. Arlt, "Internal bias in acceptor-doped BaTiO $_3$ ceramics: Numerical evaluation of increase and decrease," *J. Appl. Phys.*, vol. 68, no. 8, pp. 4220–4224, Oct. 1990, doi: 10.1063/1.346212.
[65] D. Dimos, W. L. Warren, M. B. Sinclair, B. A. Tuttle, and R. W. Schwartz, "Photoinduced hysteresis changes and optical storage in (Pb,La)(Zr,Ti)O $_3$ thin films and ceramics," *J. Appl. Phys.*, vol. 76, no. 7, pp. 4305–4315, Oct. 1994, doi: 10.1063/1.357316.
[66] M. Grossmann, O. Lohse, D. Bolten, U. Boettger, T. Schneller, and R. Waser, "The interface screening model as origin of imprint in PbZrxTi1−xO3 thin films. I. Dopant, illumination, and bias dependence," *J. Appl. Phys.*, vol. 92, no. 5, pp. 2680–2687, Sep. 2002, doi: 10.1063/1.1498966.
[67] R. Roque, "X-ray imaging using 100 µm thick Gas Electron Multipliers operating in Kr-CO2 mixtures," Unpublished, 2018. Accessed: Aug. 07, 2022. [Online]. Available: http://rgdoi.net/10.13140/RG.2.2.16794.49600
[68] European Synchrotron Radiation Facility, "QUESTIONS & ANSWERS." https://www.esrf.fr/about/ask-an-expert/questions-answers#:~:text=The%20most%20important%20advantage%20of,angular%20spread%20of%20the%20beam.
[69] M. Birkholz, "Thin Film Analysis by X-Ray Scattering," p. 381.
[70] H. Möller and J. Barbers, *Mitt Kais. Wilhelm Inst. Eisenforsch.*, vol. 16, p. 21, 1934.
[71] P. Gravereau, "Introduction à la pratique de la diffraction des rayons X par les poudres," p. 210.
[72] Newville, Matthew ; Stensitzki, Till ; Allen, Daniel B. ; Rawlik, Michal ; Ingargiola, Antonino ; Nelson, Andrew, "LMFIT: Non-Linear Least-Square Minimization and Curve-Fitting for Python", doi: 10.5281/zenodo.11813.
[73] Q. M. Zhang, W. Y. Pan, and L. E. Cross, "Laser interferometer for the study of piezoelectric and electrostrictive strains," *J. Appl. Phys.*, vol. 63, no. 8, pp. 2492–2496, Apr. 1988, doi: 10.1063/1.341027.
[74] A. L. Kholkin, Ch. Wütchrich, D. V. Taylor, and N. Setter, "Interferometric measurements of electric field-induced displacements in piezoelectric thin films," *Rev. Sci. Instrum.*, vol. 67, no. 5, pp. 1935–1941, May 1996, doi: 10.1063/1.1147000.
[75] Z. Huang and R. W. Whatmore, "A double-beam common path laser interferometer for the measurement of electric field-induced strains of piezoelectric thin films," *Rev. Sci. Instrum.*, vol. 76, no. 12, p. 123906, Dec. 2005, doi: 10.1063/1.2149002.

[76] “PyVISA: Control your instruments with Python.” https://pyvisa.readthedocs.io/en/latest/
[77] N. Vaxelaire *et al.*, “Effect of structural in-depth heterogeneities on electrical properties of Pb(Zr0.52Ti0.48) O3 thin films as revealed by nano-beam X-ray diffraction,” *J. Appl. Phys.*, vol. 120, no. 10, p. 104101, Sep. 2016, doi: 10.1063/1.4962427.
[78] B. Noheda *et al.*, “Tetragonal-to-monoclinic phase transition in a ferroelectric perovskite: The structure of PbZr 0.52 Ti 0.48 O 3,” *Phys. Rev. B*, vol. 61, no. 13, pp. 8687–8695, Apr. 2000, doi: 10.1103/PhysRevB.61.8687.
[79] S. K. Sayyed and S. A. Acharya, “Synthesis of PZT nanorods and study of dielectric behaviour,” presented at the PROCEEDING OF INTERNATIONAL CONFERENCE ON RECENT TRENDS IN APPLIED PHYSICS AND MATERIAL SCIENCE: RAM 2013, Bikaner, Rajasthan, India, 2013, pp. 111–112. doi: 10.1063/1.4810125.
[80] Wojciech Paszkowicz, “Application of a powder diffractometer equipped with a strip detector and Johansson monochromator to phase analysis and structure refinement,” *Nucl. Instrum. Methods Phys. Res. Sect. Accel. Spectrometers Detect. Assoc. Equip.*, vol. 551, no. 1, pp. 162–177, Oct. 2005, doi: 10.1016/j.nima.2005.07.068.
[81] K. T. Li and V. C. Lo, “Simulation of thickness dependence in ferroelectric thin films,” *Solid State Commun.*, vol. 132, no. 1, pp. 49–54, Oct. 2004, doi: 10.1016/j.ssc.2004.07.013.
[82] M. Dekkers, M. D. Nguyen, R. Steenwelle, P. M. te Riele, D. H. A. Blank, and G. Rijnders, “Ferroelectric properties of epitaxial Pb(Zr,Ti)O3 thin films on silicon by control of crystal orientation,” *Appl. Phys. Lett.*, vol. 95, no. 1, p. 012902, Jul. 2009, doi: 10.1063/1.3163057.
[83] Yu. V. Podgorny, D. S. Seregin, A. S. Sigov, and K. A. Vorotilov, “Effect of Sol-Gel PZT Film Thickness on the Hysteresis Properties,” *Ferroelectrics*, vol. 439, no. 1, pp. 74–79, Jan. 2012, doi: 10.1080/00150193.2012.741952.
[84] A. J. Fox, B. Drawl, G. R. Fox, B. J. Gibbons, and S. Trolier-McKinstry, “Control of crystallographic texture and surface morphology of Pt/Tio2 templates for enhanced PZT thin film texture,” *IEEE Trans. Ultrason. Ferroelectr. Freq. Control*, vol. 62, no. 1, pp. 56–61, Jan. 2015, doi: 10.1109/TUFFC.2014.006671.
[85] E. M. Alkoy, S. Alkoy, and T. Shiosaki, “The effect of crystallographic orientation and solution aging on the electrical properties of sol–gel derived Pb(Zr0.45Ti0.55)O3 thin films,” *Ceram. Int.*, vol. 33, no. 8, pp. 1455–1462, Dec. 2007, doi: 10.1016/j.ceramint.2006.06.010.
[86] Y. Kim, H. Han, I. Vrejoiu, W. Lee, D. Hesse, and M. Alexe, “Origins of domain wall pinning in ferroelectric nanocapacitors,” *Nano Converg.*, vol. 1, no. 1, p. 24, Dec. 2014, doi: 10.1186/s40580-014-0024-4.
[87] J. A. Christman, R. R. Woolcott, A. I. Kingon, and R. J. Nemanich, “Piezoelectric measurements with atomic force microscopy,” p. 4.
[88] O. Kuffer, I. Maggio-Aprile, J.-M. Triscone, O. Fischer, and Ch. Renner, “Piezoelectric response of epitaxial Pb(Zr0.2Ti0.8)O3 films measured by scanning tunneling microscopy,” *Appl. Phys. Lett.*, vol. 77, no. 11, pp. 1701–1703, Sep. 2000, doi: 10.1063/1.1309017.
[89] A. L. Kholkin, Ch. Wütchrich, D. V. Taylor, and N. Setter, “Interferometric measurements of electric field-induced displacements in piezoelectric thin films,” *Rev. Sci. Instrum.*, vol. 67, no. 5, pp. 1935–1941, May 1996, doi: 10.1063/1.1147000.
[90] Z. Huang and R. W. Whatmore, “A double-beam common path laser interferometer for the measurement of electric field-induced strains of piezoelectric thin films,” *Rev. Sci. Instrum.*, vol. 76, no. 12, p. 123906, Dec. 2005, doi: 10.1063/1.2149002.
[91] H. Weitzing, G. A. Schneider, J. Steffens, M. Hammer, and M. J. Hoffmann, “Cyclic fatigue due to electric loading in ferroelectric ceramics,” *J. Eur. Ceram. Soc.*, vol. 19, no. 6, pp. 1333–1337, Jun. 1999, doi: 10.1016/S0955-2219(98)00429-4.
[92] R. Herbiet, H. Tenbrock, and G. Arlt, “The aging behaviour of the complex material parameters ε, d and s in ferroelectric PZT ceramics,” *Ferroelectrics*, vol. 76, no. 1, pp. 319–326, Dec. 1987, doi: 10.1080/00150198708016952.
[93] J. E. Daniels *et al.*, “Heterogeneous grain-scale response in ferroic polycrystals under electric field,” *Sci. Rep.*, vol. 6, no. 1, p. 22820, Mar. 2016, doi: 10.1038/srep22820.

[94] Q. Li and M. Kuna, “Inhomogeneity and material configurational forces in three dimensional ferroelectric polycrystals,” *Eur. J. Mech. - ASolids*, vol. 31, no. 1, pp. 77–89, Jan. 2012, doi: 10.1016/j.euromechsol.2011.07.004.
[95] L. Fan, W. Werner, S. Subotić, D. Schneider, M. Hinterstein, and B. Nestler, “Multigrain phase-field simulation in ferroelectrics with phase coexistences: An improved phase-field model,” *Comput. Mater. Sci.*, vol. 203, p. 111056, Feb. 2022, doi: 10.1016/j.commatsci.2021.111056.
[96] H. Simons *et al.*, “Long-range symmetry breaking in embedded ferroelectrics,” *Nat. Mater.*, vol. 17, no. 9, pp. 814–819, Sep. 2018, doi: 10.1038/s41563-018-0116-3.
[97] E. K. H. Salje, S. Li, M. Stengel, P. Gumbsch, and X. Ding, “Flexoelectricity and the polarity of complex ferroelastic twin patterns,” *Phys. Rev. B*, vol. 94, no. 2, p. 024114, Jul. 2016, doi: 10.1103/PhysRevB.94.024114.
[98] J. Novak, U. Bismayer, and E. K. H. Salje, “Simulated equilibrium shapes of ferroelastic needle domains,” *J. Phys. Condens. Matter*, vol. 14, no. 3, pp. 657–664, Jan. 2002, doi: 10.1088/0953-8984/14/3/332.
[99] A. S. Karapuzha, N. K. James, H. Khanbareh, S. van der Zwaag, and W. A. Groen, “Structure, dielectric and piezoelectric properties of donor doped PZT ceramics across the phase diagram,” *Ferroelectrics*, vol. 504, no. 1, pp. 160–171, Nov. 2016, doi: 10.1080/00150193.2016.1240571.
[100] M. Budimir, D. Damjanovic, and N. Setter, “Enhancement of the piezoelectric response of tetragonal perovskite single crystals by uniaxial stress applied along the polar axis: A free-energy approach,” *Phys. Rev. B*, vol. 72, no. 6, p. 064107, Aug. 2005, doi: 10.1103/PhysRevB.72.064107.
[101] E.-M. Anton, R. E. García, T. S. Key, J. E. Blendell, and K. J. Bowman, “Domain switching mechanisms in polycrystalline ferroelectrics with asymmetric hysteretic behavior,” *J. Appl. Phys.*, vol. 105, no. 2, p. 024107, Jan. 2009, doi: 10.1063/1.3068333.
[102] C. Lichtensteiger, J.-M. Triscone, J. Junquera, and P. Ghosez, “Ferroelectricity and Tetragonality in Ultrathin P b T i O 3 Films,” *Phys. Rev. Lett.*, vol. 94, no. 4, p. 047603, Feb. 2005, doi: 10.1103/PhysRevLett.94.047603.
[103] C. A. Randall, N. Kim, J.-P. Kucera, W. Cao, and T. R. Shrout, “Intrinsic and Extrinsic Size Effects in Fine-Grained Morphotropic-Phase-Boundary Lead Zirconate Titanate Ceramics,” *J. Am. Ceram. Soc.*, vol. 81, no. 3, pp. 677–688, 1998, doi: 10.1111/j.1151-2916.1998.tb02389.x.
[104] Y. Wei, C. Jin, P. Ye, P. Li, Y. Zeng, and G. Xu, “Structural evolution, electrical properties and electric-field-induced changes of (0.8−x)PbTiO3–xBiFeO3–0.2BaZrO3 system near the morphotropic phase boundary,” *Appl. Phys. A*, vol. 123, no. 4, p. 218, Apr. 2017, doi: 10.1007/s00339-016-0736-x.
[105] B. Allouche, I. Gueye, G. L. Rhun, P. Gergaud, and N. Vaxelaire, “In-situ X-ray diffraction on functional thin films using a laboratory source during electrical biasing,” *Mater. Des.*, vol. 154, pp. 340–346, Sep. 2018, doi: 10.1016/j.matdes.2018.05.016.
[106] K. Nguyen, E. Bellec, E. Zatterin, G. Le Rhun, P. Gergaud, and N. Vaxelaire, “Structural Insights of Electrical Aging in PZT Thin Films as Revealed by In Situ Biasing X-ray Diffraction,” *Materials*, vol. 14, no. 16, Art. no. 16, Jan. 2021, doi: 10.3390/ma14164500.

Chapter II: Experimental methods

Introduction

The second chapter of this manuscript presents the fundamental and the working principles of the techniques used in this thesis. Firstly, X-ray diffraction is introduced. In this part, the principle of operation, the measurement configuration, the different applications as well as data analysis are presented. Then, we will describe the different techniques for electrical characterization of ferroelectric materials. This chapter will mention the electrical model of ferroelectric materials along with different electrical circuits as well as strategies for electrical measurement of ferroelectric materials. Next, the techniques for piezoelectric coefficient measurement will be introduced. This chapter ends with an introduction to the in-situ biasing XRD setup developed in our laboratory.

1. X-ray Diffraction method

1.1. Definition of X-rays

X-ray is a type of electromagnetic radiation, discovered by Röntgen at the end of 19th century. X-rays travel at the speed of light with a wavelength between 0.1 and 100 Å (Figure 2.1). X-rays are sources of radiant energy, characterized by its wavelength or frequency. The relation between energy and wavelength is the following:

$$E = 12.3981/\lambda \tag{2.1}$$

where *E* is the energy in the range of keV and λ is the wavelength in the range of Å. Therefore, the energy of X-rays range from 100 eV to 100 keV, with the X-rays whose energy are higher than 5 keV are called hard X-ray while those with lower energies are called soft X-ray. When interacting with the objects, there are different types of interactions:

- Photoelectrons/Auger electrons emission: In this case, the X-ray photon interact with the electrons within the atoms. The bounded electrons absorb the energy from electromagnetic radiation and are excited to a higher energy level. If the energy acquired by the electron is higher than the work function of the material, it is ejected. An outer electron will fill the vacant electron position and produce either a characteristic X-ray or an Auger electron

- Inelastic interaction (Compton scattering): Inelastic interaction take place with one or many free electrons of the atom. The incident X-ray photon loses a part of its energy and this energy will take two forms: a kinetic energy transferred to the electron and scattered x-ray having lower energy and thus a higher wavelength. The wavelength of the scattered photon depends on the observation direction. Thus, the scattering is incoherent and no interference can take place.

- Elastic scattering (Thomson scattering): Elastic interaction occurs with free electrons of the atom and does not modify the internal structure of the atom. The electromagnetic wave scattered by the atom is similar to the incident one, thus it is called coherent scattering. In the case of ordered spatial distribution of atoms, constructive interference can be produced, which is known as diffraction.

It is also possible that no interaction happens between the incident beam and matter, in this case the beam will transmit through the matter. By studying the interaction from radiation sources with matter, the scientists can obtained different information about the structure and composition of the samples. Because of that, the synchrotron radiation is very useful for many applications such as materials engineering, structural biology, medical, renewable energy, cultural heritages…

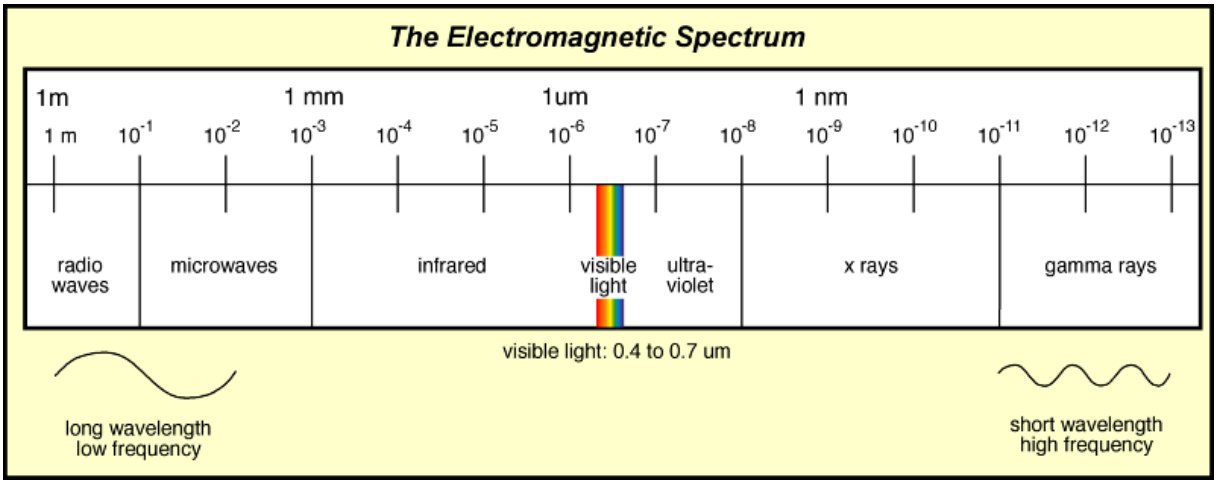

Figure 2.1: Electromagnetic spectrum

1.2. Generation of X-rays

1.2.1. Laboratory source

X-rays are generated when electrons of high kinetic energy in the keV range collide with a target. For laboratory XRD equipment, the X-ray beam is generated using an X-ray tube, which consists of a cathode filament and an anode plate made of a material chosen according to the expected emission wavelength. While the cathode filament is heated in order to emit electrons, these electrons are then transferred to the anode by applying a high electric field between the filament and the anode. The collision between the high-energy electrons and the anode plate lead to the emission of x-rays. During the collision with the target, most of the kinetic energy of the high-velocity electron beam is dissipated as heat. As a result, only about 1% of the total energy is emitted in the form of X-rays through two mechanisms: characteristic X-ray fluorescence emission of the cathode and Bremsstrahlung emission.

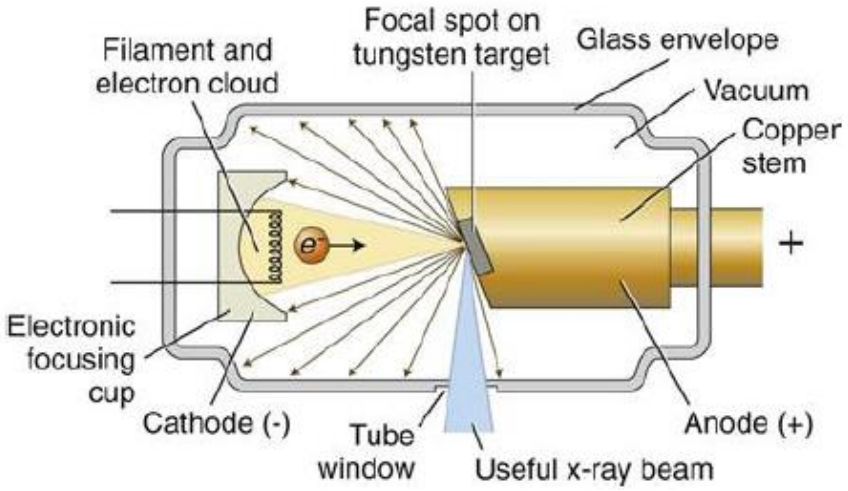

Figure 2.2: Structure of a conventional X-ray tube [67]

For x-ray fluorescence, if the incoming electron has enough energy, it will knock out an orbital electron of the inner electron shell of the target atom. As a result, electrons from higher energy levels will fill the vacancies, thus emitting an X-ray photon with an energy equal to the difference in energy between the two orbital levels. This process generates an emission spectrum of X-rays with intense discrete frequencies, known as spectral lines as shown in Figure 2.3. Usually, these are the transitions from the

upper shells to the K shell (so-called K lines), to the L shell (so-called L lines) and so on. If the transition is from *2p orbital* to *1s orbital*, it is named *Kα*, and if it is from *3p orbital* to *1s orbital* it is named *Kβ*. The frequencies of these lines depend on the material of the target. In our case, we used the Cu anode which generates at characteristic wavelength equal to 0.154 and 0.139 nm for *Kα* and *Kβ*, respectively. Moreover, due to the splitting in the *2p* orbitals in copper, the *Kα* line actually has a doublet profile, consisting of $K\alpha_1$ and $K\alpha_2$ component. However, because the splitting of *2p* orbital (or the splitting of energy levels L_{II} and L_{III}) is very small, the two wavelengths $K\alpha_1$ and $K\alpha_2$ are very similar (0.154059 and 0.154441 nm, respectively) and not observable on Figure 2.3.

The second phenomenon occurring with the fluorescence at the impact of the electrons on the cathode is called the Bremsstrahlung emission. It consists in the emission of X-ray photons due to the presence of the strong electric field of electrons near the nuclei. Unlike the first mechanism, the X-rays emitted by the Bremsstrahlung mechanism have wavelength spread over a continuous and wide spectrum and the frequency is limited by the energy of incident electrons.

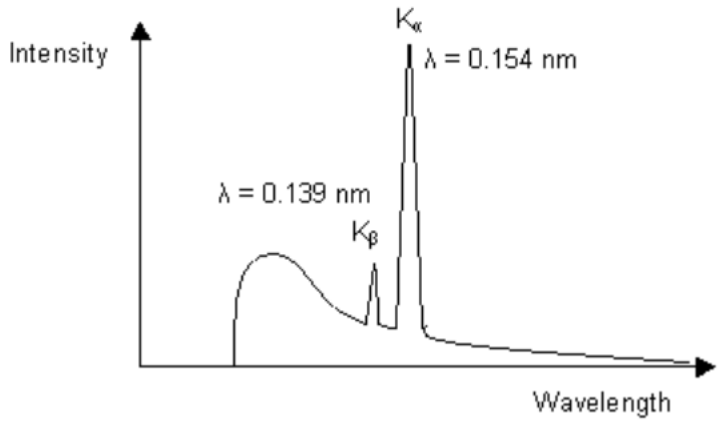

Figure 2.3: X-ray spectrum generated by a laboratory Copper x-ray tube with fluorescence and Bremsstrahlung emission

1.2.2.Synchrotron source

Synchrotron radiation (also known as Magnetobremsstrahlung radiation) is the electromagnetic radiation emitted when charged particles are accelerated radially (e.g. electrons accelerated in a magnetic field). Synchrotron radiations were first produced in a particle accelerator in 1947 at the General Electric Synchrotron in USA. However, for a long time it was considered as a problem for the high energy particle accelerator as it represents the main source of energy loss. Only in the late of 1960s, the usefulness of such radiations was found for the research in condensed matter physics. Since then, synchrotron radiations have been exploited extensively to study the structure of matters at atomic and molecular scale, from solids to protein molecules.

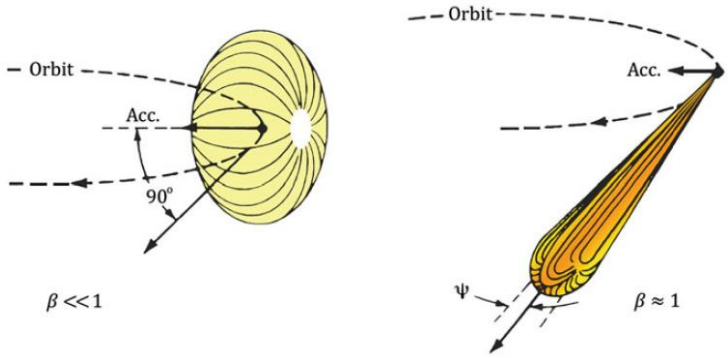

Figure 2.4: The radiation patterns from the charged particles moving in a circular orbit at different speed regime. The dipole pattern obtained at slow particles (left) (β = v/c << 1) is distorted into a narrow cone when β ≈1 (right)

A key feature of the synchrotron radiation is the relativistic effect, which happens when the electrons move at approximately the speed of light (*c*). In this situation, the angular range of the radiation pattern is compressed to a narrow cone in the propagation direction of the electrons, resulting in an emission in the tangential direction to the particle orbit as shown in Figure 2.4.

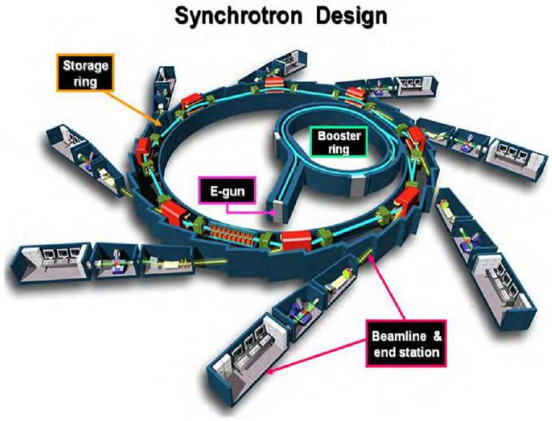

Figure 2.5: Structure of a synchrotron radiation facility

The synchrotron radiation facilities consist of four main components as shown in Figure 2.5: A linear accelerator (or Linac), a booster ring, a storage ring and beamlines. In order to generate the synchrotron radiation, the electrons are produced in the Linac by an electron gun. Here, these electrons are accelerated to an energy of several millions of electron volts (MeV). After that, the electrons are transferred to the booster ring. Here, the electrons are accelerated to an energy of billions of electron volts (GeV) before being injected in the storage ring. Then, the electrons are forced to follow the circular trajectory by a magnetic field produced by bending magnets and in the process it will produce the X-rays. Finally, the emitted X-rays are directed towards the beamlines around the storage ring. Because synchrotron radiation extends over a broad energy range from the infrared to hard X-ray, it can penetrate deep into the matters, interacts with atoms and enable the study of diffraction, scattering or re-emitted beams. When comparing between the synchrotron and laboratory radiation source, the most important advantage of synchrotron source is the brilliance, which is defined as the number of photons emitted per unit source area over a unit angle of emission and per unit energy (ph/s/mm^2/°). This quantity in a synchrotron source is more than a billion times higher than a laboratory source [68]. Higher brilliance allows performing the measurements in shorter amount of time and the smaller beam size which allows studying small samples. Furthermore, the energy range of synchrotron source is wider than the laboratory one, which is normally limited between 4.5 keV (Ti anode) and 22 keV (Ag anode), or white source with W anode. . In Synchrotron source, the photon energy is accordable at the eV resolution from few ten of eV (on some synchrotron facilities like Soleil) and few hundred of keV. In my PhD project, synchrotron-based experiments were carried out at the European Synchrotron Radiation Facility (ESRF) in Grenoble, France. It is a 3rd

generation synchrotron source with a storage ring energy of 6 GeV and by the time our experiment was performed, the 4th generation source was not opened.

1.3. X-ray scattering and diffraction

1.3.1. Elastic interaction between X-rays and a single electron

Elastic interaction is illustrated in Figure 2.6 for a single free electron having a charge e, mass m and at position R_0. The incident beam is represented by a planar wave $E_0 exp(-is_0 E_0)$, where E_0 and s_0 are the electric field and the wave vector, respectively. The direction of incident and scattered radiations is given by the directions of s_0 and s and the plane containing these two vectors is known as the scattering plane. For elastic scattering, one has:

$$|\boldsymbol{s_0}| = |\boldsymbol{s}| = \frac{2\pi}{\lambda} \tag{2.2}$$

The angle between $\boldsymbol{s_0}$ and $\boldsymbol{s}$ is the scattering angle and is usually denoted as 2θ in X-ray diffraction, which can be defined as

$$2\theta = \frac{\langle \boldsymbol{s}, \boldsymbol{s_0} \rangle}{\boldsymbol{s s_0}} \tag{2.3}$$

The difference between s and s_0 is called the scattering vector and is denoted $\boldsymbol{Q}$:

$$\boldsymbol{Q} = \boldsymbol{s} - \boldsymbol{s_0} \tag{2.4}$$

The scattering vector has the dimensionality of an inverse length, while its direction is along the bisection of incoming and scattered beam. One can demonstrate through geometrical considerations that $|\boldsymbol{Q}| = 4\pi sin\theta/\lambda$. As a result, the scattering vector depends on both the geometry of the scattering through the θ angle and also the wavelength of the incident beam.

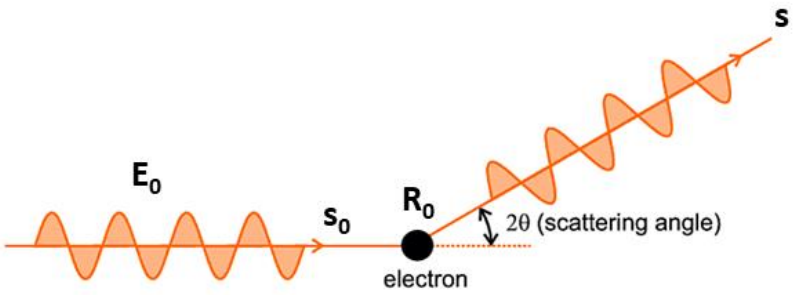

Figure 2.6: Elastic scattering of an X-ray beam by an electron

1.3.2. Interferences of scattered waves

We will now turn to the core of diffraction: the interference of scattered waves that results in the diffraction pattern. We will start by considering the interference of scattered wave by a single electron, then the scattering by multiple electrons and finally the coherent scattering by crystals, which is the diffraction.

To understand this process, two scattering centers O and O' have to be taken into account as shown in Figure 2.7. If these two points are excited by a plane wave, they emit secondary waves which will interfere with each other.

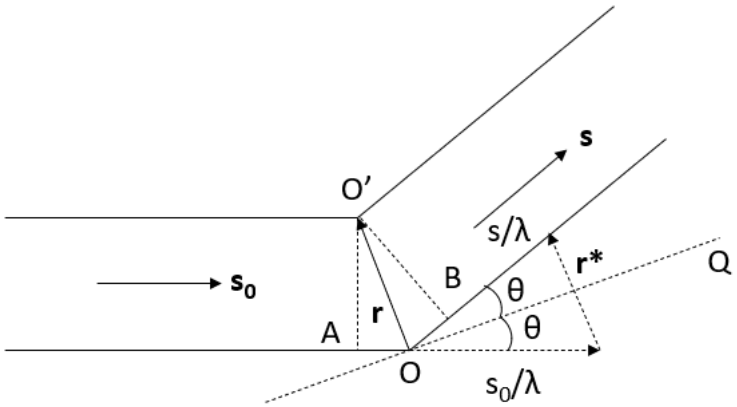

*Figure 2.7: Scattering of the incident plane wave by two scatterers O and O'. **s** and **s_0** are unit vectors*

In this case, the phase difference between the wave scattered by O and that scattered in the same direction by O' can be expressed as:

$$\delta = \frac{2\pi}{\lambda}(\boldsymbol{s} - \boldsymbol{s_0}) \cdot \boldsymbol{r} = 2\pi \boldsymbol{r}^* \cdot \boldsymbol{r} \tag{2.5}$$

With

$$\boldsymbol{r}^* = \lambda^{-1}(\boldsymbol{s} - \boldsymbol{s_0}) \tag{2.6}$$

with λ being the wavelength of the incident wave.

Considering that A_O is the amplitude of the wave scattering by the scattering center O, the wave scattered by O' is described as A_O,exp $(2\pi i \boldsymbol{r}^* \cdot \boldsymbol{r})$. If there are N point scatterers along the path of the incident plane then:

$$F(\boldsymbol{r}^*) = \sum_{j=1}^{N} A_j \exp(2\pi i \boldsymbol{r}^* \cdot \boldsymbol{r_j}) \tag{2.7}$$

where A_j is the amplitude of the wave scattered by the j^{th} point.

If there is a certain number of electrons concentrated in O' that undergo Thomson scattering, the factor *f* can be defined, for which $f_{O'}$ expresses the number of electrons. In this case, the equation (2.7) can be expressed as:

$$F(\boldsymbol{r}^*) = \sum_{j=1}^{N} f_j \exp(2\pi i \boldsymbol{r}^* \cdot \boldsymbol{r_j}) \tag{2.8}$$

In the case of continuum scattering centers, and considering that $\rho(\boldsymbol{r})$ is the density of electrons in an element of volume $d\boldsymbol{r}$, this volume would contain $\rho(\boldsymbol{r})d\boldsymbol{r}$ electrons. The total amplitude of scattered wave is

$$F(\boldsymbol{r}^*) = \int_V \rho(\boldsymbol{r}) \exp\left(2\pi i \boldsymbol{r}^* \cdot \boldsymbol{r_j}\right) d\boldsymbol{r} = T[\rho(\boldsymbol{r})] \tag{2.9}$$

where T represents the Fourier transform operator. In crystallography the space of r^* is called the reciprocal space.

1.3.3. Scattering by electrons

In fact, the intensity I_{eTh} of scattered radiation is the sum of coherent and incoherent scattering: I_{coe} + I_{incoe} = I_{eTh}. The coherent intensity I_{coe} can be calculated using these observations: atomic electrons can be represented by their distribution function $\rho_e(\boldsymbol{r}) = |\Psi(\boldsymbol{r})|^2$, where $\Psi(\boldsymbol{r})$ is the wave function of the Schrödinger equation. A volume dv contains $\rho_e dv$ electrons and scatters elementary waves that will interfere with other scattered waves from the other elements in that volume. Because of that, the electron scattering in a region of space S in which the probability of finding an electron is different from 0 will be:

$$f_e(\boldsymbol{r}^*) = \int_S p_e(\boldsymbol{r}) \exp(2\pi i \boldsymbol{r}^* - \boldsymbol{r})\, d\boldsymbol{r} \tag{2.10}$$

Hence, considering a spherical distribution of the electrons, the equation above can be approximated to a more convenient form:

$$f_e(\boldsymbol{r}^*) = \int_0^\infty U_e(\boldsymbol{r}) \frac{sin2\pi \boldsymbol{r}\boldsymbol{r}^*}{2\pi \boldsymbol{r}\boldsymbol{r}^*} \tag{2.11}$$

where $U_e(\boldsymbol{r}) = 4\pi r^2 p_e(\boldsymbol{r})$ is the radial distribution of the electron.

1.3.4. Scattering by atoms

To express the scattering by atoms containing Z electrons, we can consider the atomic scattering factor f_a obtained by inversing the Fourier transform of the density of electrons in a volume dv of $p_a(\boldsymbol{r})$**.** In a first approximation, we can consider that $p_a(\boldsymbol{r})$ has a spherical symmetry, and in the same way as for atomic electrons scattering, we obtain:

$$f_a(\boldsymbol{r}^*) = \int_0^\infty U_a(\boldsymbol{r}) \frac{sin2\pi \boldsymbol{r}\boldsymbol{r}^*}{2\pi \boldsymbol{r}\boldsymbol{r}^*} = \sum_{j=1}^{Z} f_{e_j} \tag{2.12}$$

where $U_a(\boldsymbol{r}) = 4\pi r^2 p_a(\boldsymbol{r})$ is the radial distribution function for the atom.

1.3.5.Scattering by a crystal

In the case of a three-dimensional infinite crystal, we can start from a discrete approximation of the crystals in order to define its properties. Atoms can be described as centers of scattering characterized by their individual atomic scattering factor. An ideal crystal is constructed by the infinite repetition of identical structural units in space according to three vectors (***a***, ***b***, ***c***). A position *r* represents the position of the elementary lattice of the *n* atom:

$$Crystal_{\infty} = Pattern \otimes Lattice \tag{2.13}$$

In other terms, the electron density function of the whole crystal is the convolution of the lattice function $L(\boldsymbol{r})$ with the electron density in the unit cell $p_M(\boldsymbol{r})$:

$$p_{\infty}(\boldsymbol{r}) = p_M(\boldsymbol{r}) \otimes L(\boldsymbol{r}) \tag{2.14}$$

with

$$L(\boldsymbol{r}) = \sum_{\boldsymbol{u},\boldsymbol{v},\boldsymbol{w}=-\infty}^{+\infty} \boldsymbol{\delta}(\boldsymbol{r} - \boldsymbol{r}_{\boldsymbol{u},\boldsymbol{v},\boldsymbol{w}}) \tag{2.15}$$

where δ is the Dirac delta function, $\boldsymbol{r}_{\boldsymbol{u},\boldsymbol{v},\boldsymbol{w}} = u\boldsymbol{a} + v\boldsymbol{b} + w\boldsymbol{c}$ and u, v and w are integers.

From this, the amplitude of the wave scattered by the whole crystal can be described as

$$F_{\infty}(\boldsymbol{r}^*) = T[\rho_M(\boldsymbol{r}) \cdot T[L(\boldsymbol{r})] = \frac{1}{V} F_M(\boldsymbol{H}) \sum_{\boldsymbol{u},\boldsymbol{v},\boldsymbol{w}=-\infty}^{+\infty} \boldsymbol{\delta}(\boldsymbol{r} - \boldsymbol{r}_{\boldsymbol{u},\boldsymbol{v},\boldsymbol{w}}) \tag{2.16}$$

where V is the volume of the unit cell and $\boldsymbol{r}^*_{\boldsymbol{H}} = h\boldsymbol{a}^* + k\boldsymbol{b}^* + l\boldsymbol{c}^*$ is the generic lattice vector of the reciprocal space. If the scatterer object is non-periodic, the amplitude of the scattered wave $F_M(\boldsymbol{r}^*)$ can take non-zero values for any value of $\boldsymbol{r}^*$. If the scatterer centers are periodic, then a non-zero amplitude is given only when $\boldsymbol{r}^*$ coincides with a reciprocal space point:

$$\boldsymbol{r}^* = \boldsymbol{r}^*_{\boldsymbol{H}} \tag{2.17}$$

If the definition of $\boldsymbol{r}^*$ is introduced and by multiplying the above equation ***a***, ***b*** and ***c*** then we obtain

$$\boldsymbol{a} \cdot (\boldsymbol{s} - \boldsymbol{s_0}) = h\lambda \qquad \boldsymbol{b} \cdot (\boldsymbol{s} - \boldsymbol{s_0}) = k\lambda \qquad \boldsymbol{c} \cdot (\boldsymbol{s} - \boldsymbol{s_0}) \tag{2.18}$$

The relation above is named Laue conditions and the direction ***s*** which satisfies the Laue condition are called diffraction direction. When the diffraction by a crystal is considered, the function $F_M(\boldsymbol{H})$ is called the structure factor of vectorial index ***H*** (or indexes h, k, k f we make reference to the components of r^*_H) and is indicated as:

$$F_{\boldsymbol{H}} = \sum_{j=1}^{N} f_j \exp\,(2\pi i \boldsymbol{r}^*_{\boldsymbol{H}} \cdot \boldsymbol{r}_j) \tag{2.19}$$

where *N* is the number of atoms in the unit cell.

The equation could also be written in a more explicit form:

$$F_{\boldsymbol{H}} = \sum_{j=1}^{N} f_j \exp\; 2\pi i(hx_j + ky_j + lz_j) \tag{2.20}$$

1.3.6.Principle of X-ray diffraction

Crystalline structure has an ordered structure with a periodic lattice composed of individual atoms, which can be imagined as diffraction gratings. The incident X-ray waves are elastically scattered by the atoms of the periodic lattice, giving rise to constructive or destructive interferences and generating a diffraction pattern specific of the crystalline material. The condition of diffraction can be written as the so-called Bragg's law:

$$\lambda = 2d_{hkl}\sin(\theta)$$

Where θ is the incident angle of the X-ray beam, d_{hkl} is the d-spacing of the planes *(hkl) as shown in* Figure 2.8.

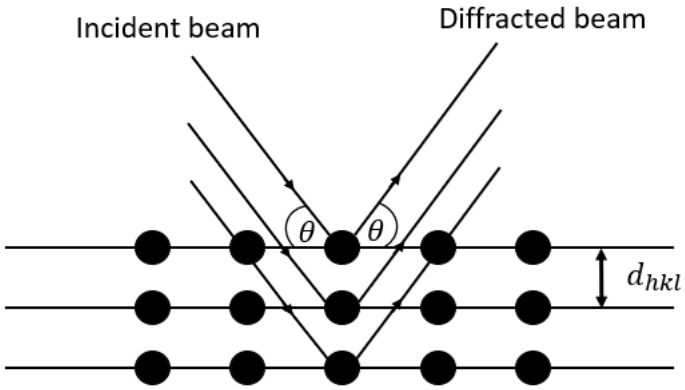

Figure 2.8: Diffraction of X-rays by a crystal

In the XRD pattern of a crystalline phase, well-defined diffraction peak are present at specific diffraction angles while the XRD pattern of an armophous phase shows a broad band extended over a large range of diffraction angles. The orientation of the atomic planes in cyrstals is described by Miller indices (hkl), which may denote a single or a set of parallel planes.

1.4. Information accessible with X-ray Diffraction

1.4.1.Crystallite size evaluation

Given the crystal system and the hkl value of the diffraction peak, the crystallite size (or coherent diffracting domain size) can be determined by the Debye - Scherrer equation:

$$\tau = \frac{K\lambda}{\beta cos\theta} \tag{2.21}$$

Where τ is the size of crystallite (nm), *K* is the dimensionless shape factor which is closed to unity, β is the full width half maximum of the peak expressed in radian, θ is the Bragg angle and λ is the wavelength (nm). It should be noted that the equation above is applicable only for nano-scale domains

(below few hundred of nm). Furthermore, it provides a lower bound to the crystallite size due to the fact that there are many factors which may contribute to the width of the diffraction peak, such as instrumental effects, inhomogeneous strain and lattice imperfections.

1.4.2.Phase identification

Most of solid materials have crystalline atomic structure. The diffraction pattern from crystalline materials contains many peaks corresponding to different atomic planes. From Bragg's Law, the peaks at low 2θ angles belong to atomic planes with small d-spacing while those at high 2θ angles are from atomic planes with high d-spacing. Each phase – a region that has uniform chemical composition, physical properties and structure - will give a unique diffraction pattern. From a powder sample in which crystals are randomly oriented, the set of d-spacing and their intensities are a fingerprint of a unique phase. In case of a mixture, the composition of the sample can be determined via quantitative analysis. To do so, peak position and intensity are compared with the X-ray Diffraction file – a database of over 300,000 inorganic and 450,000 organic and organometallic phases. This database is managed by the International Centre for Diffraction Data (ICDD) and is published annually. From each file of the database, a lot of information can be extracted: chemical formula and name, physical and optical data, set of d-spacing, Laue indices and their relative intensities arranged in the order of decreasing d-spacing. Finally, each file is assigned with a quality mark to indicate the reliability of the data.

1.4.3. Strain measurement

The analysis of strain using X-ray Diffraction was first reported in 1934s [70]. In this technique, the length variation of the internal strain gauge of the material, which is the interplanar d-spacings of a family of planes of the crystal, is measured. As mentioned above, using Bragg's equation, the d-spacing of a family of plane *(hkl)* can be calculated. In the case of piezo/ferroelectric material, under the application of an external electric field, the d-spacing of the material is modified, resulting in the shift of the position of the diffraction peak. Because of that, the strain generated under external electric field can be deduced from the following equation:

$$\varepsilon = \frac{d - d_0}{d_0} \tag{2.22}$$

where *d* and d_0 are the interplanar spacing of a family of planes with and without external electric field, respectively. When replacing *d* by the expression of the Bragg's law, the above equation becomes:

$$\varepsilon = \frac{\sin\theta_0}{\sin\theta} - 1 \tag{2.23}$$

where θ_0 and θ denote Bragg's angle in the absence of external electric field and under electric field, respectively. From the differentiated form of the Bragg's law, the strain can also be written as:

$$\varepsilon = -\frac{1}{2} cotg(\theta_0)\Delta 2\theta \tag{2.24}$$

with $\Delta 2\theta = 2\theta\text{-}2\theta_0$. From the equation above, it can be deduced that for a given strain, the displacement $\Delta 2\theta$ is more pronounced at high θ_0. As a result, it is preferable to work at high diffraction angles to improve the accuracy.

1.4.4.Texture analysis

Usually, crystallites within a polycrystalline thin film are usually not randomly distributed as in an ideal powder sample. In most cases, it exists one or several preferred orientations with respect to the reference coordinates system of the sample. These preferred orientations defined the crystallographic texture in material science. The physical properties (piezoelectricity, conductivity, thermal expansion, etc.) of crystalline materials are often anisotropic and their values are impacted by the texture of the crystallites. As a result, the texture analysis is an important step for the determination of the relationship between structure and functional properties of the materials. For the analysis of preferential orientation in thin films, x-ray diffraction is commonly used. As mentioned above, the relative intensities of the diffraction peaks of non-textured samples are stored in the database. If those intensities are not matched in a certain sample, it means that it is textured. This texture could be quantified through the texture coefficient, which is calculated based on the observed peak intensity ratios and the expected ratios:

$$C_{hkl} = \frac{\frac{I_{hkl}}{I_{0,hkl}}}{\frac{1}{N} \cdot \sum^{N} \frac{I_{hkl}}{I_{0,hkl}}} \tag{2.25}$$

with I_{hkl} and $I_{0,hkl}$ being the normalized and measured intensities for the hkl peak. Here, the I_{hkl} comes from the measured sample and $I_{0,hkl}$ comes from a on a standard sample (no texture), or extracted from a record of the ICDD database. The coefficients are equal to 1 for a non-textured sample. On the other hand, if the sample is textured along a certain *(hkl)* orientation, then C_{hkl} tends to *N*, where *N* is the number of peaks used to analyze the plane *(hkl)* and 0 for all the others. Based on the texture coefficients, the preferential orientation degree (σ), could be determined by the standard deviation of all the C_{hkl} compared with the values of a non-textured sample:

$$\sigma = \frac{\sqrt{\sum^{N}(C_{hkl} - 1)^2}}{\sqrt{N}} \tag{2.26}$$

For a non-textured sample, σ = 0. It is necessary to note that the texture coefficients and the orientation degree depend on the number of the analyzed planes. Moreover, the analysis of texture by XRD also shows two main limitations. Firstly the degree of texture depends on the number of hkl planes consider in the phase diagram. Secondly, only diffracting planes with structure factor different from zero are considered. Therefore, the texture analysis is relative to these planes only. Due to the above problems, the usage of this method should be limited to only samples not too textured.

1.5. Some optical configurations of X-ray diffraction

In X-ray diffraction technique, an important problem is the optimization of the optical configuration to achieve the diffraction peaks which satisfy the requirements of the application. In order to achieve this objective, different optical components could be added to tune the properties of the X-ray beam such as intensity, beam footprint, monochromacy, … In the following part, the different configurations that have been tested in the work in both laboratory and synchrotron facility will be introduced.

1.5.1. Optical configurations used in laboratory sources

In the θ/2θ scanning mode, the Bragg-Brentano is one of the most widely used configuration. This is a symmetrical setup whose incident and diffracted beam converge to the reception slit placed on the focusing circle as shown in Figure 2.9. This configuration allows to obtain very fine diffraction peaks

and to recover a remarkable diffracted intensity. This configuration allows recovering a remarkable diffracted intensity because the incident beam diverges onto the sample so it covers a larger range of sample area in comparison to parallel beam. Furthermore, as the incident beams are not parallel to each other (and the same for the diffracted beams), this configuration allows getting better intensity for the planes whose directions are deviated from the perpendicular orientation.

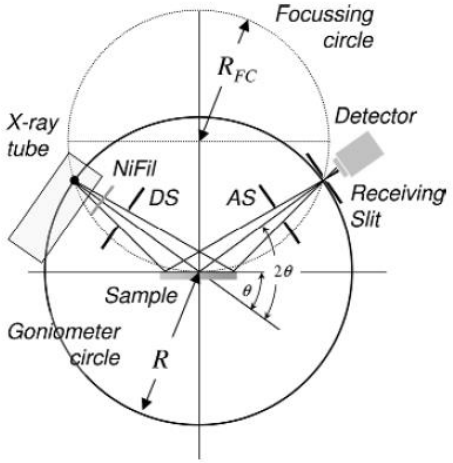

Figure 2.9: Schematic representation of the Bragg-Brentano configuration [69]

Another optical component which was tested during the thesis work is a parallel plate collimator (PPC). The PPC is installed on both the incidence and diffraction sides to confine the incidence and diffracted beam to the parallel rays. When applied to the θ/2θ scanning mode, this configuration gives a better intensity for the out-of-plane peak in comparison to the Bragg-Brentano configuration. However, the width of the peak is larger in this case because the diffracted beam is not focused to the detector. In our application, this is a disadvantage as it makes it more complicated to extract the information from each component of the triplet profile of (200) peak.

In order to optimize the width of the peak, a device was added to the XRD equipment is a monochromator. The hybrid monochromator consists of a parabolic graded multilayer mirror (X-ray mirror) and a channel-cut Ge crystal combined in one module. This device allows decreasing the divergence of the beam and eliminating the contribution of the Kα2 spectrum to the peaks. As a result, a monochromatic beam of Kα1 spectrum is generated and thus the FWHM of the diffraction peaks is decreased.

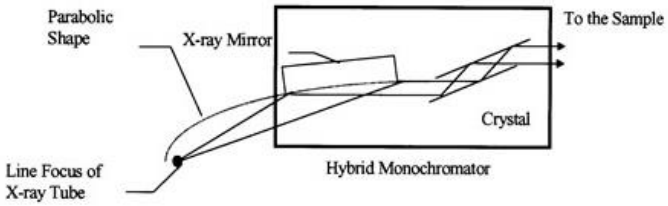

Figure 2.10: Structure of the hybrid monochromator XRD configuration

Even though this allows having better resolution of the XRD peak, one disadvantage is the decrease in the intensity of the peaks in comparison to the beam consisting of both Kα1 and Kα2 spectra. As a result, a solution for this is to combine the monochromatic beam with the Bragg-Brentano XRD configuration to obtain better intensity. For the monochromatic beam, a configuration named Johansson, whose structure is shown in Figure 2.11, can be used. In this configuration, a curved Johansson monochromator is used to cancel the contribution of the Ka2 spectrum. Then the monochromatized beam is sent through the divergence slit before being focused onto the sample.

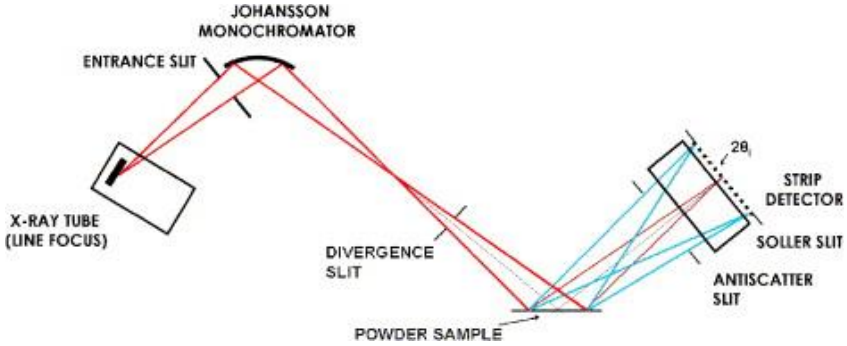

Figure 2.11: Structure of the Johansson XRD configuration

In order to extract the behavior of each domain variant, it is necessary to fit the intensity of each peak composing the XRD pattern. The reliability of the fit of each peak depends on their discernibility and on the intensity of each peak (counting statistics). In fact, the quality of the fit can be improved by increasing the counting time of the XRD scan. However, this also means increasing the electrical bias application time, which might lead to the breakdown of the sample. Therefore, for in situ biasing XRD experiment, the counting time is usually limited to around two minutes. As a result, in order to improve the discernibility of the peaks, the selection of the optimal XRD configuration is necessary. Figure 2.12 illustrates a comparison of the (200) peaks obtained by Bragg-Brentano using 1D detector, parallel plate collimator (PPC) and Hybrid configurations both using 0D detector. In this case, the XRD scan was done on the same sample during the same counting time. Here, we clearly demonstrated that the peak achieved by Bragg-Brentano configuration shows better peaks discernibility, thus it is more advantageous for the analysis of each domain variant. This improvement comes from the better angular resolution of Bragg Brentano as well as the usage of 1D detector, which gives better counting statistics for the XRD peak.

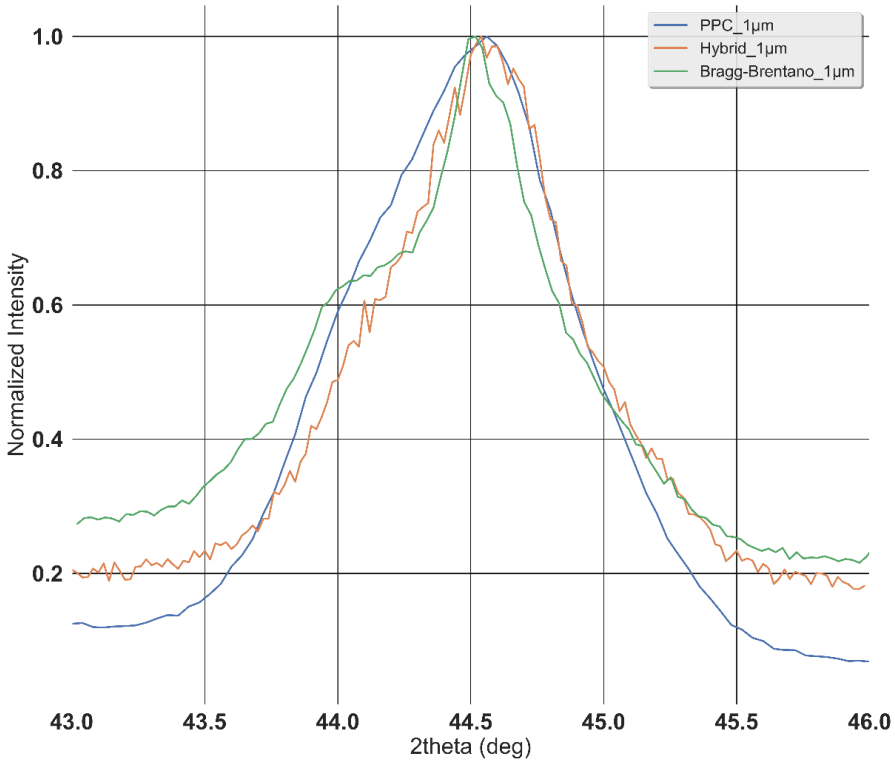

Figure 2.12: Comparison of the (200) XRD peaks obtained by Bragg-Brentano, PPC and hybrid configurations

Preliminary experiments showed that the most promising configuration is the Johansson optics applied to Bragg-Brentano configuration as shown in Figure 2.13. However, during this thesis, it was only

possible to employ this configuration with a 0D detector, leading to the low statistics of the peak. For the best usage of Bragg-Brentano with Johansson optics, a 2D detector should be employed to have the best counting statistics, which is currently not possible with the laboratory source equipment available at the CEA-LETI.

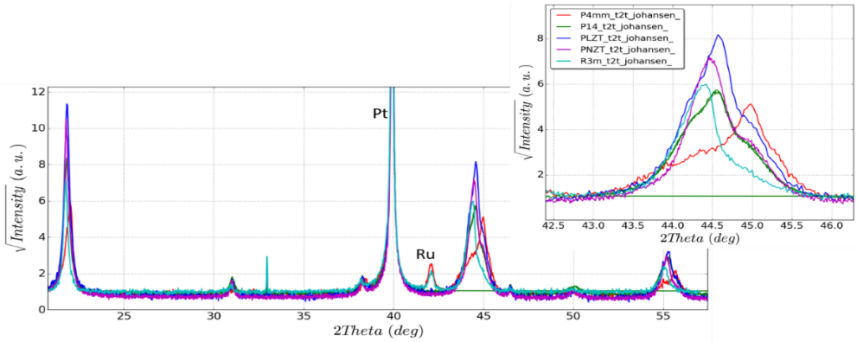

Figure 2.13: Preliminary results using Bragg-Brentano configuration with Johansson optic on different variants of PZT of different compositions

1.5.2.Optical configurations used in synchrotron source

During this work, due to the limited flux in the laboratory source XRD equipment, some experiments have been conducted using synchrotron X-ray source. Based on the applications, two different configurations have been used for in-situ biasing XRD experiments: configuration using transfocator and Fresnel Zone Plate for focusing. Concerning the transfocator, it is a tunable X-ray focusing apparatus based on compound refractive lenses as shown in Figure 2.14. By varying the number of lenses in the beam, the energy focused and the focal length can be modified throughout a large range of energies and distances. As a result, the instrument can be used to focus and collimate the beam. The transfocator can be used with other monochromators and with other focusing elements to optimize the flux. Because of that, the transfocator is exploited in our work to confine the beam to 100 µm in size, which allow studying the microscopic behaviour of the sample under applied field. The details of this research will be mentioned more in details in the later part of the thesis.

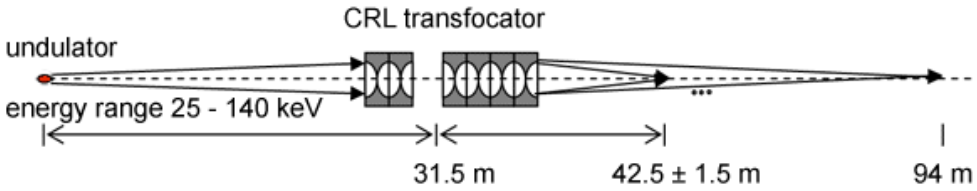

Figure 2.14: Schematic diagram of the transfocator

The second configuration that is used in the synchrotron source is the Fresnel Zone Plates (FZP), which are the circular diffraction gratings with increasing line density. By modification of the wave front, there will be a focusing effect on the X-rays. They form a concentric circular diffraction grating where the position of adjacent zones reproduces that of Fresnel half period zone. In this PhD work, the usage of FZP allows having an X-ray beam of 400 nm in size, which is compatible with the grain-scale analysis. More details on this work will be described later in this thesis.

Figure 2.15: Illustration of the Fresnel Zone Plate

1.6. X-ray Diffraction data analysis

In this thesis, the focus is put on samples of PZT with MPB composition, with a complex structure such as the coexistence of tetragonal and rhombohedral phases. This lead to XRD peaks with triplet profile with contributions from both of the above mentioned phases. As a result, in order to analyze quantitatively the microstructure of each phases, it is necessary to refine the profile of peaks with fitting techniques. In our case, we used a pseudo-Voigt model, which is mostly used by the XRD community. The pseudo-Voigt function is a weighted sum of Cauchy and Gaussian functions [71]:

$$PV(2\theta_i) = (\eta)\mathrm{L}(2\theta_i) + (1-\eta)\mathrm{G}(2\theta_i) \tag{2.27}$$

where $\mathrm{L}(2\theta_i)$ and $\mathrm{G}(2\theta_i)$ are Lorentzian and Gaussian functions, respectively and η is the mixing parameter of the linear combination which varies between 0 and 1. The Lorentzian function is described as following:

$$\mathrm{L}(2\theta_i) = \frac{I_0}{1 + (4\left(\frac{2\theta_i - 2\theta_k}{w}\right)^2)} \tag{2.28}$$

with I_0 being the intensity, $2\theta_k$ is the expected peak position corresponding to each reflection *k* and *w* is the full width half maximum (FWHM) of the peak. The Gaussian contribution is described as following:

$$\mathrm{G}(2\theta_i) = I_0 \exp\left(-4ln2\left(\frac{2\theta_i - 2\theta_k}{w}\right)^2\right) \tag{2.29}$$

In order to extract the parameters from the XRD peak such as the peak position, FWHM and intensity, a nonlinear least-square minimization technique is applied to minimize the error between the model and the experimental data. In this technique, the sum of the squares of the differences in intensity (so-called residuals) between the experimental and the modeled data points is minimized. Given a function $PV(2\theta_i)$ of the $2\theta_i$ position tabulated at m values $y_1 = PV(2\theta_1), \ldots, y_m = PV(2\theta_m)$ and the analytic form of the function is known to depend on three parameters as mentioned above $PV(2\theta_i;\ I_0,\ 2\theta_k,\ w)$, we have the overdetermined set of m equations:

$$y_1 = PV(2\theta_1;\ I_0, 2\theta_k, w) \tag{2.30}$$
$$\ldots$$

$$y_m = PV(2\theta_m;\ I_0, 2\theta_k, w) \tag{2.31}$$

We would like to solve these equations to obtain the parameters $I_0, 2\theta_k, w$ which fit best to the measured diffraction peak. In our project, the fitting procedure was carried out on Python environment using Lmfit library [72]. Because the fitting function could return more than one results with similar quality, in order to choose the best output, the coherence with the physical property of the sample has to be checked. An example is shown in Figure 2.1. This is the XRD peak corresponding to the phase (200) of a PZT sample with a Zr/Ti ratio of 30/70 being fitted with and without boundary values. These peaks are fitted with a 3-peak profile corresponding to the (002) and (200) direction of the tetragonal phase and (024) orientation of the rhombohedral phase. According to the phase diagram of PZT in Figure 1.14, at this composition, the proportion of tetragonal phase dominates. As a result, the fitting result in Figure 2.16(a) is unreasonable because in this case the intensity of (024) rhombohedral phase is closed to that of (200) tetragonal phase. After constraining the intensity of the (024) rhombohedral phase to be lower than the tetragonal ones, a more reasonable result is obtained. Taking into account that the residual of the two fitting strategies are similar, the result in Figure 2.16(b) will be choosen because it is more physical.

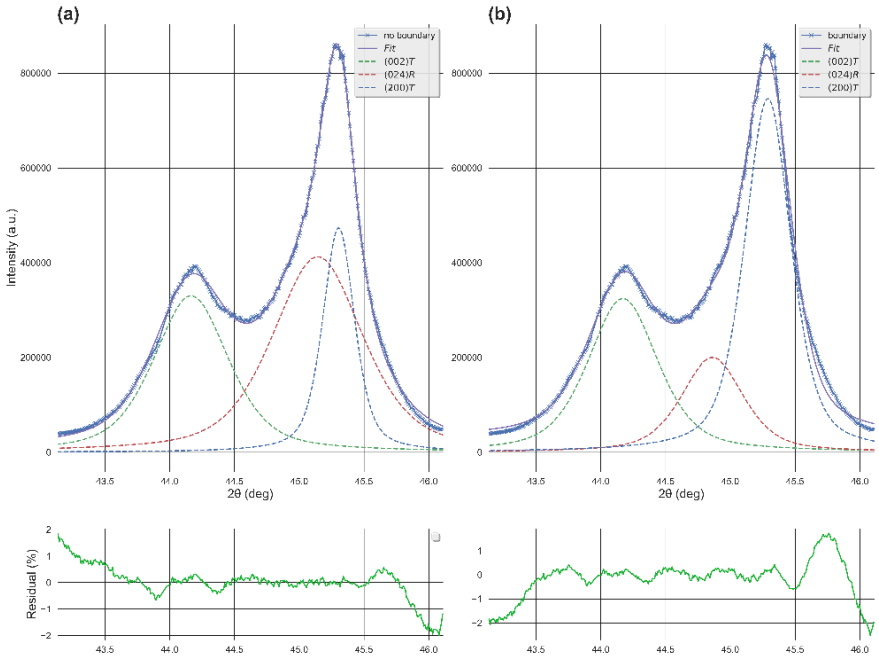

Figure 2.16: Examples of fitting (a) without and (b) with boundaries

2. Electrical characterization

2.1. Definition of electrical polarization

Electric charge is what causes it to experience a force when put in an electromagnetic field. Electric charge consists of two types: positive and negative charges, carried by proton and electron, respectively. When two point charges of different signs are separated by a distance *d*, an electric dipole moment $\vec{p}$ directed from the negative to positive charge is formed it is described by the following equation:

$$\vec{p} = q\vec{d} \tag{2.32}$$

with q being the magnitude of charge and $\vec{d}$ is the displacement vector. The density of electric dipole in a dielectric material can be expressed by a vector field named polarization density $\vec{P}$ and the electric dipole moment induced per unit volume – also called the electric polarization – can be expressed by the following formula:

$$\vec{P} = \frac{\vec{p}}{V} \tag{2.33}$$

where V is the volume of the material. When the dielectric material is placed in an external electric field, the field causes a torque on the molecules inside the material, leading to a displacement of the charged elements bounded to the molecules. Positive charged elements are displaced in the direction of the field while negative charged elements are directed to the opposite direction.

2.2. Methods of measuring the polarization of ferroelectric materials

Due to the interesting electrical properties, the electrical characterization is a crucial part in the research of ferroelectric materials. Traditionally, the electrical properties are characterized through three main techniques: polarization vs electric field (P-E), capacitance vs voltage (C-V) and dielectric loss tan(δ). In this work, a "portable" electrical tester has been developed to carry out the electrical characterization in parallel with the structural characterization of ferroelectric films. These characterizations could be performed in "large signal" mode (applied field larger than coercive field) or in "small signal" mode (applied field lower than coercive field). The developed setup also allows performing reliability tests of the ferroelectric films by applying a bipolar or unipolar cycling at high frequency. This is interesting for several applications such as MEMS where the devices are usually operated by unipolar signal using small signal while for memory applications, the ferroelectric films are operated by large signal of bipolar signal in order to perform the "reading" or "writing" process.

2.2.1. The circuits for ferroelectric measurement

2.2.1.1. The Sawyer-Tower method

In the Sawyer-Tower method, a reference capacitor of known value C_n is connected in series with the ferroelectric capacitor C_{FE} of interest as shown in Figure 2.17. The whole system is subjected to an alternating voltage. By doing so, the surface density of charges accumulated on plates is measured, and can be expressed as:

$$D = \varepsilon_0 E + P \tag{2.34}$$

Where ε_0 is the permittivity of the vacuum, E being the electric field applied to the ferroelectric film, and P the total polarization of the ferroelectric film.

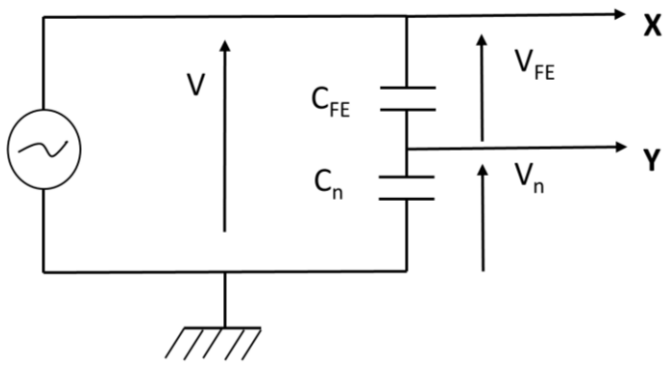

Figure 2.17: The circuit of Sawyer-Tower method

By measuring the voltage V_n across the standard capacitor C_n in series with the ferroelectric film, the charge Q_{FE} of the film can be measured. Considering that the two capacitors are in series and by neglecting the currents that pass through them (ideal capacitive circuit), the electrical charge accumulated by each of the two capacitors is the same. As a result, $Q_{FE} = Q_n$ with $Q_{FE} = D.S_{FE}$ and $Q_n = C_n.V_n$ with S_{FE} being the area of the capacitors. As a result, the following relation could be obtained:

$$D = \frac{C_n.V_n}{S_{FE}} \approx P \tag{2.35}$$

As a consequence, the measurement of V_n (using the Y channel of the oscilloscope) provides the surface charge density D. In the case of ferroelectric materials, the contribution of polarization is much higher than the electric field, therefore, D can be assimilated to P. From the X channel of the oscilloscope, the electric field E in the ferroelectric film is measured. The voltage V of the generator is written as:

$$V = V_{FE} + V_n \tag{2.36}$$

In practice, C_n is chosen to be much larger than C_{FE} so that its impedance is negligible compared to the one across the ferroelectric capacitor. As a result, $V \approx V_{FE}$. Assuming a uniform electric field in the film, E could be expressed as:

$$E = \frac{V_{FE}}{d} \tag{2.37}$$

where d denotes the thickness of the film.

2.2.1.2. Shunt method

The circuit of this method is similar to one of the Sawyer Tower method except that the reference capacitor is replaced by a reference resistor (shunt resistor). Unlike the Sawyer-Tower method, this method is based on the current measurement: the current due to domain switching is measured as a voltage drop at the shunt resistor through Ohm's law. After that, this current is integrated numerically to get the polarization charge through the following equation:

$$Q = \int I dt \tag{2.38}$$

Where Q denotes the polarization charge, I the current switching and t the time over which the current is integrated.

2.2.2. Ferroelectric measurement techniques implemented in ferroelectric analyzer TF2000 (Aixaact)

2.2.2.1. Dynamic Hysteresis Measurement technique

In this technique, the waveform, which consists of a prepol pulse followed by three bipolar excitation signals as illustrated in Figure 2.18, are applied. Between two consecutive pulses, there is a relaxation time of one second. The prepol pulse and the second pulse of excitation helps defining the polarization states of the sample. While the prepol pulse relaxes the remanent polarization in the negative state, the second pulse has a positive relaxed remanent polarization state.

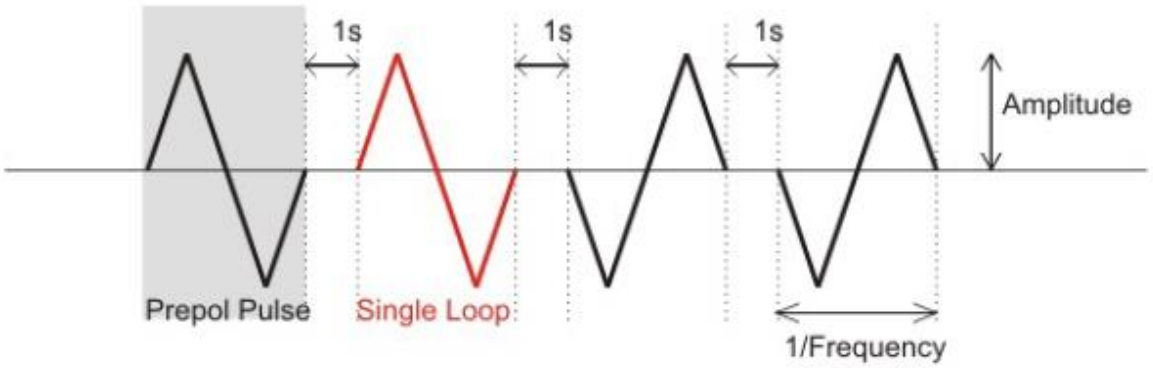

Figure 2.18: Waveform signal of DHM measurement (screenshot from the aixPlorer software)

To record the hysteresis loop, the first triangular signal with similar waveform as the prepol pulse is applied. As a result, the polarization will start from the negative relaxed remanent polarization state (P_{rrel-}) and increase to the positive saturation (P_{max+}) before going to the positive remanent polarization state (P_{r+}). Afterward it turns into the negative saturation (P_{max-}) and finishing at the negative remanent polarization state (P_{r-}). This value is normally not equal to the initial one due to the loss of polarization over time as shown in the inlet of Figure 2.19.

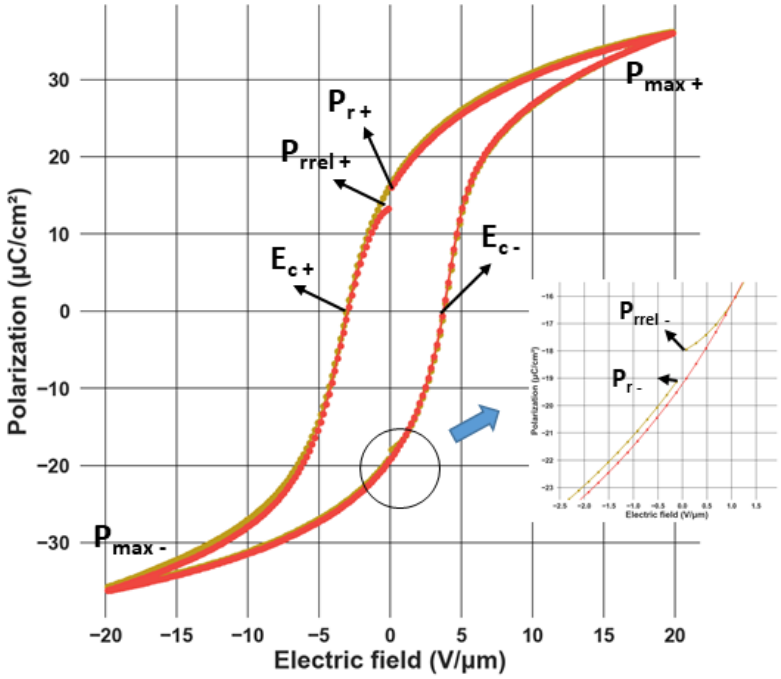

Figure 2.19: Polarization loop obtained from DHM technique

The second pulse for measurement of hysteresis loop is applied with the waveform similar to the one of the third pulse. In this case, the polarization starts at the positive relaxed remanent state (P_{rrel+}) then going to the negative saturation (P_{max-}) before crossing the point of zero volts in the negative remanent polarization state (P_{r-}). After that, it is driven into the positive saturation value (P_{max+}) before finishing at the positive remanent polarization state (P_{r+}).

2.2.2.2. Positive Up Negative Down (PUND) technique

.

In order to understand the principle of the measurement of polarization switching current, it is necessary to mention the current density model (*J(t)*) of our sample, a ferroelectric material as follows:

$$J(t) = J_{switching} + J_{displacement} + J_{leakage} \tag{2.39}$$

where $J_{switching} = \frac{\partial P(t)}{\partial t}$ is the current from the switching of the polarization *P(t)*; $J_{displacement} = C\frac{\partial E(t)}{\partial t}$ is the dielectric displacement current from the time-variation of the electric field and proportional to the capacitance of the material and $J_{leakage}$ is the leakage current. The switching of the polarization is characterized by the switching current $J_{switching}$ but it is hidden by the effects of displacement and leakage current. $J_{displacement}$ is directly proportional to the capacitance of the material while $J_{leakage}$ is unavoidable due to the tunneling effect in thin films. In Sawyer-Tower or DHM technique, the polarization is calculated by integrating over all of the three contributions. As a result, it is necessary to eliminate the parasitic contributions to the switching current and in this thesis we use a technique called Positive Up Negative Down (PUND). This method is based on a waveform applied on the sample in order to substract the leakage and displacement current from the switching current as shown in Figure 2.20(a).

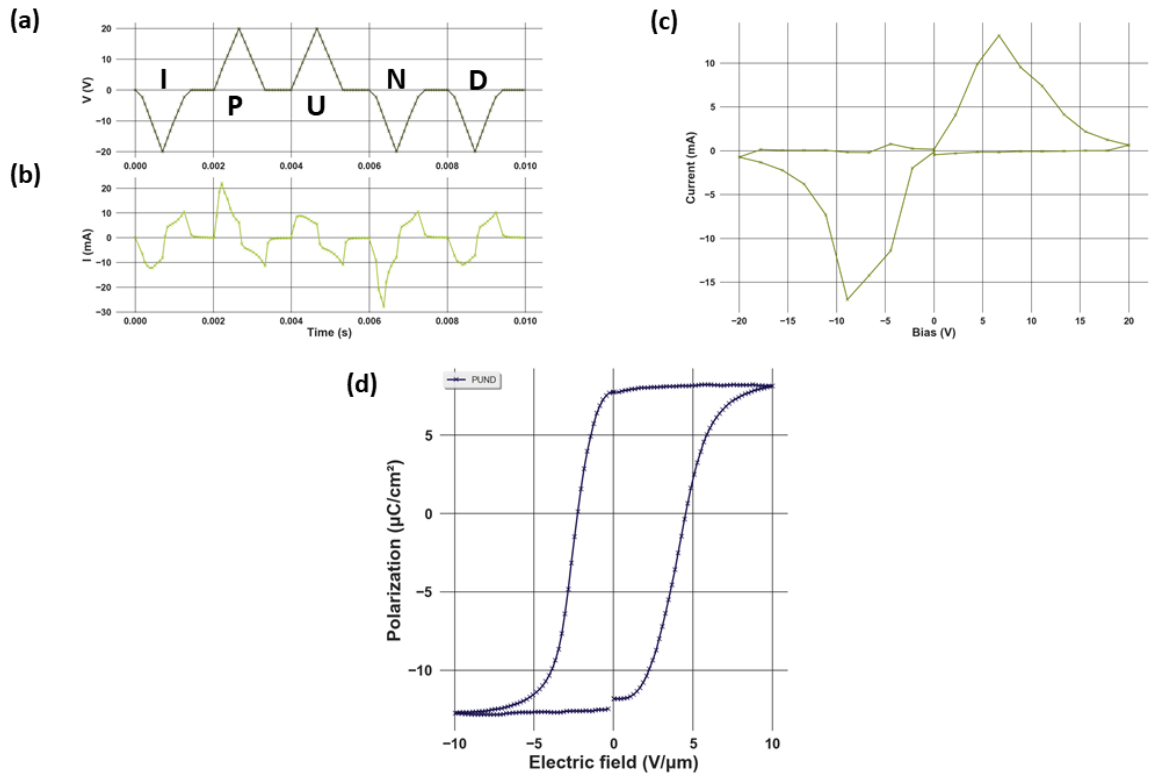

Figure 2.20: (a) The sequence of applied voltage in the PUND technique, (b) the current response of the PUND waveform, (c) the I-V curve and (d) the Polarization obtained after correction

The first pulse of voltage called pre-switch (**I**) is applied in order to bring all dipoles to the same orientation. After that, the pulse **P** is applied in the opposite orientation to reverse the polarization. In this case, the generated current originate from all three mechanisms: switching, displacement and leakage. Then the pulse **U** is applied in the same direction as the previous pulse **P**. However, as all the dipoles pointed in the same direction, only the displacement and the leakage current are measured. The contribution to the current response of each pulse can be summarized in the following equations:

$$I = initial\ pulse \tag{2.40}$$

$$P = J_{switch} + J_{displacement} + J_{leakage} \tag{2.41}$$

$$U = J_{displacement} + J_{leakage} \tag{2.42}$$

$$N = J_{switch} + J_{displacement} + J_{leakage} \tag{2.43}$$

$$D = J_{displacement} + J_{leakage} \tag{2.44}$$

By subtracting the current of the pulse **P** to that of pulse **U** and the same procedure for the pulse **N** and **D**, the I-V curve can be deduced as shown in Figure 2.20(c). Finally, the polarization loop (Figure 2.20(d)) of the sample can be deduced from the integration of the switching current density *J(t)* over time as following:

$$P(t) = \frac{Q}{A} = \frac{\int_0^t i(t)dt}{A} = \int_0^t J(t)dt \tag{2.45}$$

where *A* is the area of the electrode.

In our electrical measurement setup, the PUND was performed by a Source-Measure Unit (SMU). SMU is an instrument providing a sourcing function and a measurement one. In our case, the SMU was used to apply the PUND waveform and measure the current response using the shunt method. From this, the switching current is extracted and the polarization can be calculated by integrating the current density as described above. Using the SMU enable the possible modification of several parameters related to the measurements such as the applied voltage, the number of cycles, the compliance, the delay between two consecutive measurements as well as the number of power line cycles (NPLC). NPLC represents the duration of signal sampling (or integration time) and their relation is equal to $T_{int} = \frac{NPLC}{50}$ where T_{int} denotes the integration time and 50 is the frequency of the power line in Hertz. In electrical measurement, the interference of AC power might lead to the error in the output results. In order to reduce this noise, the measurement period could be taken over several NPLC. As a consequence, various interferences can cancel each other out in one cycle. The details on the implementation of PUND on the SMU will be mentioned later in this chapter.

3. Piezoelectric coefficient measurement

3.1. Double beam laser interferometer

The principle of laser interferometry consists in measuring the interference light intensity I at a detection point between a monochromatic light of wavelength λ with a reference beam:

$$I = I_P + I_r + 2I_P I_r \cos(\frac{4\pi \Delta d}{\lambda}) \tag{2.46}$$

where I_P and I_r are the light intensity for the probing beam and the reference beam, respectively, λ is the wavelength and Δd is the optical path-length difference between the two beams. A relative change Δd between the two beams results in a change in the interference light intensity which is expressed as following:

$$I = \left(\frac{1}{2}\right)(I_{max} + I_{min}) + \left(\frac{1}{2}\right)(I_{max} - I_{min}) \cos(\frac{4\pi \Delta d}{\lambda}) \tag{2.47}$$

where I_{max} and I_{min} are the maximum and minimum interference light intensities, respectively.

For small displacement measurement, it is best to set the interference between the two beams at a point about (2n+1)/8 (also called π/2 point) with n being the order of interference, where the light intensity change will be maximized for the same displacement change in *Δd*. Near this point *Δd* could be written as

$$\Delta d = d_{ac} + (2n+1)\lambda/8 \tag{2.48}$$

where d_{ac} is the displacement due to electric field. Now the interference light intensity can be written as:

$$I = I_P + I_r \pm 2I_P I_r \sin\left(\frac{4\pi d_{ac}}{\lambda}\right) \tag{2.49}$$

With the sign "+" or "-"depends on whether n is even or odd. This equation indicates that the light

intensity change is proportional to the change d_{ac} for small displacement [73].

As a result, the interferometry method can be used for the measurement of longitudinal effective piezoelectric coefficient ($d_{33,eff}$) through the converse piezoelectric effect. In this effect, the applied electric field will generate a mechanical strain, which is described by the following equation:

$$S_{ij} = s^{E}_{ijkl} T_{kl} + d_{kij} E_K \tag{2.50}$$

here *S* stands for mechanical strain, *s* is the elastic compliance at constant electric field, *T* refers to mechanical stress induced and *E* being the electric field applied to the material. For the measurement of small displacement, the interferometry method is usually implemented using two main optical schemes: the single-beam Michelson and the double-beam Mach-Zender interferometer. Considering the first configuration, even though it is simple and sensitive, the single-beam Michelson has a serious drawback because it is measuring the displacement of the front face of the sample. And the whole displacement in the sample is assumed to be constant and equal to this quantity. This assumption is only correct if the back face of the sample is fixed, which is not the case in bulk sample. In bulk sample, the back face is deformed against the material placed between the sample and the holder and this deformation becomes stronger with increasing the frequency. Considering the case of thin films, even though the film is clamped to the substrate, the bending of the substrate due to piezoelectric effect should be taken into account. The driving field applied in perpendicular direction causes not only the change of film thickness but also the stress in the in-plane direction. In this case, the "film + substrate" system will behave as a "bimorph" system, which consists of a passive and an active element (the piezoelectric film). Therefore, the piezoelectric response will consists of the bending element if the substrate is not fixed. In order to solve this problem, a system which consists of double-beam interferometer (DBLI) is used. In this technique, the beam is reflected both from the front and the back surface of the sample, thus eliminating the bending effect of the substrate [74]. The structure of the DBLI setup is shown in Figure 2.21.

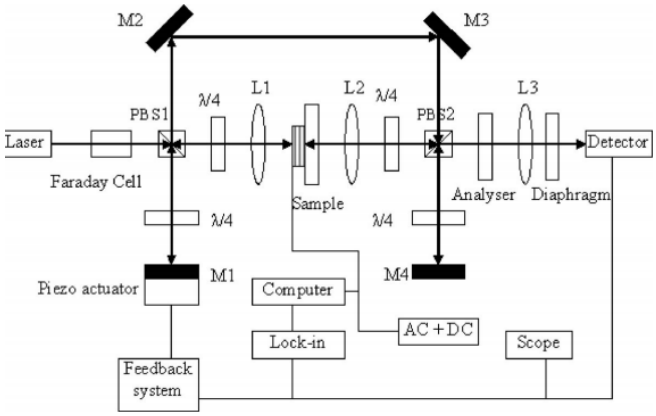

Figure 2.21: Structure of the Double-beam laser interferometer (DBLI) system [75]

In the DBLI setup, the laser beam will first pass through a Faraday isolator before coming to the polarizing beam splitter Polarized Beamsplitter 1 (PBS1). PBS1 splits the beam into measuring and reference beams with mutually perpendicular polarization direction. The reference beams travel through a quarter wave plate (λ) and is then reflected by the mirror M1, which is installed on a piezoactuator. This reference beam then passes through a (λ/4 plate again before being transmitted through the PBS1. Considering the measuring beam, it goes through a λ/4 plate, and is then reflected by the sample surface, passes through the λ/4 plate again to be reflected by the PBS1. After being

reflected by the two 45°-tilted mirrors M2 and M3, the measuring beam is reflected by the PBS2 before going through a λ/4 plate and is reflected by the back surface of the sample. The two lenses, L1 and L2 at either sides of the sample focus the beam onto the sample surfaces and collect beams reflected from there. Thanks to these lenses, beams reflected from sample surfaces with slightly different tiltes will become parallel. After PBS2, the measuring and reference beams meet at the analyzer and the interference is broadened by lens L3 and the signals are detected by a photodiode and preamplifier detector [75].

In this thesis, we used a aixDBLI equipment from AixACCT manufacturer. The system consists of a measurement chamber, a wafer prober for x-, y- and z-positioning, a Class IIIa-Medium Power Laser and additional optics to create the optical path and a rack mount system for storing the electronics components. The laser beam path is covered in the measurement chamber for security purpose as well as to isolate the highly sensitive setup from the thermal streaming and reduces the impact of parasitic noise. The rack mount system consists of all electrical circuitry, including the safety circuit, the drawer for keyboard and mouse, the ferroelectric analyzer (TF2000), the control unit, additional power supply and the Uninteruptable Power Supply.

In order to measurement the coefficient $d_{33,eff,}$ the Piezo Measurement (PZM) mode is used. In this measurement mode, the polarization hysteresis is measured simultaneously with the sample displacement. This allows the investigation of the relation between the hysteresis loop and the piezoelectric displacement. The $d_{33,eff}$ is measured by doing the linear regression on the displacement vs electric field curve along the point t/4 to below t/2 for positive side (d_{33}av+ in Figure 2.22) and 3t/4 to below t for negative side (d_{33}av- in Figure 2.22) where t is the total number of measurement point. These points correspond to the non-switching branches of the butterfly curve of displacement vs Electric field as shown in Figure 2.22.

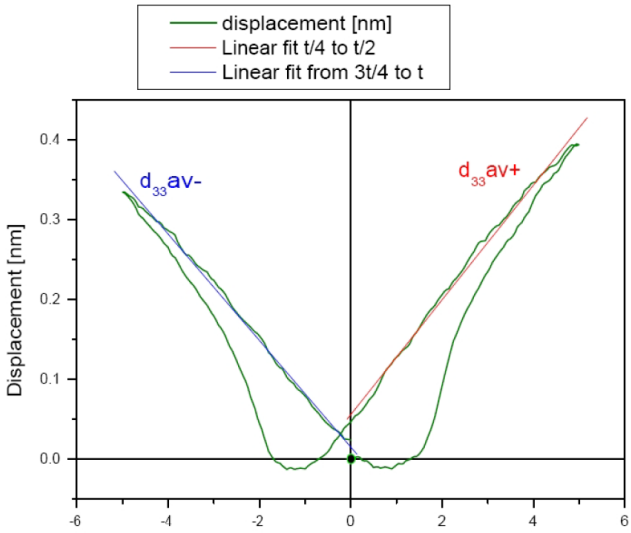

Figure 2.22: Extraction of d_{33} by linear regression on DBLI system [Manual TF2000]

3.2. X-ray Diffraction

The strain induced by applied field in piezoelectric film can be measured by XRD technique. To do so, the x-ray diffractometer is coupled with a generator to measure the structural changes in the film induced by the applied field. XRD makes use of the deformation of the lattice and the resulting shift of the diffraction peaks. This shift in position can be used to deduce the strain enabling a direct measuring of the piezoelectric coefficient. In piezoelectric thin films, the effective piezoelectric coefficient ($d_{33,eff}$) is defined as

$$d_{33,eff} = \frac{\partial S_3}{\partial E_3} \tag{2.51}$$

Where S_3 and E_3 are the strain and the applied field in the orientation perpendicular to the sample surface, respectively. Similar to the DBLI technique, the strain vs electric field (S-E) curve obtained by XRD also shows a butterfly behavior. In order to extract the $d_{33,eff}$, a linear fitting along the slope of the non-switching parts of the S-E curve is necessary. As a result, the resulting strain in these regions is mostly generated by the piezoelectric effect. The $d_{33,eff}$ could also be extracted from doing the fit along the negative or positive slope. The values obtained from those two slopes might be different from each other, which could be due to the built-in electric field - an internal field that exists due to the defects. This field leads to the existence of a preferred polarization orientation in the sample and thus, the domains take less energy to be switched to the preferred direction. As a result, the strain along the preferred orientation could be larger than along the other one and leading to the difference in the $d_{33,eff}$. In this thesis, we also compare the $d_{33,eff}$ of a sample PZT 0.5 µm thickness obtained by both XRD and DBLI setup. It was found that there is a difference of around 10% (~93 for DBLI and ~ 85 ± 2 pm/V pm/V for XRD). This difference could stem from the fact that the investigated samples are polycrystalline films with (100) texture. Because of that, the Bragg peaks corresponding to other orientations such as (110) or (111) also exist. In using XRD technique, the $d_{33,eff}$ is extracted from the strain along only one crystallographic orientation and in our case, only the (200) orientation because it has the highest peak intensity and splitting. As a result, it would be interesting to compare the $d_{33,eff}$ value of an epitaxial film of PZT obtained from XRD and DBLI technique. In epitaxial films, there exists highly ordered atomic arrangement following their seed crystals, as a result, they have a single orientation or a twinned structure corresponding to ferroelectric or ferroelastic domain structure. Because of that, the $d_{33,eff}$ measured by XRD is expected to be more coherent with the results from DBLI.

4. In-situ biasing X-ray Diffraction setup

In order to carry out the in situ biasing XRD experiments, the XRD set-up is coupled with a Source Measure Unit (SMU, Tektronix K2635B), which is controlled by a homemade Python program as shown in Figure 2.23. For the lab-source equipment (Empyrean, Malvern Panalytical®), the experiment is carried out using Bragg-Brentano configuration. On the incident beam optic, a Soller slit of 0.04 radians is used with the beam mask of 5 mm. The irradiated length is chosen to be 1.5 mm. These parameters allow confining the incident beam to the top electrode of the capacitor of interest. For the diffracted beam path, a Soller slit of 0.04 radians is combined with an anti-scatter slit and a beta-filter. The detector used is a Pixcel® 1D detector which provides a higher counting rate and dynamic range than a 0D detector. As a result, an XRD peak of good quality could be achieved in shorter amount of time. This allows reducing the experiment time.

During our beamtime on ESRF ID01 beamline, the energy was set at 8 keV (very similar 2theta value as measured on a Cu cathode lab source). The diffracted beam is recorded with a 2D pixel detector (Maxipix) made of a 516x516 array of 55 µm square pixels.

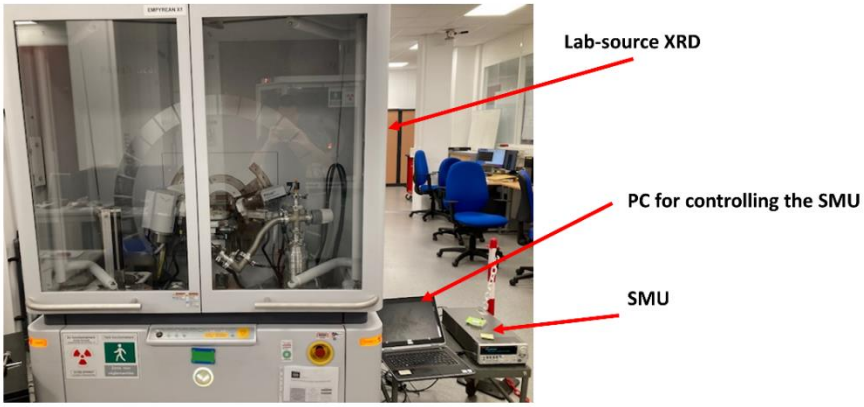

Figure 2.23: an in-situ biasing XRD setup using lab source

For the experiments conducted on the lab-source equipment, it is necessary to verify if the beam is centered on the targeted capacitor. To do so, the position of the beam is calibrated based on the variation of the intensity of Platinum (Pt) (111) diffraction peak across the sample. The Pt signal comes from the underneath bottom electrode and can be altered by the presence of PZT thin film or the top electrode made out of Ruthenium (Ru), as illustrated in Figure 2.24(b). The alteration of Pt intensity across the sample along the x-axis is shown in Figure 2.24(c). At the beginning, a strong intensity of Pt can be seen as this region corresponding to the region at bottom of the sample in which the Pt film is not covered by PZT and Ru as illustrated in Figure 2.24(a) and (b) . After that, the intensity decrease as the beam enters the region of PZT. The PT intensity is then going up and down as the beam pass by a region of $1mm^2$ cover with a Ru top electrode. The same procedure is continued until the desired sample is found. Finally, the beam should be positioned into the "valley" as it is where is electric field is applied. For the lab-source equipment, due to the divergence of the beam, it is impossible to focus on $1mm^2$ area and as a result, all the experiments are conducted on the sample with beam footprint of 2x8 mm^2(HxV).

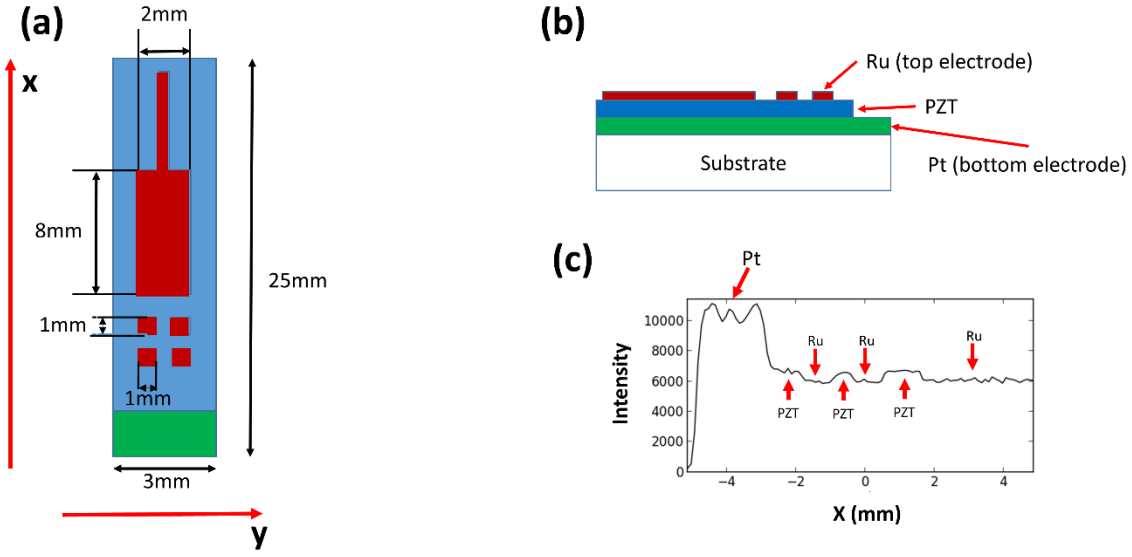

Figure 2.24: Schematic of the sample from (a) top-view as well as (b) cross-section view and the variation of Pt intensity along the sample in the x-axis

An important challenge in performing the experiment is to establish a stable electrical connection between the sample and the SMU. To solve this problem, a special sample holder for the lab XRD equipment has been designed and fabricated. On this sample holder, a Bayonet Neill-Concelman (BNC) connector is fixed with a screw. Then it is connected to two mini-probers, which are stabilized on the

sample holder by magnetic force to establish the electrical connection with the sample as shown in Figure 2.25(a). For the synchrotron experiment, as the sample holder used in lab-source equipment is not compatible, the BNC connectors are installed directly onto the piezo stage as illustrated in Figure 2.25(b). And the BNC connectors are connected to the mini-probers by soldered electrical wires.

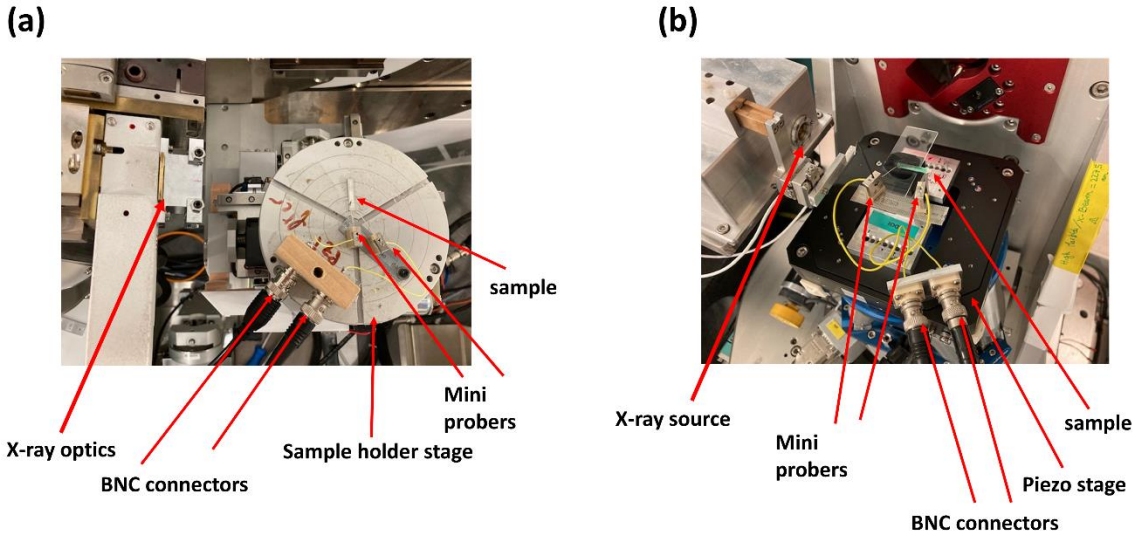

Figure 2.25: the electrical contacts for in-situ biasing on (a) lab-source and (b) synchrotron source XRD equipment

The main component of the electrical measurement installation is a SMU, which has the ability to provide a voltage up to ±200V and a reading speed of 20000 reading/s. In our project, it is used for two main purposes: applying the electric field for in-situ biasing XRD experiment and measuring the polarization of the ferroelectric samples. The SMU is connected with the BNC on the sample holder using biaxial cable with the help of a triaxial-to-biaxial adapter. The equipment is controlled by a computer equipped with a VISA backend (NI-VISA) from National Instrument for communication with the SMU and an automatic measurement is performed by a Python program using pyVISA [76] front end library. Concerning the program for polarization measurement, it is programmed to apply the *Positive Up Negative Down* (PUND) method. As mentioned above, the PUND method consists of five pulses and in Python, the values of the bias applied is embedded in a matrix of 5 columns and 100 rows, corresponding to 5 pulses and 100 values of bias for each pulse as following:

$$V_{I,P,U,N,D;i} = \begin{bmatrix} V_{I1} & V_{P1} & V_{U1} & V_{N1} & V_{D1} \\ V_{I2} & V_{P2} & V_{U2} & V_{N2} & V_{D2} \\ \dots & \dots & \dots & \dots & \dots \\ V_{I100} & V_{P100} & V_{U100} & V_{N100} & V_{D100} \end{bmatrix}$$

The values in each of the column will be sent to the SMU to apply the bias and the current respond is measured. To avoid latency between the SMU and the computer, all the parameters are initiated in the PC and sent to the SMU. From the triggering of all the protocols to the data acquisition and saving, everything is done within the SMU with the data saved in the internal buffer. After that, the measured current and the timestamps is sent back to the PC, saved and analyzed.

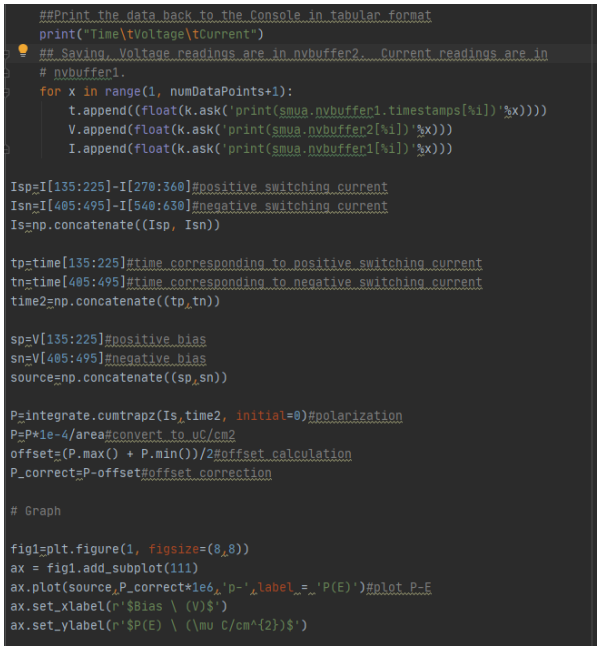

```
    ##Print the data back to the Console in tabular format
    print("Time\tVoltage\tCurrent")
    ## Saving  Voltage readings are in nvbuffer2,  Current readings are in
    # nvbuffer1.
    for x in range(1, numDataPoints+1):
        t.append((float(k.ask('print(smua.nvbuffer1.timestamps[%i])'%x))))
        V.append(float(k.ask('print(smua.nvbuffer2[%i])'%x)))
        I.append(float(k.ask('print(smua.nvbuffer1[%i])'%x)))

Isp=I[135:225]-I[270:360]#positive switching current
Isn=I[405:495]-I[540:630]#negative switching current
Is=np.concatenate((Isp, Isn))

tp=time[135:225]#time corresponding to positive switching current
tn=time[405:495]#time corresponding to negative switching current
time2=np.concatenate((tp,tn))

sp=V[135:225]#positive bias
sn=V[405:495]#negative bias
source=np.concatenate((sp,sn))

P=integrate.cumtrapz(Is,time2, initial=0)#polarization
P=P*1e-4/area#convert to uC/cm2
offset=(P.max() + P.min())/2#offset calculation
P_correct=P-offset#offset correction

# Graph

fig1=plt.figure(1, figsize=(8,8))
ax = fig1.add_subplot(111)
ax.plot(source,P_correct*1e6,'p-',label='P(E)')#plot P-E
ax.set_xlabel(r'$Bias \ (V)$')
ax.set_ylabel(r'$P(E) \ (\mu C/cm^{2})$')
```

Figure 2.26: Captured image of a part of the polarization measurement program written in Python

Before sending the bias values in the next column, a command is sent to the SMU to reset the memory. After that, the bias values will be sent and the measurement is carried out. The process is repeated until all the current response of all the five pulses are measured and saved in the PC. Finally, the integration is conducted in Python to obtain the polarization and plotting. The principle of the program is illustrated in Figure 2.27 (a). To verify the accuracy of the obtained results, the ferroelectric polarization loop measured by SMU is compared with the one measured by a commercial ferroelectric analyzer (TF2000, Aixaact) as shown in Figure 2.273(b). Results showed that only a small difference exists between them (less than 1 µC/cm^2 for P_R and 1 V/µm for E_c), which confirms the reliability of the data measured by our setup. Concerning the application of the bias for in-situ biasing XRD, another program is prepared and the duration of the bias is chosen to be coherent with the sum of the acquisition time and the initialization time of the diffractometer. An in-situ biasing XRD experiment is generally conducted in three steps: firstly, the polarization of the film is measured to verify the electrical contact. If a hysteresis loop is obtained, it indicates that a good electrical contact is established and the in-situ biasing XRD is carried out. Finally, after the XRD measurements are finished, a finale polarization loop is measured to assure that a robust electrical contact was maintained throughout the whole experiment.

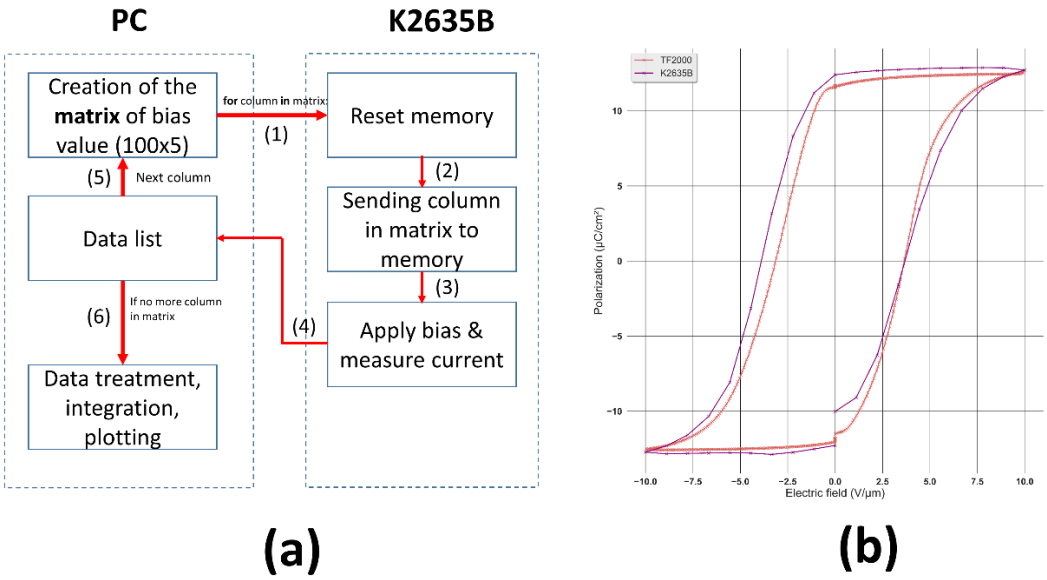

Figure 2.27: (a) Block diagram demonstrating the working principle of the program for PUND measurement and (b) comparison between the polarization loop obtained by homemade program (K2635B) and that obtained by commercial equipment (TF2000)

However, due to the limitation in terms of the working frequency of the SMU, it is not possible to apply high frequency bias cycling. The reading speed of K2635B is limited to 20 000 readings/s. In our experiment, we would like to apply the bipolar cycling of 10 kHz. At this frequency, the sampling rate of only 2 readings per second, or per cycle, is possible. As a result, an Arbitrary Functional Generator (AFG, Tektronix AFG1000) was used. With this equipment, users can apply a cycling with the frequency of up to 25 MHz. Thanks to the homemade Python programs, the measurement parameters can be modified on both equipment such as the range of applied voltage, the frequency, the number of measurement points, etc.

References for chapter II

[1] J. Evans *et al.*, "A discrete ferroelectric memory," in *2012 12th Annual Non-Volatile Memory Technology Symposium Proceedings*, Singapore: IEEE, Oct. 2012, pp. 33–36. doi: 10.1109/NVMTS.2013.6632857.

[2] Jérôme Mouly, "PIEZOELECTRIC DEVICES: FROM BULK TO THIN-FILM 2019," Yole development.

[3] Eric Mounier, Dimitrios Damianos, "Status of the MEMS industry 2019," Yole development.

[4] J. Bok and C. Kounelis, "Paul Langevin (1872-1946) - De la butte Montmartre au Panthéon : parcours d'un physicien d'exception," *Reflets Phys.*, no. 1, pp. 14–16, Sep. 2006, doi: 10.1051/refdp/2006007.

[5] J. Valasek, "Piezo-Electric and Allied Phenomena in Rochelle Salt," *Phys. Rev.*, vol. 17, no. 4, pp. 475–481, Apr. 1921, doi: 10.1103/PhysRev.17.475.

[6] A. T. Gen Shirane, "Phase Transitions in Solid Solutions of PbZrO3 and PbTiO3 (I) Small Concentrations of PbTiO3," *J. Phys. Soc. Jpn.*, vol. 7, pp. 5–11, Jan. 1952, doi: https://doi.org/10.1143/JPSJ.7.5.

[7] G. H. Haertling, "Ferroelectric Ceramics: History and Technology," *J. Am. Ceram. Soc.*, vol. 82, no. 4, pp. 797–818, Apr. 1999, doi: 10.1111/j.1151-2916.1999.tb01840.x.

[8] M. Ishida, S. Tsuji, K. Kimura, H. Matsunami, and T. Tanaka, "EPITAXIAL GROWTH OF FERROELECTRIC PLZT [(Pb, La)(Zr,Ti)Oa1 THIN FILMS," p. 6.

[9] M. Oikawa and K. Toda, "Preparation of Pb(Zr,Ti)O $_3$ thin films by an electron beam

evaporation technique," *Appl. Phys. Lett.*, vol. 29, no. 8, pp. 491–492, Oct. 1976, doi: 10.1063/1.89133.
[10] M. Ishida, H. Matsunami, and T. Tanaka, "Preparation and properties of ferroelectric PLZT thin films by rf sputtering," p. 4.
[11] H. Adachi, T. Kawaguchi, K. Setsune, K. Ohji, and K. Wasa, "Electro-optic effects of (Pb, La)(Zr, Ti)O_3 thin films prepared by rf planar magnetron sputtering," *Appl. Phys. Lett.*, vol. 42, no. 10, pp. 867–868, May 1983, doi: 10.1063/1.93795.
[12] K. Iijima, Y. Tomita, R. Takayama, and I. Ueda, "Preparation of *c* -axis oriented $PbTiO_3$ thin films and their crystallographic, dielectric, and pyroelectric properties," *J. Appl. Phys.*, vol. 60, no. 1, pp. 361–367, Jul. 1986, doi: 10.1063/1.337654.
[13] N. Shohata, S. Matsubara, Y. Miyasaka, and M. Yonezawa, "Epitaxial Growth of PbTiO3on MgAl2O4/Si Substrates," in *Sixth IEEE International Symposium on Applications of Ferroelectrics*, Jun. 1986, pp. 580–584. doi: 10.1109/ISAF.1986.201210.
[14] S. K. Dey, K. D. Budd, and D. A. Payne, "Thin-film ferroelectrics of PZT of sol-gel processing," *IEEE Trans. Ultrason. Ferroelectr. Freq. Control*, vol. 35, no. 1, pp. 80–81, Jan. 1988, doi: 10.1109/58.4153.
[15] J. Xu, A. S. Shaikh, and R. W. Vest, "High K BaTiO/sub 3/ films from metalloorganic precursors," *IEEE Trans. Ultrason. Ferroelectr. Freq. Control*, vol. 36, no. 3, pp. 307–312, May 1989, doi: 10.1109/58.19168.
[16] G. M. Davis and M. C. Gower, "Epitaxial growth of thin films of $BaTiO_3$ using excimer laser ablation," *Appl. Phys. Lett.*, vol. 55, no. 2, pp. 112–114, Jul. 1989, doi: 10.1063/1.102393.
[17] M. Okada, S. Takai, M. Amemiya, and K. Tominaga, "Preparation of *c* -Axis-Oriented $PbTiO_3$ Thin Films by MOCVD under Reduced Pressure," *Jpn. J. Appl. Phys.*, vol. 28, no. Part 1, No. 6, pp. 1030–1034, Jun. 1989, doi: 10.1143/JJAP.28.1030.
[18] K. Iijima, T. Terashima, K. Yamamoto, K. Hirata, and Y. Bando, "Preparation of ferroelectric $BaTiO_3$ thin films by activated reactive evaporation," *Appl. Phys. Lett.*, vol. 56, no. 6, pp. 527–529, Feb. 1990, doi: 10.1063/1.103300.
[19] R. A. Roy, K. F. Etzold, and J. J. Cuomo, "Ferroelectric Film Synthesis, Past and Present: A Select Review," *MRS Proc.*, vol. 200, p. 141, 1990, doi: 10.1557/PROC-200-141.
[20] N. Menou, "Technologie FeRAM: fiabilité et mécanismes de défaillance de condensateurs ferroélectriques élémentaires et intégrés," p. 239.
[21] C. M. Fancher *et al.*, "The contribution of 180° domain wall motion to dielectric properties quantified from in situ X-ray diffraction," *Acta Mater.*, vol. 126, pp. 36–43, Mar. 2017, doi: 10.1016/j.actamat.2016.12.037.
[22] D. Damjanovic, "Ferroelectric, dielectric and piezoelectric properties of ferroelectric thin films and ceramics," *Rep. Prog. Phys.*, vol. 61, no. 9, pp. 1267–1324, Sep. 1998, doi: 10.1088/0034-4885/61/9/002.
[23] S. Wada and T. Tsurumi, "Enhanced piezoelectricity of barium titanate single crystals with engineered domain configuration," *Br. Ceram. Trans.*, vol. 103, no. 2, pp. 93–96, Apr. 2004, doi: 10.1179/096797804225012747.
[24] K. Lefki and G. J. M. Dormans, "Measurement of piezoelectric coefficients of ferroelectric thin films," *J. Appl. Phys.*, vol. 76, no. 3, pp. 1764–1767, Aug. 1994, doi: 10.1063/1.357693.
[25] S. Trolier-Mckinstry and P. Muralt, "Thin Film Piezoelectrics for MEMS," p. 11.
[26] E. Jabari, F. Ahmed, F. Liravi, E. B. Secor, L. Lin, and E. Toyserkani, "2D printing of graphene: a review," *2D Mater.*, vol. 6, no. 4, p. 042004, Aug. 2019, doi: 10.1088/2053-1583/ab29b2.
[27] S. Nicolas *et al.*, "Fabrication and characterization of a new varifocal liquid lens with embedded PZT actuators for high optical performances," in *2015 28th IEEE International Conference on Micro Electro Mechanical Systems (MEMS)*, Jan. 2015, pp. 65–68. doi: 10.1109/MEMSYS.2015.7050887.
[28] H. Wang, Z. Chen, and H. Xie, "A high-SPL piezoelectric MEMS loud speaker based on thin ceramic PZT," *Sens. Actuators Phys.*, vol. 309, p. 112018, Jul. 2020, doi: 10.1016/j.sna.2020.112018.

[29] M. Tani, M. Akamatsu, Y. Yasuda, and H. Toshiyoshi, “A two-axis piezoelectric tilting micromirror with a newly developed PZT-meandering actuator,” in *2007 IEEE 20th International Conference on Micro Electro Mechanical Systems (MEMS)*, Jan. 2007, pp. 699–702. doi: 10.1109/MEMSYS.2007.4432994.

[30] P. Laitinen and J. Mawnpaa, “Enabling mobile haptic design: piezoelectric actuator technology properties in hand held devices,” in *2006 IEEE International Workshop on Haptic Audio Visual Environments and their Applications (HAVE 2006)*, Nov. 2006, pp. 40–43. doi: 10.1109/HAVE.2006.283787.

[31] H. K. Ma, B. R. Hou, H. Y. Wu, C. Y. Lin, J. J. Gao, and M. C. Kou, “Development and application of a diaphragm micro-pump with piezoelectric device,” *Microsyst. Technol.*, vol. 14, no. 7, pp. 1001–1007, Jul. 2008, doi: 10.1007/s00542-007-0462-6.

[32] P. Muralt, “PZT thin films for microsensors and actuators: Where do we stand?,” *IEEE Trans. Ultrason. Ferroelectr. Freq. Control*, vol. 47, no. 4, pp. 903–915, Jul. 2000, doi: 10.1109/58.852073.

[33] “What is a SAW Filter ?,” *everythingRF*. https://www.everythingrf.com/community/what-is-a-saw-filter

[34] T. Giffney, M. Yu, K. C. Aw, and H. Zhang, “Contactless RF MEMS switch using PZT actuation,” in *The 8th Annual IEEE International Conference on Nano/Micro Engineered and Molecular Systems*, Apr. 2013, pp. 861–864. doi: 10.1109/NEMS.2013.6559860.

[35] J. S. Meena, S. M. Sze, U. Chand, and T.-Y. Tseng, “Overview of emerging nonvolatile memory technologies,” *Nanoscale Res. Lett.*, vol. 9, no. 1, p. 526, Dec. 2014, doi: 10.1186/1556-276X-9-526.

[36] Volker Rzehak, “Low-Power FRAM Microcontrollers and Their Applications,” Texas Instrument, 2019.

[37] J. Müller *et al.*, “Ferroelectricity in yttrium-doped hafnium oxide,” *J. Appl. Phys.*, vol. 110, no. 11, p. 114113, Dec. 2011, doi: 10.1063/1.3667205.

[38] T. Francois *et al.*, “Demonstration of BEOL-compatible ferroelectric Hf0.5Zr0.5O2 scaled FeRAM co-integrated with 130nm CMOS for embedded NVM applications,” in *2019 IEEE International Electron Devices Meeting (IEDM)*, Dec. 2019, p. 15.7.1-15.7.4. doi: 10.1109/IEDM19573.2019.8993485.

[39] S. Priya *et al.*, “A Review on Piezoelectric Energy Harvesting: Materials, Methods, and Circuits,” *Energy Harvest. Syst.*, vol. 4, no. 1, pp. 3–39, Aug. 2019, doi: 10.1515/ehs-2016-0028.

[40] B. Noheda *et al.*, “Tetragonal-to-monoclinic phase transition in a ferroelectric perovskite: The structure of PbZr 0.52 Ti 0.48 O 3,” *Phys. Rev. B*, vol. 61, no. 13, pp. 8687–8695, Apr. 2000, doi: 10.1103/PhysRevB.61.8687.

[41] M. Ahart *et al.*, “Origin of morphotropic phase boundaries in ferroelectrics,” *Nature*, vol. 451, no. 7178, pp. 545–548, Jan. 2008, doi: 10.1038/nature06459.

[42] G. A. Rossetti and A. G. Khachaturyan, “Inherent nanoscale structural instabilities near morphotropic boundaries in ferroelectric solid solutions,” *Appl. Phys. Lett.*, vol. 91, no. 7, p. 072909, Aug. 2007, doi: 10.1063/1.2771095.

[43] R. Ahluwalia, T. Lookman, A. Saxena, and W. Cao, “Domain-size dependence of piezoelectric properties of ferroelectrics,” *Phys. Rev. B*, vol. 72, no. 1, p. 014112, Jul. 2005, doi: 10.1103/PhysRevB.72.014112.

[44] N. Setter *et al.*, “Ferroelectric thin films: Review of materials, properties, and applications,” *J. Appl. Phys.*, vol. 100, no. 5, p. 051606, Sep. 2006, doi: 10.1063/1.2336999.

[45] R. Guo, L. E. Cross, S.-E. Park, B. Noheda, D. E. Cox, and G. Shirane, “Origin of the High Piezoelectric Response in PbZr 1 − x Ti x O 3,” *Phys. Rev. Lett.*, vol. 84, no. 23, pp. 5423–5426, Jun. 2000, doi: 10.1103/PhysRevLett.84.5423.

[46] L. Bellaiche, A. García, and D. Vanderbilt, “Finite-Temperature Properties of Pb (Zr 1 − x Ti x) O 3 Alloys from First Principles,” *Phys. Rev. Lett.*, vol. 84, no. 23, pp. 5427–5430, Jun. 2000, doi: 10.1103/PhysRevLett.84.5427.

[47] M. Hinterstein *et al.*, “Structural Description of the Macroscopic Piezo- and Ferroelectric Properties of Lead Zirconate Titanate,” *Phys. Rev. Lett.*, vol. 107, no. 7, p. 077602, Aug. 2011, doi: 10.1103/PhysRevLett.107.077602.

[48] V. Kovacova, N. Vaxelaire, G. Le Rhun, P. Gergaud, T. Schmitz-Kempen, and E. Defay, “Correlation between electric-field-induced phase transition and piezoelectricity in lead zirconate titanate films,” *Phys. Rev. B*, vol. 90, no. 14, p. 140101, Oct. 2014, doi: 10.1103/PhysRevB.90.140101.

[49] T. W. Cornelius *et al.*, “Piezoelectric response and electrical properties of Pb(Zr 1-x Ti x)O 3 thin films: The role of imprint and composition,” *J. Appl. Phys.*, vol. 122, no. 16, pp. 164104–164104, Oct. 2017, doi: 10.1063/1.4994939.

[50] T. W. Cornelius *et al.*, “Piezoelectric Properties of Pb1−xLax(Zr0.52Ti0.48)1−x/4O3 Thin Films Studied by In Situ X-ray Diffraction,” *Materials*, vol. 13, no. 15, p. 3338, Jul. 2020, doi: 10.3390/ma13153338.

[51] P. Jiang *et al.*, “Wake-Up Effect in HfO2-Based Ferroelectric Films,” *Adv. Electron. Mater.*, vol. 7, no. 1, p. 2000728, 2021, doi: 10.1002/aelm.202000728.

[52] Q. Y. Jiang, E. C. Subbarao, and L. E. Cross, “Effect of composition and temperature on electric fatigue of La-doped lead zirconate titanate ceramics,” *J. Appl. Phys.*, vol. 75, no. 11, pp. 7433–7443, Jun. 1994, doi: 10.1063/1.356637.

[53] M. Majkut, J. E. Daniels, J. P. Wright, S. Schmidt, and J. Oddershede, “Electromechanical Response of Polycrystalline Barium Titanate Resolved at the Grain Scale,” *J. Am. Ceram. Soc.*, vol. 100, no. 1, pp. 393–402, Jan. 2017, doi: 10.1111/jace.14481.

[54] H. N. Al-Shareef, A. I. Kingon, X. Chen, K. R. Bellur, and O. Auciello, “Contribution of electrodes and microstructures to the electrical properties of Pb(Zr $_{0.53}$ Ti $_{0.47}$)O $_3$ thin film capacitors,” *J. Mater. Res.*, vol. 9, no. 11, pp. 2968–2975, Nov. 1994, doi: 10.1557/JMR.1994.2968.

[55] C. Künneth, R. Batra, G. A. Rossetti, R. Ramprasad, and A. Kersch, “Thermodynamics of Phase Stability and Ferroelectricity From First Principles,” in *Ferroelectricity in Doped Hafnium Oxide: Materials, Properties and Devices*, Elsevier, 2019, pp. 245–289. doi: 10.1016/B978-0-08-102430-0.00006-1.

[56] M. Pešić *et al.*, “Physical Mechanisms behind the Field-Cycling Behavior of HfO2-Based Ferroelectric Capacitors,” *Adv. Funct. Mater.*, vol. 26, no. 25, pp. 4601–4612, 2016, doi: https://doi.org/10.1002/adfm.201600590.

[57] W. L. Warren *et al.*, “Polarization suppression in Pb(Zr,Ti)O $_3$ thin films,” *J. Appl. Phys.*, vol. 77, no. 12, pp. 6695–6702, Jun. 1995, doi: 10.1063/1.359083.

[58] H. M. Duiker *et al.*, “Fatigue and switching in ferroelectric memories: Theory and experiment,” *J. Appl. Phys.*, vol. 68, no. 11, pp. 5783–5791, Dec. 1990, doi: 10.1063/1.346948.

[59] J. F. Scott, C. A. Araujo, B. M. Melnick, L. D. McMillan, and R. Zuleeg, “Quantitative measurement of space-charge effects in lead zirconate-titanate memories,” *J. Appl. Phys.*, vol. 70, no. 1, pp. 382–388, Jul. 1991, doi: 10.1063/1.350286.

[60] H. Zou, “Effect of Nb Doping on Crystalline Orientation, Electric and Fatigue Properties of PZT Thin Films Prepared by Sol-Gel Process,” *J. Ceram. Sci. Technol.*, no. 04, 2017, doi: 10.4416/JCST2017-00031.

[61] H. Sun, Y. Zhang, X. Liu, S. Guo, Y. Liu, and W. Chen, “The effect of Mn/Nb doping on dielectric and ferroelectric properties of PZT thin films prepared by sol–gel process,” *J. Sol-Gel Sci. Technol.*, vol. 74, no. 2, pp. 378–386, May 2015, doi: 10.1007/s10971-014-3608-x.

[62] J. M. Benedetto, “Imprint induced failure modes in ferroelectric non-volatile memories,” *Integr. Ferroelectr.*, vol. 15, no. 1–4, pp. 29–38, Feb. 1997, doi: 10.1080/10584589708015694.

[63] G. Arlt and H. Neumann, “Internal bias in ferroelectric ceramics: Origin and time dependence,” *Ferroelectrics*, vol. 87, no. 1, pp. 109–120, Nov. 1988, doi: 10.1080/00150198808201374.

[64] R. Lohkämper, H. Neumann, and G. Arlt, “Internal bias in acceptor-doped BaTiO $_3$ ceramics: Numerical evaluation of increase and decrease,” *J. Appl. Phys.*, vol. 68, no. 8, pp. 4220–4224, Oct. 1990, doi: 10.1063/1.346212.

[65] D. Dimos, W. L. Warren, M. B. Sinclair, B. A. Tuttle, and R. W. Schwartz, “Photoinduced hysteresis changes and optical storage in (Pb,La)(Zr,Ti)O $_3$ thin films and ceramics,” *J. Appl. Phys.*, vol. 76, no. 7, pp. 4305–4315, Oct. 1994, doi: 10.1063/1.357316.
[66] M. Grossmann, O. Lohse, D. Bolten, U. Boettger, T. Schneller, and R. Waser, “The interface screening model as origin of imprint in PbZrxTi1−xO3 thin films. I. Dopant, illumination, and bias dependence,” *J. Appl. Phys.*, vol. 92, no. 5, pp. 2680–2687, Sep. 2002, doi: 10.1063/1.1498966.
[67] R. Roque, “X-ray imaging using 100 µm thick Gas Electron Multipliers operating in Kr-CO2 mixtures,” Unpublished, 2018. Accessed: Aug. 07, 2022. [Online]. Available: http://rgdoi.net/10.13140/RG.2.2.16794.49600
[68] European Synchrotron Radiation Facility, “QUESTIONS & ANSWERS.” https://www.esrf.fr/about/ask-an-expert/questions-answers#:~:text=The%20most%20important%20advantage%20of,angular%20spread%20of%20the%20beam.
[69] M. Birkholz, “Thin Film Analysis by X-Ray Scattering,” p. 381.
[70] H. Möller and J. Barbers, *Mitt Kais. Wilhelm Inst. Eisenforsch.*, vol. 16, p. 21, 1934.
[71] P. Gravereau, “Introduction à la pratique de la diffraction des rayons X par les poudres,” p. 210.
[72] Newville, Matthew ; Stensitzki, Till ; Allen, Daniel B. ; Rawlik, Michal ; Ingargiola, Antonino ; Nelson, Andrew, “LMFIT: Non-Linear Least-Square Minimization and Curve-Fitting for Python”, doi: 10.5281/zenodo.11813.
[73] Q. M. Zhang, W. Y. Pan, and L. E. Cross, “Laser interferometer for the study of piezoelectric and electrostrictive strains,” *J. Appl. Phys.*, vol. 63, no. 8, pp. 2492–2496, Apr. 1988, doi: 10.1063/1.341027.
[74] A. L. Kholkin, Ch. Wütchrich, D. V. Taylor, and N. Setter, “Interferometric measurements of electric field-induced displacements in piezoelectric thin films,” *Rev. Sci. Instrum.*, vol. 67, no. 5, pp. 1935–1941, May 1996, doi: 10.1063/1.1147000.
[75] Z. Huang and R. W. Whatmore, “A double-beam common path laser interferometer for the measurement of electric field-induced strains of piezoelectric thin films,” *Rev. Sci. Instrum.*, vol. 76, no. 12, p. 123906, Dec. 2005, doi: 10.1063/1.2149002.
[76] “PyVISA: Control your instruments with Python.” https://pyvisa.readthedocs.io/en/latest/
[77] N. Vaxelaire *et al.*, “Effect of structural in-depth heterogeneities on electrical properties of Pb(Zr0.52Ti0.48) O3 thin films as revealed by nano-beam X-ray diffraction,” *J. Appl. Phys.*, vol. 120, no. 10, p. 104101, Sep. 2016, doi: 10.1063/1.4962427.
[78] B. Noheda *et al.*, “Tetragonal-to-monoclinic phase transition in a ferroelectric perovskite: The structure of PbZr 0.52 Ti 0.48 O 3,” *Phys. Rev. B*, vol. 61, no. 13, pp. 8687–8695, Apr. 2000, doi: 10.1103/PhysRevB.61.8687.
[79] S. K. Sayyed and S. A. Acharya, “Synthesis of PZT nanorods and study of dielectric behaviour,” presented at the PROCEEDING OF INTERNATIONAL CONFERENCE ON RECENT TRENDS IN APPLIED PHYSICS AND MATERIAL SCIENCE: RAM 2013, Bikaner, Rajasthan, India, 2013, pp. 111–112. doi: 10.1063/1.4810125.
[80] Wojciech Paszkowicz, “Application of a powder diffractometer equipped with a strip detector and Johansson monochromator to phase analysis and structure refinement,” *Nucl. Instrum. Methods Phys. Res. Sect. Accel. Spectrometers Detect. Assoc. Equip.*, vol. 551, no. 1, pp. 162–177, Oct. 2005, doi: 10.1016/j.nima.2005.07.068.
[81] K. T. Li and V. C. Lo, “Simulation of thickness dependence in ferroelectric thin films,” *Solid State Commun.*, vol. 132, no. 1, pp. 49–54, Oct. 2004, doi: 10.1016/j.ssc.2004.07.013.
[82] M. Dekkers, M. D. Nguyen, R. Steenwelle, P. M. te Riele, D. H. A. Blank, and G. Rijnders, “Ferroelectric properties of epitaxial Pb(Zr,Ti)O3 thin films on silicon by control of crystal orientation,” *Appl. Phys. Lett.*, vol. 95, no. 1, p. 012902, Jul. 2009, doi: 10.1063/1.3163057.
[83] Yu. V. Podgorny, D. S. Seregin, A. S. Sigov, and K. A. Vorotilov, “Effect of Sol-Gel PZT Film Thickness on the Hysteresis Properties,” *Ferroelectrics*, vol. 439, no. 1, pp. 74–79, Jan. 2012,

doi: 10.1080/00150193.2012.741952.
[84] A. J. Fox, B. Drawl, G. R. Fox, B. J. Gibbons, and S. Trolier-McKinstry, “Control of crystallographic texture and surface morphology of Pt/Tio2 templates for enhanced PZT thin film texture,” *IEEE Trans. Ultrason. Ferroelectr. Freq. Control*, vol. 62, no. 1, pp. 56–61, Jan. 2015, doi: 10.1109/TUFFC.2014.006671.
[85] E. M. Alkoy, S. Alkoy, and T. Shiosaki, “The effect of crystallographic orientation and solution aging on the electrical properties of sol–gel derived Pb(Zr0.45Ti0.55)O3 thin films,” *Ceram. Int.*, vol. 33, no. 8, pp. 1455–1462, Dec. 2007, doi: 10.1016/j.ceramint.2006.06.010.
[86] Y. Kim, H. Han, I. Vrejoiu, W. Lee, D. Hesse, and M. Alexe, “Origins of domain wall pinning in ferroelectric nanocapacitors,” *Nano Converg.*, vol. 1, no. 1, p. 24, Dec. 2014, doi: 10.1186/s40580-014-0024-4.
[87] J. A. Christman, R. R. Woolcott, A. I. Kingon, and R. J. Nemanich, “Piezoelectric measurements with atomic force microscopy,” p. 4.
[88] O. Kuffer, I. Maggio-Aprile, J.-M. Triscone, O. Fischer, and Ch. Renner, “Piezoelectric response of epitaxial Pb(Zr0.2Ti0.8)O3 films measured by scanning tunneling microscopy,” *Appl. Phys. Lett.*, vol. 77, no. 11, pp. 1701–1703, Sep. 2000, doi: 10.1063/1.1309017.
[89] A. L. Kholkin, Ch. Wütchrich, D. V. Taylor, and N. Setter, “Interferometric measurements of electric field-induced displacements in piezoelectric thin films,” *Rev. Sci. Instrum.*, vol. 67, no. 5, pp. 1935–1941, May 1996, doi: 10.1063/1.1147000.
[90] Z. Huang and R. W. Whatmore, “A double-beam common path laser interferometer for the measurement of electric field-induced strains of piezoelectric thin films,” *Rev. Sci. Instrum.*, vol. 76, no. 12, p. 123906, Dec. 2005, doi: 10.1063/1.2149002.
[91] H. Weitzing, G. A. Schneider, J. Steffens, M. Hammer, and M. J. Hoffmann, “Cyclic fatigue due to electric loading in ferroelectric ceramics,” *J. Eur. Ceram. Soc.*, vol. 19, no. 6, pp. 1333–1337, Jun. 1999, doi: 10.1016/S0955-2219(98)00429-4.
[92] R. Herbiet, H. Tenbrock, and G. Arlt, “The aging behaviour of the complex material parameters ε, d and s in ferroelectric PZT ceramics,” *Ferroelectrics*, vol. 76, no. 1, pp. 319–326, Dec. 1987, doi: 10.1080/00150198708016952.
[93] J. E. Daniels *et al.*, “Heterogeneous grain-scale response in ferroic polycrystals under electric field,” *Sci. Rep.*, vol. 6, no. 1, p. 22820, Mar. 2016, doi: 10.1038/srep22820.
[94] Q. Li and M. Kuna, “Inhomogeneity and material configurational forces in three dimensional ferroelectric polycrystals,” *Eur. J. Mech. - ASolids*, vol. 31, no. 1, pp. 77–89, Jan. 2012, doi: 10.1016/j.euromechsol.2011.07.004.
[95] L. Fan, W. Werner, S. Subotić, D. Schneider, M. Hinterstein, and B. Nestler, “Multigrain phase-field simulation in ferroelectrics with phase coexistences: An improved phase-field model,” *Comput. Mater. Sci.*, vol. 203, p. 111056, Feb. 2022, doi: 10.1016/j.commatsci.2021.111056.
[96] H. Simons *et al.*, “Long-range symmetry breaking in embedded ferroelectrics,” *Nat. Mater.*, vol. 17, no. 9, pp. 814–819, Sep. 2018, doi: 10.1038/s41563-018-0116-3.
[97] E. K. H. Salje, S. Li, M. Stengel, P. Gumbsch, and X. Ding, “Flexoelectricity and the polarity of complex ferroelastic twin patterns,” *Phys. Rev. B*, vol. 94, no. 2, p. 024114, Jul. 2016, doi: 10.1103/PhysRevB.94.024114.
[98] J. Novak, U. Bismayer, and E. K. H. Salje, “Simulated equilibrium shapes of ferroelastic needle domains,” *J. Phys. Condens. Matter*, vol. 14, no. 3, pp. 657–664, Jan. 2002, doi: 10.1088/0953-8984/14/3/332.
[99] A. S. Karapuzha, N. K. James, H. Khanbareh, S. van der Zwaag, and W. A. Groen, “Structure, dielectric and piezoelectric properties of donor doped PZT ceramics across the phase diagram,” *Ferroelectrics*, vol. 504, no. 1, pp. 160–171, Nov. 2016, doi: 10.1080/00150193.2016.1240571.
[100] M. Budimir, D. Damjanovic, and N. Setter, “Enhancement of the piezoelectric response of tetragonal perovskite single crystals by uniaxial stress applied along the polar axis: A free-energy approach,” *Phys. Rev. B*, vol. 72, no. 6, p. 064107, Aug. 2005, doi: 10.1103/PhysRevB.72.064107.

[101] E.-M. Anton, R. E. García, T. S. Key, J. E. Blendell, and K. J. Bowman, “Domain switching mechanisms in polycrystalline ferroelectrics with asymmetric hysteretic behavior,” *J. Appl. Phys.*, vol. 105, no. 2, p. 024107, Jan. 2009, doi: 10.1063/1.3068333.
[102] C. Lichtensteiger, J.-M. Triscone, J. Junquera, and P. Ghosez, “Ferroelectricity and Tetragonality in Ultrathin P b T i O 3 Films,” *Phys. Rev. Lett.*, vol. 94, no. 4, p. 047603, Feb. 2005, doi: 10.1103/PhysRevLett.94.047603.
[103] C. A. Randall, N. Kim, J.-P. Kucera, W. Cao, and T. R. Shrout, “Intrinsic and Extrinsic Size Effects in Fine-Grained Morphotropic-Phase-Boundary Lead Zirconate Titanate Ceramics,” *J. Am. Ceram. Soc.*, vol. 81, no. 3, pp. 677–688, 1998, doi: 10.1111/j.1151-2916.1998.tb02389.x.
[104] Y. Wei, C. Jin, P. Ye, P. Li, Y. Zeng, and G. Xu, “Structural evolution, electrical properties and electric-field-induced changes of (0.8−x)PbTiO3–xBiFeO3–0.2BaZrO3 system near the morphotropic phase boundary,” *Appl. Phys. A*, vol. 123, no. 4, p. 218, Apr. 2017, doi: 10.1007/s00339-016-0736-x.
[105] B. Allouche, I. Gueye, G. L. Rhun, P. Gergaud, and N. Vaxelaire, “In-situ X-ray diffraction on functional thin films using a laboratory source during electrical biasing,” *Mater. Des.*, vol. 154, pp. 340–346, Sep. 2018, doi: 10.1016/j.matdes.2018.05.016.
[106] K. Nguyen, E. Bellec, E. Zatterin, G. Le Rhun, P. Gergaud, and N. Vaxelaire, “Structural Insights of Electrical Aging in PZT Thin Films as Revealed by In Situ Biasing X-ray Diffraction,” *Materials*, vol. 14, no. 16, Art. no. 16, Jan. 2021, doi: 10.3390/ma14164500.

Chapter III. Macroscopic behavior of PZT thin films under external electric field

Introduction

The third chapter of this manuscript is dedicated to the macroscopic behavior of PZT thin films under applied electric field. This chapter starts with the introduction of the sample preparation by sol-gel technique and the investigation of the composition gradient along the thickness of the sample by nano diffraction technique. Afterwards, some results from the morphological investigation by SEM, TEM and precession electron diffraction technique are presented. Then, the impact of the structural properties and the XRD peak profile will be discussed, from both simulation and experimental point of view. In this part, the choice of the XRD configuration for the laboratory source is also explained.

Next, the study of the functional and structural properties relation will be showed. Firstly, the impact of thickness and preferred crystallographic orientation, so-called texture, on the ferroelectric and piezoelectric performance of the sample will be analyzed by comparing the electrical parameters and the structural properties as well as the $d_{33,eff}$ between different samples of different thicknesses and textures. To extract these information, electrical measurements as well as in-situ biasing XRD experiments were carried out using laboratory and synchrotron sources. While the electrical measurement gives the polarization and the I-V curves, the in-situ biasing XRD experiment provides the structural properties and the strain-electric field (S-E) butterfly curve of each sample. The $d_{33,eff}$ of each sample is then deduced by doing the first-order fitting along the slope of the curve.

Then, we studied the impact of AC field cycling on the structural properties of the sample by investigating the XRD peak obtained after each cycling point between 1 and 10^8 cycles. Next, we discussed the evolution of the macroscopic $d_{33,eff}$ of PZT as a function of aging. To extract this information, the in-situ biasing XRD experiment was performed (using synchrotron source) alternatively with the application of high-frequency AC electric field cycling with the number of cycle varying between 1 and 10^8 cycles. The center of gravity of each XRD peak of the triplet profile characteristic of PZT with MPB composition was first calculated in order to extract the macroscopic $d_{33,eff}$,. From this, the average strain generated by the sample could be calculated and the average S-E curve of the sample was deduced, allowing the calculation of the averaged $d_{33,eff}$. Then, the evolution of $d_{33,eff}$ is coupled with the polarization evolution, which helps drawing the impact of aging effect on the piezoelectric and ferroelectric properties of the sample. Finally, the S-E butterfly curves corresponding to each domain variant was obtained from the 3-peak fitting of the XRD peaks after each step of cycling, . The analysis of the evolution of these S-E curves under AC field cycling enable to quantify the impact of AC cycling on each the behavior of each domain variant.

1. Sample preparation procedure developed at the CEA-LETI

At the CEA-LETI, the PZT films are fabricated on 200 mm substrates. Firstly, a thermal oxide layer of 500 nm is grown on a Silicon (Si) substrate at a temperature of 1100°C in the presence of oxygen and steam for passivation. Then, a 10 nm layer of titanium oxide (TiO_2) is deposited by Physical Vapor Deposition (PVD) sputtering to ensure a good adhesion of the Platinum (Pt) bottom electrode and to prevent the diffusion of lead. The PVD deposition is followed by a thermal annealing at 700°C in oxygen to obtain a 20 nm-thick layer of TiO_2. Afterwards, the Pt is deposited by sputtering at 450°C, which promotes the (111) Pt orientation and tensile stress in Pt film. After that, the PZT film can be deposited.

The raw material for the PZT sol-gel deposition process is a mixture of partially hydrolyzed metallic precursors, so-called sol, in a solution containing solvents. This metal-organic solution has a specific composition which gives the desired morphotropic composition of PZT which is 52% or Zr and 48% of Ti. Concerning the deposition process, firstly, the PZT solution is dropped on the 200 mm platinized Si wafer. The wafer is then spun at a rotation speed of 1000 rpm to disperse the solution uniformly. As the solution is in contact with the water present in air, the sol hydrolyses and become gel.

After the spin-coating step, the wafer is dried on a hot plate at 130°C during 5 minutes. This step allows the elimination of residual solvents within the gel by evaporation. Then, the calcination (or pyrolysis) is performed at 360°C during 6 minutes, in order to get rid of solvents and organic compounds which did not evaporate during drying. After calcination, the deposition process of PZT layer can be reproduced until three layers are deposited. The first layer is an exception as it acts as a seed layer for the growth along the (100) direction of the other layers. However, after calcination, the PZT film is still in an amorphous state. In order to crystallize the film into perovskite phase, a Rapid Thermal Annealing (RTA) step is performed at 700°C during 1 minute under oxygen. Once the layers are crystallized, the whole process is repeated until the desired thickness is reached. In this work, the PZT samples with three different thickness are used: 0.5 µm, 1 µm and 2 µm. The process of elaboration of PZT films by sol-gel route is shown in Figure 3.1.

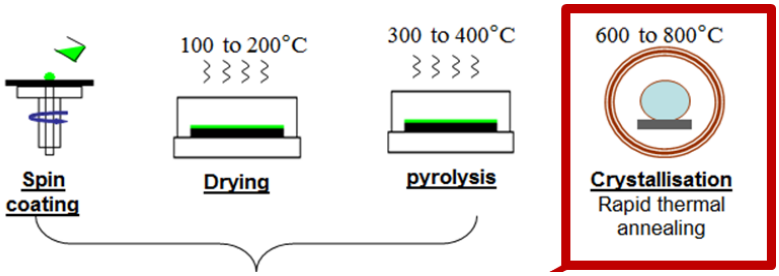

Figure 3.1: The sol-gel process for PZT thin films deposition developed in CEA-LETI. The crystallization by RTA is performed every six deposited layers

Finally, the top electrode of Ruthenium (Ru) is deposited by PVD sputtering at room temperature. In order to perform the electric, piezoelectric measurements and in situ biasing XRD, the patterning of Ru and PZT films is required. The patterning is done by photolithography. To do so, a photoresist is deposited on the Ru top electrode before being exposed to UV light through a mask containing the desired pattern. As a result, the part of the resist protected by the mask stays on the Ru while the exposed resist is dissolved, thus leaving the Ru film unprotected. The wafer is then wet-etched with sodium hypochloride (NaOCl) to remove the unprotected Ru and the resist. The patterned Ru will then act as a hard-mask for the underneath PZT film. Consequently, PZT is etched with a solution containing hydrochloric acid (HCl) and water. Once the PZT film is etched, Ru can be patterned and etched again in order to obtain a more proper design. A summary the total deposition steps can be found in Figure 3.2.

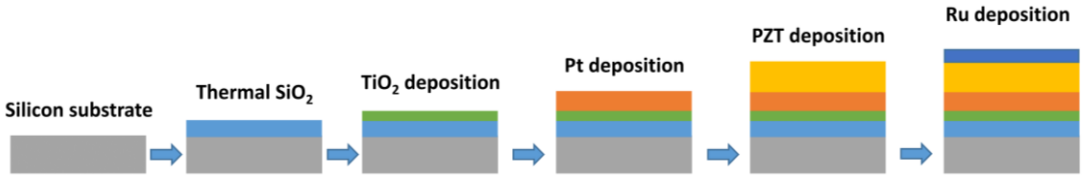

Figure 3.2: Summary of the elaboration process of PZT thin films

In CEA-LETI, three different precursors with three different Zr/Ti ratios are available, respectively 59/41, 52/48 and 43/57. Different combinations of different precursors will lead to presence of different structures and properties. The combinations used in CEA-LETI is summarized in the following table 3-1. For the ease of understanding, the precursors of Zr/Ti ratios of 59/41, 52/48 and 43/57 are named A, B and C, respectively.

Table 3-1: The denomination of different sample in this manuscript and their respective deposition sequence

Sample name in the manuscript	**Deposition sequence**
PZT P4mm	CCC, RTA each 3 layers
PZT R3m	AAA, RTA each 3 layers
PZT MPB standard	BBBBBB, RTA each 6 layers
PZT gradient free	AABBCC, RTA each 6 layers
PZT amplified gradient	CCBBAA, RTA each 6 layers
PZT with La-doping (PLZT)	La = 2.5% BBB, RTA each 3 layers
PZT with Nb-doping (PNZT)	Nb = 2 % BBB, RTA each 3 layers

During the fabrication process, a gradient of Zr/Ti ratio through the film thickness is appearing due to thermodynamic and kinetic effects. In order to study in detail this problem, nano diffraction technique has been employed by N. Vaxelaire et al. [77]. In this article, an x-ray beam of 100nm was used to study heterogeneities of the chemical composition as well as the electric and piezoelectric properties of the PZT thin films of gradient free (GF) and amplified gradient (AG). The evolution of the composition along the thickness of the sample is shown in Figure 3.3. The GF sample has an average 47.6% of tetragonal crystals and 52.4% of rhombohedral crystals and the AG sample contains an average of 37.2% tetragonal crystals and 62.8% rhombohedral crystals. As a result, the phase composition of GF sample corresponds to the MPB composition, which is 48% of Ti and 52% of Zr.

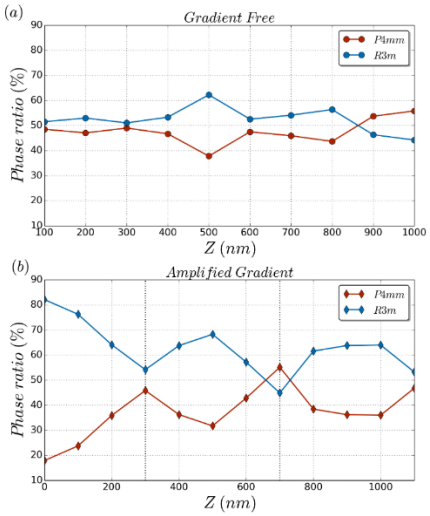

Figure 3.3: Typical in-depth phase gradient found for a MPB (a) gradient free and (b) amplified gradient. The Ru top electrode is on the left while the Pt bottom electrode is on the right hand side of the depicted profile [1].

In the case of GF sample (Figure 3.3(a)), it can be seen that near the bottom electrode, close to Z=1000 nm, the P4mm phase dominates, which could be due to the lower enthalpy of formation of the $PbTiO_3$ with respect to $PbZrO_3$. However, when Zr is in excess, the formation of R3m is energetically favourable, which consumes more Zr. Progressively, a Ti excess occurs, making the P4mm phase more favourable, leading to the in-depth gradient observed in the amplified gradient sample. In general, the GF sample has almost 5% of residual heterogeneities while the AG one has 9.6% of fluctuations.

2. Morphological aspect

The morphology of the films from the top and cross-sectional views are visualized by Scanning and Transmission Electron Microscopy (SEM and TEM, respectively) techniques. The SEM top view of the PZT film before the deposition of Ru top electrode is shown in Figure 3.4, which shows a grain size around 200 nm. In order to study the local microstructure of the films, TEM and precession electron diffraction techniques are used.

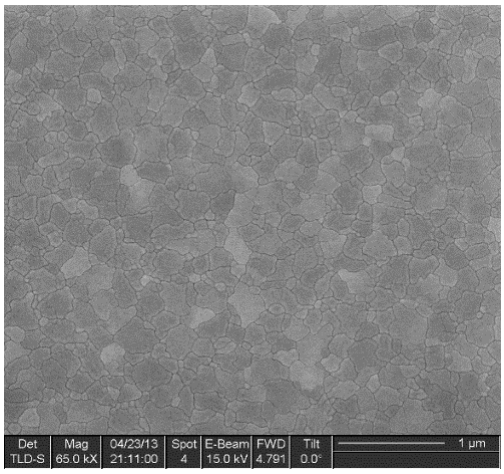

Figure 3.4: SEM top view of PZT layer prior to deposition of the top electrode

Figure 3.5(a) illustrates the cross-sectional TEM image in bright field mode of the PZT films after RTA. It was shown that the grains have a lamella shape. Furthermore, the TEM image also shows the interfaces between different layers of RTA crystallisation. From this image, one can see that the grain boundaries are continuous from one layer to another, indicating that the orientation is continuous through the RTA interface. To investigate the local microstructure of the film, precession electron

diffraction was performed on PZT lamella. Figure 3.5(b) illustrates the orientation distribution according to the z-axis and the corresponding pole figure is shown in the inset. It was observed that the PZT lamella were mainly oriented along the out-of-plane orientation (100), which confirms the (100)-fiber texture of PZT.

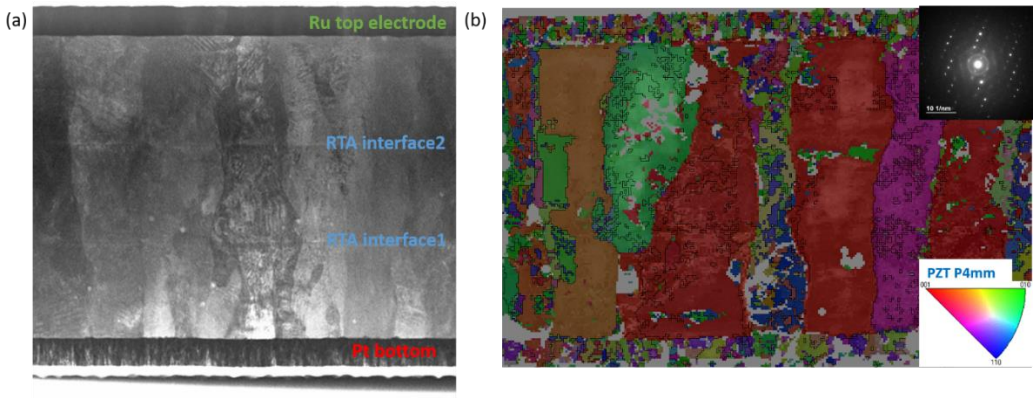

Figure 3.5: (a) cross sectional TEM bright field mode. (b) Precession map where diffraction patterns (see an example in inset) is indexed in tetragonal phase. Orientation continuity through RTA interface is confirmed.

3. PZT and peak profiles

3.1. XRD peak simulation

In this part, the simulation of the (200) peak profile of a pseudo-cubic phase for P4mm tetragonal and a R3c rhombohedral space group at different crystallite size (denoted L*) is performed at the energy of 8 keV based on the Debye-Scherrer formula. The reason why the (200) peak attracts our interest lies in the fact that our sample has a (100) textured. As a result, beside the (200) peak, we could also achieve the (100) and (400) peaks in the diffractograms. While the (100) peak gives better intensity at the expense of lower peaks separation, the (400) peak has the reversed property. As a result, the choice of (200) peak gives the best compromise in term of peak separation and intensity.

In the algorithm used for the simulation, firstly, the FWHM of the peaks are deduced from the crystallite size and the d-spacing, which is taken from the Power Diffraction File (PDF) references of PZT for P4mm [78] and R3c [79] space groups. The amplitude of the peaks from the PDF files was multiplied by the ratio of the P4mm/R3m phases, set to 0.5 in this case. After that, each profile of the (200) pseudo-cubic peak is calculated using a pseudo-Voigt model. Each peak of the triplet is then summed to get the full peak profile. The principle of the algorithm is summarized in Figure 3.6.

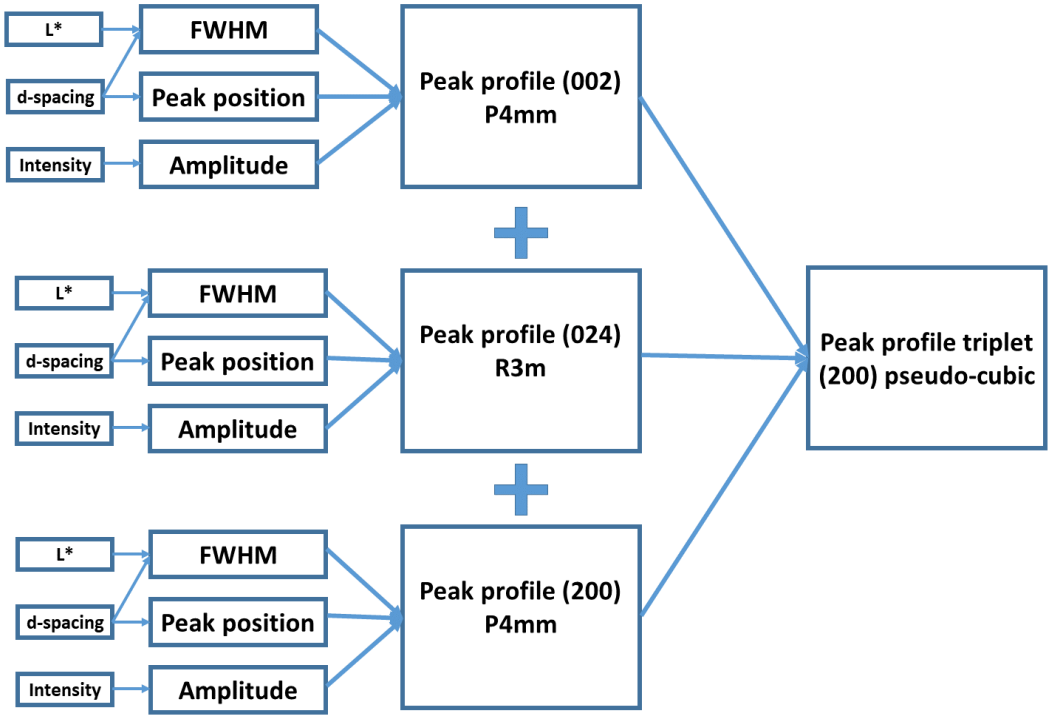

Figure 3.6: A block map demonstrating the principle of the algorithm for simulating the (200) pseudo-cubic peak profile

In this case, as the coherence length of the beam is in the range of 50 – 100 nm in transversal and 1 µm in longitudinal orientations, the nanodomains are diffracting coherently, as a result, the XRD peaks correspond to the mixture of large and fine domains. It is seen from Figure 3.7(a) that with domain size of 500 nm, the (200) pseudo-cubic phase is finely separated into three peaks, corresponding to the (002) and (200) reflection of P4mm phase at 42.6 and 43.6° and (024) reflection of R3c phase at 43.3°. It is also observed that as the size of domains decreases, the peak separation decreases due to the broadening of each peak. From 20 nm domain size illustrated on Figure 3.7(c), the three peaks are no longer separated but merged into a single peak with shoulders at low and high-angle sides (with 5 nm domain size on Figure 3.7(f)), the shoulders can hardly be seen). In reality, if the size of domain is in the range of 10 – 50 nm, the peaks are not well separated, leading to difficulty in fitting the peaks to obtain structural information. One solution is to increase the counting time of XRD experiment. However, for in situ biasing experiment, this also means increasing the electric field application time, which might lead to the breakdown of the sample. As a result, the counting time is a compromise between the photon flux and the breakdown time of the sample.

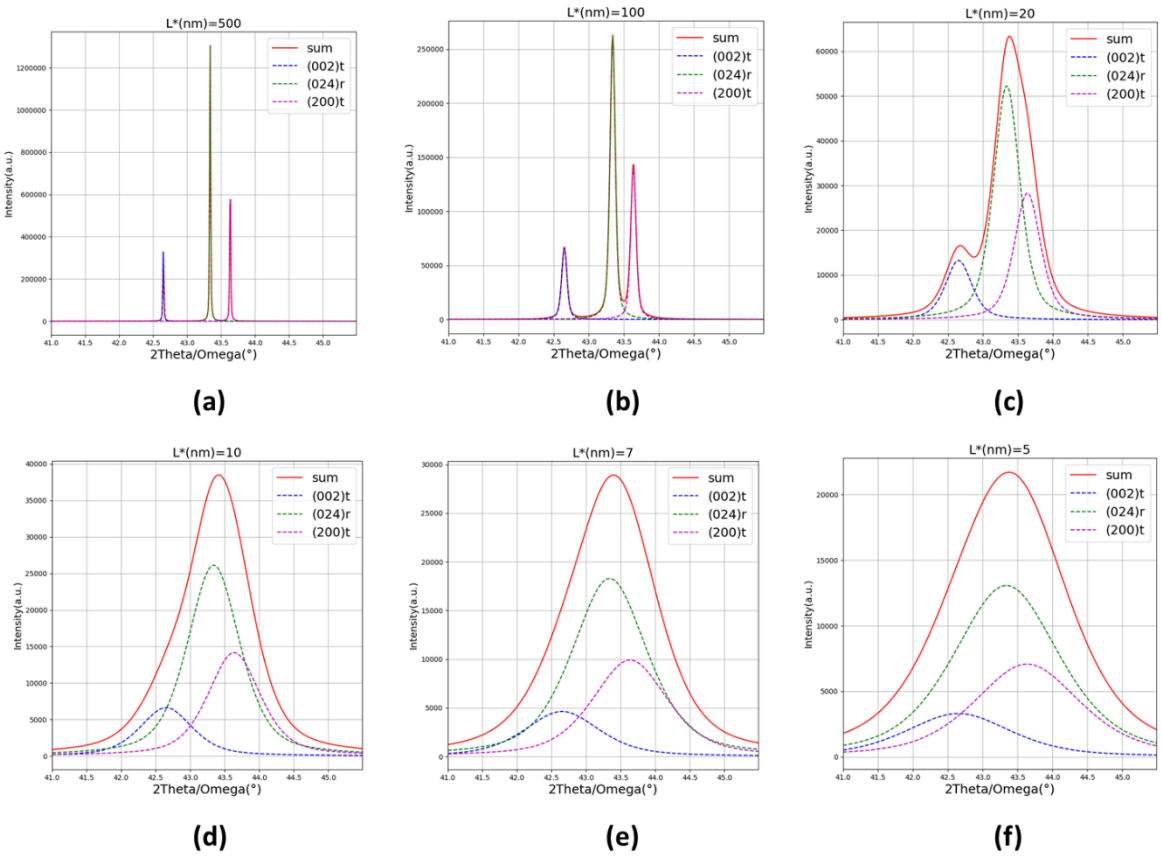

Figure 3.7: Examples of (200) pseudo-cubic phase for P4mm and R3m for coherent diffraction domain (CDD with the domain size of (a) 500, (b) 100, (c) 20, (d) 10, (e) 7 and (f) 5 nm at E = 8 keV

3.2. Experimental study

3.2.1. The variation of XRD profile at different composition of PZT

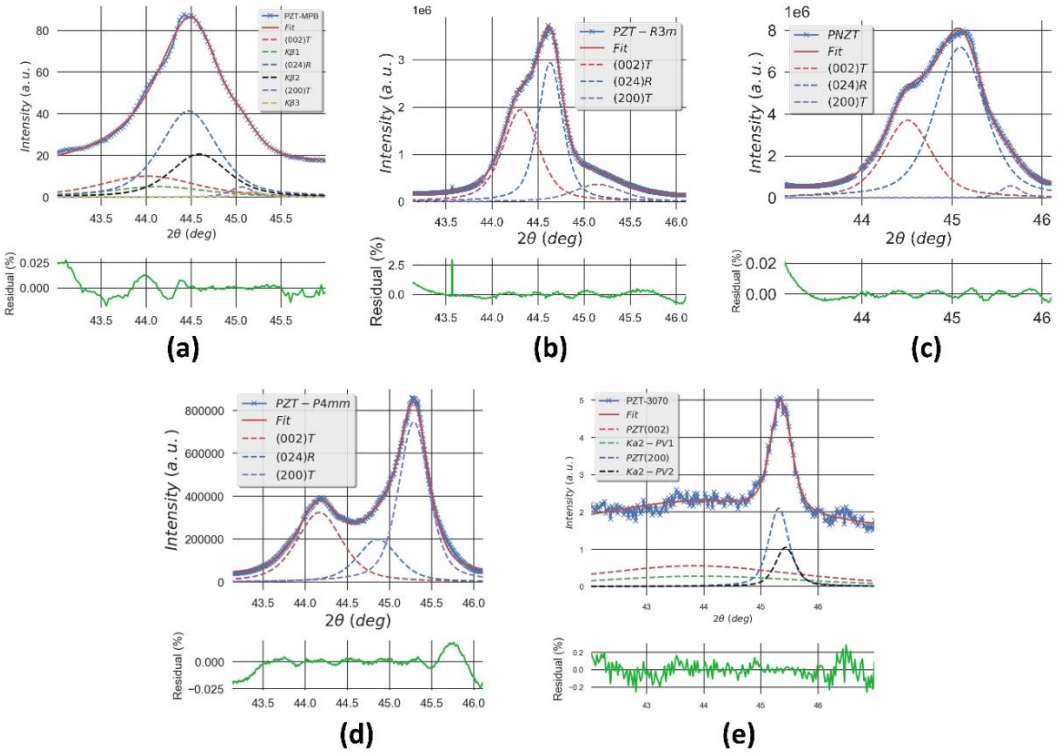

Figure 3.8: (200) XRD peak profile of different variants of PZT (a) PZT MPB standard, (b) PZT MPB with R3m space group (rhombohedral), (c) PZT with Nb doping, (d) PZT P4mm with Zr/Ti ratio of 43/57 and (e) PZT with Zr/Ti ratio of 30/70

Figure 3.8 illustrates the XRD peak profiles of different variants of PZT obtained by laboratory using Bragg-Brentano configuration (Figure 3.8(a) and (e)) and synchrotron sources Figure 3.8((b), (c) and (d)). In these figures, the fittings of the peaks are also shown, which is achieved by setting the initial values for the three main parameters of the fit: peak intensity, peak position and FWHM. From Figure 3.8(a), (b) and (c), it can be seen that the peak profiles are almost identical for the PZT MPB standard, the PZT MPB with R3m space group and the PZT with Nb doping. The main peak at ~44.5 degrees is corresponding to the (024)R phase while the two shoulders on both side can be attributed to the (002)T and (200)T phases. However, for the sample PZT P4mm with Zr/Ti ratios of 43/57 and 30/70, the peak profiles are significantly different, as shown on Figure 3.8(d) and (e). For the sample with a Zr/Ti ratio of 43/57 as illustrated Figure 3.8(d), it means that the composition lies more in the tetragonal region of the phase diagram. As a result, the dominant peak is no longer the (024)R but the one corresponding to the tetragonal phase (200T) and the lower-angle shoulder could be attributed to the (024)R phase. The existence of (024)R phase could be due to the existence of the Zr/Ti ratio gradient along the thickness of the sample. For the sample with a Zr/Ti ratio of 30/70 (Figure 3.8(e)), the composition is positioned deeper in the tetragonal region in the phase diagram, as a result, no contribution from rhombohedral is found, and it is only possible to fit on two peaks, corresponding to the (200) and (002) reflections of the tetragonal phase.

4. The impact of thickness on the macroscopic properties of PZT with MPB composition

The scaling down of ferroelectric devices requires a better understanding of the influence of thickness on the ferroelectricity. This allows to have a better control over the device performance and to reveal

the underlying physical origin of these phenomena [81]. In this thesis, the impact of the thickness on the electrical properties of PZT thin films with MPB composition was studied by performing PUND measurements with the ferroelectric tester TF2000 from Aixaact®. To investigate the impact of thickness on the electrical properties, the measurements were carried out on three samples of PZT with thicknesses of 0.55, 1.0 and 2.0 µm. The polarization curves, the remnant polarization and the coercive field corresponding to the three samples are shown below. From Figure 3.9(a), it can be seen that for all the thicknesses, a hysteresis polarization loop is always achieved, indicating the ferroelectricity of the samples. However, significant variation can be observed for the three samples indicating that the film properties are not the same. Therefore, it reveals the impact of the thickness variation on the ferroelectricity properties.

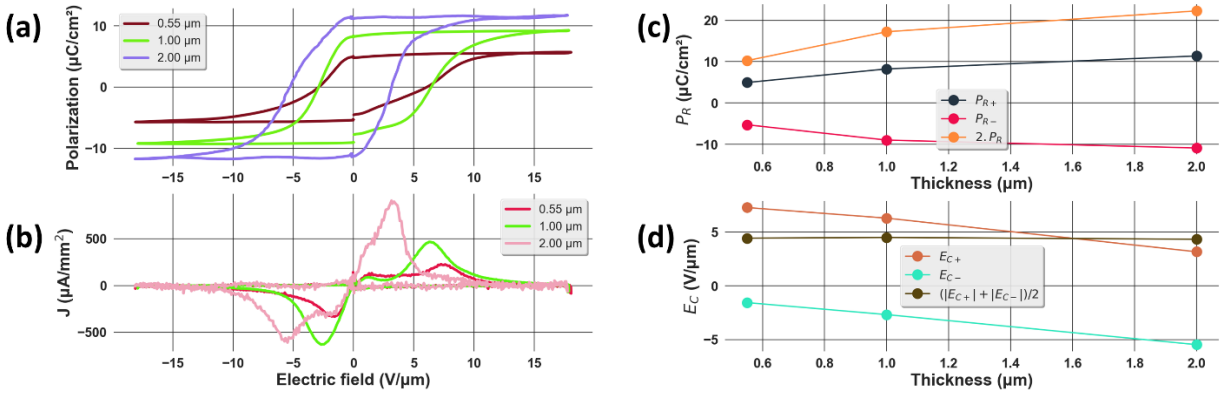

Figure 3.9: the evolution of the (a) polarization curve, (b) current density vs electric field (J-E), (c) polarization remnant and (d) coercive field of PZT films as a function of the thickness

Figure 3.9(b) shows the current density vs applied field (J-E) curve. Firstly, in all of the curves, beside the main peaks due to domain switching, secondary peak close to zero field can be observed. These peaks are attributed to the existence of non-ferroelectric phase in the sample [82]. Regarding the main peaks corresponding to the domain switching effect, the peak amplitude increases with the thickness. This leads to an increase in the polarization as a function of thickness, which is illustrated by the increase in the remnant polarization. From Figure 3.9(c), it can be seen that there is an increase in the total polarization remnant, representing by the increase in $2.P_R$ ($2.P_R = P_{R+} - P_{R-}$) by 117.7% ($2.P_R$ (0.5 µm) = 10.2 µC/cm^2, $2.P_R$ (1 µm) = 17.2 µC/cm^2 and $2.P_R$ (2 µm) = 22.2 µC/cm^2). This increase in remnant polarization is coherent with the results reported in the article by Podgorny et al. [83], where an increase in the remnant polarization as a function of thickness was also observed in PZT films with MPB composition. This observation could be due to two reasons: firstly, the ferroelectricity is a result of a collaborative effect of many dipoles in the sample. As a result, a decrease in the size of the sample could lead to the decrease in the ferroelectric polarization [81]. Secondly, as mentioned in Chapter I.3.2, near the electrode, there might exist a layer with properties different from the rest of the film. This surface layer might screen from the film from the applied field. This might lead to an inhomogeneity over the thickness of the sample and this inhomogeneity becomes more important as the thickness of the sample decreases [66].

Concerning the coercive field, as shown in Figure 3.9(d), the average value, calculated by $(|E_{C+}| + |E_{C-}|)/2$, does not change as a function of thickness (4.4 V/µm). However, a remarkable difference between $|E_{C+}|$ and $|E_{C-}|$ is seen (ΔE_C (0.5 µm) = 5.7 V/µm, ΔE_C (1 µm) = 3.6 V/µm and ΔE_C (2 µm) = -2.3 V/µm with $\Delta E_C = |E_{C+}| - |E_{C-}|$), indicating a strong imprint effect in the sample. This could be due to the existence of charged defects in the sample, leading to the pinning of the ferroelectric domains. By comparing the imprint at different thicknesses, it could be seen that ΔE_C is highest for the sample with a 0.5 µm thickness and that ΔE_C decreases gradually as the thickness increases. Furthermore, as the thickness of the sample increases, the sign of ΔE_C changes from positive to negative, indicating a change of the preferred polarization orientation from negative to positive. In conclusion, when

increasing the thickness of the film, the most important observation is the increase in the polarization. This can be understood as a consequence of the increase in the amount of dipoles as well as the decrease of the inhomogeneity of the sample under applied field.

5. The impact of texture on the macroscopic properties of PZT with MPB composition

The piezo- and ferroelectric properties also exhibit the anisotropy of the atomic structure and as a result, the properties could be optimized by growing the sample in a specific orientation [84]. In this thesis, the impact of texture on the properties of PZT films has been investigated by performing the electrical measurement on two samples of PZT with different preferred orientations: (100) and (111) of the same thickness. The diffractograms of the two sample are shown in Figure 3.10, which Reflected the intense PZT (111) peak (top) and PZT (100) peak (bottom). They correspond to a texture degree of ~ 85% for the (111) peak and 79% for the (100) peak, thus confirming the texture of the sample.

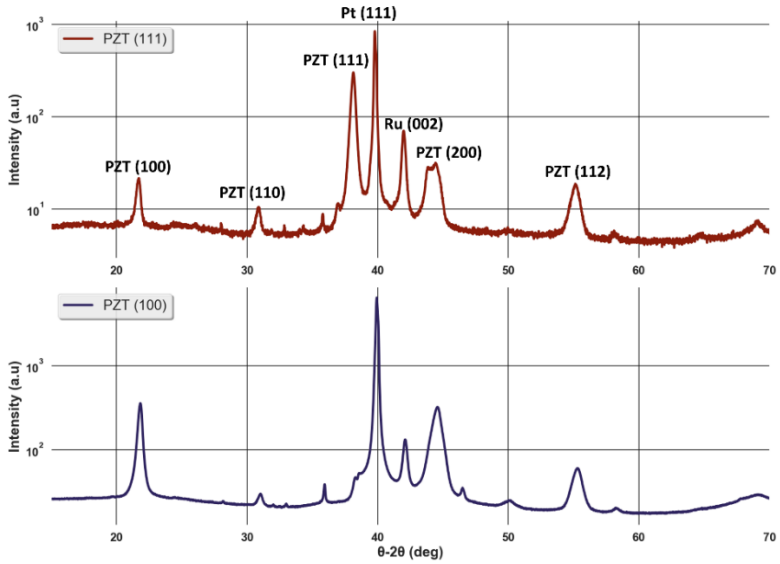

Figure 3.10: the theta-2theta diffractogram of (top) PZT (111) and (bottom) PZT (100) of MPB composition measured by laboratory XRD equipment in Bragg-Brentano configuration

The P-E loop of the two samples where measured using the PUND technique on the ferroelectric analyzer and the results are shown in Figure 3.11. It can be seen that the polarization is higher in (111) textured sample (P_R = 22 vs 16 µC/cm^2). The P-E loop of (100) sample is slightly tilted in comparison with that of (111) sample.

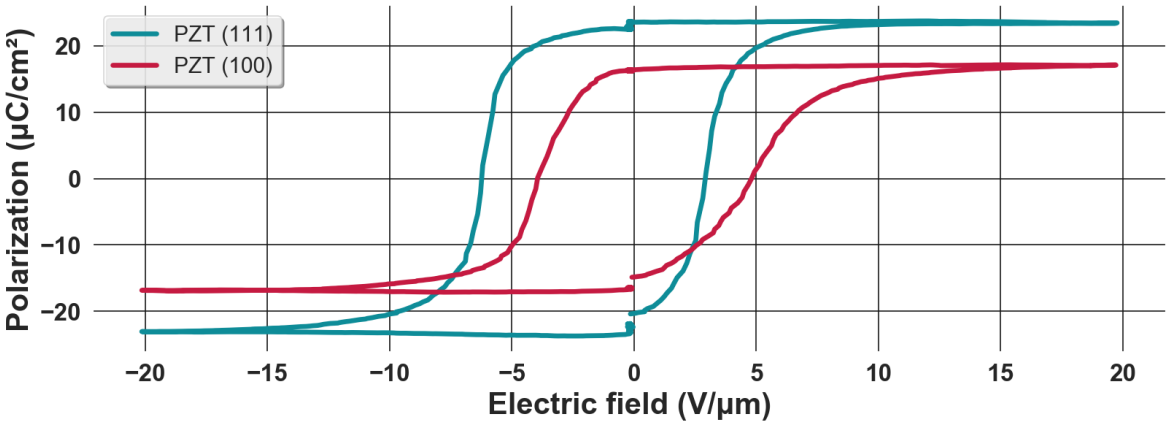

Figure 3.11: the evolution of the polarization of PZT films as a function of the texture

Concerning the (100) textured films, the polarization direction 1 (as shown in Figure 3.12 (a)) is parallel to the applied field direction, which is normal to the sample surface and direction 6 is its reverse equivalent. The directions 2, 3, 4 and 5 are perpendicular to the field direction and lies within the film plane. When the field direction is reversed from upward to downward, domains along direction 1 will be reversed first as they coincide with the applied field orientation. Concerning the domains along 2, 3, 4 and 5 directions, their switching requires 90° domain switching as they are perpendicular to the applied field. The 90° domain switching requires higher electric fields and possibly compressive stresses in the films parallel to the film surface due to small lattice mismatches with the surface. As a result, the P-E curve of (100) textured sample is slightly tilted and the remnant polarization is lower [85]. In (111) textured film, the polarization directions 1, 2 and 3 make an angle of 54.7° away from the applied field direction, which is perpendicular to the sample surface, and the directions 4, 5 and 6 are their reverse equivalent as illustrated in Figure 3.12(b). Therefore, remnant polarization of (111) textured films are expected to be higher than the (100)/(001) textured films. Furthermore, when the domains are switched from upward to downward, the domains along 1, 2 and 3 are switched simultaneously to 4, 5 and 6. This leads to an abrupt change in the domain reversal segment of the P-E hysteresis curves, thus the P-E curve is more squared [85].

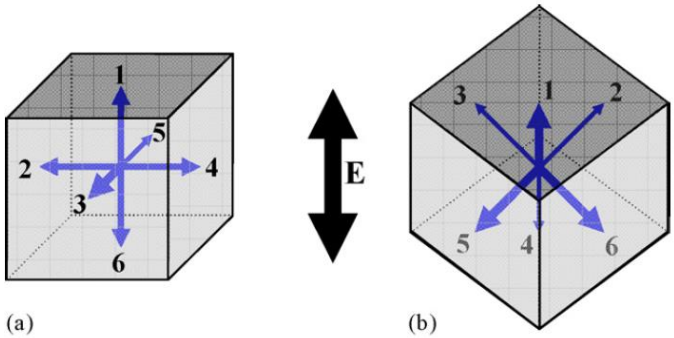

Figure 3.12: Possible spontaneous polarization directions for PZT films with (a) (100)/(001) and (b) (111) texture of tetragonal structure [85]

Beside the electrical properties, the structural and mechanical properties of the two samples have also been studied by in-situ biasing XRD. The experimental setup is described in Chapter II.4. The two most intense peaks, corresponding to the preferred orientations of each sample: (111) and (200) peaks, are chosen to investigate the structural evolution under applied field as well as the $d_{33,eff}$. The (111) peak was measured with a laboratory equipment (Empyrean©, Malvern Panalytical) while the (200) peak was obtained with a synchrotron source using an energy of 10.37 keV. As mentioned in Chapter II.4, the diffraction signal is captured by a 2D detector for the synchrotron experiment. As a result, a 2D image is recorded with the full Debye ring. In order to extract the information about the sample, the 2D image is converted to a 1D profile by Azimuthal integration, shown in Figure 3.13(b).

For the (111) peak, due to the existence of only a single peak without overlapping, the refinement using a single peak profile based on Pseudo-Voigt model is sufficient to extract the structural properties as illustrated in Figure 3.13(a). For the case of (200) peak, because of the overlapping between the (024) peak of rhombohedral phase and the two peaks (002) and (200) of tetragonal phase, the triplet profile refinement has been done as shown in Figure 3.13(b) using the least-square minimization technique.

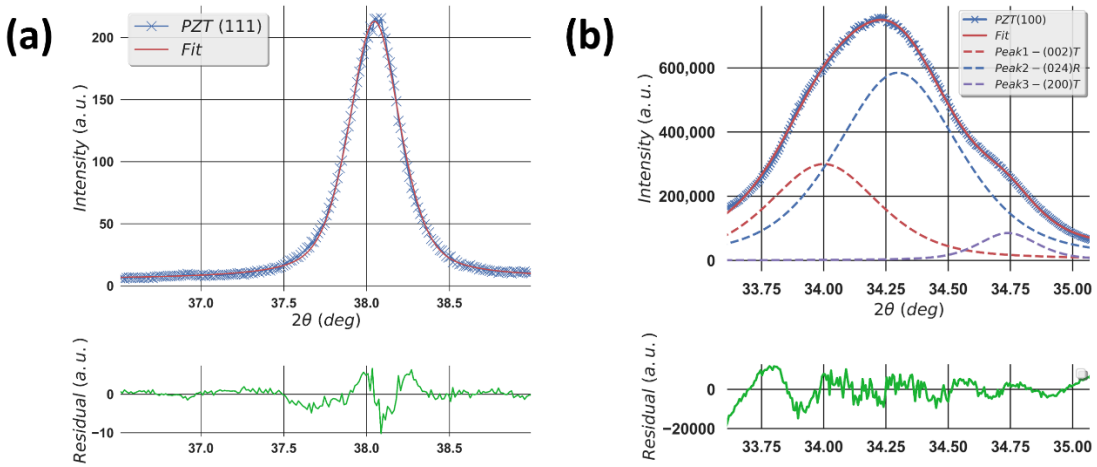

Figure 3.13: Refinement of the (a) PZT (111) peak and (b) PZT (200) peak

From the fitting results, different parameters about the peaks were extracted such as the peak intensity, full width half maximum (FWHM), integrated intensity and the peak position. The evolution of these parameters as a function of applied field for the PZT (111) peak is shown in Figure 3.14.

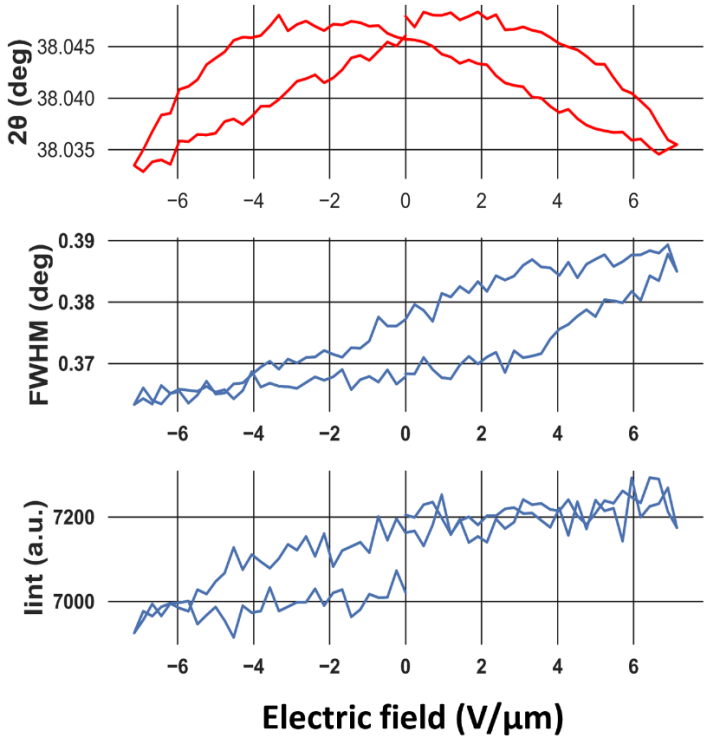

Figure 3.14: Evolution of (from top to bottom) peak position, FWHM and integrated intensity of PZT (111) peak as a function of applied field

It can be seen that variation the peak position exhibits a butterfly behavior, which can be latter transferred into the butterfly behavior of the strain as a function of electric field as illustrated below in Figure 3.16(a). This is the signature of the ferroelectricity in the sample. Considering the FWHM and the integrated intensity of the peak, these parameters tend to reach a maximum and a minimum at the positive and the negative maximum field, respectively. Therefore, the maximum and minimum values of the size of domains and the proportion of (111) phase is reached at the maximum positive and negative field, respectively. Considering the PZT (200) peak, due to the 3-peak fitting, the parameters from the peaks (024) rhombohedral, (002) and (200) tetragonal – corresponding to the r-, c- and a-domain were extracted and presented in Figure 3.15(a), (b) and (c).

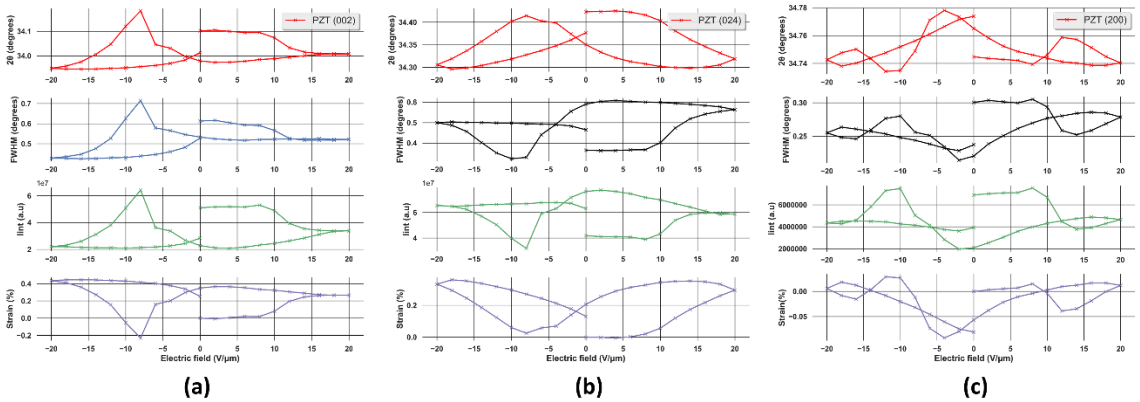

Figure 3.15: The evolution of (from top to bottom) peak position, FWHM, integrated intensity and strain of (a) (002)T phase, (b) (024)R phase and (c) (200)T phase as a function of applied field

Unlike the case of the peak PZT (111), the butterfly behavior is achieved even for FWHM and integrated intensity of (002) and (024) peaks. For the (200) peak, it is less evident and likely due to the weaker intensity of the peak. By analyzing the integrated intensity, it can be seen that at high electric field, the intensity of the(024) peak increases while intensities of (002) and (200) peaks reduce, indicating the transformation from tetragonal to rhombohedral phases, which is coherent with the results reported in [48]. Furthermore, from the evolution of strain in each phase, it is possible to deduce the average strain generated by the peak (200) by calculating the center of gravity of the peak as following:

$$\text{Center of gravity} = \frac{I_{int002}2\theta_{002} + Iint_{024}2\theta_{024} + Iint_{200}2\theta_{200}}{Iint_{002} + Iint_{024} + I_{int200}} \qquad (3.1)$$

where $Iint_{hkl}$ is the integrated intensity and $2\theta_{hkl}$ is the peak position of a specific atomic plane *(hkl)* in 2θ, or domain variant in the sample. From this, the d-spacing corresponding to the center of gravity could be deduced through the Bragg's law and the average strain could be calculated using the formula illustrated in Chapter II. 1.4.3. As a result, the S-E curve corresponding to the center of gravity of the (200) peak is obtained as shown in Figure 3.16(b). With the first-order fitting along the slope of the S-E curve, the $d_{33,eff}$ was calculated and found to be ~ **42.3 ± 1 pm/V** and **81.7 ± 2 pm/V** for (111) and (200) peaks, respectively, indicating that the piezoelectric property is better for (100) textured sample.

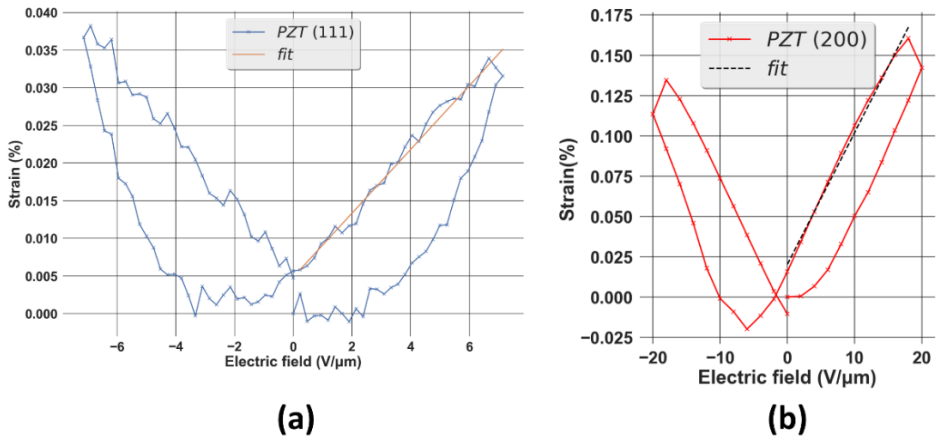

Figure 3.16: the S-E curves and first-order fitting of (a) (111) and (b) (200) peaks in the sample of PZT with (111) and (100) texture, respectively

6. The impact of AC field cycling on the macroscopic properties of PZT

6.1. Materials and method

A prototypical 0.5 µm thick $PbZr_{0.52}Ti_{0.48}O_3$ thin film was studied. Its fabrication process was mentioned earlier in this chapter. Electrical measurement was performed on the sample thanks to a 1x1mm^2 top electrode. Preliminary characterization by laboratory XRD using an energy of 8.05 keV indicates that the sample has a strong preferred (100) pseudo-cubic out of plane orientation as shown in Figure 3.17.

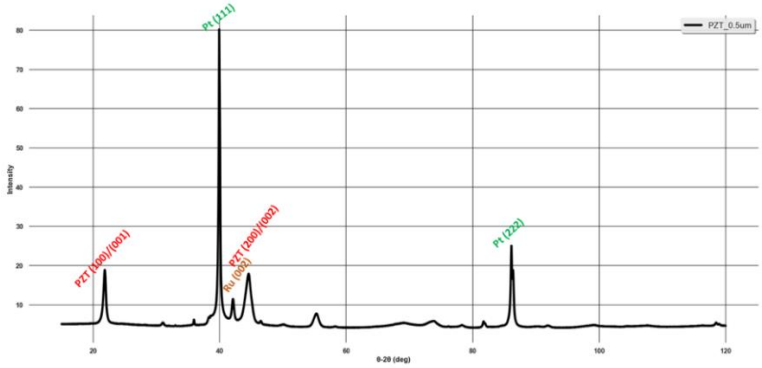

Figure 3.17: XRD diffractogram of the sample PZT with MPB composition

The experiment of the impact of AC field cycling was performed in ESRF and the procedure is illustrated in Figure 3.18. Firstly, the high frequency cycling was performed with a triangular waveform between ± 10V on the sample using an Arbitrary Functional Generator (Tektronix AFG1000) at the frequency of 10 kHz. After that, the polarization was measured using the PUND method by the Source-Measure Unit (SMU). Next, the in-situ biasing XRD was performed. Finally, the polarization was obtained using the PUND method to follow the change in the polarization before and after the in-situ biasing XRD. This procedure was repeated while varying the number of cycles between 1 and 10^8.

Using a 100x100-µm^2 beam monochromatized to an energy of 10.37 keV, the in-situ X-ray diffraction experiment was conducted at the ESRF using a 2D detector as indicated in Chapter II.4. After that, a 1D spectrum was created by integrating the measured Debye rings. The strong flux at the beamline allowed a good peak intensity with only a counting time of one second. The PZT's (200) pseudo-cubic peak was measured in a symmetrical coplanar arrangement (i.e. the observed domains are oriented in the direction of electric field). The electric field was applied between ±20V/µm by the step of ±2 V/µm. For each step of biasing, an XRD diagram is recorded. The control of the applied voltage as well as the duration of the pulse were done with a Python script and the duration of the pulse matched exactly the acquisition time of a single XRD scan. Considering the camera read-out, the in-situ cycle frequency was performed at approximatively 10 mHz.

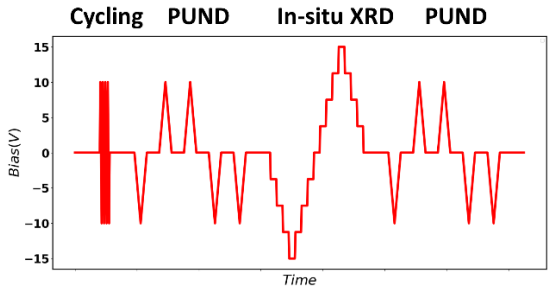

Figure 3.18: The procedure of the experiment

6.2. The evolution of structural properties of PZT due to AC field cycling

In order to evaluate the impact of AC field cycling on the structural properties, the first XRD peak of the in-situ biasing XRD scan at 0V is studied. By doing the fitting on the XRD peak profiles, we are able to deduce the full width half maximum (FWHM), the position and the surface area (or integrated intensity) of the peak. The first parameter provides an estimation of the size of the domains whereas the third parameter shows the volume of various crystallographic phases in the direction of reflection. Even though no remarkable change in the peak position with respect to the number of cycles was seen (not shown here), the FWHM and surface area of the peak underwent substantial changes, as can be seen in Figure 3.19(a) and (b). The FWHM of the (002)T and (200)T phases decreased after the first cycle, which is consistent with an increase in domain size. This might be a result of the lattice's defects being eliminated. The accumulation of defects in ferroelectric materials may have an impact on domain size and domain wall motion [28]. Therefore, fewer defects would result in bigger domain sizes, which might be accompanied by a reduction in the FHWM. At the same time, an increase in the FWHM of the (024)R phase, corresponding to a decrease in the domain size, is observed. After this wake-up phase, while the FWHM of the (002)T and (024)R phases increase – corresponding to a decrease in the domain size, that of the (200)T phase decreases, indicating an increase in the domain size. Considering the surface area of the peak, after the first cycle, a strong increase in the (024)R was obtained along with the decrease for the tetragonal phases, showing that there is a phase transformation from tetragonal to rhombohedral. After that, while the surface area of (024)R varies slightly, a sharp decrease was seen for (200)T phase up to 10^8 cycles, illustrating a decrease in the volume of this phase. Considering the (002)T phase, it can be seen that its volume increases gradually after 10^2 cycles. A direct correlation to the total remanent $2.P_R$, which decreases from this point, is reported in Figure 3.19(c).

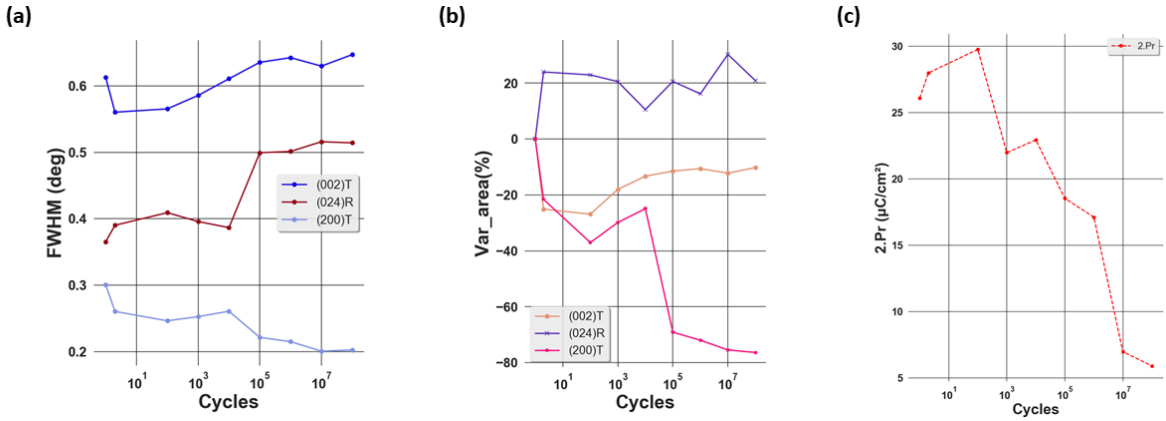

Figure 3.19: evolution of (a) FWHM, (b) surface area of the XRD peak of different phases and (c) the total remanent $2.P_R$ ($2.P_R = |P_{R+}| + |P_{R-}|$) as a function of electric cycling

6.3. Evolution of effective piezoelectric coefficient $d_{33,eff}$ as a function of cycling

Piezoelectric materials deforms under applied electric field, this phenomenon can be described from the microscopically point of view as a variation in the d-spacing of the material under external field. This deformation can be visualized by the shift of the XRD peak position since the d-spacing is related to the peak position 2θ through Bragg's law, which is mentioned in Chapter II.1.2.2. The shifting of the XRD peak is illustrated in Figure 3.20. From the change in the d-spacing of each domain variant, their respective strain can be calculated and thus, the S-E butterfly curve can be deduced.

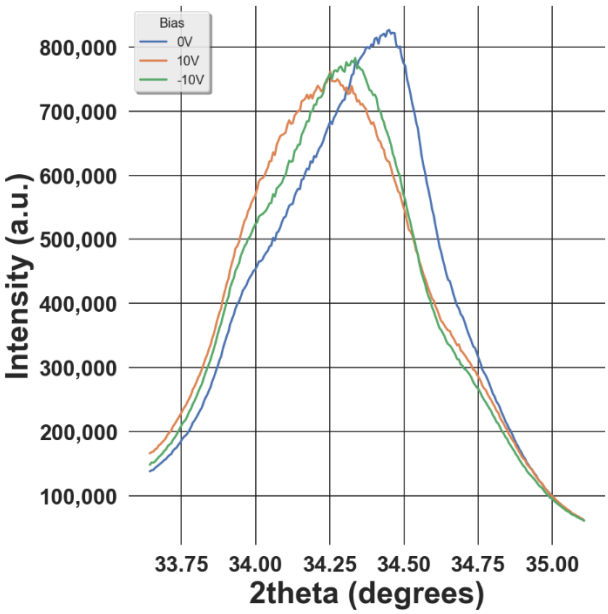

Figure 3.20: evolution of (200) PZT peak under applied bias measured by synchrotron X-ray source

The lifespan of the piezo/ferroelectric materials is crucial for technological applications. The stability of a piezoelectric material's performance after exposure to external factors is referred to as the reliability. The performance of piezoelectric materials may be impacted by a variety of elements during the course of their lifespan, including the formation of oxygen vacancies, domain wall pinning, or defects [86] [47]. As a result, numerous investigations have been carried out to better understand how piezo/ferroelectric materials aged.

In order to supplement electrical testing diagnostics, piezoresponse force microscopy (PFM) [87] [88] and double beam laser interferometer (DBLI) [89] [48] are used for the determination of the effective piezoelectric coefficient $d_{33,eff}$. These methods do have some drawbacks. The extraction of the effective $d_{33,eff}$ may contain artefacts due to the correlation of the $d_{33,eff}$ with the d_{15} coefficient (PFM) or the appearance of numerous noise sources (thermal drift, variations in optical characteristics, and electrical and mechanical instabilities) in the case of DBLI [90].

In addition to the ferroelectric measurement, this study investigates the reliability of a prototypical PZT thin film at the Morphotropic Phase Boundary (MPB) utilizing an in situ biasing X-ray diffraction (XRD) approach. Piezoelectric stability is measured by following the evolution of the effective piezoelectric coefficient $d_{33,eff}$, which is taken from the S-E curves. It is not the $d_{33,eff}$ of a single domain variant but the average $d_{33,eff}$ of the sample is taken into account, which is extracted from first-order fitting of the slope of the S-E curve of the average strain generated by the sample. The formula for the calculation of the average strain has been mentioned earlier in this chapter and the results are shown in Figure 3.21.

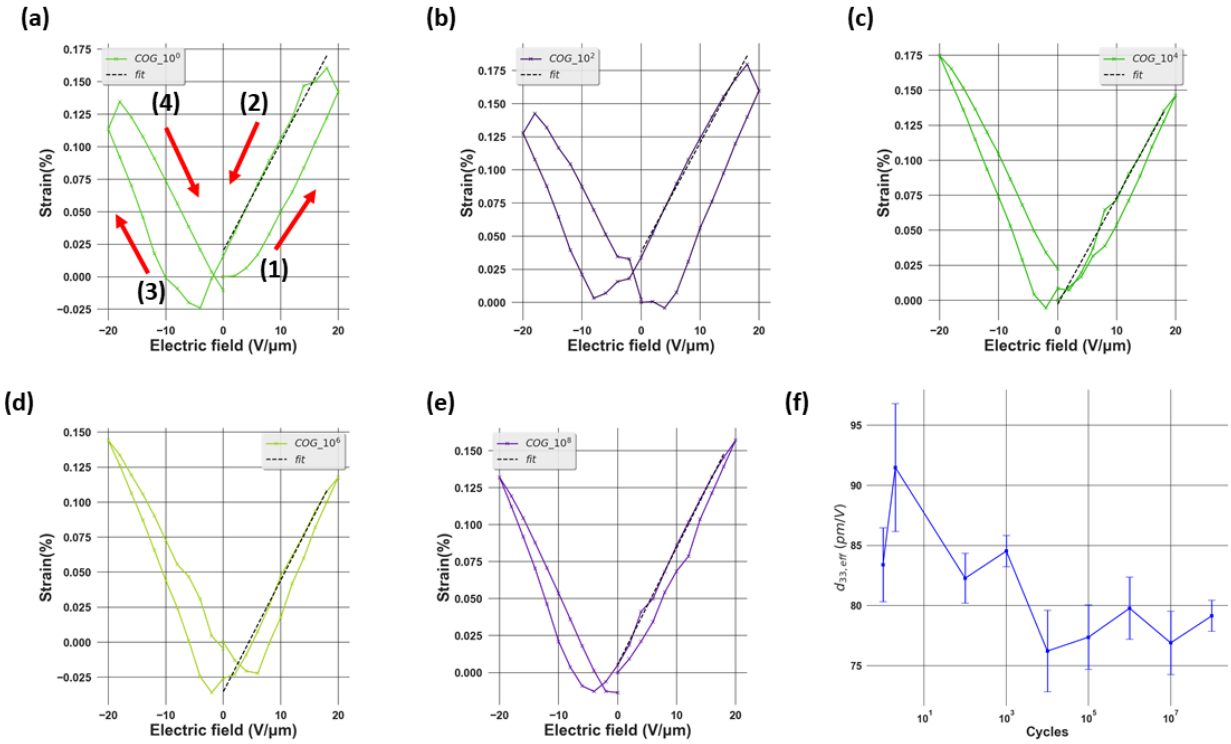

Figure 3.21: (a-e) the S-E curve at different number of electric field cycle with the first-order fitting for $d_{33,eff}$ calculation and (f) the variation of $d_{33,eff}$ as a function number of electric field cycle; the error bar indicates the error from doing the first-order fitting

The first feature seen when looking at Figure 3.21(a)-(e) is a rise in the S-E loop's asymmetry and the collapse of the right wing of the butterfly curve with increasing the number of cycling. The existence of an internal bias and the domain pinning effect can both be used to explain this [91]. The effective bias field of the sample, which is the superposition of the internal bias and the applied bias field, becomes asymmetric due to the existence of an internal bias.

To understand the collapse of the butterfly curve it is important to remember that under external electric field, there are two basic mechanisms that cause strain in ferroelectric materials: intrinsic and extrinsic mechanisms. The first one is caused by the linear piezoelectric effect while the second one results from the domain switching effect [48]. In our study, the intrinsic mechanism can be characterized by a shifting of the XRD peak, whereas the extrinsic mechanism is demonstrated by an increase in the intensity of the (002)T peak at the expense of the (200)T phase under an applied electric field, as shown in Figure 3.20—an effect that is related to non-180° domain switching. Because of the domain-pinning effect, the domain walls are pinned so that the domains remain in the preferred polarization orientation even if an external field is applied. As a result, the intrinsic mechanism produces the majority of the strain.

Furthermore, it is evident that the maximum strain varies from one to 10^8 cycles of the electric field. From one to 10^2 cycles, the maximum strain increases from 0.16% to 0.18%. This could be understood as a result of the wake-up effect, which is evidenced from the increase of the remnant ($2.P_R$) as illustrated in Figure 3.19(c). During this cycling range, the domains are de-pinned. Thus, the amount of switched domains due to non-180° switching mechanism increases, leading to higher strain.

From 10^2 up to 10^8 cycles, the maximum strain decreases from 0.18 to approximately 0.16%, and this could be explained by the fatigue state – demonstrated by the decrease of $2.P_R$ after 10^2 cycles as shown in Figure 3.19(c). In this state, the pinned domains are more difficult to switch, thus decreasing the strain.

The fluctuation of $d_{33,eff}$ as a function of the number of aging cycles is depicted in Figure 3.21(f). We can see that this quantity rises from approximately 87 to 96 pm/V after two cycles. This might be caused by the domains' de-pinning impact, which increases the non-180° domain switching. Following that, the $d_{33,eff}$ progressively drops to about 80 pm/V at 10^8 cycles. This decrease might be explained by a decrease in non-180° domain switching, which results from the domain pinning effect in the fatigued sample [92].

6.4. The evolution of the domain behavior of PZT under AC field cycling

Figure 3.22 (a), (b), and (c) illustrate the butterfly curves of integrated intensity and the strain as a function of applied electric field in c-, r- and a-domain, respectively. The integrated intensity of the rhombohedral peak is shown to rise as the applied electric field is increased, indicating an increase in the volume of this phase. On the other hand, the integrated intensity of the (200) peak and (002) peak drops at high electric field, indicating a decrease in the volume of these phases. Given those two findings, it can be inferred that this sample undergoes a phase transformation from tetragonal to rhombohedral in an external electric field. This phase transformation is predicted given the MPB composition of the sample [48] [47]. Furthermore, after 10^8 cycles, we observed the shifting of the butterfly loops toward the positive side, which could be understood with the domain pinning effect in the fatigue state of the film. Due to this effect, higher electric field is needed to switch the domains. As a result, a collapse of the butterfly curve is observed which indicates that the mechanism of strain generation is dominated by the intrinsic effect. Combining this observation with the evolution of the $d_{33,eff}$ mentioned above, it can be concluded that the ferroelectricity is more impacted by the fatigue effect than the piezoelectricity of the sample.

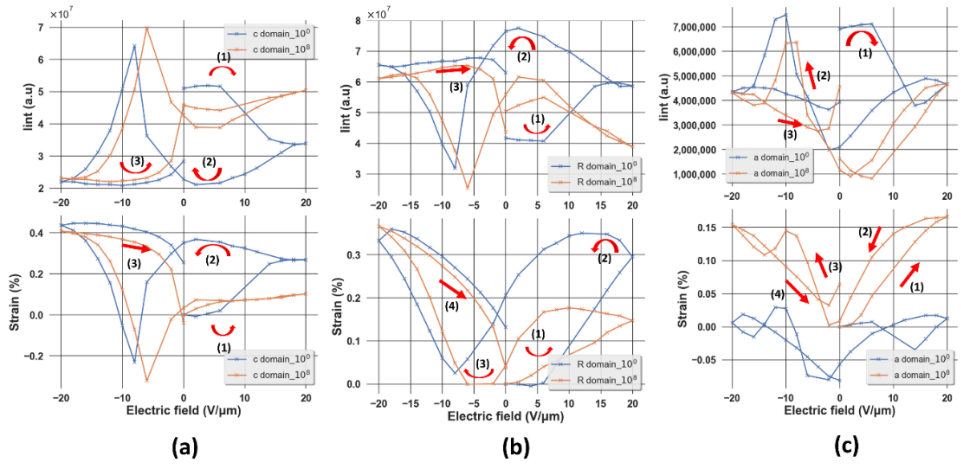

Figure 3.22: Evolution of the butterfly curves of the integrated intensity (Iint) and the strain of (a) c-, (b) r- and (c) a-domain between 10^0 and 10^8 cycles of aging

Conclusions of Chapter III

In conclusion, in this chapter, macroscopic behaviour of PZT films under applied electric field is studied. The chapter started by an introduction to the elaboration process of the sample by sol-gel method. The composition of the elaborated sample was studied by nano diffraction technique, which showed the existence of a gradient of Zr/Ti ratio. The morphological properties of the sample were also studied, showing the lamella shape orienting along the (100) direction of the grain and this orientation is found to be continuous over the different layers.

After that, the impacts of domain size and Zr/Ti ratio on the XRD peak profile were studied by both

simulation and experimental studies. From simulation, it was found that the separation of the three elements of the peaks ((002)T, (024)R and (200)T) is more evidenced with increasing the grain size. From experimental study, it was also found that the different Zr/Ti ratio leads to important changes in the peak profile.

The next part of the chapter is dedicated to the impact of thickness and texture on the functional properties of the film. Firstly, it was found that by increasing the thickness of the film, it polarization is improved, which could be due to the increase in the amount of dipole as well as the decrease in the inhomogeneities of the film under electric field. Considering the impact of texture, the study showed that the sample of (111) texture showed better polarization but worst piezoelectric properties than the sample with (100) preferred orientation.

The last part of the chapter discussed on the impact of external AC field cycling on the functional properties of the sample. It was shown that at 10^8 cycles of AC field cycling, there exists an imprint effect on the S-E curve. This is accompanied by a collapse of the curve, indicating the fatigue effect in the sample. The AC field also leads to a decrease of the $d_{33,eff}$ of the sample. However, the decrease in $d_{33,eff}$ is less important than the decrease in the remnant polarization, indicating that the fatigue effect impacts the ferroelectricity more than the piezoelectricity.

References for chapter III

[1] J. Evans *et al.*, "A discrete ferroelectric memory," in *2012 12th Annual Non-Volatile Memory Technology Symposium Proceedings*, Singapore: IEEE, Oct. 2012, pp. 33–36. doi: 10.1109/NVMTS.2013.6632857.

[2] Jérôme Mouly, "PIEZOELECTRIC DEVICES: FROM BULK TO THIN-FILM 2019," Yole development.

[3] Eric Mounier, Dimitrios Damianos, "Status of the MEMS industry 2019," Yole development.

[4] J. Bok and C. Kounelis, "Paul Langevin (1872-1946) - De la butte Montmartre au Panthéon : parcours d'un physicien d'exception," *Reflets Phys.*, no. 1, pp. 14–16, Sep. 2006, doi: 10.1051/refdp/2006007.

[5] J. Valasek, "Piezo-Electric and Allied Phenomena in Rochelle Salt," *Phys. Rev.*, vol. 17, no. 4, pp. 475–481, Apr. 1921, doi: 10.1103/PhysRev.17.475.

[6] A. T. Gen Shirane, "Phase Transitions in Solid Solutions of PbZrO3 and PbTiO3 (I) Small Concentrations of PbTiO3," *J. Phys. Soc. Jpn.*, vol. 7, pp. 5–11, Jan. 1952, doi: https://doi.org/10.1143/JPSJ.7.5.

[7] G. H. Haertling, "Ferroelectric Ceramics: History and Technology," *J. Am. Ceram. Soc.*, vol. 82, no. 4, pp. 797–818, Apr. 1999, doi: 10.1111/j.1151-2916.1999.tb01840.x.

[8] M. Ishida, S. Tsuji, K. Kimura, H. Matsunami, and T. Tanaka, "EPITAXIAL GROWTH OF FERROELECTRIC PLZT [(Pb, La)(Zr,Ti)Oa1 THIN FILMS," p. 6.

[9] M. Oikawa and K. Toda, "Preparation of Pb(Zr,Ti)O $_3$ thin films by an electron beam evaporation technique," *Appl. Phys. Lett.*, vol. 29, no. 8, pp. 491–492, Oct. 1976, doi: 10.1063/1.89133.

[10] M. Ishida, H. Matsunami, and T. Tanaka, "Preparation and properties of ferroelectric PLZT thin films by rf sputtering," p. 4.

[11] H. Adachi, T. Kawaguchi, K. Setsune, K. Ohji, and K. Wasa, "Electro-optic effects of (Pb, La)(Zr, Ti)O $_3$ thin films prepared by rf planar magnetron sputtering," *Appl. Phys. Lett.*, vol. 42, no. 10, pp. 867–868, May 1983, doi: 10.1063/1.93795.

[12] K. Iijima, Y. Tomita, R. Takayama, and I. Ueda, "Preparation of *c* -axis oriented PbTiO $_3$ thin films and their crystallographic, dielectric, and pyroelectric properties," *J. Appl. Phys.*, vol. 60, no. 1, pp. 361–367, Jul. 1986, doi: 10.1063/1.337654.

[13] N. Shohata, S. Matsubara, Y. Miyasaka, and M. Yonezawa, "Epitaxial Growth of PbTiO3on

MgAl2O4/Si Substrates," in *Sixth IEEE International Symposium on Applications of Ferroelectrics*, Jun. 1986, pp. 580–584. doi: 10.1109/ISAF.1986.201210.
[14] S. K. Dey, K. D. Budd, and D. A. Payne, "Thin-film ferroelectrics of PZT of sol-gel processing," *IEEE Trans. Ultrason. Ferroelectr. Freq. Control*, vol. 35, no. 1, pp. 80–81, Jan. 1988, doi: 10.1109/58.4153.
[15] J. Xu, A. S. Shaikh, and R. W. Vest, "High K BaTiO/sub 3/ films from metalloorganic precursors," *IEEE Trans. Ultrason. Ferroelectr. Freq. Control*, vol. 36, no. 3, pp. 307–312, May 1989, doi: 10.1109/58.19168.
[16] G. M. Davis and M. C. Gower, "Epitaxial growth of thin films of $BaTiO_3$ using excimer laser ablation," *Appl. Phys. Lett.*, vol. 55, no. 2, pp. 112–114, Jul. 1989, doi: 10.1063/1.102393.
[17] M. Okada, S. Takai, M. Amemiya, and K. Tominaga, "Preparation of *c* -Axis-Oriented $PbTiO_3$ Thin Films by MOCVD under Reduced Pressure," *Jpn. J. Appl. Phys.*, vol. 28, no. Part 1, No. 6, pp. 1030–1034, Jun. 1989, doi: 10.1143/JJAP.28.1030.
[18] K. Iijima, T. Terashima, K. Yamamoto, K. Hirata, and Y. Bando, "Preparation of ferroelectric $BaTiO_3$ thin films by activated reactive evaporation," *Appl. Phys. Lett.*, vol. 56, no. 6, pp. 527–529, Feb. 1990, doi: 10.1063/1.103300.
[19] R. A. Roy, K. F. Etzold, and J. J. Cuomo, "Ferroelectric Film Synthesis, Past and Present: A Select Review," *MRS Proc.*, vol. 200, p. 141, 1990, doi: 10.1557/PROC-200-141.
[20] N. Menou, "Technologie FeRAM: fiabilité et mécanismes de défaillance de condensateurs ferroélectriques élémentaires et intégrés," p. 239.
[21] C. M. Fancher *et al.*, "The contribution of 180° domain wall motion to dielectric properties quantified from in situ X-ray diffraction," *Acta Mater.*, vol. 126, pp. 36–43, Mar. 2017, doi: 10.1016/j.actamat.2016.12.037.
[22] D. Damjanovic, "Ferroelectric, dielectric and piezoelectric properties of ferroelectric thin films and ceramics," *Rep. Prog. Phys.*, vol. 61, no. 9, pp. 1267–1324, Sep. 1998, doi: 10.1088/0034-4885/61/9/002.
[23] S. Wada and T. Tsurumi, "Enhanced piezoelectricity of barium titanate single crystals with engineered domain configuration," *Br. Ceram. Trans.*, vol. 103, no. 2, pp. 93–96, Apr. 2004, doi: 10.1179/096797804225012747.
[24] K. Lefki and G. J. M. Dormans, "Measurement of piezoelectric coefficients of ferroelectric thin films," *J. Appl. Phys.*, vol. 76, no. 3, pp. 1764–1767, Aug. 1994, doi: 10.1063/1.357693.
[25] S. Trolier-Mckinstry and P. Muralt, "Thin Film Piezoelectrics for MEMS," p. 11.
[26] E. Jabari, F. Ahmed, F. Liravi, E. B. Secor, L. Lin, and E. Toyserkani, "2D printing of graphene: a review," *2D Mater.*, vol. 6, no. 4, p. 042004, Aug. 2019, doi: 10.1088/2053-1583/ab29b2.
[27] S. Nicolas *et al.*, "Fabrication and characterization of a new varifocal liquid lens with embedded PZT actuators for high optical performances," in *2015 28th IEEE International Conference on Micro Electro Mechanical Systems (MEMS)*, Jan. 2015, pp. 65–68. doi: 10.1109/MEMSYS.2015.7050887.
[28] H. Wang, Z. Chen, and H. Xie, "A high-SPL piezoelectric MEMS loud speaker based on thin ceramic PZT," *Sens. Actuators Phys.*, vol. 309, p. 112018, Jul. 2020, doi: 10.1016/j.sna.2020.112018.
[29] M. Tani, M. Akamatsu, Y. Yasuda, and H. Toshiyoshi, "A two-axis piezoelectric tilting micromirror with a newly developed PZT-meandering actuator," in *2007 IEEE 20th International Conference on Micro Electro Mechanical Systems (MEMS)*, Jan. 2007, pp. 699–702. doi: 10.1109/MEMSYS.2007.4432994.
[30] P. Laitinen and J. Mawnpaa, "Enabling mobile haptic design: piezoelectric actuator technology properties in hand held devices," in *2006 IEEE International Workshop on Haptic Audio Visual Environments and their Applications (HAVE 2006)*, Nov. 2006, pp. 40–43. doi: 10.1109/HAVE.2006.283787.
[31] H. K. Ma, B. R. Hou, H. Y. Wu, C. Y. Lin, J. J. Gao, and M. C. Kou, "Development and application of a diaphragm micro-pump with piezoelectric device," *Microsyst. Technol.*, vol. 14, no. 7, pp. 1001–1007, Jul. 2008, doi: 10.1007/s00542-007-0462-6.

[32] P. Muralt, “PZT thin films for microsensors and actuators: Where do we stand?,” *IEEE Trans. Ultrason. Ferroelectr. Freq. Control*, vol. 47, no. 4, pp. 903–915, Jul. 2000, doi: 10.1109/58.852073.
[33] “What is a SAW Filter ?,” *everythingRF*. https://www.everythingrf.com/community/what-is-a-saw-filter
[34] T. Giffney, M. Yu, K. C. Aw, and H. Zhang, “Contactless RF MEMS switch using PZT actuation,” in *The 8th Annual IEEE International Conference on Nano/Micro Engineered and Molecular Systems*, Apr. 2013, pp. 861–864. doi: 10.1109/NEMS.2013.6559860.
[35] J. S. Meena, S. M. Sze, U. Chand, and T.-Y. Tseng, “Overview of emerging nonvolatile memory technologies,” *Nanoscale Res. Lett.*, vol. 9, no. 1, p. 526, Dec. 2014, doi: 10.1186/1556-276X-9-526.
[36] Volker Rzehak, “Low-Power FRAM Microcontrollers and Their Applications,” Texas Instrument, 2019.
[37] J. Müller *et al.*, “Ferroelectricity in yttrium-doped hafnium oxide,” *J. Appl. Phys.*, vol. 110, no. 11, p. 114113, Dec. 2011, doi: 10.1063/1.3667205.
[38] T. Francois *et al.*, “Demonstration of BEOL-compatible ferroelectric Hf0.5Zr0.5O2 scaled FeRAM co-integrated with 130nm CMOS for embedded NVM applications,” in *2019 IEEE International Electron Devices Meeting (IEDM)*, Dec. 2019, p. 15.7.1-15.7.4. doi: 10.1109/IEDM19573.2019.8993485.
[39] S. Priya *et al.*, “A Review on Piezoelectric Energy Harvesting: Materials, Methods, and Circuits,” *Energy Harvest. Syst.*, vol. 4, no. 1, pp. 3–39, Aug. 2019, doi: 10.1515/ehs-2016-0028.
[40] B. Noheda *et al.*, “Tetragonal-to-monoclinic phase transition in a ferroelectric perovskite: The structure of PbZr 0.52 Ti 0.48 O 3,” *Phys. Rev. B*, vol. 61, no. 13, pp. 8687–8695, Apr. 2000, doi: 10.1103/PhysRevB.61.8687.
[41] M. Ahart *et al.*, “Origin of morphotropic phase boundaries in ferroelectrics,” *Nature*, vol. 451, no. 7178, pp. 545–548, Jan. 2008, doi: 10.1038/nature06459.
[42] G. A. Rossetti and A. G. Khachaturyan, “Inherent nanoscale structural instabilities near morphotropic boundaries in ferroelectric solid solutions,” *Appl. Phys. Lett.*, vol. 91, no. 7, p. 072909, Aug. 2007, doi: 10.1063/1.2771095.
[43] R. Ahluwalia, T. Lookman, A. Saxena, and W. Cao, “Domain-size dependence of piezoelectric properties of ferroelectrics,” *Phys. Rev. B*, vol. 72, no. 1, p. 014112, Jul. 2005, doi: 10.1103/PhysRevB.72.014112.
[44] N. Setter *et al.*, “Ferroelectric thin films: Review of materials, properties, and applications,” *J. Appl. Phys.*, vol. 100, no. 5, p. 051606, Sep. 2006, doi: 10.1063/1.2336999.
[45] R. Guo, L. E. Cross, S.-E. Park, B. Noheda, D. E. Cox, and G. Shirane, “Origin of the High Piezoelectric Response in PbZr 1 − x Ti x O 3,” *Phys. Rev. Lett.*, vol. 84, no. 23, pp. 5423–5426, Jun. 2000, doi: 10.1103/PhysRevLett.84.5423.
[46] L. Bellaiche, A. García, and D. Vanderbilt, “Finite-Temperature Properties of Pb (Zr 1 − x Ti x) O 3 Alloys from First Principles,” *Phys. Rev. Lett.*, vol. 84, no. 23, pp. 5427–5430, Jun. 2000, doi: 10.1103/PhysRevLett.84.5427.
[47] M. Hinterstein *et al.*, “Structural Description of the Macroscopic Piezo- and Ferroelectric Properties of Lead Zirconate Titanate,” *Phys. Rev. Lett.*, vol. 107, no. 7, p. 077602, Aug. 2011, doi: 10.1103/PhysRevLett.107.077602.
[48] V. Kovacova, N. Vaxelaire, G. Le Rhun, P. Gergaud, T. Schmitz-Kempen, and E. Defay, “Correlation between electric-field-induced phase transition and piezoelectricity in lead zirconate titanate films,” *Phys. Rev. B*, vol. 90, no. 14, p. 140101, Oct. 2014, doi: 10.1103/PhysRevB.90.140101.
[49] T. W. Cornelius *et al.*, “Piezoelectric response and electrical properties of Pb(Zr 1-x Ti x)O 3 thin films: The role of imprint and composition,” *J. Appl. Phys.*, vol. 122, no. 16, pp. 164104–164104, Oct. 2017, doi: 10.1063/1.4994939.
[50] T. W. Cornelius *et al.*, “Piezoelectric Properties of Pb1−xLax(Zr0.52Ti0.48)1−x/4O3 Thin Films

Studied by In Situ X-ray Diffraction," *Materials*, vol. 13, no. 15, p. 3338, Jul. 2020, doi: 10.3390/ma13153338.
[51] P. Jiang *et al.*, "Wake-Up Effect in HfO2-Based Ferroelectric Films," *Adv. Electron. Mater.*, vol. 7, no. 1, p. 2000728, 2021, doi: 10.1002/aelm.202000728.
[52] Q. Y. Jiang, E. C. Subbarao, and L. E. Cross, "Effect of composition and temperature on electric fatigue of La-doped lead zirconate titanate ceramics," *J. Appl. Phys.*, vol. 75, no. 11, pp. 7433–7443, Jun. 1994, doi: 10.1063/1.356637.
[53] M. Majkut, J. E. Daniels, J. P. Wright, S. Schmidt, and J. Oddershede, "Electromechanical Response of Polycrystalline Barium Titanate Resolved at the Grain Scale," *J. Am. Ceram. Soc.*, vol. 100, no. 1, pp. 393–402, Jan. 2017, doi: 10.1111/jace.14481.
[54] H. N. Al-Shareef, A. I. Kingon, X. Chen, K. R. Bellur, and O. Auciello, "Contribution of electrodes and microstructures to the electrical properties of Pb(Zr $_{0.53}$ Ti $_{0.47}$)O $_3$ thin film capacitors," *J. Mater. Res.*, vol. 9, no. 11, pp. 2968–2975, Nov. 1994, doi: 10.1557/JMR.1994.2968.
[55] C. Künneth, R. Batra, G. A. Rossetti, R. Ramprasad, and A. Kersch, "Thermodynamics of Phase Stability and Ferroelectricity From First Principles," in *Ferroelectricity in Doped Hafnium Oxide: Materials, Properties and Devices*, Elsevier, 2019, pp. 245–289. doi: 10.1016/B978-0-08-102430-0.00006-1.
[56] M. Pešić *et al.*, "Physical Mechanisms behind the Field-Cycling Behavior of HfO2-Based Ferroelectric Capacitors," *Adv. Funct. Mater.*, vol. 26, no. 25, pp. 4601–4612, 2016, doi: https://doi.org/10.1002/adfm.201600590.
[57] W. L. Warren *et al.*, "Polarization suppression in Pb(Zr,Ti)O $_3$ thin films," *J. Appl. Phys.*, vol. 77, no. 12, pp. 6695–6702, Jun. 1995, doi: 10.1063/1.359083.
[58] H. M. Duiker *et al.*, "Fatigue and switching in ferroelectric memories: Theory and experiment," *J. Appl. Phys.*, vol. 68, no. 11, pp. 5783–5791, Dec. 1990, doi: 10.1063/1.346948.
[59] J. F. Scott, C. A. Araujo, B. M. Melnick, L. D. McMillan, and R. Zuleeg, "Quantitative measurement of space-charge effects in lead zirconate-titanate memories," *J. Appl. Phys.*, vol. 70, no. 1, pp. 382–388, Jul. 1991, doi: 10.1063/1.350286.
[60] H. Zou, "Effect of Nb Doping on Crystalline Orientation, Electric and Fatigue Properties of PZT Thin Films Prepared by Sol-Gel Process," *J. Ceram. Sci. Technol.*, no. 04, 2017, doi: 10.4416/JCST2017-00031.
[61] H. Sun, Y. Zhang, X. Liu, S. Guo, Y. Liu, and W. Chen, "The effect of Mn/Nb doping on dielectric and ferroelectric properties of PZT thin films prepared by sol–gel process," *J. Sol-Gel Sci. Technol.*, vol. 74, no. 2, pp. 378–386, May 2015, doi: 10.1007/s10971-014-3608-x.
[62] J. M. Benedetto, "Imprint induced failure modes in ferroelectric non-volatile memories," *Integr. Ferroelectr.*, vol. 15, no. 1–4, pp. 29–38, Feb. 1997, doi: 10.1080/10584589708015694.
[63] G. Arlt and H. Neumann, "Internal bias in ferroelectric ceramics: Origin and time dependence," *Ferroelectrics*, vol. 87, no. 1, pp. 109–120, Nov. 1988, doi: 10.1080/00150198808201374.
[64] R. Lohkämper, H. Neumann, and G. Arlt, "Internal bias in acceptor-doped BaTiO $_3$ ceramics: Numerical evaluation of increase and decrease," *J. Appl. Phys.*, vol. 68, no. 8, pp. 4220–4224, Oct. 1990, doi: 10.1063/1.346212.
[65] D. Dimos, W. L. Warren, M. B. Sinclair, B. A. Tuttle, and R. W. Schwartz, "Photoinduced hysteresis changes and optical storage in (Pb,La)(Zr,Ti)O $_3$ thin films and ceramics," *J. Appl. Phys.*, vol. 76, no. 7, pp. 4305–4315, Oct. 1994, doi: 10.1063/1.357316.
[66] M. Grossmann, O. Lohse, D. Bolten, U. Boettger, T. Schneller, and R. Waser, "The interface screening model as origin of imprint in PbZrxTi1−xO3 thin films. I. Dopant, illumination, and bias dependence," *J. Appl. Phys.*, vol. 92, no. 5, pp. 2680–2687, Sep. 2002, doi: 10.1063/1.1498966.
[67] R. Roque, "X-ray imaging using 100 µm thick Gas Electron Multipliers operating in Kr-CO2 mixtures," Unpublished, 2018. Accessed: Aug. 07, 2022. [Online]. Available: http://rgdoi.net/10.13140/RG.2.2.16794.49600
[68] European Synchrotron Radiation Facility, "QUESTIONS & ANSWERS."

https://www.esrf.fr/about/ask-an-expert/questions-answers#:~:text=The%20most%20important%20advantage%20of,angular%20spread%20of%20the%20beam.
[69] M. Birkholz, “Thin Film Analysis by X-Ray Scattering,” p. 381.
[70] H. Möller and J. Barbers, *Mitt Kais. Wilhelm Inst. Eisenforsch.*, vol. 16, p. 21, 1934.
[71] P. Gravereau, “Introduction à la pratique de la diffraction des rayons X par les poudres,” p. 210.
[72] Newville, Matthew ; Stensitzki, Till ; Allen, Daniel B. ; Rawlik, Michal ; Ingargiola, Antonino ; Nelson, Andrew, “LMFIT: Non-Linear Least-Square Minimization and Curve-Fitting for Python”, doi: 10.5281/zenodo.11813.
[73] Q. M. Zhang, W. Y. Pan, and L. E. Cross, “Laser interferometer for the study of piezoelectric and electrostrictive strains,” *J. Appl. Phys.*, vol. 63, no. 8, pp. 2492–2496, Apr. 1988, doi: 10.1063/1.341027.
[74] A. L. Kholkin, Ch. Wütchrich, D. V. Taylor, and N. Setter, “Interferometric measurements of electric field-induced displacements in piezoelectric thin films,” *Rev. Sci. Instrum.*, vol. 67, no. 5, pp. 1935–1941, May 1996, doi: 10.1063/1.1147000.
[75] Z. Huang and R. W. Whatmore, “A double-beam common path laser interferometer for the measurement of electric field-induced strains of piezoelectric thin films,” *Rev. Sci. Instrum.*, vol. 76, no. 12, p. 123906, Dec. 2005, doi: 10.1063/1.2149002.
[76] “PyVISA: Control your instruments with Python.” https://pyvisa.readthedocs.io/en/latest/
[77] N. Vaxelaire *et al.*, “Effect of structural in-depth heterogeneities on electrical properties of Pb(Zr0.52Ti0.48) O3 thin films as revealed by nano-beam X-ray diffraction,” *J. Appl. Phys.*, vol. 120, no. 10, p. 104101, Sep. 2016, doi: 10.1063/1.4962427.
[78] B. Noheda *et al.*, “Tetragonal-to-monoclinic phase transition in a ferroelectric perovskite: The structure of PbZr 0.52 Ti 0.48 O 3,” *Phys. Rev. B*, vol. 61, no. 13, pp. 8687–8695, Apr. 2000, doi: 10.1103/PhysRevB.61.8687.
[79] S. K. Sayyed and S. A. Acharya, “Synthesis of PZT nanorods and study of dielectric behaviour,” presented at the PROCEEDING OF INTERNATIONAL CONFERENCE ON RECENT TRENDS IN APPLIED PHYSICS AND MATERIAL SCIENCE: RAM 2013, Bikaner, Rajasthan, India, 2013, pp. 111–112. doi: 10.1063/1.4810125.
[80] Wojciech Paszkowicz, “Application of a powder diffractometer equipped with a strip detector and Johansson monochromator to phase analysis and structure refinement,” *Nucl. Instrum. Methods Phys. Res. Sect. Accel. Spectrometers Detect. Assoc. Equip.*, vol. 551, no. 1, pp. 162–177, Oct. 2005, doi: 10.1016/j.nima.2005.07.068.
[81] K. T. Li and V. C. Lo, “Simulation of thickness dependence in ferroelectric thin films,” *Solid State Commun.*, vol. 132, no. 1, pp. 49–54, Oct. 2004, doi: 10.1016/j.ssc.2004.07.013.
[82] M. Dekkers, M. D. Nguyen, R. Steenwelle, P. M. te Riele, D. H. A. Blank, and G. Rijnders, “Ferroelectric properties of epitaxial Pb(Zr,Ti)O3 thin films on silicon by control of crystal orientation,” *Appl. Phys. Lett.*, vol. 95, no. 1, p. 012902, Jul. 2009, doi: 10.1063/1.3163057.
[83] Yu. V. Podgorny, D. S. Seregin, A. S. Sigov, and K. A. Vorotilov, “Effect of Sol-Gel PZT Film Thickness on the Hysteresis Properties,” *Ferroelectrics*, vol. 439, no. 1, pp. 74–79, Jan. 2012, doi: 10.1080/00150193.2012.741952.
[84] A. J. Fox, B. Drawl, G. R. Fox, B. J. Gibbons, and S. Trolier-McKinstry, “Control of crystallographic texture and surface morphology of Pt/Tio2 templates for enhanced PZT thin film texture,” *IEEE Trans. Ultrason. Ferroelectr. Freq. Control*, vol. 62, no. 1, pp. 56–61, Jan. 2015, doi: 10.1109/TUFFC.2014.006671.
[85] E. M. Alkoy, S. Alkoy, and T. Shiosaki, “The effect of crystallographic orientation and solution aging on the electrical properties of sol–gel derived Pb(Zr0.45Ti0.55)O3 thin films,” *Ceram. Int.*, vol. 33, no. 8, pp. 1455–1462, Dec. 2007, doi: 10.1016/j.ceramint.2006.06.010.
[86] Y. Kim, H. Han, I. Vrejoiu, W. Lee, D. Hesse, and M. Alexe, “Origins of domain wall pinning in ferroelectric nanocapacitors,” *Nano Converg.*, vol. 1, no. 1, p. 24, Dec. 2014, doi: 10.1186/s40580-014-0024-4.

[87] J. A. Christman, R. R. Woolcott, A. I. Kingon, and R. J. Nemanich, “Piezoelectric measurements with atomic force microscopy,” p. 4.
[88] O. Kuffer, I. Maggio-Aprile, J.-M. Triscone, O. Fischer, and Ch. Renner, “Piezoelectric response of epitaxial Pb(Zr0.2Ti0.8)O3 films measured by scanning tunneling microscopy,” *Appl. Phys. Lett.*, vol. 77, no. 11, pp. 1701–1703, Sep. 2000, doi: 10.1063/1.1309017.
[89] A. L. Kholkin, Ch. Wütchrich, D. V. Taylor, and N. Setter, “Interferometric measurements of electric field-induced displacements in piezoelectric thin films,” *Rev. Sci. Instrum.*, vol. 67, no. 5, pp. 1935–1941, May 1996, doi: 10.1063/1.1147000.
[90] Z. Huang and R. W. Whatmore, “A double-beam common path laser interferometer for the measurement of electric field-induced strains of piezoelectric thin films,” *Rev. Sci. Instrum.*, vol. 76, no. 12, p. 123906, Dec. 2005, doi: 10.1063/1.2149002.
[91] H. Weitzing, G. A. Schneider, J. Steffens, M. Hammer, and M. J. Hoffmann, “Cyclic fatigue due to electric loading in ferroelectric ceramics,” *J. Eur. Ceram. Soc.*, vol. 19, no. 6, pp. 1333–1337, Jun. 1999, doi: 10.1016/S0955-2219(98)00429-4.
[92] R. Herbiet, H. Tenbrock, and G. Arlt, “The aging behaviour of the complex material parameters ε, d and s in ferroelectric PZT ceramics,” *Ferroelectrics*, vol. 76, no. 1, pp. 319–326, Dec. 1987, doi: 10.1080/00150198708016952.
[93] J. E. Daniels *et al.*, “Heterogeneous grain-scale response in ferroic polycrystals under electric field,” *Sci. Rep.*, vol. 6, no. 1, p. 22820, Mar. 2016, doi: 10.1038/srep22820.
[94] Q. Li and M. Kuna, “Inhomogeneity and material configurational forces in three dimensional ferroelectric polycrystals,” *Eur. J. Mech. - ASolids*, vol. 31, no. 1, pp. 77–89, Jan. 2012, doi: 10.1016/j.euromechsol.2011.07.004.
[95] L. Fan, W. Werner, S. Subotić, D. Schneider, M. Hinterstein, and B. Nestler, “Multigrain phase-field simulation in ferroelectrics with phase coexistences: An improved phase-field model,” *Comput. Mater. Sci.*, vol. 203, p. 111056, Feb. 2022, doi: 10.1016/j.commatsci.2021.111056.
[96] H. Simons *et al.*, “Long-range symmetry breaking in embedded ferroelectrics,” *Nat. Mater.*, vol. 17, no. 9, pp. 814–819, Sep. 2018, doi: 10.1038/s41563-018-0116-3.
[97] E. K. H. Salje, S. Li, M. Stengel, P. Gumbsch, and X. Ding, “Flexoelectricity and the polarity of complex ferroelastic twin patterns,” *Phys. Rev. B*, vol. 94, no. 2, p. 024114, Jul. 2016, doi: 10.1103/PhysRevB.94.024114.
[98] J. Novak, U. Bismayer, and E. K. H. Salje, “Simulated equilibrium shapes of ferroelastic needle domains,” *J. Phys. Condens. Matter*, vol. 14, no. 3, pp. 657–664, Jan. 2002, doi: 10.1088/0953-8984/14/3/332.
[99] A. S. Karapuzha, N. K. James, H. Khanbareh, S. van der Zwaag, and W. A. Groen, “Structure, dielectric and piezoelectric properties of donor doped PZT ceramics across the phase diagram,” *Ferroelectrics*, vol. 504, no. 1, pp. 160–171, Nov. 2016, doi: 10.1080/00150193.2016.1240571.
[100] M. Budimir, D. Damjanovic, and N. Setter, “Enhancement of the piezoelectric response of tetragonal perovskite single crystals by uniaxial stress applied along the polar axis: A free-energy approach,” *Phys. Rev. B*, vol. 72, no. 6, p. 064107, Aug. 2005, doi: 10.1103/PhysRevB.72.064107.
[101] E.-M. Anton, R. E. García, T. S. Key, J. E. Blendell, and K. J. Bowman, “Domain switching mechanisms in polycrystalline ferroelectrics with asymmetric hysteretic behavior,” *J. Appl. Phys.*, vol. 105, no. 2, p. 024107, Jan. 2009, doi: 10.1063/1.3068333.
[102] C. Lichtensteiger, J.-M. Triscone, J. Junquera, and P. Ghosez, “Ferroelectricity and Tetragonality in Ultrathin P b T i O 3 Films,” *Phys. Rev. Lett.*, vol. 94, no. 4, p. 047603, Feb. 2005, doi: 10.1103/PhysRevLett.94.047603.
[103] C. A. Randall, N. Kim, J.-P. Kucera, W. Cao, and T. R. Shrout, “Intrinsic and Extrinsic Size Effects in Fine-Grained Morphotropic-Phase-Boundary Lead Zirconate Titanate Ceramics,” *J. Am. Ceram. Soc.*, vol. 81, no. 3, pp. 677–688, 1998, doi: 10.1111/j.1151-2916.1998.tb02389.x.
[104] Y. Wei, C. Jin, P. Ye, P. Li, Y. Zeng, and G. Xu, “Structural evolution, electrical properties and electric-field-induced changes of (0.8−x)PbTiO3–xBiFeO3–0.2BaZrO3 system near the

morphotropic phase boundary," *Appl. Phys. A*, vol. 123, no. 4, p. 218, Apr. 2017, doi: 10.1007/s00339-016-0736-x.
[105] B. Allouche, I. Gueye, G. L. Rhun, P. Gergaud, and N. Vaxelaire, "In-situ X-ray diffraction on functional thin films using a laboratory source during electrical biasing," *Mater. Des.*, vol. 154, pp. 340–346, Sep. 2018, doi: 10.1016/j.matdes.2018.05.016.
[106] K. Nguyen, E. Bellec, E. Zatterin, G. Le Rhun, P. Gergaud, and N. Vaxelaire, "Structural Insights of Electrical Aging in PZT Thin Films as Revealed by In Situ Biasing X-ray Diffraction," *Materials*, vol. 14, no. 16, Art. no. 16, Jan. 2021, doi: 10.3390/ma14164500.

Chapter IV. Grain-scale analysis of the behavior of PZT thin-film under applied electric field

Introduction

In chapter III, the macroscopic properties of PZT film under applied electric field have been discussed. In this chapter, the behaviors at grain-scale will be presented. Piezoelectric thin-films are particularly difficult to model at the grain scale. Moreover, this problem is sparsely experimentally documented due to the lack of adequate methods. Here an original methodology is proposed to study the behavior of single grains during in-situ biasing. $Pb(Zr,Ti)O_3$ films have been probed thanks to an in-situ biasing XRD technique performed on a synchrotron source with a sub-micrometer X-ray beam. Small capacitors have been biased with DC voltage between zero and ± 20 V and at each step of bias a XRD patterns was recorded. By selecting an appropriate region of interest, the evolution of a single grain peak was followed. The fine analysis of these peaks allows to calculate the effective piezoelectric coefficient $d_{33,eff}$, the proportion of each domain variants, the tetragonality inside each grain as well as their evolution during the electrical biasing. A higher heterogeneity in sample with morphotropic phase boundary composition is observed. In this chapter, we will present the state of the art concerning the grain-scale analysis of ferroelectric materials. After that, the experimental procedure will be introduced, with the measurement setup at the ESRF as well as the method used to track the region of interest of the grain. Next, we will present the achieved results, consisting of the extraction of both the structural and functional properties of the sample. The chapter ends with discussion and a summary of the study.

1. State of the art in the grain-scale analysis of ferroelectric materials

Certain efforts were made to understand the coupling of ferroic properties at grain scale in polycrystalline materials. In research by J.E Daniels [93], the heterogeneity at the grain scale in ferroic polycrystals has been studied using three-dimensional X-ray diffraction (3D-XRD) under external stimuli on a sample of $(0.82)Bi_{0.5}Na_{0.5}TiO_3 – (0.18)Bi_{0.5}K_{0.5}TiO_3$ (BNT-BKT) based ceramics. Results have proved the impact of the grain orientation on the resulting phase and domain structure under electric field. For example, while most grains were found to transform to rhombohedral phase under electric field, those with <100> orientation displayed a remarkable volume fraction that either remained in the cubic state or transformed into tetragonal or lower symmetry structure. Furthermore, authors also found that there is a difference in the domain switching strain in grains oriented along different directions. In fact, the maximum domain switching strain is observed in the <111> grains while the minimum strain is obtained in <100> grains. However, a remarkable variation in the magnitude of response exists at grain scale, which is illustrated in the Figure 4.1 through the heterogeneity in the resulting domain texture strain observed for grains with similar orientations. The origin of this heterogeneity is believed to stem from the interactions of grain-neighbour strain magnitudes, electric field magnitude inhomogeneity and the interaction of ferroic domains at grain boundaries.

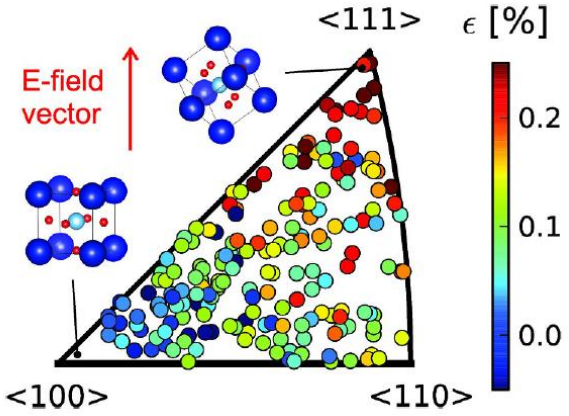

Figure 4.1: Inverse pole figure of indexed grain orientations. The colour bar illustrated the level of strain in each grain [93]

In another research by Majkut et al. [53], an in-situ biasing 3D-XRD technique was applied to reconstruct a 3D grain map of polycrystalline $BaTiO_3$ ceramics and to track the non-180° domain switching strain at grain scale. The researchers found that although the average strain response of the sample was as expected, the behavior of individual grains of similar orientations is strongly heterogeneous. It is observed that these heterogeneities are not only restricted to the ferroelastic strain response, but in fact, it existed also in the initial as-processed state of the sample. These variations at grain-scale were suggested to initiate from the highly heterogeneous local strain and electrostatic neighborhoods within the bulk polycrystal, which is evidenced on the grain map of two selected bulk grains presented on Figure 4.2 with similar orientation, size and number of neighbors. Furthermore, the diffraction data also indicated the existence of remarkable lattice strain within the domains, accumulating mainly in the grain-boundary regions to accommodate the transition between domains and to guarantee the stress equilibrium. The obtained results indicate that the heterogeneities in both the as-processed state as well as under applied field stem from the minimization of electrostatic potentials at grain boundaries due to the interactions between ferroelectric domains.

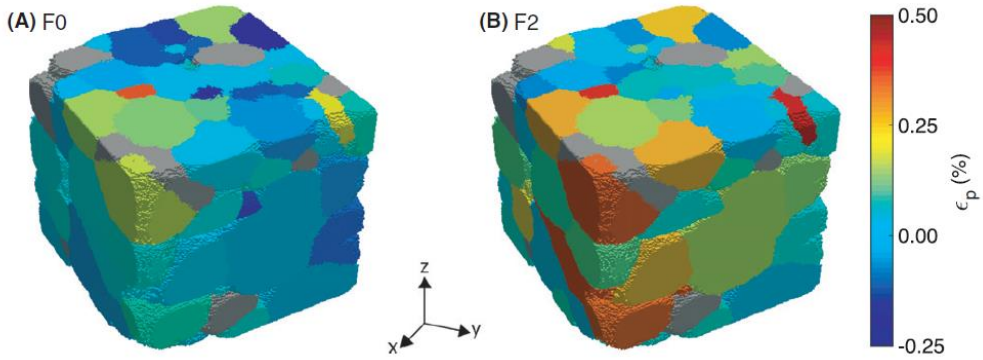

Figure 4.2: Grain maps of the entire sample color coded according to (A) ep,F0, and (B) ep,F2. The poling direction is along the vertical z-axis. The gray grains are the ones where the fit of domain volume fractions failed [53]

Besides experimental studies, simulation works have also been done to study the grain-scale behavior of ferroelectric materials. In the study of Q. Li et al. [94], a 3D finite element method is implemented to simulate the macroscopic mechanical and electrical response over the whole multi-grains body as well as for each single grain. Considering the whole multi-grains body, the authors observed the mechanical butterfly loop as well as the electrical hysteresis loop as a result of the macroscopic electromechanical response to an applied electric field. At the microscopic scale, the response at the grain scale indicates a clear heterogeneity. The stresses or strains show a great fluctuation in the Figure 4.3 created by grain to grain interactions due to the random orientation of grains in the initial process. Significantly higher values of stress or strain are found at grain boundaries as the material needs to accommodate with surrounding grains. As a result, the failure processes due to intergranular strain could be triggered. In contrast, the domain evolution reveals that the direction of remanent polarization tends to orient along the applied field direction regardless of grain orientations even though its magnitude still shows a dependency on the grain orientation.

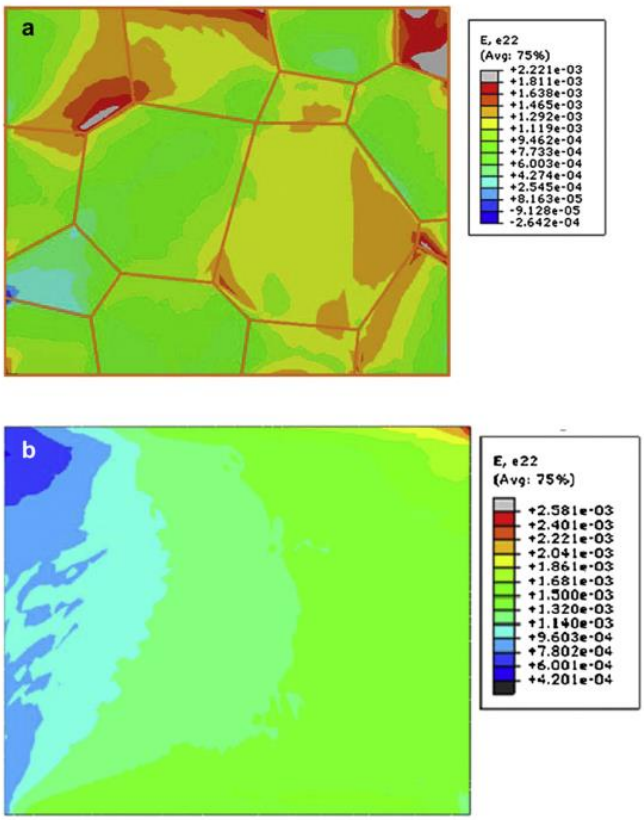

Figure 4.3: Local distribution of strain ε_{22} at an applied electric field of $4E_c$ in multi-grains: (a) with randomly different orientations and (b) with same orientations [94]

In another research by L.Fan et al. [95], a new 3D phase-field model has been developed by combining the Landau-Devonshire theory with the general multiphase phase-field functional in order to understand the domain structure and phase transformation with phase coexistences. In polycrystalline MPB ferroelectrics, the temporal domain structure and phase transformation with and without applied field have been studied. Without applied field, the polycrystalline equilibrium depends on the cooperative motion between the polarization evolution and the phase transformation. Under applied electric field, the externally induced polarization switching happens first, followed by the phase transformation. It has been observed that the phase transformation under electric field is orientation-dependent. Figure 4.4 illustrates the phase transformation and domain evolution when the field is applied along (100) direction. Here the light and dark grey regions illustrate the tetragonal (F_T) and rhombohedral (F_R) phases, respectively. Firstly, in the Figure 4.4(a) and (b) it is seen that the 90° domain structure disappears under applied field, which is due to the switching of the dipole in tetragonal phase (F_T). Furthermore, from Figure 4.4(c), it can be seen that the F_R transforms into F_T at the boundary between two phases. This could be due to the fact that the field is applied along the F_T crystallographic direction, thus F_T is favourable energetically, causing field-induced transformation. As a result, when the field is applied along (111) orientation, the transformation is reversed, from F_T to F_R, as (111) is the crystallographic direction of F_R. It is also observed that the magnitude of the applied electric field plays an important role in the manipulation of domain structure as well as the proportion of the phase volume fraction. Under applied field of 30 kV/mm along (111) orientation, the polarization switching happens after only 10 to 50 time steps. In the contrary, when no field is applied, after 5 x 10^2 steps, the domain structure is still in the nucleation state and it is until after 2.5 x 10^3 steps that the dipole inside each phase starts to orient along its crystallographic orientation.

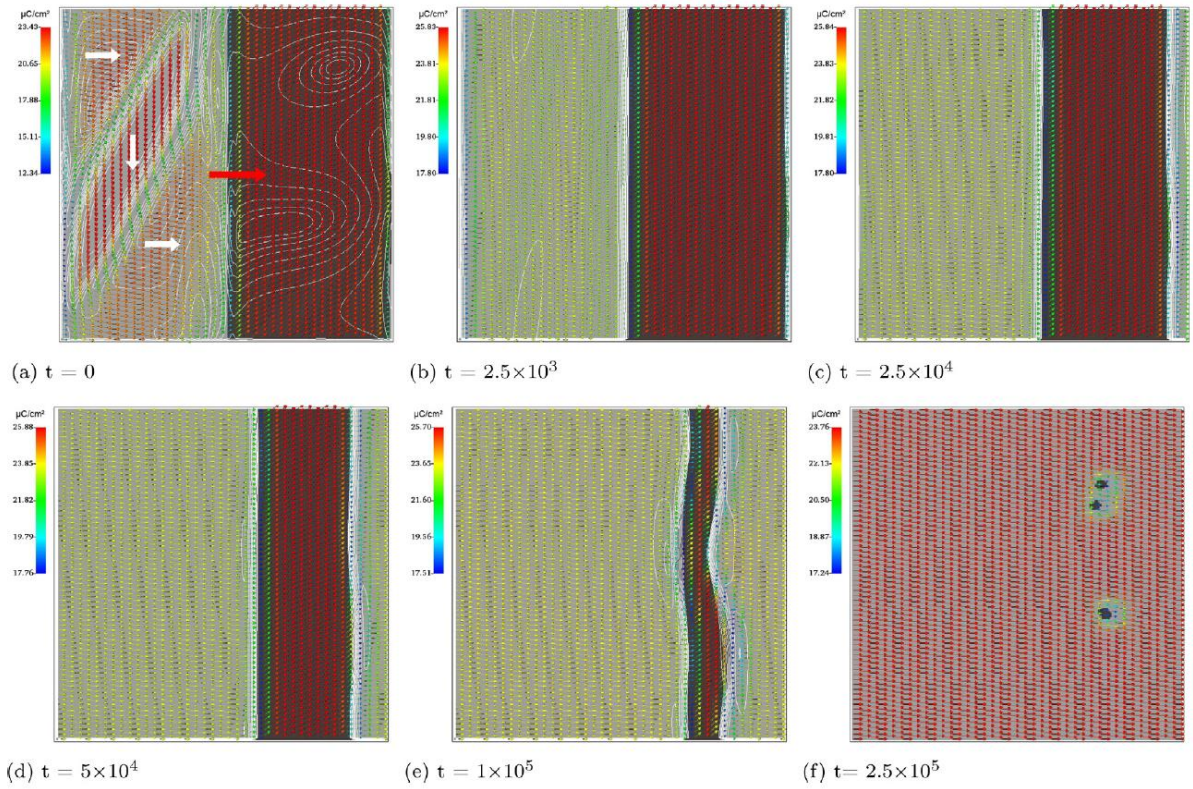

Figure 4.4: Temporal evolution of the domain structure and the phase transformation of the multiphase in a single crystal with E_{ext} = 10 kV/mm (the black thick arrow), along the [100] direction. The white thick arrows in the F_T phase demonstrate the polarization direction, t represents the simulation time step [95]

In the research by H. Simons et al. [96], the magnitude and distribution of axial strain and lattice misorientation around grain boundaries and ferroelastic domain walls within a buried grain of $BaTiO_3$ ceramic have been measured by dark-field X-ray microscopy. An individual domain is shown in Figure 4.5(a). Moreover, the evolution of embedded domain structure and its local changes in symmetry

under electric field is recorded in situ. By doing this, the authors succeeded in creating a clear picture of the impact of extrinsic strain (defined as any strain in addition to the spontaneous strain) on the ferroelectric topology and the response of embedded grains and volumes. It was found that the strained neighborhoods surrounding the embedded grain boundaries and domain walls could extend up to several micrometres as shown in Figure 4.5, which is approximately an order of magnitude higher than the predictions provided by many simulations of nanoscale complex domain topologies [97] [98]. As a result, the symmetry of entire grains and their local electrochemical response to applied fields are altered. This indicates that the macroscopic behaviour of the material is not only determined by the nominal symmetry but also fundamentally affected by the local heterogeneities deep inside the material. These include networks of strain gradients, which may give rise to local flexoelectric effect.

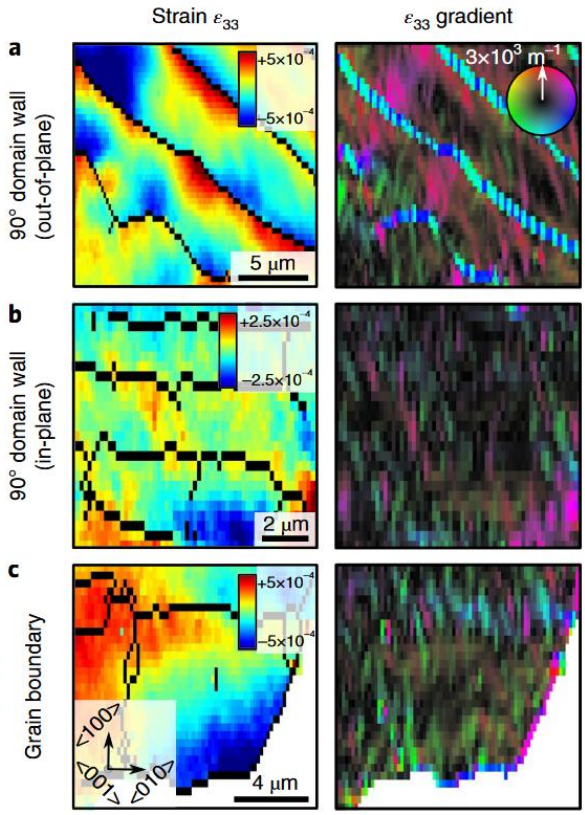

Figure 4.5: Local lattice distortions around embedded structural interface. a-c, Quantitative map of local axial strain and axial strain gradient of (a) 90°(out-of-plane) domain walls, (b) 90°(in-plane) domain walls and (c) grain boundaries [96]

As illustrated by the presented studies, significant efforts have been performed to study ferroelectric materials at the grain-scale. While it is an interesting first step, most of the studies are still simulation works or experimental ones carried out on bulk ceramic sample. In our work, we will focus on PZT thin films, where we demonstrate the implementation of an in situ biasing XRD technique using micronic synchrotron X-ray beam. Thanks to this technique, a number of functional and structural parameters of a single grain are extracted.

2. Experimental method

Prototypical [100]-textured Nb (2%)-doped $PbZr_{0.52}Ti_{0.48}O_3$ (PZT52) and undoped $PbZr_{0.43}Ti_{0.57}O_3$ (PZT43) of 1µm thick films have been studied. Samples were fabricated by sol-gel method on a 200 mm Si(001) substrate with 500 nm of SiO_2 layer on top. In order to carry out in-situ electrical characterization, PZT thin films were stacked in the metal-insulator-metal (MIM) structure with 100 nm thick Pt bottom and Ru top electrodes. A layer of 20 nm TiO_2 has been deposited between SiO_2 and Pt in order to enhance

the adhesion of Pt. The deposition sequence of the PZT layer could be found in Chapter III.1.

The in-situ X-ray microdiffraction measurements were carried out at the ID01 beamline at the European Synchrotron Radiation Facility (ESRF) using a monochromatic beam at an energy of 8 keV. The beam was focused down to 0.4x0.4 μm^2, leading to a footprint of 0.4 x 1 μm^2 in the chosen Bragg geometry. The diffracted signal of the {200} PZT reflections was recorded with a 2D detector Medipix (4^o in angular aperture) in a symmetric coplanar geometry. The illustration of the XRD configuration is shown in Figure 4.6a. In this experiment, an electric field of ±20 V/µm was applied using a SPEC® voltage source (Keithley 487, Keithley Instruments®) and at each step of bias, an x-ray diffraction pattern was collected. The duration of each bias step was 700 (PZT43) and 1000s (PZT52), corresponding to a quasi-static bias application (frequency less than 0.0001 Hz). The complete electrical cycle was performed in 4 (PZT43) or 8 hours (PZT52).

Concerning the XRD experiment, a section of the Debye ring was intercepted by the 2D detector at each step of bias. As the beam size is only a few times larger than the average grain size (i.e around 200 nm as deduced by top view scanning electron microscopy), an inhomogeneous Debye ring is obtained. This inhomogeneous Debye ring consists of different grains and each orientation of grain gives a XRD signal in a given orientation. By performing a large rocking curve (eta scan), a 3D reciprocal space mapping stack of the {200} reflections is recorded as shown in Figure 4.6(b). Then, a high resolution {200} pole figure is extracted from this 3D dataset (see Figure 4.6(c) and (d)) where individual grain can be observed. A q_z extraction (i.e. theta/2theta scan) for each selected single spot is calculated using an appropriate region of interest. The XRD intensity is summed along Eta (qy direction) and Nu (qx) and this operation is repeated for each bias step. Some of the diffraction spots went out of the range of the pole figure during the biasing (e.g. rotation). In the following analysis, only the spots that remain in pole figure during the whole biasing cycle are investigated (as shown in Figure 4.6(c) and (d)).

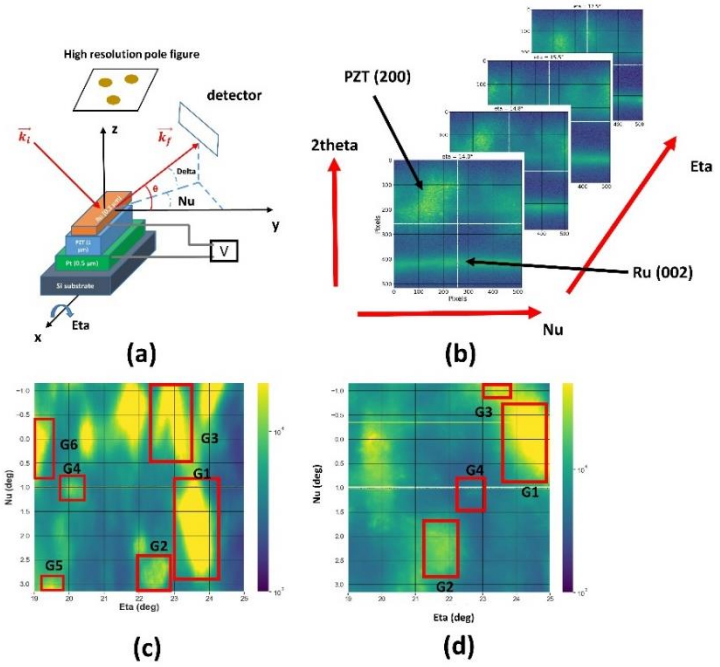

Figure 4.6: (a) XRD configuration used in the experiment, (b) the Debye rings of PZT (200) and Ru (200) phases obtained from the 2D detector at different angles of eta, the {200} pole figure generated at 0V of the selected section of the Debye ring of (c) PZT52 and (d) PZT 43 thin-film

As a result, in the data analysis procedure, one of the first task is the tracking of the position of a single grain in the pole figure. Due to the piezoelectric effect, under applied electric field the position of a particular grain might be different from its initial position. If these grains move out of the region of the Debye ring intercepted by the detector, the intensity of the grain is lost. Another possible scenario is the pinning of the domain walls under applied field leading the domains to not fully switch between (200), (002) or (024) orientations. As a result, the diffraction signal cannot be collected by the detector positioned at 2theta = 44.5°. An example is shown in Figure 4.7 (a), (b) and (c), where the intensity of the grain of interest (marked by the red square) is too weak to identifiy the position in the pole figure at 20V. As a result, this grain was not kept for this study. In the contrary, Figure 4.7(d), (e) and (f) show the case of a grain in which it is always visible at 20V. As a result, it was kept for further analysis.

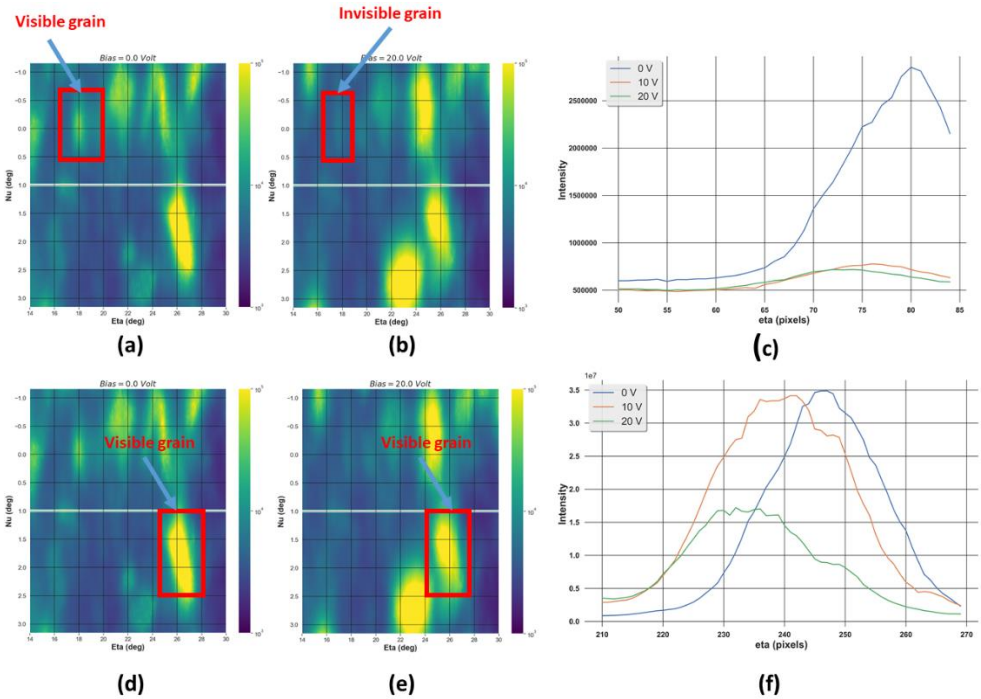

Figure 4.7: Illustration of the grains that are (a), (b) notkept and (d), (e) kept on the pole figure at 0 and 20V. The variation of the intensity of the bad and good grains at different bias is are shown in (c) and (f), respectively

3. Results and discussions

After doing the integration of a specific grain, in both samples, we can observe the (200) pseudo-cubic peak consisting of three peaks originating from the (002), (200) peaks of the tetragonal phase (so called c- and a-domain, respectively) and the (024) peak of the rhombohedral phase (so called r-domain). However, due to the difference in the Zr/Ti ratio between the two samples, a dissimilarity could be noticed in their peak profiles. In the case of PZT52 sample, at the as-processed state, the (024)R peak dominates as shown in Figure 4.8(a), while for the PZT with Zr/Ti ratio of 43/57 , it is the (200)T peak as illustrated in Figure 4.8(b). As expected, the origin of this difference is related to the position of the two compositions in the phase diagram. While the PZT52 is closed to the morphotropic phase boundary [99], the PZT 43/57 is slightly shifted towards the tetragonal region [40]. In order to extract the proportion of each type of domain in a particular grain as well as their behaviour under external electric field in the z- direction, a three-peak fitting was done. Using the least-square minimization Python package (LmFit) with a pseudo-Voigt peak shape, the peak position as well as the intensity and peak width of each of the three phases is obtained. The details on the fitting process were mentioned in Chapter II.1.6.

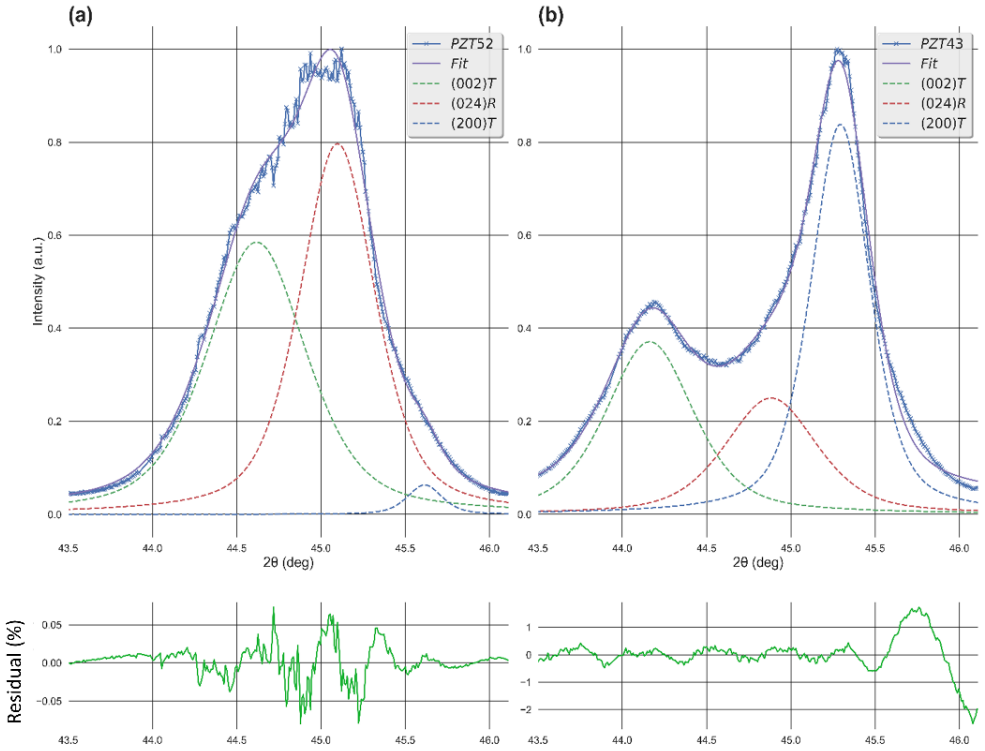

Figure 4.8: 3-peak fitting of the XRD peaks of a single grain at the as-processed state of (a) PZT52 and (b) PZT43 samples based on pseudo-Voigt model

In order to study the mechanical behaviour at grain-scale, the effective longitudinal piezoelectric coefficient $d_{33,eff}$ of each grain is calculated from the Strain – Electric field (S-E) curve of the average strain. To obtain this parameter, it is necessary to calculate the center of gravity of the peak, whose formula is shown in Chapter III.4. From the center of gravity of the peak, the d-spacing corresponding could be deduced using the Bragg's law. The average strain generated by the sample due to applied field can also be extracted as demonstrated in Chapter II.1.5.3.

From the deduced strain, the $d_{33,eff}$ could be extracted by doing the first-order fitting along the slope of the butterfly curve as described in Chapter II.3.2. In our case, due to the strong wake-up behaviour of the samples, the $d_{33,eff}$ extracted from the positive non-switching slope is not reliable. As a result, we took into account the $d_{33,eff}$ extracted from the negative non-switching slope as shown in Figure 4.7(a) and (b).

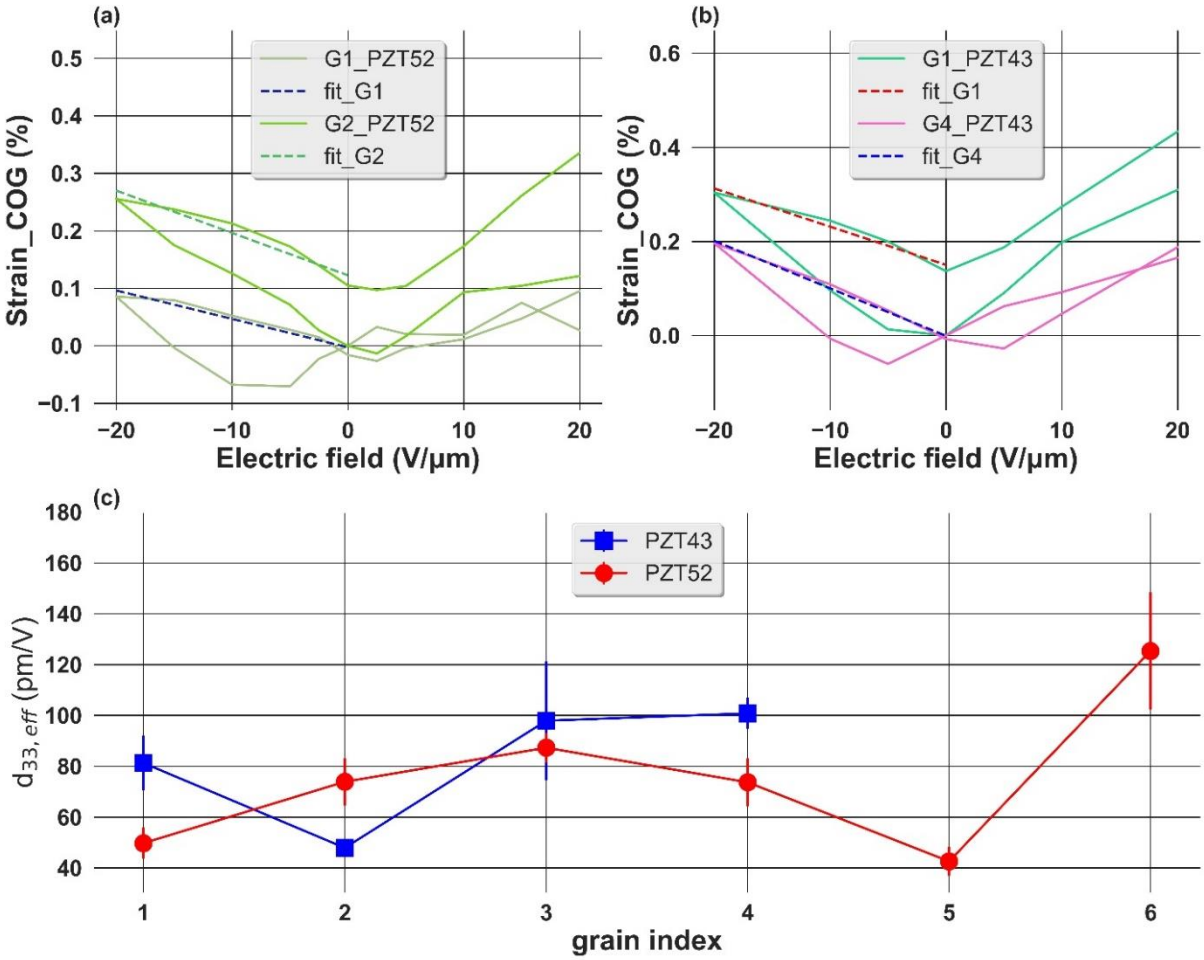

Figure 4.7: The overplot of S-E curve at the grain-scale of (a) PZT52 and (b) PZT43 as well as (c) the extracted $d_{33,eff}$ of 4 grains of PZT43 and 6 grains of PZT52; the dashed lines indicate the $d_{33,eff}$ obtained at pseudo-average scale

The absolute value of $d_{33,eff}$ of PZT43 and PZT52 are shown in Figure 4.7(c) and the error bar indicates the errors from the first-order fitting along the negative slope. It can be seen that there is a variation of $|d_{33,eff}|$ in different grains, indicating an heterogeneity in the mechanical response, which is consistent with the results in the article of Daniels et al. [93] and Majkut et al. [53]. To explain this phenomenon, Majkut et al. proposed that some grains are more favorably aligned relative to the field vector than others while from the article of Daniels et al., it is observed that the local variation in mechanical response could stem from domain morphologies difference at grain scale, leading to the interaction of ferroic domains at grain boundaries [93]. In the paper by Simons et.al [96], an insight on the lattice distortion around embedded domain walls and grain boundaries has been performed, which showed the existence of a symmetry-breaking strain fields which might extend up to several micrometers from domain wall. This strain gradient might lead to the local polarization rotation through flexoelectricity. This non-uniform rotation of polarization leads to a heterogeneity in the mechanical response at grain-scale. Furthermore, in the article by Budimir et al. [100], the relative orientation between the extrinsic and the spontaneous strain has also been reported to impact the d_{33}. If the extrinsic strain is oblique to the spontaneous strain, the symmetry is lower, thus decreasing the stability of the ferroelectric structure while enhancing the piezoelectric property by promoting field-induced rotations of the spontaneous polarization. In the contrary, when the external strain is parallel to the spontaneous strain, the ferroelectric structure is stabilized leading to decreased ferro and piezoelectric properties. As a result, a ferroelectric sample might consist of regions in which the properties are enhanced or reduced. They also lead to the deviation of the local properties from the average ones.

The degree of heterogeneity in the $|d_{33,eff}|$ for the MPB and non-MPB samples is respectively 29.6 and 24.3 pm/V. From previous analysis, $d_{33,eff}$ is found to be around 100 and 50 pm/V for MPB and non-MPB films when analysing the XRD peaks obtained from integrating over the whole Deybye ring. As compared to these absolute values, the degree of d33 heterogeneity is higher in the non-MPB sample. This indicates that the most heterogeneous strain environment at the grain scale is in the non-MPB sample.

To understand these heterogeneities in $d_{33,eff}$, we studied the domain variant evolution. The proportion of each domain variant in a single grain was calculated by dividing the corresponding peak intensity by the sum of the intensity of all the three domain variants in the sample. The results are shown in Figure 4.8 and Figure 4.9 for PZT52 and PZT43, respectively, at 0, -10 and -20V. Without the applied field, the bar charts show a variation inside different grains, indicating a heterogeneity in the proportion of the three domain variants at grain scale in both of the samples, which is consistent with the results reported on bulk ferroelectric sample [53]. The origin of this observation could be due to the anisotropic thermal expansion coefficient and resultant residual stress heterogeneities [53]. During the cooling process, the mechanically interlocked grains contract at unequal rate due to the anisotropy of the thermal expansion tensor and the local disorientation of the grains [101]. As a result, the volume of different domain variants inside each grain differs from each other.

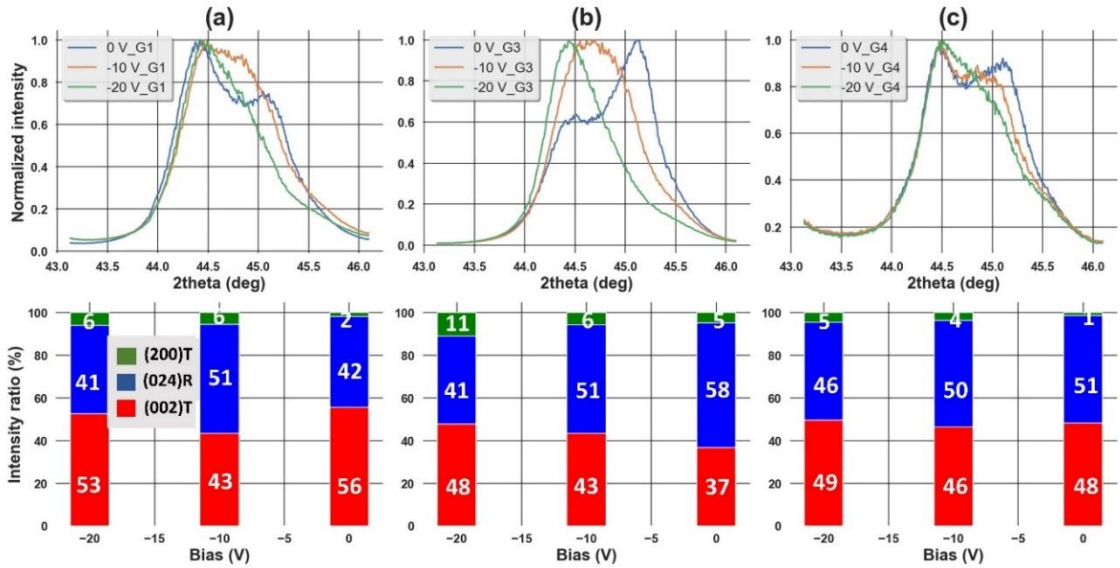

Figure 4.8: The evolution of XRD peak (top) and intensity ratio (bottom) of (a) Grain 1, (b) Grain 3 and (c) Grain 4 of PZT52 sample at 0, -10 and -20V

Under applied electric field, it can be seen that the XRD peak profiles at grains-scale of PZT52 and PZT43 change remarkably in term of both the peak position and intensity. This indicates that the applied electric field lead to changes in the d-spacing and the evolution of the proportion of each domain variant. In the case of PZT52 sample as shown in Figure 4.8(a-c), the (200)T (a-domain) ratio tends to increase from 0 to -20V for all the three mentioned grains. Concerning the c- and r- ratio, the evolution of these domains are not homogeneous for the three grains. In the case of grain 1, the ratio of r-domain increases between 0 and -10V by 9% before decreasing by 10% at -20V. While in the case of grain 3 and grain 4, the proportion of r-domain decreases continuously from 0 to -20V by 17 and 5%, respectively. Considering the average behaviour of the sample, which is obtained by integrating over the complete pole figure as shown in Figure 4.10(a), similarly to the grain 3 and grain 4, the r-domain decreases continuously from 0 to -20V by approximately 11 %. This illustrates that the phase

transformation from rhombohedral to tetragonal dominates under applied field in MPB sample.

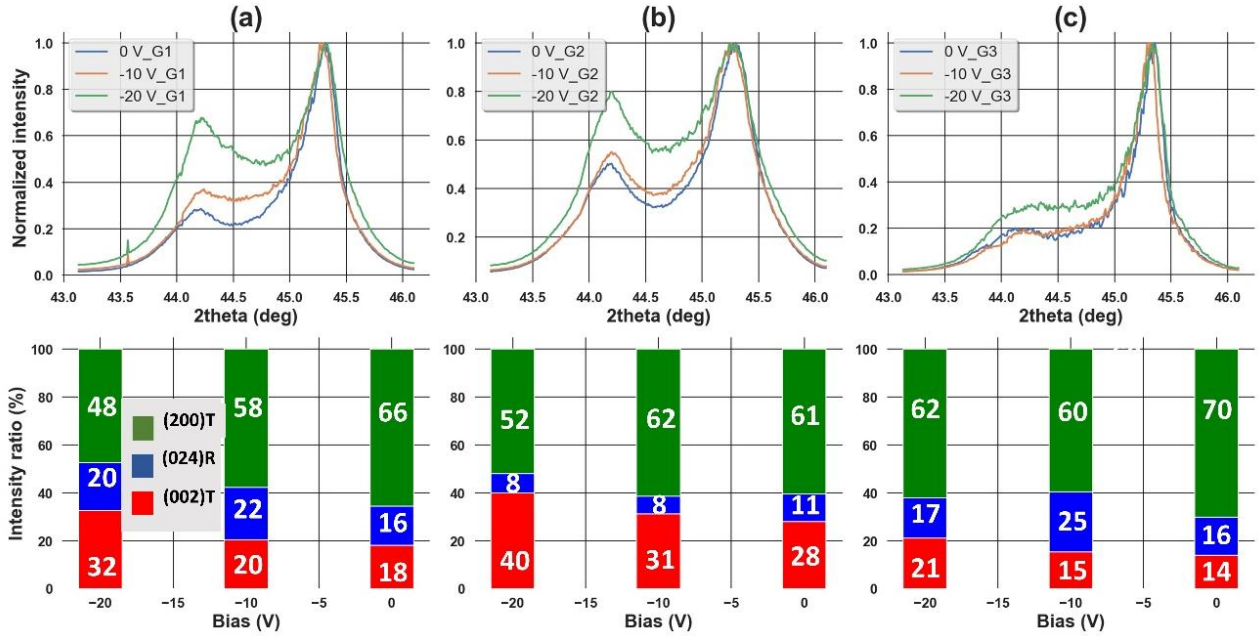

Figure 4.9: The evolution of XRD peak (top) and intensity ratio (bottom) of (a) Grain 1, (b) Grain 2 and (c) Grain 3 of PZT43 sample at 0, -10 and -20V

For the PZT43 sample, in all of the three grains, an increase in the ratio of c- at the expense of a-domain is observed between 0 and -20V, indicating the domain switching effect from a- to c-domain as shown in Figure 4.9(a-c). In comparison with the results published by Daniels et al., our data are consistent in the case of PZT43 as very little phase transformation is observed under applied field between 0 and -20V. Concerning the case of PZT52 (MPB) sample, the observations are not coherent which could be due to the difference in the composition between our sample and the one used by Daniels et al. In our case the sample has MPB composition which facilitates the phase transformation under electric field while Daniels et al. used samples with a majority of tetragonal phase. However, at the intermediate point of -10V, there are differences in the behaviour of the different grains. In the case of grain 1 and 3, a temporary increase in the proportion of r-domain is seen. This indicates that a transformation of a- to r-domain might act as an intermediate step in the switching from a- to c-domain in these grains. Similar to the PZT52 sample, the behaviour of a single grain in PZT43 is not always the same as the average behaviour as no decrease in the proportion of r-domain between -10 and -20V. This indicates that the behaviour at grain scale is localized and it does not always mimic the macroscopic behaviour of the sample.

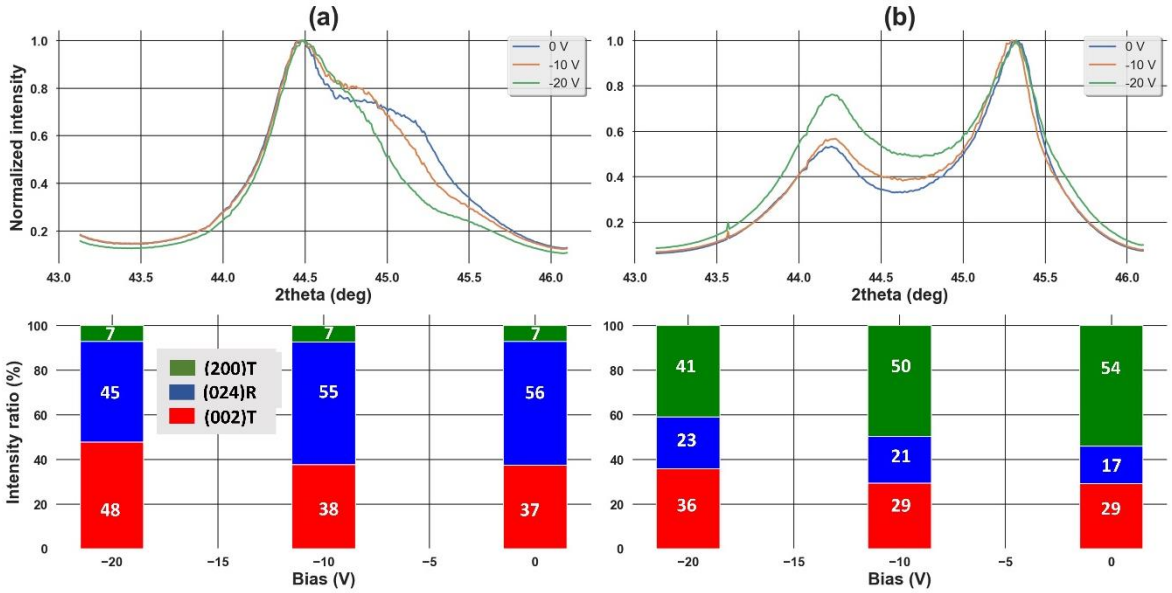

Figure 4.10: The average behaviour of XRD peak (top) and intensity ratio (bottom) of (a) PZT52 and (b) PZT43 at 0, -10 and -20V

A detailed analysis of XRD data provides the lattice parameters of the tetragonal structure, c and a, which could be used to calculate the c/a ratio or tetragonality by the following equation:

$$\frac{\mathbf{1}}{\boldsymbol{d}_{\boldsymbol{hkl}}^{\mathbf{2}}} = \frac{\boldsymbol{h}^{\mathbf{2}} + \boldsymbol{k}^{\mathbf{2}}}{\boldsymbol{a}^{\mathbf{2}}} + \frac{\boldsymbol{l}^{\mathbf{2}}}{\boldsymbol{c}^{\mathbf{2}}} \qquad (4.1)$$

where *d* is the d-spacing of the lattice which can be deduced from the Bragg's equation. The tetragonality is widely studied in ferroelectric materials because it is shown to be correlated with the ferroelectric properties [102] [103] [104].

Firstly, concerning the pseudo-average tetragonality of different grains in the as-processed state, it was found that this quantity is higher in the case of PZT43 (1,023 vs 1,019). This could be explained as the result of the higher proportion of Ti in PZT43 sample used in this study. According to PZT phase diagram, a Ti proportion of 57% will position the sample into the tetragonal region, leading to the higher c/a ratio in PZT43. Under applied electric field, the tetragonality increased to 1.025 and 1.026 in PZT43 and PZT52, respectively. This could be a result of the growth of c-domains under applied field [105]

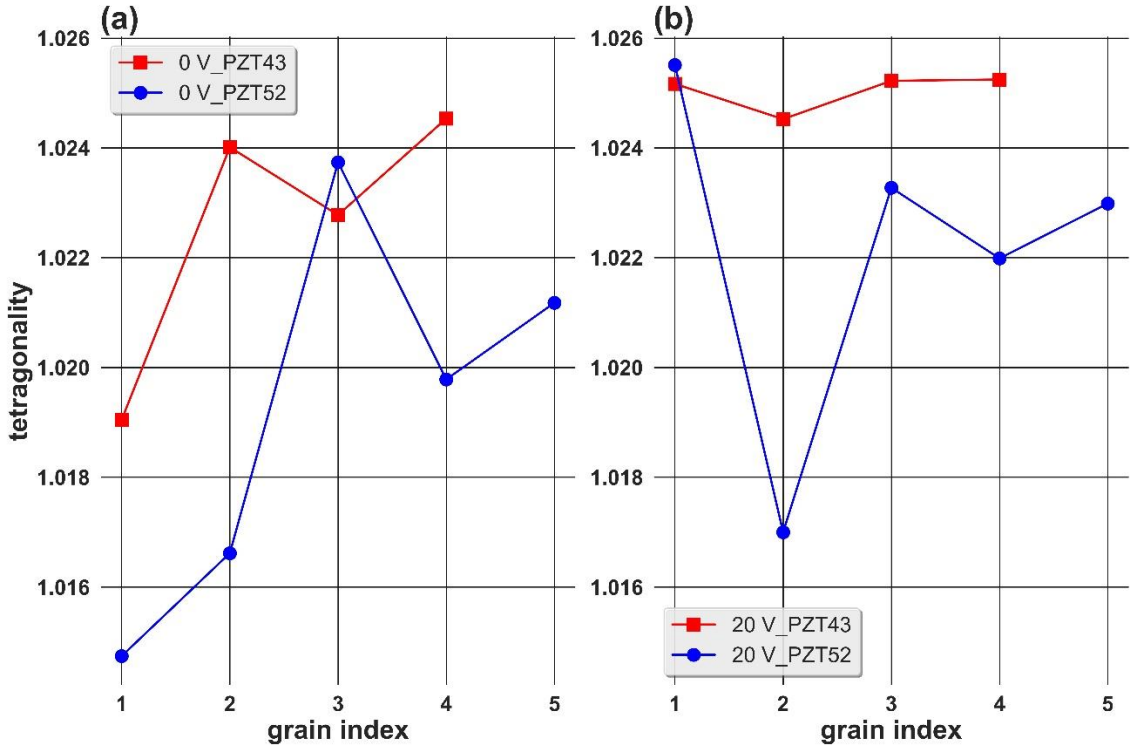

Figure 4.11: Tetragonality of PZT43 and PZT52 at (a) 0V and (b) 20V

. When getting down to the individual grains, it can be observed from Figure 4.11(a) and (b) that in both of the samples the behavior differs from grain to grain, indicating a heterogeneity in both the c/a ratio as well as its evolution under electric field. For example, in the case of grain 2 and grain 3 in PZT52, its tetragonality stays almost the same between 0 and 20V (1.017 for grain 2 and 1.023 for grain 3) while in the case of grain 1, an increase from 1.014 to 1.025 was seen. Finally, to compare the rate of heterogeneity between the two kinds of sample, the standard deviations of the c/a ratio at 0 and 20 V have been calculated. The results showed that in both cases, the dispersion is higher in PZT52 ($3.5\text{x}10^{-3}$ vs $2.9\text{x}10^{-4}$ at 0V and $2.5\text{x}10^{-3}$ vs $3.4\text{x}10^{-4}$ at 20V), indicating a higher heterogeneity in the MPB sample. An explanation for these observations could be that the crystallographic structure is more complex in the case of MPB sample, whose composition stays at the interface between rhombohedral and tetragonal phases. As a result, under external stimuli, the crystallographic structure inside each grain might transform more easily between the tetragonal and rhombohedral phases in both directions [106].

Conclusions

In this study, we have succeeded in implementing the in-situ biasing technique with a micronic X-ray beam using synchrotron source to study the grain-scale behavior in ferroelectric thin films of PZT with or without MPB composition. From the recorded XRD peaks of both samples, the effective piezoelectric coefficient $d_{33,eff}$ of individual grains have been quantified. A dispersion is observed and is attributed to the interaction between grain at grain boundaries, the existence of a strain gradient and the relative orientation between the extrinsic and spontaneous strain. The origin of this local piezoresponse is then discussed in term of domain ratio and tetragonality evolution with an applied

bias. In the MPB sample, the rhombohedral domain is dominant while non-MPB one is in the minority. The dispersion in the initial state of r- and c-domain ratio is observed between grains and the average behavior leading to an increase of c-domain at high field is quite disperse at the grain scale. Furthermore, the standard deviation of tetragonality and $d_{33,eff}$ is higher in the case of PZT52 sample, indicating that the heterogeneity is higher in the MPB sample for structural property at the grain scale. Being the first effort in implementing the in-situ biasing micro-XRD for studying ferroelectric thin film, in the future, the experiment could be improved by doing a rocking curve with larger range of eta, allowing the study of more grains. Furthermore, the grain identification process could also be optimized by an automatic grain identification program, which could help reduce the data analysis time.

References for chapter IV

[1] J. Evans *et al.*, "A discrete ferroelectric memory," in *2012 12th Annual Non-Volatile Memory Technology Symposium Proceedings*, Singapore: IEEE, Oct. 2012, pp. 33–36. doi: 10.1109/NVMTS.2013.6632857.

[2] Jérôme Mouly, "PIEZOELECTRIC DEVICES: FROM BULK TO THIN-FILM 2019," Yole development.

[3] Eric Mounier, Dimitrios Damianos, "Status of the MEMS industry 2019," Yole development.

[4] J. Bok and C. Kounelis, "Paul Langevin (1872-1946) - De la butte Montmartre au Panthéon : parcours d'un physicien d'exception," *Reflets Phys.*, no. 1, pp. 14–16, Sep. 2006, doi: 10.1051/refdp/2006007.

[5] J. Valasek, "Piezo-Electric and Allied Phenomena in Rochelle Salt," *Phys. Rev.*, vol. 17, no. 4, pp. 475–481, Apr. 1921, doi: 10.1103/PhysRev.17.475.

[6] A. T. Gen Shirane, "Phase Transitions in Solid Solutions of PbZrO3 and PbTiO3 (I) Small Concentrations of PbTiO3," *J. Phys. Soc. Jpn.*, vol. 7, pp. 5–11, Jan. 1952, doi: https://doi.org/10.1143/JPSJ.7.5.

[7] G. H. Haertling, "Ferroelectric Ceramics: History and Technology," *J. Am. Ceram. Soc.*, vol. 82, no. 4, pp. 797–818, Apr. 1999, doi: 10.1111/j.1151-2916.1999.tb01840.x.

[8] M. Ishida, S. Tsuji, K. Kimura, H. Matsunami, and T. Tanaka, "EPITAXIAL GROWTH OF FERROELECTRIC PLZT [(Pb, La)(Zr,Ti)Oa1 THIN FILMS," p. 6.

[9] M. Oikawa and K. Toda, "Preparation of Pb(Zr,Ti)O $_3$ thin films by an electron beam evaporation technique," *Appl. Phys. Lett.*, vol. 29, no. 8, pp. 491–492, Oct. 1976, doi: 10.1063/1.89133.

[10] M. Ishida, H. Matsunami, and T. Tanaka, "Preparation and properties of ferroelectric PLZT thin films by rf sputtering," p. 4.

[11] H. Adachi, T. Kawaguchi, K. Setsune, K. Ohji, and K. Wasa, "Electro-optic effects of (Pb, La)(Zr, Ti)O $_3$ thin films prepared by rf planar magnetron sputtering," *Appl. Phys. Lett.*, vol. 42, no. 10, pp. 867–868, May 1983, doi: 10.1063/1.93795.

[12] K. Iijima, Y. Tomita, R. Takayama, and I. Ueda, "Preparation of *c* -axis oriented PbTiO $_3$ thin films and their crystallographic, dielectric, and pyroelectric properties," *J. Appl. Phys.*, vol. 60, no. 1, pp. 361–367, Jul. 1986, doi: 10.1063/1.337654.

[13] N. Shohata, S. Matsubara, Y. Miyasaka, and M. Yonezawa, "Epitaxial Growth of PbTiO3on MgAl2O4/Si Substrates," in *Sixth IEEE International Symposium on Applications of Ferroelectrics*, Jun. 1986, pp. 580–584. doi: 10.1109/ISAF.1986.201210.

[14] S. K. Dey, K. D. Budd, and D. A. Payne, "Thin-film ferroelectrics of PZT of sol-gel processing," *IEEE Trans. Ultrason. Ferroelectr. Freq. Control*, vol. 35, no. 1, pp. 80–81, Jan. 1988, doi: 10.1109/58.4153.

[15] J. Xu, A. S. Shaikh, and R. W. Vest, "High K BaTiO/sub 3/ films from metalloorganic precursors," *IEEE Trans. Ultrason. Ferroelectr. Freq. Control*, vol. 36, no. 3, pp. 307–312, May

1989, doi: 10.1109/58.19168.
[16] G. M. Davis and M. C. Gower, “Epitaxial growth of thin films of $BaTiO_3$ using excimer laser ablation,” *Appl. Phys. Lett.*, vol. 55, no. 2, pp. 112–114, Jul. 1989, doi: 10.1063/1.102393.
[17] M. Okada, S. Takai, M. Amemiya, and K. Tominaga, “Preparation of *c* -Axis-Oriented $PbTiO_3$ Thin Films by MOCVD under Reduced Pressure,” *Jpn. J. Appl. Phys.*, vol. 28, no. Part 1, No. 6, pp. 1030–1034, Jun. 1989, doi: 10.1143/JJAP.28.1030.
[18] K. Iijima, T. Terashima, K. Yamamoto, K. Hirata, and Y. Bando, “Preparation of ferroelectric $BaTiO_3$ thin films by activated reactive evaporation,” *Appl. Phys. Lett.*, vol. 56, no. 6, pp. 527–529, Feb. 1990, doi: 10.1063/1.103300.
[19] R. A. Roy, K. F. Etzold, and J. J. Cuomo, “Ferroelectric Film Synthesis, Past and Present: A Select Review,” *MRS Proc.*, vol. 200, p. 141, 1990, doi: 10.1557/PROC-200-141.
[20] N. Menou, “Technologie FeRAM: fiabilité et mécanismes de défaillance de condensateurs ferroélectriques élémentaires et intégrés,” p. 239.
[21] C. M. Fancher *et al.*, “The contribution of 180° domain wall motion to dielectric properties quantified from in situ X-ray diffraction,” *Acta Mater.*, vol. 126, pp. 36–43, Mar. 2017, doi: 10.1016/j.actamat.2016.12.037.
[22] D. Damjanovic, “Ferroelectric, dielectric and piezoelectric properties of ferroelectric thin films and ceramics,” *Rep. Prog. Phys.*, vol. 61, no. 9, pp. 1267–1324, Sep. 1998, doi: 10.1088/0034-4885/61/9/002.
[23] S. Wada and T. Tsurumi, “Enhanced piezoelectricity of barium titanate single crystals with engineered domain configuration,” *Br. Ceram. Trans.*, vol. 103, no. 2, pp. 93–96, Apr. 2004, doi: 10.1179/096797804225012747.
[24] K. Lefki and G. J. M. Dormans, “Measurement of piezoelectric coefficients of ferroelectric thin films,” *J. Appl. Phys.*, vol. 76, no. 3, pp. 1764–1767, Aug. 1994, doi: 10.1063/1.357693.
[25] S. Trolier-Mckinstry and P. Muralt, “Thin Film Piezoelectrics for MEMS,” p. 11.
[26] E. Jabari, F. Ahmed, F. Liravi, E. B. Secor, L. Lin, and E. Toyserkani, “2D printing of graphene: a review,” *2D Mater.*, vol. 6, no. 4, p. 042004, Aug. 2019, doi: 10.1088/2053-1583/ab29b2.
[27] S. Nicolas *et al.*, “Fabrication and characterization of a new varifocal liquid lens with embedded PZT actuators for high optical performances,” in *2015 28th IEEE International Conference on Micro Electro Mechanical Systems (MEMS)*, Jan. 2015, pp. 65–68. doi: 10.1109/MEMSYS.2015.7050887.
[28] H. Wang, Z. Chen, and H. Xie, “A high-SPL piezoelectric MEMS loud speaker based on thin ceramic PZT,” *Sens. Actuators Phys.*, vol. 309, p. 112018, Jul. 2020, doi: 10.1016/j.sna.2020.112018.
[29] M. Tani, M. Akamatsu, Y. Yasuda, and H. Toshiyoshi, “A two-axis piezoelectric tilting micromirror with a newly developed PZT-meandering actuator,” in *2007 IEEE 20th International Conference on Micro Electro Mechanical Systems (MEMS)*, Jan. 2007, pp. 699–702. doi: 10.1109/MEMSYS.2007.4432994.
[30] P. Laitinen and J. Mawnpaa, “Enabling mobile haptic design: piezoelectric actuator technology properties in hand held devices,” in *2006 IEEE International Workshop on Haptic Audio Visual Environments and their Applications (HAVE 2006)*, Nov. 2006, pp. 40–43. doi: 10.1109/HAVE.2006.283787.
[31] H. K. Ma, B. R. Hou, H. Y. Wu, C. Y. Lin, J. J. Gao, and M. C. Kou, “Development and application of a diaphragm micro-pump with piezoelectric device,” *Microsyst. Technol.*, vol. 14, no. 7, pp. 1001–1007, Jul. 2008, doi: 10.1007/s00542-007-0462-6.
[32] P. Muralt, “PZT thin films for microsensors and actuators: Where do we stand?,” *IEEE Trans. Ultrason. Ferroelectr. Freq. Control*, vol. 47, no. 4, pp. 903–915, Jul. 2000, doi: 10.1109/58.852073.
[33] “What is a SAW Filter ?,” *everythingRF*. https://www.everythingrf.com/community/what-is-a-saw-filter
[34] T. Giffney, M. Yu, K. C. Aw, and H. Zhang, “Contactless RF MEMS switch using PZT actuation,” in *The 8th Annual IEEE International Conference on Nano/Micro Engineered and Molecular*

Systems, Apr. 2013, pp. 861–864. doi: 10.1109/NEMS.2013.6559860.
[35] J. S. Meena, S. M. Sze, U. Chand, and T.-Y. Tseng, "Overview of emerging nonvolatile memory technologies," *Nanoscale Res. Lett.*, vol. 9, no. 1, p. 526, Dec. 2014, doi: 10.1186/1556-276X-9-526.
[36] Volker Rzehak, "Low-Power FRAM Microcontrollers and Their Applications," Texas Instrument, 2019.
[37] J. Müller *et al.*, "Ferroelectricity in yttrium-doped hafnium oxide," *J. Appl. Phys.*, vol. 110, no. 11, p. 114113, Dec. 2011, doi: 10.1063/1.3667205.
[38] T. Francois *et al.*, "Demonstration of BEOL-compatible ferroelectric Hf0.5Zr0.5O2 scaled FeRAM co-integrated with 130nm CMOS for embedded NVM applications," in *2019 IEEE International Electron Devices Meeting (IEDM)*, Dec. 2019, p. 15.7.1-15.7.4. doi: 10.1109/IEDM19573.2019.8993485.
[39] S. Priya *et al.*, "A Review on Piezoelectric Energy Harvesting: Materials, Methods, and Circuits," *Energy Harvest. Syst.*, vol. 4, no. 1, pp. 3–39, Aug. 2019, doi: 10.1515/ehs-2016-0028.
[40] B. Noheda *et al.*, "Tetragonal-to-monoclinic phase transition in a ferroelectric perovskite: The structure of PbZr 0.52 Ti 0.48 O 3," *Phys. Rev. B*, vol. 61, no. 13, pp. 8687–8695, Apr. 2000, doi: 10.1103/PhysRevB.61.8687.
[41] M. Ahart *et al.*, "Origin of morphotropic phase boundaries in ferroelectrics," *Nature*, vol. 451, no. 7178, pp. 545–548, Jan. 2008, doi: 10.1038/nature06459.
[42] G. A. Rossetti and A. G. Khachaturyan, "Inherent nanoscale structural instabilities near morphotropic boundaries in ferroelectric solid solutions," *Appl. Phys. Lett.*, vol. 91, no. 7, p. 072909, Aug. 2007, doi: 10.1063/1.2771095.
[43] R. Ahluwalia, T. Lookman, A. Saxena, and W. Cao, "Domain-size dependence of piezoelectric properties of ferroelectrics," *Phys. Rev. B*, vol. 72, no. 1, p. 014112, Jul. 2005, doi: 10.1103/PhysRevB.72.014112.
[44] N. Setter *et al.*, "Ferroelectric thin films: Review of materials, properties, and applications," *J. Appl. Phys.*, vol. 100, no. 5, p. 051606, Sep. 2006, doi: 10.1063/1.2336999.
[45] R. Guo, L. E. Cross, S.-E. Park, B. Noheda, D. E. Cox, and G. Shirane, "Origin of the High Piezoelectric Response in PbZr 1 − x Ti x O 3," *Phys. Rev. Lett.*, vol. 84, no. 23, pp. 5423–5426, Jun. 2000, doi: 10.1103/PhysRevLett.84.5423.
[46] L. Bellaiche, A. García, and D. Vanderbilt, "Finite-Temperature Properties of Pb (Zr 1 − x Ti x) O 3 Alloys from First Principles," *Phys. Rev. Lett.*, vol. 84, no. 23, pp. 5427–5430, Jun. 2000, doi: 10.1103/PhysRevLett.84.5427.
[47] M. Hinterstein *et al.*, "Structural Description of the Macroscopic Piezo- and Ferroelectric Properties of Lead Zirconate Titanate," *Phys. Rev. Lett.*, vol. 107, no. 7, p. 077602, Aug. 2011, doi: 10.1103/PhysRevLett.107.077602.
[48] V. Kovacova, N. Vaxelaire, G. Le Rhun, P. Gergaud, T. Schmitz-Kempen, and E. Defay, "Correlation between electric-field-induced phase transition and piezoelectricity in lead zirconate titanate films," *Phys. Rev. B*, vol. 90, no. 14, p. 140101, Oct. 2014, doi: 10.1103/PhysRevB.90.140101.
[49] T. W. Cornelius *et al.*, "Piezoelectric response and electrical properties of Pb(Zr 1-x Ti x)O 3 thin films: The role of imprint and composition," *J. Appl. Phys.*, vol. 122, no. 16, pp. 164104–164104, Oct. 2017, doi: 10.1063/1.4994939.
[50] T. W. Cornelius *et al.*, "Piezoelectric Properties of Pb1−xLax(Zr0.52Ti0.48)1−x/4O3 Thin Films Studied by In Situ X-ray Diffraction," *Materials*, vol. 13, no. 15, p. 3338, Jul. 2020, doi: 10.3390/ma13153338.
[51] P. Jiang *et al.*, "Wake-Up Effect in HfO2-Based Ferroelectric Films," *Adv. Electron. Mater.*, vol. 7, no. 1, p. 2000728, 2021, doi: 10.1002/aelm.202000728.
[52] Q. Y. Jiang, E. C. Subbarao, and L. E. Cross, "Effect of composition and temperature on electric fatigue of La-doped lead zirconate titanate ceramics," *J. Appl. Phys.*, vol. 75, no. 11, pp. 7433–7443, Jun. 1994, doi: 10.1063/1.356637.

[53] M. Majkut, J. E. Daniels, J. P. Wright, S. Schmidt, and J. Oddershede, “Electromechanical Response of Polycrystalline Barium Titanate Resolved at the Grain Scale,” *J. Am. Ceram. Soc.*, vol. 100, no. 1, pp. 393–402, Jan. 2017, doi: 10.1111/jace.14481.
[54] H. N. Al-Shareef, A. I. Kingon, X. Chen, K. R. Bellur, and O. Auciello, “Contribution of electrodes and microstructures to the electrical properties of Pb(Zr $_{0.53}$ Ti $_{0.47}$)O $_3$ thin film capacitors,” *J. Mater. Res.*, vol. 9, no. 11, pp. 2968–2975, Nov. 1994, doi: 10.1557/JMR.1994.2968.
[55] C. Künneth, R. Batra, G. A. Rossetti, R. Ramprasad, and A. Kersch, “Thermodynamics of Phase Stability and Ferroelectricity From First Principles,” in *Ferroelectricity in Doped Hafnium Oxide: Materials, Properties and Devices*, Elsevier, 2019, pp. 245–289. doi: 10.1016/B978-0-08-102430-0.00006-1.
[56] M. Pešić *et al.*, “Physical Mechanisms behind the Field-Cycling Behavior of HfO2-Based Ferroelectric Capacitors,” *Adv. Funct. Mater.*, vol. 26, no. 25, pp. 4601–4612, 2016, doi: https://doi.org/10.1002/adfm.201600590.
[57] W. L. Warren *et al.*, “Polarization suppression in Pb(Zr,Ti)O $_3$ thin films,” *J. Appl. Phys.*, vol. 77, no. 12, pp. 6695–6702, Jun. 1995, doi: 10.1063/1.359083.
[58] H. M. Duiker *et al.*, “Fatigue and switching in ferroelectric memories: Theory and experiment,” *J. Appl. Phys.*, vol. 68, no. 11, pp. 5783–5791, Dec. 1990, doi: 10.1063/1.346948.
[59] J. F. Scott, C. A. Araujo, B. M. Melnick, L. D. McMillan, and R. Zuleeg, “Quantitative measurement of space-charge effects in lead zirconate-titanate memories,” *J. Appl. Phys.*, vol. 70, no. 1, pp. 382–388, Jul. 1991, doi: 10.1063/1.350286.
[60] H. Zou, “Effect of Nb Doping on Crystalline Orientation, Electric and Fatigue Properties of PZT Thin Films Prepared by Sol-Gel Process,” *J. Ceram. Sci. Technol.*, no. 04, 2017, doi: 10.4416/JCST2017-00031.
[61] H. Sun, Y. Zhang, X. Liu, S. Guo, Y. Liu, and W. Chen, “The effect of Mn/Nb doping on dielectric and ferroelectric properties of PZT thin films prepared by sol–gel process,” *J. Sol-Gel Sci. Technol.*, vol. 74, no. 2, pp. 378–386, May 2015, doi: 10.1007/s10971-014-3608-x.
[62] J. M. Benedetto, “Imprint induced failure modes in ferroelectric non-volatile memories,” *Integr. Ferroelectr.*, vol. 15, no. 1–4, pp. 29–38, Feb. 1997, doi: 10.1080/10584589708015694.
[63] G. Arlt and H. Neumann, “Internal bias in ferroelectric ceramics: Origin and time dependence,” *Ferroelectrics*, vol. 87, no. 1, pp. 109–120, Nov. 1988, doi: 10.1080/00150198808201374.
[64] R. Lohkämper, H. Neumann, and G. Arlt, “Internal bias in acceptor-doped BaTiO $_3$ ceramics: Numerical evaluation of increase and decrease,” *J. Appl. Phys.*, vol. 68, no. 8, pp. 4220–4224, Oct. 1990, doi: 10.1063/1.346212.
[65] D. Dimos, W. L. Warren, M. B. Sinclair, B. A. Tuttle, and R. W. Schwartz, “Photoinduced hysteresis changes and optical storage in (Pb,La)(Zr,Ti)O $_3$ thin films and ceramics,” *J. Appl. Phys.*, vol. 76, no. 7, pp. 4305–4315, Oct. 1994, doi: 10.1063/1.357316.
[66] M. Grossmann, O. Lohse, D. Bolten, U. Boettger, T. Schneller, and R. Waser, “The interface screening model as origin of imprint in PbZrxTi1−xO3 thin films. I. Dopant, illumination, and bias dependence,” *J. Appl. Phys.*, vol. 92, no. 5, pp. 2680–2687, Sep. 2002, doi: 10.1063/1.1498966.
[67] R. Roque, “X-ray imaging using 100 µm thick Gas Electron Multipliers operating in Kr-CO2 mixtures,” Unpublished, 2018. Accessed: Aug. 07, 2022. [Online]. Available: http://rgdoi.net/10.13140/RG.2.2.16794.49600
[68] European Synchrotron Radiation Facility, “QUESTIONS & ANSWERS.” https://www.esrf.fr/about/ask-an-expert/questions-answers#:~:text=The%20most%20important%20advantage%20of,angular%20spread%20of%20the%20beam.
[69] M. Birkholz, “Thin Film Analysis by X-Ray Scattering,” p. 381.
[70] H. Möller and J. Barbers, *Mitt Kais. Wilhelm Inst. Eisenforsch.*, vol. 16, p. 21, 1934.
[71] P. Gravereau, “Introduction à la pratique de la diffraction des rayons X par les poudres,” p. 210.

[72] Newville, Matthew ; Stensitzki, Till ; Allen, Daniel B. ; Rawlik, Michal ; Ingargiola, Antonino ; Nelson, Andrew, “LMFIT: Non-Linear Least-Square Minimization and Curve-Fitting for Python”, doi: 10.5281/zenodo.11813.
[73] Q. M. Zhang, W. Y. Pan, and L. E. Cross, “Laser interferometer for the study of piezoelectric and electrostrictive strains,” *J. Appl. Phys.*, vol. 63, no. 8, pp. 2492–2496, Apr. 1988, doi: 10.1063/1.341027.
[74] A. L. Kholkin, Ch. Wütchrich, D. V. Taylor, and N. Setter, “Interferometric measurements of electric field-induced displacements in piezoelectric thin films,” *Rev. Sci. Instrum.*, vol. 67, no. 5, pp. 1935–1941, May 1996, doi: 10.1063/1.1147000.
[75] Z. Huang and R. W. Whatmore, “A double-beam common path laser interferometer for the measurement of electric field-induced strains of piezoelectric thin films,” *Rev. Sci. Instrum.*, vol. 76, no. 12, p. 123906, Dec. 2005, doi: 10.1063/1.2149002.
[76] “PyVISA: Control your instruments with Python.” https://pyvisa.readthedocs.io/en/latest/
[77] N. Vaxelaire *et al.*, “Effect of structural in-depth heterogeneities on electrical properties of Pb(Zr0.52Ti0.48) O3 thin films as revealed by nano-beam X-ray diffraction,” *J. Appl. Phys.*, vol. 120, no. 10, p. 104101, Sep. 2016, doi: 10.1063/1.4962427.
[78] B. Noheda *et al.*, “Tetragonal-to-monoclinic phase transition in a ferroelectric perovskite: The structure of PbZr 0.52 Ti 0.48 O 3,” *Phys. Rev. B*, vol. 61, no. 13, pp. 8687–8695, Apr. 2000, doi: 10.1103/PhysRevB.61.8687.
[79] S. K. Sayyed and S. A. Acharya, “Synthesis of PZT nanorods and study of dielectric behaviour,” presented at the PROCEEDING OF INTERNATIONAL CONFERENCE ON RECENT TRENDS IN APPLIED PHYSICS AND MATERIAL SCIENCE: RAM 2013, Bikaner, Rajasthan, India, 2013, pp. 111–112. doi: 10.1063/1.4810125.
[80] Wojciech Paszkowicz, “Application of a powder diffractometer equipped with a strip detector and Johansson monochromator to phase analysis and structure refinement,” *Nucl. Instrum. Methods Phys. Res. Sect. Accel. Spectrometers Detect. Assoc. Equip.*, vol. 551, no. 1, pp. 162–177, Oct. 2005, doi: 10.1016/j.nima.2005.07.068.
[81] K. T. Li and V. C. Lo, “Simulation of thickness dependence in ferroelectric thin films,” *Solid State Commun.*, vol. 132, no. 1, pp. 49–54, Oct. 2004, doi: 10.1016/j.ssc.2004.07.013.
[82] M. Dekkers, M. D. Nguyen, R. Steenwelle, P. M. te Riele, D. H. A. Blank, and G. Rijnders, “Ferroelectric properties of epitaxial Pb(Zr,Ti)O3 thin films on silicon by control of crystal orientation,” *Appl. Phys. Lett.*, vol. 95, no. 1, p. 012902, Jul. 2009, doi: 10.1063/1.3163057.
[83] Yu. V. Podgorny, D. S. Seregin, A. S. Sigov, and K. A. Vorotilov, “Effect of Sol-Gel PZT Film Thickness on the Hysteresis Properties,” *Ferroelectrics*, vol. 439, no. 1, pp. 74–79, Jan. 2012, doi: 10.1080/00150193.2012.741952.
[84] A. J. Fox, B. Drawl, G. R. Fox, B. J. Gibbons, and S. Trolier-McKinstry, “Control of crystallographic texture and surface morphology of Pt/Tio2 templates for enhanced PZT thin film texture,” *IEEE Trans. Ultrason. Ferroelectr. Freq. Control*, vol. 62, no. 1, pp. 56–61, Jan. 2015, doi: 10.1109/TUFFC.2014.006671.
[85] E. M. Alkoy, S. Alkoy, and T. Shiosaki, “The effect of crystallographic orientation and solution aging on the electrical properties of sol–gel derived Pb(Zr0.45Ti0.55)O3 thin films,” *Ceram. Int.*, vol. 33, no. 8, pp. 1455–1462, Dec. 2007, doi: 10.1016/j.ceramint.2006.06.010.
[86] Y. Kim, H. Han, I. Vrejoiu, W. Lee, D. Hesse, and M. Alexe, “Origins of domain wall pinning in ferroelectric nanocapacitors,” *Nano Converg.*, vol. 1, no. 1, p. 24, Dec. 2014, doi: 10.1186/s40580-014-0024-4.
[87] J. A. Christman, R. R. Woolcott, A. I. Kingon, and R. J. Nemanich, “Piezoelectric measurements with atomic force microscopy,” p. 4.
[88] O. Kuffer, I. Maggio-Aprile, J.-M. Triscone, O. Fischer, and Ch. Renner, “Piezoelectric response of epitaxial Pb(Zr0.2Ti0.8)O3 films measured by scanning tunneling microscopy,” *Appl. Phys. Lett.*, vol. 77, no. 11, pp. 1701–1703, Sep. 2000, doi: 10.1063/1.1309017.
[89] A. L. Kholkin, Ch. Wütchrich, D. V. Taylor, and N. Setter, “Interferometric measurements of electric field-induced displacements in piezoelectric thin films,” *Rev. Sci. Instrum.*, vol. 67, no.

5, pp. 1935–1941, May 1996, doi: 10.1063/1.1147000.
[90] Z. Huang and R. W. Whatmore, “A double-beam common path laser interferometer for the measurement of electric field-induced strains of piezoelectric thin films,” *Rev. Sci. Instrum.*, vol. 76, no. 12, p. 123906, Dec. 2005, doi: 10.1063/1.2149002.
[91] H. Weitzing, G. A. Schneider, J. Steffens, M. Hammer, and M. J. Hoffmann, “Cyclic fatigue due to electric loading in ferroelectric ceramics,” *J. Eur. Ceram. Soc.*, vol. 19, no. 6, pp. 1333–1337, Jun. 1999, doi: 10.1016/S0955-2219(98)00429-4.
[92] R. Herbiet, H. Tenbrock, and G. Arlt, “The aging behaviour of the complex material parameters ε, d and s in ferroelectric PZT ceramics,” *Ferroelectrics*, vol. 76, no. 1, pp. 319–326, Dec. 1987, doi: 10.1080/00150198708016952.
[93] J. E. Daniels *et al.*, “Heterogeneous grain-scale response in ferroic polycrystals under electric field,” *Sci. Rep.*, vol. 6, no. 1, p. 22820, Mar. 2016, doi: 10.1038/srep22820.
[94] Q. Li and M. Kuna, “Inhomogeneity and material configurational forces in three dimensional ferroelectric polycrystals,” *Eur. J. Mech. - ASolids*, vol. 31, no. 1, pp. 77–89, Jan. 2012, doi: 10.1016/j.euromechsol.2011.07.004.
[95] L. Fan, W. Werner, S. Subotić, D. Schneider, M. Hinterstein, and B. Nestler, “Multigrain phase-field simulation in ferroelectrics with phase coexistences: An improved phase-field model,” *Comput. Mater. Sci.*, vol. 203, p. 111056, Feb. 2022, doi: 10.1016/j.commatsci.2021.111056.
[96] H. Simons *et al.*, “Long-range symmetry breaking in embedded ferroelectrics,” *Nat. Mater.*, vol. 17, no. 9, pp. 814–819, Sep. 2018, doi: 10.1038/s41563-018-0116-3.
[97] E. K. H. Salje, S. Li, M. Stengel, P. Gumbsch, and X. Ding, “Flexoelectricity and the polarity of complex ferroelastic twin patterns,” *Phys. Rev. B*, vol. 94, no. 2, p. 024114, Jul. 2016, doi: 10.1103/PhysRevB.94.024114.
[98] J. Novak, U. Bismayer, and E. K. H. Salje, “Simulated equilibrium shapes of ferroelastic needle domains,” *J. Phys. Condens. Matter*, vol. 14, no. 3, pp. 657–664, Jan. 2002, doi: 10.1088/0953-8984/14/3/332.
[99] A. S. Karapuzha, N. K. James, H. Khanbareh, S. van der Zwaag, and W. A. Groen, “Structure, dielectric and piezoelectric properties of donor doped PZT ceramics across the phase diagram,” *Ferroelectrics*, vol. 504, no. 1, pp. 160–171, Nov. 2016, doi: 10.1080/00150193.2016.1240571.
[100] M. Budimir, D. Damjanovic, and N. Setter, “Enhancement of the piezoelectric response of tetragonal perovskite single crystals by uniaxial stress applied along the polar axis: A free-energy approach,” *Phys. Rev. B*, vol. 72, no. 6, p. 064107, Aug. 2005, doi: 10.1103/PhysRevB.72.064107.
[101] E.-M. Anton, R. E. García, T. S. Key, J. E. Blendell, and K. J. Bowman, “Domain switching mechanisms in polycrystalline ferroelectrics with asymmetric hysteretic behavior,” *J. Appl. Phys.*, vol. 105, no. 2, p. 024107, Jan. 2009, doi: 10.1063/1.3068333.
[102] C. Lichtensteiger, J.-M. Triscone, J. Junquera, and P. Ghosez, “Ferroelectricity and Tetragonality in Ultrathin P b T i O 3 Films,” *Phys. Rev. Lett.*, vol. 94, no. 4, p. 047603, Feb. 2005, doi: 10.1103/PhysRevLett.94.047603.
[103] C. A. Randall, N. Kim, J.-P. Kucera, W. Cao, and T. R. Shrout, “Intrinsic and Extrinsic Size Effects in Fine-Grained Morphotropic-Phase-Boundary Lead Zirconate Titanate Ceramics,” *J. Am. Ceram. Soc.*, vol. 81, no. 3, pp. 677–688, 1998, doi: 10.1111/j.1151-2916.1998.tb02389.x.
[104] Y. Wei, C. Jin, P. Ye, P. Li, Y. Zeng, and G. Xu, “Structural evolution, electrical properties and electric-field-induced changes of (0.8−x)PbTiO3–xBiFeO3–0.2BaZrO3 system near the morphotropic phase boundary,” *Appl. Phys. A*, vol. 123, no. 4, p. 218, Apr. 2017, doi: 10.1007/s00339-016-0736-x.
[105] B. Allouche, I. Gueye, G. L. Rhun, P. Gergaud, and N. Vaxelaire, “In-situ X-ray diffraction on functional thin films using a laboratory source during electrical biasing,” *Mater. Des.*, vol. 154, pp. 340–346, Sep. 2018, doi: 10.1016/j.matdes.2018.05.016.
[106] K. Nguyen, E. Bellec, E. Zatterin, G. Le Rhun, P. Gergaud, and N. Vaxelaire, “Structural Insights of Electrical Aging in PZT Thin Films as Revealed by In Situ Biasing X-ray Diffraction,” *Materials*,

vol. 14, no. 16, Art. no. 16, Jan. 2021, doi: 10.3390/ma14164500.

General conclusions

Thin films of PZT with MPB composition elaborated by sol-gel method are one of the most widely used materials different types of MEMS devices: inkjet printheads, varifocal lenses, microspeakers, etc. thanks to their superior piezoelectric performances. In order to improve the performances of the devices, engineers and researchers need to cope with different challenges such as enhancing the performance of the materials as well as mitigating the fatigue effects and breakdown. Because the microstructure is the physical basis of the piezo/ferroelectric effects in materials, a better understanding of the correlation between the functional and structural properties is crucial for the improvement of the devices. Thus, the main objective of this PhD project was to contribute to this better understanding through the usage of in situ biasing XRD technique in couple with ferroelectric measurement. From XRD technique, several information about the microstructure of the sample could be obtained, such as the crystallographic phases ratio, thin film strain and stress, proportion between different domain variants and domain size. By performing in situ XRD on PZT capacitors while an electric field is applied, the field-induced microstructural changes occurring within PZT films could be observed. Then, by associating the results from this study with those obtained from the ferroelectric measurements performed right afterwards, the correlations between microstructure and the functional properties (electrical, mechanical) could be drawn for sol-gel based MPB PZT thin films.

This work began with the introductory chapter, which presents the background related to the thesis. This chapter began with a general introduction to ferroelectric materials, their history of development and some applications. In this part, the clamping effect, which is a special effect that differentiates the ferroelectric thin films from bulk ceramic samples, was also mentioned. The chapter then continued by focusing on the main material studied in the project, the $Pb(Zr,Ti)O_3$ (PZT). This part began with some generalities about PZT, including its phase diagram as well as the evolution of its physical properties as a function of temperature and Zr/Ti ratio. Next, we turned our attention to the sample with MPB composition, which attracts a lot of attention due to its superior piezoelectric properties. Here, a summary of the studies on the ferroelectric materials with MPB composition is introduced, which gave some explanations to the special piezoelectric performances of the MPB composition from the microstructure point of view. It is pointed out that the microstructure of MPB composition is complex with a mixture of small and unstable domains of different crystallographic phases. They have low polarization rotation energy, low shear stress and this could be the origin of the enhancement in electromechanical response. The part on the introduction of PZT terminated with an overview of the contribution of in situ biasing XRD technique to the development of PZT with MPB composition. The first chapter terminated with two main effects that degrade the properties of ferroelectric materials: fatigue and imprint effects. In this part, the definitions, origins and the strategies to alleviate these effects are presented.

The second chapter presented the experimental methods used in the thesis for the characterization of structural, electrical and mechanical properties of the PZT films. This chapter began with an introduction to XRD technique. Here, the fundamental of XRD is introduced, consisting of the definition and generation of X-rays as well as the theory of X-ray scattering. After that, the XRD configuration used in the thesis, Bragg-Brentano, is presented along with the information that can be extracted from XRD. The part on XRD technique finished with the data analysis of the XRD results based on the peak fitting using pseudo-Voigt model. Next, the electrical characterization techniques are presented. This part started with the definition of electrical polarization in ferroelectrics, followed by some methods used for the measurement of polarization ferroelectric materials. Here, the two types of measurement circuit: Sayer-Tower and shunt circuits are presented. Then two ferroelectric measurement strategies are presented: Dynamics Hysteresis measurement and Positive-Up Negative-Down (PUND). For a better understanding of the mechanism of the two strategies, the model of current density of ferroelectric materials is introduced. Afterwards, we focused on the techniques for the measurement

of effective piezoelectric coefficient $d_{33,eff}$. Firstly, the Double beam laser interferometer (DBLI) is introduced. Its working principle as well as the strategy for getting the $d_{33,eff}$ was presented. Then, the method of measurement by XRD was introduced. This part terminated with a comparison of the result obtained from the two techniques, in which the $d_{33,eff}$ obtained from DBLI showed higher value of around 10%. This could be due to the fact that in XRD the $d_{33,eff}$ was only measured from the grain oriented along (200) direction while in DBLI it is the mechanical response from the whole sample. This chapter ended with an introduction to the in situ biasing XRD setup developed in this thesis. In this part, both the hardware and software development are discussed, which consists of the designing of a special sample holder for the application of electric field and the preparation of the Python programs for the application of electric field during in-situ XRD and the measurement of the polarization using PUND technique.

The chapter III is dedicated to the macroscopic behavior of the PZT thin film under applied field. The first part describes the process of elaboration of PZT films by sol-gel technique followed by the microstructure properties of the deposited films. It is shown that the sample has the grain size of around 200 nm and from analyzing the TEM image, it seems that the grain boundary continuity is not disturbed by the RTA annealing interface. Moreover, by nano-beam XRD technique performed in synchrotron source, it was found that there exist a gradient of Zr/Ti ratio across the film thickness, which is a typical signature of PZT films elaborated by sol-gel deposition. After that, the XRD peak profiles of (200) pseudo-cubic structure obtained from simulation work is shown. The R3m of rhombohedral structure and P4mm of tetragonal structure are considered in the modelization The (200) pseudo-cubic peak has a triplet profile, consisting of (002)/(200) for P4mm structure and a single peak for R3m one. As the size of domain decreases from 200 nm to 10 nm, the separation between the peaks become less evident and at 10 nm, almost no peak separation can be seen. After that, the experimental results were shown, which indicated a difference between the (200) peak profiles between the PZT of different space groups and compositions. A comparison between different XRD configurations are also done, which indicated that the Kα1 BB in Johansson mode should be the most optimized to use in term of resolution at the cost of a large counting time (leading to potential electrical breakdown during in-situ biasing). Moreover some recurrent problems with the optic and the 1D detector also prevent the usage of Johansson mode in the project.

The next part of this chapter is the study of the relation between macroscopic properties and the texture of the PZT films. Two PZT films of (100) and (111) textured were compared, which showed an enhanced piezoelectricity in the case of (100) textured sample and an enhanced ferroelectricity for (111) textured film. The last part of this chapter is dedicated to the behavior of PZT films with MPB composition along an electrical ageing protocol (bipolar cycling at 10kHz). This experiment was performed on synchrotron source using the developed in situ biasing XRD setup. Results shown that electrical ageing impacts both the ferro- and piezoelectricity, evidenced by the decrease of both remnant polarization and $d_{33,eff}$ as a function of cycling. However, the decrease of $d_{33,eff}$ is more pronounce in the remnant polarization, indicating that the cycling process impacts the ferroelectricity more than piezoelectricity.

The chapter IV of the thesis was dedicated to the study of the PZT film at grain-scale. In-situ biasing XRD on two samples of PZT43 and a Nb-doped PZT (PZT52). These two samples represent the two families of PZT which are non-MPB and MPB samples, respectively. The first part of this chapter was an overview of the state of the art of the grain-scale analysis of ferroelectric material, which showed that even though significant efforts have been done the access the grain-scale behavior of ferroelectric materials, most of the studies are simulation or experimental works done on ceramic sample. As a result, we bring in a new study on the grain-scale analysis of thin films. Thanks to the X-ray beam of micronic size available in synchrotron source, we were able to reproduce the 3D reciprocal space map of the sample, which allowed us to study the properties of a single grains. From this, we saw that there is an evident heterogeneity in not only the mechanical properties ($d_{33,eff}$), but also in the structural

properties (phase ratio and tetragonality). We found that the proportion of different domain variants and their behavior under electric field is very localized, which do not mimic the average behavior at macroscopic scale. Finally, in order to compare the rate of heterogeneity between the two families of sample, we calculated the dispersion of the $d_{33,eff}$ and the tetragonality (c/a), which showed a higher value in the case of PZT52 sample.

To conclude, the main outcome of this work is the development of the in situ biasing XRD methodology using both laboratory and synchrotron X-ray source for the study of piezo/ferroelectric materials. Exploiting the developed setup, we have been able to give some important findings in the properties of PZT thin films. Firstly, by combing the in-situ XRD with high frequency cycling, we showed that under high frequency cycling, the ferroelectricity is degraded more than the piezoelectricity. Moreover, thanks to the usage of an X-ray beam of micrometer size, we have been able to construct the 3D reciprocal space map of PZT film and study its behavior at grain-scale. This work showed that at grain-scale there exists a heterogeneity in both structural and functional properties. The properties at grain-scale are also very localized, which are not coherent with the macroscopic properties. Lastly, we also found that the rate of heterogeneity is more remarkable in sample with MPB composition, which could stem from the more complex structure of this composition.

Perspectives

The work on in situ biasing XRD can continue beyond this thesis. Firstly, there are still rooms for improvement in terms of the methodology. In Bragg Bentano mode, we only look in Qz direction (i.e. film out-of-plane direction). A new equipment Xeuss® from Xenocs has arrived in the lab which allows to perform 2D diffraction in Grazing-Incident Wide-Angle X-ray Scattering (GIWAXS) mode as shown in Figure 6.1(a). A beam of 200x200µm² can be used which is small enough to investigate a 1mm² capacitor. In Figure 6.1(b), a 2D composite image in GIWAXS mode (incident angle of 5°) of a PZT (Zr/Ti = 30/70) 1µm film has been recorded which shows multiple Debye rings. In order to perform in-situ biasing experiment, specific instrumentation needs to be implemented to connect the MIM capacitor with the SMU (design of mini-probe station compatible with the GIWAXS stage). Since all environment is under primary vacuum, cables need to be put in the bypass to connect with the sample outside.

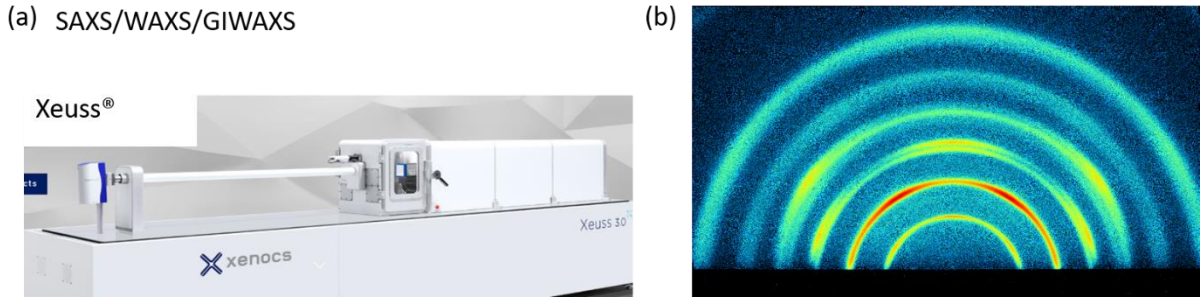

Figure 6.1: (a) The newly available SAXS/WASXS laboratory equipment and (b) the 2D composite image in GIWAXS mode (incident angle of 5°) of a PZT 30/70 1µm film where multiple Debye rings are collected

The study of sample with MPB composition using laboratory source is still difficult during this thesis, which stems from the peak profile of this composition. The profile of (200) peak with MPB sample consists of three peaks which are not well separated and overlapped themselves, making it difficult in identifying the evolution of each element under applied field. Improving the instrumental as much as possible while keeping a good signal statistic is the general objective here. With lab source, one of the potential solution is to use 1D detector combined with Bragg-Brentano in Johansson configuration which allows to select only the Kα1 radiation of the tube.

In terms of the materials, the in situ biasing XRD could be applied to other types of ferroelectric

materials, such as Potassium-sodium Niobate ($(K,Na)NbO_3$) or Hafnium Oxide (HfO_2). The usage of in situ biasing XRD will accelerate the development of these materials, which are the lead-free ferroelectric materials with the potential to replace PZT.

The in-situ biasing XRD could also be done under different temperature. This allows to observed the evolution of $d_{33,eff}$ and structural properties under varied temperature, which is interesting for many applications such as automotive or aeronautics. Feasibility tests have been carried out using standard in-situ biasing configuration and a domed hot stage (DHS) furnace (Anton Paar®). A PZT (MPB standard) sample has been measured at 100°C and room temperature. An enhanced $d_{33,eff}$ coefficient has been observed at 100°C (see Figure 6.2(b)). A new Linkam stage has also been recently acquired in the lab and will be integrated to our goniometer in a near future (Figure 6.2(a)).

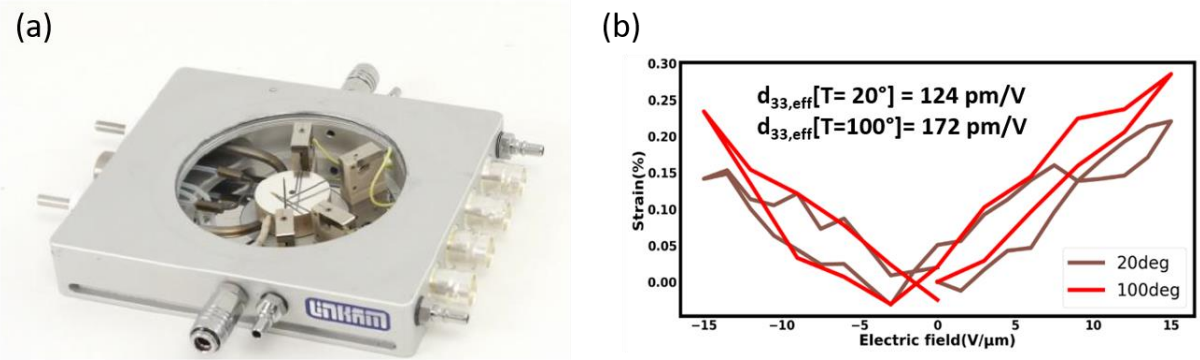

Figure 6.2: (a) Newly available Linkam TMS600-4PB and (b) the Strain extracted from (002)/(200) peaks in a PZT film with MPB standard composition at room temperature and T=200°C.

Concerning the grain-scale analysis, the experimental process could also be improved by doing the scan over a larger range of eta, giving us the ability to study a larger amount of grain. Furthermore, the grain identification process could also be ameliorated by the usage of an automatic identification program. This will helps facilitating the data analysis process, especially when working with the samples of small grain size and high grain density.

Ultimately, it would be interesting to analyze in detail the reciprocal maps of single grains (see Figure 6.3(a)). Inverse methods or appropriate simulation have to be tested to study domain fluctuations and eventually extracted some morphological parameters of domain distribution. While doing biasing, a significant speckle evolution has been recorded. This represents a complex domain re-organization through domain wall motion. The domain structure in such grain is expected to be geometrically complex as we can see in the cross-sectional TEM micrograph (Figure 6.3(b)).

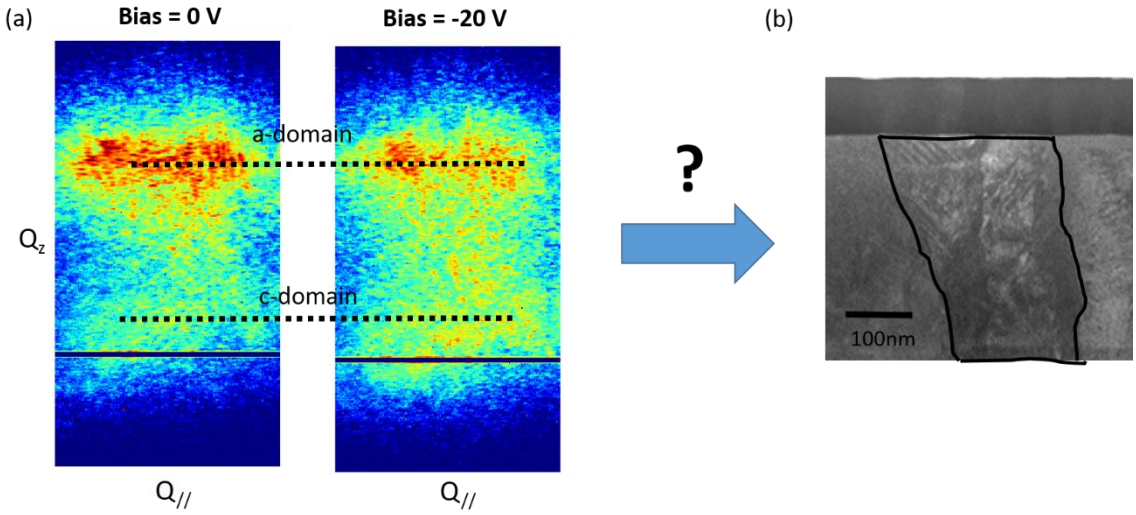

Figure 6.3: (a) Example of reciprocal space map of a single grain from PZT43 film at bias = 0V and -20V and (b) TEM bright field cross-sectional image where a complex nano-domain structure can be guessed.

Résumé

Les couches minces piézoélectriques et ferroélectriques sont essentielles dans de nombreuses applications telles que les capteurs, les actionneurs, les dispositifs pyroélectriques ou les mémoires avancées et font l'objet d'une recherche et développement active au CEA-LETI. L'amélioration des matériaux et des processus d'intégration associés est cruciale pour l'amélioration les performances des dispositifs finaux. Cette mission consiste non seulement à améliorer les propriétés du matériau, mais également à atténuer l'effet du vieillissement ainsi qu'à améliorer le temps de panne dans des conditions de travail réalistes. Par conséquent, une meilleure compréhension de la relation entre les paramètres structuraux et les propriétés fonctionnelles est nécessaire. Pour résoudre ce problème, la mesure simultanée de la réponse électrique et des informations structurelles fournies par la diffraction des rayons X (DRX), ou *in situ biasing* DRX, est particulièrement pertinente en raison de la possibilité d'obtenir une large gamme d'informations structurelles. L'objectif du projet de doctorat était triple. Tout d'abord, la configuration expérimentale pour le *in situ biasing* DRX existant dans notre plate-forme a été mise à jour. Ensuite, des expériences originales sur la configuration nouvellement développée sur des sources de rayons X de laboratoire et synchrotron ont été réalisées. Enfin, l'analyse des données a fourni de nouvelles informations sur le matériau qui sont utiles pour comprendre et anticiper la réponse macroscopique des films et des dispositifs. Le travail de thèse s'est concentré sur les prototypes de Titano-Zirconates de Plomb (PZT) où l'évolution structurale au cours du vieillissement électrique et la mobilité des domaines à la fois macroscopique et à l'échelle du grain ont été quantifiées.

Mots clefs: *couches minces piézo/ferroélectriques, diffraction des rayons X, in-situ, PZT*

Abstract

Piezoelectric and ferroelectric thin films are essential in many applications such as sensors, actuators, pyroelectric devices or advanced memories and are under active research and development in the CEA-LETI. The improvement of the materials and related integration processes are crucial for the improvement of the performance of the final devices. This mission consists of not only enhancing the material properties but also alleviating the aging effect as well as improving the time to breakdown in realistic working condition. As a result, a better comprehension of the relation between the structural parameters and the functional properties is needed. To address this problem, the simultaneous measurement of electrical response and the structural information provided by X-ray Diffraction (XRD), or *in situ biasing* XRD, is particularly relevant due to the ability to obtain a wide range of structural information. The objective of the PhD project was threefold. Firstly, the experimental setup for in situ biasing XRD existing in our platform has been upgraded. Then original experiments on the newly developed setup on both laboratory and synchrotron X-ray sources were performed. Finally, data analysis has provided new insights into the material which are useful to understand and predict the macroscopic response of the films and devices. The PhD work has been focused on the prototypes of Lead Zirconate Titante (PZT) where the structural evolution during electrical ageing and the mobility of domains at both macroscopic and grain-scale were quantified.

Keywords: *piezo/ferroelectric thin film, in-situ biasing XRD, PZT*